

---

# ADVANCEMENTS IN NONCLASSICAL GAS DYNAMICS

---

Proefschrift

ter verkrijging van de graad van doctor  
aan de Technische Universiteit Delft,  
op gezag van de Rector Magnificus prof. dr. ir. J. T. Fokkema,  
voorzitter van het College voor Promoties  
in het openbaar te verdedigen op dinsdag 12 mei 2009 om 15:00 uur

door

Nawin Ryan NANNAN

werktuigkundig ingenieur  
geboren te Paramaribo, Suriname

Dit proefschrift is goedgekeurd door de promotor:

Prof. ir. J. P. van Buijtenen

en de copromotor

Dr. P. Colonna

Samenstelling promotiecommissie:

Rector Magnificus	voorzitter
Prof. ir. J. P. van Buijtenen	Technische Universiteit Delft, promotor
Dr. P. Colonna	Technische Universiteit Delft, copromotor
Prof. dr. F. Scarano	Technische Universiteit Delft
Prof. dr. ir. M. E. H. van Dongen	Technische Universiteit Eindhoven
O.Univ.Prof. Dipl.-Ing. Dr.techn.	Technische Universität Wien,
A. Kluwick	Oostenrijk
Prof. dr. ir. C. J. Peters	The Petroleum Institute, V.A.E.
Dr. S. Rebay	Università degli Studi di Brescia, Italië
Prof. dr. G. J. Witkamp	Technische Universiteit Delft, reservelid

This research is supported by the Dutch Technology Foundation STW, applied science division of NWO and the Technology Program of the Ministry of Economic Affairs, the Netherlands, grant number DSF:6573.

ISBN 978-90-9024285-9

Copyright © by N. R. Nannan<sup>1</sup>

All rights reserved. No part of the material protected by this copyright notice may be reproduced or utilized in any form or by any means, electronic or mechanical, including photocopying, recording or by any information storage and retrieval system, without the prior permission of the author.

Front cover design by Andrea Lucchini and Martina Fantini.

---

<sup>1</sup>Author email: ryan.nannan@yahoo.com





# Summary

## Advancements in nonclassical gas dynamics

Shock waves can be formed in all states of matter, be it in the single- or multi-phase condition, when the substance is subjected to a rapid change of state, e.g., a sudden pressure or temperature variation. In the case of shock waves in gases, because of the fact that the developed theory is often based on the ideal-gas thermodynamic model, it is commonly accepted (by some even nowadays considered as an irreconcilable truth) that shock waves can be only of the compressive type, i.e., in the direction of flow, the gas experiences an abrupt increase of pressure whilst undergoing a supersonic-to-subsonic transition. Although it has been known since the late 1940s due to the works of Bethe and Zel'dovich and collaborators that it is in principle possible, from a theoretical point of view, to deliberately create expansion shock waves, provided that the correct substance and initial states are chosen, it was only until the early 1970s that the admissibility of expansion shock waves, i.e., shock waves featuring a transition such that in the direction of flow, the single-phase fluid experiences an abrupt pressure decrease, was accepted. The caloric property that is key in determining the nature of shock waves is referred to as the fundamental derivative of gas dynamics,  $\Gamma$ , of which the implications of its behavior were studied in detail by Thompson and coworkers. In honor of the above-mentioned researchers, compounds that can admit expansion shock waves due to the existence of an embedded region of  $\Gamma < 0$  in the dense-gas single-phase thermodynamic regime are referred to as BZT fluids, as first proposed by Cramer.

Further progress in the field of compressible fluid dynamics, specifically related to the study of nonclassical gas dynamic phenomena, as are for example expansion shock waves, necessitates the availability of experimental evidence. The motivation of this research stems from: i) the need of such an experiment to demonstrate the existence of nonclassical gas-dynamic phenomena in dense gases of molecularly complex fluids, the most intriguing of which is the theoretical admissibility of expansion shock waves, specifically because of the failure or ambiguity of previous two experiments (one in the early 1980s and one in the late 1990s), and ii) the fact that nonclassical gas-dynamic phenomena can be exploited in technical applications operating in the dense-gas regime or in transonic or supersonic conditions. One such example is the utilization of nonclassical gas-dynamic phenomena in small, decentralized energy conver-

---

sion systems operating according to the Rankine principle.

The research documented herein aims to develop, design, build and commission an experimental facility which can be used to generate and study nonclassical expansion shock waves in molecularly complex substances classifying as potential BZT candidates. Secondly, the facility that is to be built should be modular and flexible in its design and should therefore allow for studying both classical and nonclassical dense-gas flows. Cascading from the main goal, relevant theory has been developed. The results of these investigations are also useful/necessary for validating the proprietary software package for gas-dynamic simulations using real-gas properties.

To achieve the(se) goal(s), it is required to formulate relevant research questions, e.g., what is necessary from a physical perspective to give rise to the formation of rarefaction shock waves?, what is currently known about rarefaction shock waves in particular and nonclassical gas dynamics in general?, is it technically and economically feasible to build a facility to create and to investigate nonclassical gas-dynamic effects, how should this be done and what are the constraints?, etc. Answering these questions mandates a thorough but concise review of the theory of nonclassical gas dynamics, as documented in Chap. 2. Secondly, as was indicated, the study of Bethe has shown that certain nonclassical gas-dynamic phenomena are only permissible due to, among other things, the molecular complexity of the compound. That is, the fluid should have sufficient capability to store dynamic energy. Therefore, Chap. 3 focusses exclusively on the thermodynamic description of the test fluid from both a theoretical, semi-empirical and experimental viewpoint. Here, because of their favorable thermophysical characteristics, e.g., low toxicity, lubricating properties, etc., substances within the dimethylsiloxanes family are considered. Furthermore, the prediction of  $\Gamma$  as well as the identification of BZT-candidate fluids within the dimethylsiloxanes family is treated in Chap. 4. It is found, for example, that if highly accurate thermodynamic equations of state are available,  $\Gamma$  can be calculated with a degree of uncertainty that is suitable for the design and analysis of dense-gas applications, and, that for molecularly complex fluids, it is possible to achieve a comparatively higher level of accuracy in the estimation of  $\Gamma$  with respect to molecularly simpler fluids, if experimental data are available. For well-measured substances, technical multiparameter equations of state can be developed and the use of these can result in an appreciable improvement with respect to the uncertainty of the estimation of  $\Gamma$ . Additionally, the investigation of the vapor-liquid critical region of a single-component fluid has yielded the potential existence of nonclassical expansion-condensation shock waves in a wide class of substances not specifically classifying as BZT fluids, e.g., methane, carbon dioxide. Once the more fundamental aspects have been considered, Chap. 5 discusses various methods to experimentally demonstrate the existence of unconventional expansion shock waves in BZT fluids. The outcome of this study is that it is both theoretically and technically possible to create an unsteady nonclassical expansion shock wave in a polyatomic substance

---

classifying as a BZT fluid, namely dodecamethylcyclohexasiloxane. An assessment based on arguments for and against each identified method, taking aspects like reproducibility and repeatability of the experiment, costs, safety concerns, etc. into account, has resulted in the design and building of the Flexible Asymmetric Shock Tube (FAST) – a unique facility for high-temperature gas-dynamic experiments in organic fluids – equipped with a novel, custom-made fast-opening valve. The experiment conducted with the FAST aims at creating a so-called maximum-Mach expansion shock wave that is detected using four dynamic pressure instruments and a time-of-flight technique. The detailed design of the FAST is presented in Chap. 6. During the commissioning phase, discussed in Chap. 7, all pieces of equipment have been tested and the temperature control system has been thoroughly scrutinized. Also tests related to the intended experiment have been done with air and the time-of-flight technique has been tested. Alas, after suffering much delay (more than 1½ year) it is postponed to the follow-up of this project to provide experimental evidence of a rarefaction shock wave in dodecamethylcyclohexasiloxane. Chapter 8 gives concluding remarks and recommendations for future work.

*Nawin Ryan Nannan, April 8, 2009*



# Samenvatting

## Vorderingen in de niet-klassieke gasdynamica

Indien een medium, zij het in de één- of meergefase toestand, wordt onderworpen aan een snelle verandering van bijvoorbeeld druk of temperatuur, kan deze resulteren in de vorming van één of meerdere schokgolven. In het geval dat het schokgolven in gassen betreft, wordt vaak impliciet verondersteld, mede vanwege het feit dat de ontwikkelde theorie over schokvorming is toegespitst op ideale gassen, dat in de richting van de stroming, het gasvormig medium simultaan een abrupte compressie alsmede een supersone–subsonische transitie ondergaat. Alhoewel het sinds de late jaren 40 bekend is uit de werken van Bethe en Zeldo'vich en medewerkers dat vanuit een theoretisch oogpunt, indien een geschikte stof is gekozen, expansie schokgolven – deze zijn schokgolven waarbij het medium een abrupte drukverlaging ondervindt bij het passeren van een front, terwijl simultaan een (super)sonische–(sub)sonische transitie plaatsvindt – kunnen worden gegenereerd, heeft het tot de jaren 70 geduurd vooraleer dit werd geaccepteerd. De aard van een schokgolf wordt vanuit een thermodynamisch oogpunt bepaald door de fundamentele afgeleide der gasdynamica,  $\Gamma$ ; gedetailleerde studies betreffende de implicaties van het gedrag van  $\Gamma$  op compressibele stromingen zijn uitgevoerd mede door Thompson. Ter ere van de bijzondere bijdrage van Bethe, Zeldo'vich en Thompson aan de tak van de compressibele gasdynamica, worden stoffen die een thermodynamisch domein bezitten met  $\Gamma < 0$  in het verdichte damp gebied (dit is het domein nabij de dampvloeistof kritieke toestand van een stof, rechts van en inclusief de verzadigde damp lijn in een druk-specifiek volume,  $P$ - $v$ , toestandsdiagram), en derhalve expansie schokgolven kunnen handhaven, gerefereerd als BZT fluida. Het gasdynamisch gedrag van compressibele media als gevolg van het feit dat een stof zulk een thermodynamisch domein beschikt, wordt beschouwd als zijnde niet-klassiek.

Verdere ontwikkelingen in de niet-klassieke gasdynamica (waartoe de zojuist genoemde expansie schokgolven behoren) vergt experimenteel bewijs van BZT effecten. De motivatie voor dit onderzoek stamt uit: i) de noodzaak om experimenteel bewijs te leveren voor het bestaan van onconventionele, niet-klassieke gasdynamische fenomenen, dan wel de toelaatbaarheid van expansie

---

schokgolven, met name vanwege de discutabele resultaten van twee eerder uitgevoerde experimenten (het eerste experiment dateert uit de jaren 80 en het tweede is uitgevoerd in de late jaren 90), en ii) het feit dat niet-klassieke gasdynamische effecten kunnen worden geëxploiteerd in processen welke plaatsvinden in het verdichte damp gebied onder transsonic of supersonic condities. Een voorbeeld van zo een proces is de expansie van het werkmedium in de turbine van een mini- of microwarmtekracht unit. Zulke units werken volgens het Rankine cyclus en maken gebruik van een organisch stof en beoogde applicaties zullen worden ontwikkeld voor vermogens in de kWatt orde-grootte.

Het gedocumenteerde onderzoek richt zich op het ontwikkelen, ontwerpen en opzetten van een experimentele opstelling welke kan worden toegepast om in een moleculair complex organisch fluïdum, onconventionele expansie schokgolven te genereren en daar metingen aan te verrichten. Bijkomstig hieraan is dat de te bouwen opstelling modulair dient te zijn, zodat de opstelling flexibel is in haar gebruik. De resultaten van dit onderzoek zijn bovendien nodig voor het valideren van de binnen de afdeling ontwikkelde CFD software programma welke gebruik maakt van toestandsgrootheden van reële gassen.

Om de bovengenoemde doelstellingen te realiseren, is het nodig om juiste onderzoeksvragen te formuleren, bijvoorbeeld: wat is nodig vanuit een fysisch perspectief om expansie schokgolven te creëren?, wat is thans bekend over expansie schokgolven in het bijzonder en de niet-klassieke gasdynamica in het algemeen?, is het überhaupt mogelijk, vanuit een technisch en economisch perspectief, om een opstelling op te zetten waarmee niet-klassieke gasdynamische effecten kunnen worden bestudeerd, hoe dient zo een experiment uitgevoerd te worden en wat zijn de mogelijke beperkingen? Formulering van geschikte antwoorden op de laatstgenoemde vragen vergt, ten eerste, een grondige doch beknopte beschouwing van de theorie, zoals gedocumenteerd in Hfdst. 2. Ten tweede, zoals eerder was aangegeven, heeft de studie van Bethe aangetoond dat de toelaatbaarheid van expansie schokgolven onder andere wordt bepaald door de moleculaire complexiteit van een stof, met name, de capaciteit van het medium om dynamische energie inwendig op te slaan. Vandaar dat Hfdst. 3 primair de nadruk legt op de thermodynamische beschrijving van het testmedium. Voor dit onderzoek zijn siloxaan oliën geselecteerd, omdat deze stoffen vanuit een experimenteel perspectief gunstige thermofysische eigenschappen bezitten, zoals lage toxiciteit, goede smeeringseigenschappen, enz. Verder is de bepaling van de numerieke waarde van  $\Gamma$  alsook de identificatie van zogenoemde BZT media behandeld in Hfdst. 4. Uit de in Hfdst. 4 verrichtte studie blijkt bijvoorbeeld dat, indien nauwkeurige toestandsvergelijking aanwezig zijn voor een bepaalde stof,  $\Gamma$  kan worden uitgerekend met een nauwkeurigheid welke voldoende is om geavanceerde processen en applicaties te analyseren en te ontwikkelen. Voor stoffen waarbij er ruim voldoende experimentele, heterogene thermodynamische data beschikbaar zijn, kunnen toestandsvergelijkingen worden ontwikkeld en met deze vergelijkingen, kan de onnauwkeurigheid in de berekende  $\Gamma$ -waarde worden verkleind. In feite, indien er voldoende thermo-

---

dynamische meetwaarden zijn, kan  $\Gamma$  van moleculair complexe stoffen met een hogere nauwkeurigheid kunnen worden bepaald dan het geval is voor simpele stoffen. Een gedetailleerde studie van het damp-vloeistof kritieke gebied van enkele één-component stoffen, namelijk methaan, kooldioxide en water, met betrekking tot de waarde van  $\Gamma$ , heeft aangetoond dat de fundamentele afgeleide divergeert nabij de kritieke punt, ongeacht de moleculaire complexiteit (onder de validiteit van een set hypothesen). Berekeningen tonen bijvoorbeeld aan dat  $\Gamma$  negatief is in het twee-fase kritieke gebied voor de geselecteerde één-component stoffen en toepassing van de schoktoelaatbaarheidscondities leert dat, in principe, expansie schokgolven met condensatie toelaatbaar zijn onder correct gekozen initiële condities. Nadat de fundamentele items zijn behandeld, geeft Hfdst. 5 een analyse van verschillende potentiële mogelijkheden om BZT effecten, met nadruk op een expansie schokgolf, experimenteel aan te tonen. Uit deze studie volgt dat het zowel theoretisch alsook technisch mogelijk is om een stationair bewegende schokgolf te genereren in een polyatomische stof welke bovendien kan worden geklassificeerd als BZT fluidum, namelijk dodecamethylcyclohexasiloxaan. Op basis van geformuleerde argumenten voor en tegen iedere geïdentificeerde optie, waarbij aspecten als reproduceerbaarheid en herhaalbaarheid van de metingen, kosten, veiligheid, enz. zijn meegenomen, is voortgevloeid dat een schokbuis kan worden gebruikt. Deze schokbuis, Flexible Asymmetric Shock Tube (FAST) genaamd, is een hoge-temperatuur opstelling voorzien van een unieke klep (de fast-opening valve), voor het uitvoeren van gasdynamische experimenten in organische stoffen. De gedetailleerde beschrijving van het ontwerp van de FAST is te vinden in Hfdst. 6. De openingstijd van de klep onder de voorziene hoge temperatuur is in de orde van 4–6 ms. Het experiment dat wordt uitgevoerd middels de FAST heeft tot doel om een expansie schokgolf te creëren welke beweegt met de grootst mogelijk golf-Mach waarde, waarbij het dampvormig medium een supersonische transitie ondergaat. De beweegsnelheid van de golf wordt bepaald door middel van een zogenaamde “time-of-flight” methode, waarbij de tijd die nodig is voor de golf om een nauwkeurig bepaalde afstand af te leggen, wordt geregistreerd middels gesynchroniseerde dynamische drukopnemers. Alvorens het experiment uit te voeren met het organisch BZT medium, zijn de componenten, de opstelling als geheel, de meetinstrumenten en het acquisitie- en regelsysteem met succes getest, zie Hfdst. 7. Echter, na heel veel vertraging opgelopen te hebben (meer dan  $1\frac{1}{2}$  jaar), zal in het vervolg van dit project uitsluitel moeten worden gegeven of inderdaad expansie schokgolven kunnen worden gegenereerd met de FAST in dodecamethylcyclohexasiloxaan. Hoofdstuk 8 presenteert de conclusies en geeft enkele aanbevelingen voor vervolg onderzoek.

*Nawin Ryan Nannan, 8 april 2009*



# Table of Contents

<b>1</b>	<b>Introduction</b>	<b>1</b>
1.1	A brief in nonclassical gas dynamics . . . . .	1
1.2	Motivation and thesis outline . . . . .	3
<b>2</b>	<b>Nonclassical gas dynamics and Bethe-Zel'dovich-Thompson fluids</b>	<b>7</b>
2.1	Theory of shock waves in the dense-gas regime . . . . .	8
2.2	Compression waves through the BZT-region . . . . .	18
2.3	Expansion waves through the BZT-region . . . . .	24
<b>3</b>	<b>Thermodynamic properties of selected dimethylsiloxanes</b>	<b>35</b>
3.1	Introduction . . . . .	37
3.2	Ideal-gas isobaric heat capacities of selected linear and cyclic dimethylsiloxanes . . . . .	38
3.2.1	Overview . . . . .	38
3.2.2	Experimental section . . . . .	39
3.2.2.1	The resonator . . . . .	40
3.2.2.2	Sample purity . . . . .	42
3.2.2.3	Calibration . . . . .	42
3.2.2.4	Measurement procedure . . . . .	43
3.2.3	Experimental results . . . . .	44
3.2.3.1	Experimental data for D <sub>4</sub> . . . . .	44
3.2.3.2	Experimental data for D <sub>5</sub> . . . . .	46
3.2.4	Ab initio calculations . . . . .	47
3.2.4.1	Basis-set dependence . . . . .	48
3.2.4.2	Frequency scaling factor . . . . .	50
3.2.4.3	Predicted ideal-gas isobaric heat capacities . . . . .	52
3.3	Equations of state for selected linear and cyclic siloxanes . . . . .	55
3.3.1	Introduction . . . . .	55
3.3.2	Data survey – MDM, [(CH <sub>3</sub> ) <sub>3</sub> -Si-O <sub>1/2</sub> ] <sub>2</sub> -[(CH <sub>3</sub> ) <sub>2</sub> -Si-O] . . . . .	58
3.3.3	Substance-specific parameters for the equations of state . . . . .	67
3.3.4	Performance evaluation of the equation of state – MDM, [(CH <sub>3</sub> ) <sub>3</sub> -Si-O <sub>1/2</sub> ] <sub>2</sub> -[(CH <sub>3</sub> ) <sub>2</sub> -Si-O] as an example . . . . .	70

<b>4</b>	<b>On the computation of the fundamental derivative of gas dynamics in the dense-gas region</b>	<b>83</b>
4.1	Introduction . . . . .	84
4.2	Critical review of previous studies . . . . .	86
4.3	The fundamental derivative of gas dynamics for selected alkanes .	89
4.3.1	Reference equations of state . . . . .	89
4.3.2	Simpler equations of state . . . . .	98
4.4	The fundamental derivative of gas dynamics for selected siloxanes	99
4.5	The fundamental derivative of gas dynamics in the vapor-liquid critical region of pure fluids . . . . .	104
4.5.1	Introduction . . . . .	104
4.5.2	Previous work related to compressible dynamics in the critical region . . . . .	111
4.5.3	The fundamental derivative of compressible dynamics in the two-phase critical region . . . . .	115
4.6	Concluding remarks . . . . .	118
<b>5</b>	<b>Methods for the experimental investigation of nonclassical gas-dynamic phenomena</b>	<b>127</b>
5.1	Introduction . . . . .	127
5.2	Unsteady experiments . . . . .	128
5.2.1	The triple-discontinuity experiment . . . . .	128
5.2.1.1	The shock tube . . . . .	128
5.2.1.2	Initial fluid-states for a triple-discontinuity experiment . . . . .	132
5.2.1.3	Influence of secondary effects on shock-tube experiments . . . . .	137
5.2.2	Point explosions in dense gases . . . . .	144
5.3	Steady experiments . . . . .	146
5.3.1	Nonclassical shock waves in a classical nozzle . . . . .	146
5.3.1.1	Overview – steady isentropic flows of BZT fluids in one dimension . . . . .	146
5.3.1.2	Creating steady nonclassical shock waves in classical nozzles . . . . .	149
5.3.2	Supersonic flow in two dimensions - oblique shock waves	155
5.4	Comparison between the experimental options . . . . .	161
5.5	The proposed experimental facility . . . . .	166
5.6	Working fluid selection . . . . .	167
<b>6</b>	<b>Rarefaction-shock-wave experiments in the flexible asymmetric shock tube (FAST)</b>	<b>171</b>
6.1	Introduction . . . . .	172
6.2	Preliminary design . . . . .	172
6.2.1	Fast-opening valve and charge-tube length . . . . .	175

6.2.2	Charge-tube diameter . . . . .	177
6.2.3	Nozzle design . . . . .	179
6.2.4	Reservoir design . . . . .	181
6.3	Verification of the preliminary design . . . . .	182
6.3.1	Numerical simulation of the FAST experiment . . . . .	182
6.3.2	Uncertainties due to the thermodynamic model . . . . .	184
6.3.3	Wave-speed measurement . . . . .	184
6.4	Experimental procedures . . . . .	187
<b>7</b>	<b>Commissioning of the FAST</b>	<b>191</b>
7.1	The FAST, as built . . . . .	192
7.1.1	Main components and assemblies of the FAST . . . . .	192
7.1.2	The data-acquisition and control system . . . . .	198
7.1.3	Procedures to conduct RSW-experiments . . . . .	200
7.2	Temperature control of the charge tube . . . . .	202
7.3	Compression-shock-wave experiment using air . . . . .	205
<b>8</b>	<b>Conclusions and recommendations for future research</b>	<b>219</b>
8.1	Conclusions . . . . .	219
8.2	Recommendations . . . . .	222
<b>A</b>	<b>Experimental speed-of-sound data for fluids <math>D_4</math>, <math>[(CH_3)_2-Si-O]_4</math>, and <math>D_5</math>, <math>[(CH_3)_2-Si-O]_5</math></b>	<b>227</b>
<b>B</b>	<b>Relevant expressions for computing the fundamental derivative of gas dynamics from a canonical Helmholtz function</b>	<b>231</b>
<b>C</b>	<b>Equations valid in the critical region – The revised and extended linear model</b>	<b>233</b>
<b>D</b>	<b>Thermodynamic properties in the VLE-region of a single-component fluid</b>	<b>243</b>
	<b>Bibliography</b>	<b>251</b>



*“You know, I’m the President during this period of time, but I think when the history of this period is written, people will realize a lot of the decisions that were made on Wall Street took place over a decade or so, before I arrived in President, during I arrived in President.”*

President George W. Bush, ABC News interview, December 1, 2008

# 1

## Introduction

### 1.1 A brief in nonclassical gas dynamics

Studies involving compressible gas dynamics are often either implicitly or explicitly based on the assumption that the fluid properties can be described with the, be it polytropic, ideal-gas equation of state (EoS). However, as is well-known, substances in the vapor phase can exhibit an appreciable departure from ideal-gas behavior even at moderate pressures; see for example the generalized compressibility chart in a fundamental textbook on engineering thermodynamics, e.g., Moran and Shapiro [151] (pg. 90). Moreover, if pressures and temperatures are of the order of their critical-point value or close to saturated conditions, the ideal-gas thermodynamic model fails to predict physically correct behavior. Consequently, the study of compressible flows of superheated vapor in this so-called dense-gas thermodynamic regime requires the utilization of thermodynamic models that possess the capability to take real-gas effects into account. If real-gas behavior is considered, for example through use of the polytropic Van der Waals EoS, various studies have demonstrated that under specific conditions, certain substances composed of polyatomic molecules can exhibit gas-dynamic phenomena which feature significant differences from both a qualitative and quantitative point of view, with respect to their ideal-gas counterparts. Gas-dynamic phenomena in ideal gases for example include the admissibility of only pure compression shock waves and expansion fans. Most notable examples include the admissibility of expansion shock waves and compression fans – phenomena that are forbidden to occur under the hypothesis of validity

of the ideal-gas EoS due to violation of the second law of thermodynamics (see also Jouguet [106], Zemplén [233] and Rayleigh [168]) – sonic shock waves, composite waves, e.g. compressive shock-fans or expansive fan-shock-fans, etc. A review of these nonclassical gas-dynamic phenomena is given by Menikoff and Plohr [166].

Focussing on the study of gas-dynamic discontinuities, viz. shock waves, as was pointed out by Becker [12] (pg. 322 and 357) and anticipating the results of Sec. 2.1, the admissibility of the type of shock wave, viz. expansive or compressive, is dependent on the magnitude of the variation of the zero-frequency speed of sound with isentropic density perturbations. According to Hayes [89] and Landau and Lifshitz [123], the nonlinear variation of the speed of sound with isentropic density changes can conveniently be expressed in a non-dimensional form as (a list with the used nomenclature is provided at the end of this and each subsequent chapter)

$$\Gamma \equiv 1 + \frac{\rho}{c} \left( \frac{\partial c}{\partial \rho} \right)_s = \frac{v^3}{2c^2} \left( \frac{\partial^2 P}{\partial v^2} \right)_s, \quad (1.1)$$

where  $\rho$  is the density,  $s$  denotes the entropy,  $P$  is the pressure,  $v = \rho^{-1}$  is the specific volume, and  $c$  denotes the zero-frequency (or thermodynamic) speed of sound, namely

$$c \equiv \sqrt{\left( \frac{\partial P}{\partial \rho} \right)_s}. \quad (1.2)$$

The thermodynamic property  $\Gamma$  is referred to as the fundamental derivative of gas dynamics due to its importance in many facets of compressible gas dynamics [196, 41, 42, 46, 47]. These include not only shock-wave theory, but also the study of isentropic and Fanno flows of dense gases. Formulated in terms of the fundamental derivative of gas dynamics, a polytropic ideal gas can only admit compression shock waves and expansion fans, whilst satisfying the thermodynamic and mechanical constraints (as is to be demonstrated in Sec. 2.1), exclusively because  $\Gamma = (\gamma + 1)/2 > 1 > 0$ , where  $\gamma$  is the ratio of the isobaric heat capacity with respect to the isochoric heat capacity, i.e.,  $\gamma \equiv C_P/C_v$ . If real-gas effects are taken into account and if  $\Gamma$  changes sign and becomes negative, see Fig. 1.1, the resulting finite interval of concavity of the strictly monotonous  $P$ - $v$ -isentropes enables the admissibility of expansion shock waves, compression fans, and composite waves, whilst satisfying the thermodynamic and mechanical constraints (see Sec. 2.1). The composite wave fields are the result of mixed nonlinearity, that is, they result from the fact that  $\Gamma$ , at least locally, changes its sign.

That  $\Gamma$  can indeed be negative can be explained by considering the behavior of the critical isotherm in the  $P$ - $v$ -plane. It is known that at the critical point both  $(\partial P/\partial v)_T$  and  $(\partial^2 P/\partial v^2)_T$  of the critical isotherm are zero and that

in the ideal-gas limit, the critical isotherm is convex. Moreover, the isothermal compressibility,  $\kappa_T \equiv -1/v (\partial v / \partial P)_T$ , is positive for all substances in all phases. The critical isotherm therefore, must display a limited interval of concavity located between the critical specific volume  $v_C$  and the ideal-gas limit where  $v \rightarrow \infty$ . For substances composed of sufficiently complex polyatomic molecules, as classified in Ref. [29], due to the large isochoric heat capacity (excluding the critical region), the behavior of isentropes is similar to that of isotherms and for this reason, isentropes also feature a region of concavity. Indeed, both Bethe [14] and Zel'dovich [231] have independently shown that  $\Gamma$  can become negative for a polytropic Van der Waals fluid provided that the ideal-gas isochoric heat capacity is sufficiently large.<sup>1</sup> Figure 1.1 shows the region of  $\Gamma < 0$  for a hypothetical polytropic Van der Waals fluid with large ideal-gas isochoric heat capacity; examples of real fluids that exhibit a region of  $\Gamma < 0$  are provided in Sec. 4.1.

Apart from the analysis of nonclassical phenomena admissible in the single-phase dense-gas region, Zel'dovich and Raizer [232] have pointed out that expansion shock waves can also occur during polymorphic phase transition in solids due to the discontinuity of isentropes such that  $\Gamma \rightarrow -\infty$  at the phase boundary. See the paper by Ivanov and Novikov [103] on the observation of expansion shock waves in iron due to solid-solid phase transition and Ref. [11] on expansion shock waves observed in fused silica which is an amorphous solid. Similarly,  $\Gamma \rightarrow -\infty$  for certain thermodynamic states located on the vapor- and liquid saturation lines of a retrograde fluid, as first demonstrated by Bethe, ergo supersonic flows of retrograde fluids with phase changes also exhibit phenomena associated with mixed nonlinearity, e.g., evaporation expansion shock waves (refer for example to the works of Thompson and coworkers, e.g., Refs. [202, 199, 200]). Because of the pioneering work of Bethe, Zel'dovich and Thompson in the field of nonclassical gas dynamics, i.e., the study of compressible wave fields in the dense-gas thermodynamic regime of a molecularly complex compound, substances that exhibit a region of  $\Gamma < 0$  in the single-phase dense-gas regime are known as Bethe-Zel'dovich-Thompson (BZT) fluids [45], and phenomena that ensue from the fact that a substance has an embedded region of negative nonlinearity (region of  $\Gamma < 0$ ) are referred to as BZT effects.

## 1.2 Motivation and thesis outline

In spite of the important amount of theoretical knowledge gained especially in the last 35 years, no successful experimental observation of BZT effects in a gas is available. To the knowledge of the author, two attempts to demonstrate BZT effects in single-phase dense-gases have been made in the past. The first of

<sup>1</sup>According to Ref. [201], Bethe however dismissed the fact that real fluids can display a region of finite size where  $\Gamma < 0$ .

these is the experiment reported by Borisov et. al. [17, 119]. However, the result reported in Ref. [17] on the observation of a single-phase expansion shock wave has been criticized by Ferguson [65] as not providing experimental evidence of a single-phase expansion shock wave. Ferguson’s assessment was based on the fact that model EoS’s (as are the cubic EoS’s) and multiparameter EoS’s do not predict freon-13, i.e., the test fluid used by Borisov et. al., to exhibit a region of  $\Gamma < 0$  in the dense-gas thermodynamic regime. Moreover, Ferguson demonstrates numerically that the expansion wave created and documented in Ref. [17] potentially displays phase transition and/or non-equilibrium transition. The second experiment is the one conducted by Ferguson and documented in his PhD thesis [65]; Ferguson’s experiment was not successful due to thermochemical decomposition of the test fluid, namely a perfluorocarbon, at

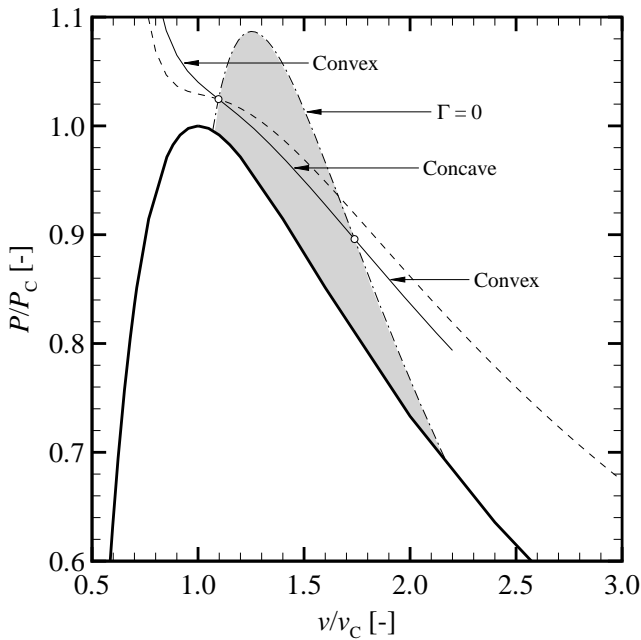


Figure 1.1: The shaded area represents the region where  $\Gamma < 0$  for a hypothetical polytropic Van der Waals fluid with  $C_v/R = 50$  ( $C_v$  is the specific isochoric heat capacity and  $R$  is the specific gas constant). Also shown are an isentrope which exhibits both convex and concave behavior (solid line) and an isotherm (dashed line).  $\circ$ : thermodynamic states where the isentrope has its inflection points,  $v_C$  denotes the critical specific volume and  $P_C$  is the critical pressure.

the high experimental temperature.

Experimental evidence of nonclassical gas-dynamic effects in general is important for further progress in the field of compressible fluid dynamics. The motivation of this research stems from the need of such an experiment to demonstrate the existence of nonclassical gas-dynamic phenomena in dense gases of molecularly complex fluids, the most intriguing of which is the theoretical admissibility of expansion shock waves. Furthermore, nonclassical gas-dynamic phenomena can be exploited in technical applications operating in the dense-gas regime or in transonic or supersonic conditions. One such example is the utilization of BZT effects in organic-Rankine-cycle engines, where, under suitably chosen conditions, shock wave formation can be avoided or, as far as shock waves are generated, they are weak and boundary layer detachment is suppressed. This behavior which is typical of BZT fluids, can be beneficial during part-load operation of the organic-Rankine-cycle engine.

The aim of this research is to develop, design, build and commission an experimental facility which can be used to generate and study nonclassical expansion shock waves in molecularly complex substances classifying as potential BZT candidates. Secondly, the facility that is to be built must be modular and flexible in its design and should therefore allow for investigating both classical and nonclassical dense-gas flows. Moreover, cascading from the main goal, relevant theory has been developed. The results of these investigations are also useful/necessary for validating the proprietary software package zFlow [36], i.e., a CFD software package for compressible gas-dynamic simulations using real-gas properties [38].

The thesis is structured as follows. Firstly, Chap. 2 outlines the theoretical background with respect to shock waves, where, starting from the formation of shock waves in general, the admissibility of unconventional gas-dynamic discontinuities like the mentioned expansion shock waves, is treated. The thermodynamic description of the fluid is key to both identifying potential BZT candidates, and to the design of an experimental facility in which nonclassical wave fields are to be formed. Herein, prior to the development of a thermodynamic model of the fluid, the use of the EoS for the design and analysis of technical applications was also taken into consideration. For this purpose, Chap. 3 treats the development of consistent multiparameter EoS's for dimethylsiloxanes, which in this study have been selected as test fluids. Dimethylsiloxanes have been chosen for the envisaged experiment(s) because of their favorable characteristics regarding the design of the facility, e.g., limited flammability and toxicity, and from the viewpoint of the application of the results of this research in the near future, e.g., the development and testing of organic-Rankine-cycle turbines. Accurate computation of the value of the fundamental derivative of gas dynamics is a necessity for understanding and describing real-gas processes occurring in the dense-gas regime. The influence of the functional relation of the thermodynamic model regarding the computation of  $\Gamma$  is discussed in Chap. 4. This includes a study of  $\Gamma$  in the single- and two-phase critical region using physically

based scaling laws. After these preliminary chapters which are mainly related to theory, Chap. 5 discusses experimental options that can be used to generate an expansion shock wave in a BZT fluid. The assessment of a variety of possible and technically feasible experimental options has resulted in the choice of an experiment and thus of a facility which incorporates the operational ease, modularity and versatility of both the variable-cross-section shock tube and the Ludwig tube. The preliminary design of this facility is treated in Chap. 6 and the commissioning of the setup as built, is discussed in Chap. 7. Finally, Chap. 8 summarizes conclusions and recommendations for future research activities.

### Nomenclature

Symbol	Description
$C_P$	Specific isobaric heat capacity
$C_v$	Specific isochoric heat capacity
$c$	Thermodynamic speed of sound
$P$	Pressure
$R$	Specific gas constant
$s$	Specific entropy
$T$	Absolute temperature
$v$	Specific volume
$\Gamma$	Fundamental derivative of gas dynamics
$\gamma$	Heat capacity ratio
$\kappa_T$	Isothermal compressibility
$\rho$	Density

“Do you have blacks, too?”

President George W. Bush speaking to President Fernando Cardoso, Washington, D.C., November 8, 2001

# 2

## Nonclassical gas dynamics and Bethe-Zel’dovich-Thompson fluids

### Abstract

*Dense gases of so-called Bethe-Zel’dovich-Thompson (BZT) fluids can theoretically display unusual gas-dynamic phenomena, notably the admissibility of single-phase expansion shock waves and compression fans. That these phenomena – which are typical only of BZT fluids if the pressure and temperature are of the order of their vapor-liquid-critical-point value – are considered unconventional, stems from the fact that experimental evidence is unavailable. It is the goal of this chapter to present the theoretical background of the field of science, nowadays referred to as nonclassical gas dynamics. More specifically, the focus herein is on how a compound is classified as being a BZT fluid and what the conditions are that give rise to the admissibility of nonclassical gas-dynamic phenomena. The contents of this chapter are as follows: for the sake of completeness, Sec. 2.1 provides a brief introduction to the theory of shock waves, treating the formation of shock waves, the shock admissibility conditions, and the structure of weak shock waves. The subsequent sections, Secs. 2.2 and 2.3, respectively give a qualitative description of compression and expansion waves traversing the negative-nonlinearity region, i.e., the  $\Gamma < 0$ -region. Furthermore, double sonic shock waves, these are the strongest expansion shock waves that can be admitted, and maximum-Mach expansion shock waves, these are shock waves with the greatest supersonic to sonic transition, are discussed. These nonclassical BZT effects are important also from an exper-*

imental viewpoint.

## 2.1 Theory of shock waves in the dense-gas regime

A shock wave is defined as a relatively thin geometric surface through which there is flow of matter which experiences abrupt, seemingly discontinuous, variation of state. This type of mechanical wave originates when a substance is subjected to rapid compression or expansion. The evolution of an initially smooth disturbance into a discontinuity was theoretically discovered by Riemann [170], Rankine [167] and Hugoniot [97]. Following the mathematical treatment of Riemann, consider a (quasi-) one-dimensional flow through a duct of constant cross-sectional area with an initially continuous density and velocity profile. If in addition the flow is homentropic, i.e.,  $\mathcal{D}s/\mathcal{D}t = 0 \wedge \nabla s = 0$ , where  $\mathcal{D}/\mathcal{D}t$  represents the material (convective) derivative and  $\nabla$  denotes the gradient vector, and if body forces can be neglected, the conservation equations for mass and momentum are of the form (if required, refer to the list at the end of this chapter explaining the adopted nomenclature)

$$\begin{cases} \frac{\partial \rho}{\partial t} + \rho \frac{\partial u}{\partial x} + u \frac{\partial \rho}{\partial x} = 0 \\ \frac{\partial u}{\partial t} + u \frac{\partial u}{\partial x} + \frac{1}{\rho} \frac{\partial P}{\partial x} = 0. \end{cases} \quad (2.1)$$

Here,  $P$  is the pressure,  $t$  is the time,  $u$  is the absolute velocity,  $x$  represents the spatial coordinate, and  $\rho$  denotes the fluid density. Because the flow is homentropic, the pressure is related to the density as<sup>1</sup>

$$\frac{\partial P}{\partial x} = c^2 \frac{\partial \rho}{\partial x}, \quad (2.2)$$

where  $c$  is the thermodynamic speed of sound. Substitution of Eq. (2.2) in the conservation equations yields

$$\begin{cases} \frac{\partial \ln \rho}{\partial t} + \frac{\partial u}{\partial x} + u \frac{\partial \ln \rho}{\partial x} = 0 \\ \frac{\partial u}{\partial t} + u \frac{\partial u}{\partial x} + c^2 \frac{\partial \ln \rho}{\partial x} = 0. \end{cases} \quad (2.3)$$

Next, identify the thermodynamic function

$$F(\rho(x, t)) \equiv \int_{\rho_0}^{\rho} c d(\ln \rho) = \int_{P_0}^P \frac{dP}{\rho c} = \int_{c_0}^c \frac{dc}{\Gamma - 1}, \quad (2.4)$$

<sup>1</sup>For isentropic flows, Eq. (2.2) is valid along individual streamlines.

whereby the subscript “0” in the lower limit of integration represents a reference state and  $\Gamma$  is the fundamental derivative of gas dynamics defined in Eq. (1.1) in Chap. 1. The function  $F(x, t)$  is meaningful only for isentropic flows, i.e., flows that satisfy  $\mathcal{D}s/\mathcal{D}t = 0$ . Furthermore, for reasons that will become clear in the following, introduce the notation  $\mathcal{J}^+(x, t) \equiv u(x, t) + F(x, t)$  and  $\mathcal{J}^-(x, t) \equiv u(x, t) - F(x, t)$ . Formulated in terms of  $F(x, t)$  and  $\mathcal{J}^\pm(x, t)$  and after some symbolic manipulation, the governing equations of the flow reduce to

$$\begin{cases} \left( \frac{\partial}{\partial t} + (u - c) \frac{\partial}{\partial x} \right) \mathcal{J}^- = 0 \\ \left( \frac{\partial}{\partial t} + (u + c) \frac{\partial}{\partial x} \right) \mathcal{J}^+ = 0. \end{cases} \quad (2.5)$$

The governing equations of the flow, as formulated in Eqns. (2.5), are first-order quasi-linear hyperbolic partial differential equations of the form

$$\underbrace{\alpha_1(x, t)}_{=1} \frac{\partial \mathcal{J}^\pm}{\partial t} + \underbrace{\alpha_2(x, t)}_{=u \pm c} \frac{\partial \mathcal{J}^\pm}{\partial x} + \underbrace{\alpha_3(x, t)}_{=0} \mathcal{J}^\pm = 0, \quad (2.6)$$

provided that  $\mathcal{J}^\pm \neq 0$ . First-order quasi-linear hyperbolic partial differential equations can be solved using the method of characteristics whereby the initial problem which is formulated in terms of  $(x, t)$ , is converted into a new coordinate system  $(x_0, l)$  in which each partial differential equation is transformed into two ordinary differential equations along certain curves, namely characteristic curves described by  $\{[x(l), t(l)] : 0 < l < \infty\}$ , in the  $x$ - $t$ -plane. Variable  $x_0$  changes only along the initial curve in the  $x$ - $t$ -plane, so at  $t = 0$ , and it remains constant along the characteristic curve; conversely, variable  $l$  changes along the characteristic curve. The characteristic curves for Eqns. (2.5) are  $dt/dl = \alpha_1(x, t) = 1$  and  $dx^\pm/dl = \alpha_2(x, t) = u \pm c$ , where  $\alpha_2(x, t)$  represents the wave speed (or convected sound speed). It equals  $u + c$  for positive waves or so-called right-running characteristics and  $u - c$  for negative wave or so-called left-running characteristics.<sup>2</sup> Then  $d\mathcal{J}^\pm/dl = \partial\mathcal{J}^\pm/\partial t + (u \pm c) \partial\mathcal{J}^\pm/\partial x \stackrel{\text{Eqns. (2.5)}}{=} 0$ , implying that  $\mathcal{J}^\pm$  are invariant along their respective characteristic curves, taking the aforementioned assumptions into consideration. In general, each characteristic curve  $i$  has a different  $\mathcal{J}_i^\pm$  which remains constant along the curve. The method just described, if applied to Eqns. (2.5), allows for the determination of weak solutions – these are solutions that may have a discontinuity, may not be differentiable everywhere and that may be less smooth – like for example shock waves.

<sup>2</sup>This definition of positive and negative waves is based on the standard that in one dimension, rightward pointing vectors are positive and leftward pointing vectors are negative.

To illustrate the coalescence of an initially continuous wave into a shock wave, consider a weak triangular pressure disturbance shown in Fig. 2.1 propagating into the positive  $x$ -direction (so towards to right). Such a wave can be created by moving a piston forward and backward. In this context “weak” implies that  $P_{\max}/P_0$ , with  $P_0$  the pressure at the undisturbed state, is of the order unity such that irreversible effects can be neglected. Using the results of the previous paragraph for simple waves, it is found that (see also Ref. [197])

$$d\sigma^+ = d(u + c) = \frac{\Gamma}{\rho c} dP, \tag{2.7}$$

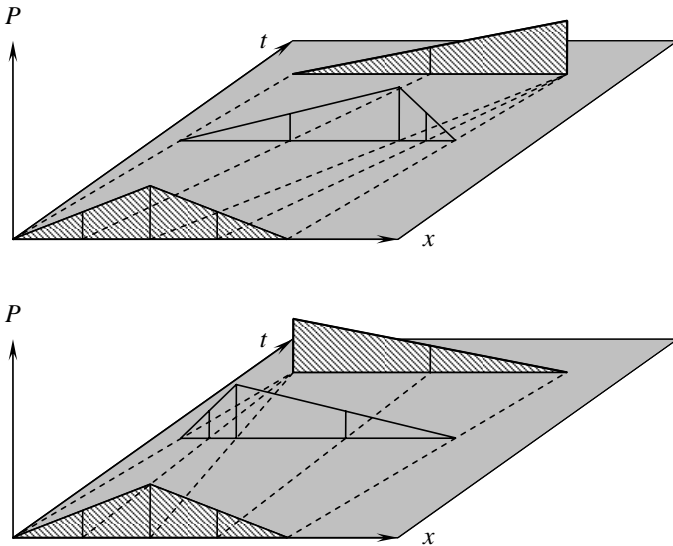


Figure 2.1: Above: the  $\sigma_i^+$ -convected-sound-waves (dashed lines) converge for the compressive part of the pressure disturbance to form a compression shock wave. The (shock) wave classifies as simple and moves into a region of uniform flow. The wave distortion is the result of an increase of the wave-speed  $u + c$  at higher pressure with respect to  $P_0$ , because  $\Gamma > 0$  and does not change sign across the wave. The  $\sigma_i^-$ -convected-sound-waves are not shown. Below: the  $\sigma_i^+$ -convected-sound-waves (dashed lines) converge for the expansive part of the pressure disturbance to form an expansion shock wave. The (shock) wave classifies as simple and moves into a region of uniform flow. The wave distortion is the result of a decrease of the wave-speed at higher pressure with respect to  $P_0$ , since  $\Gamma < 0$  and does not change sign across the wave. The  $\sigma_i^-$ -convected-sound-waves are not shown.

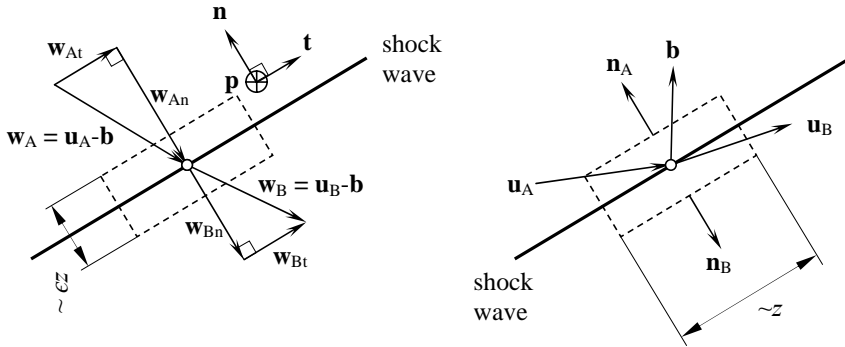


Figure 2.2: *The shock front locally enclosed by an arbitrarily thin control volume. Left: velocities according to an observer moving with the shock wave. Right: velocities according to a laboratory frame of reference. The indices A and B refer to the pre- and post-shock state respectively, and  $\mathbf{u}$  = absolute velocity ( $u = \|\mathbf{u}\|$ ),  $\mathbf{w}$  = relative velocity ( $w = \|\mathbf{w}\|$ ),  $\mathbf{b}$  = shock speed ( $b = \|\mathbf{b}\|$ ), and  $\mathbf{n}$  = unit vector locally normal to the surface parallel to the shock wave (by definition positive if outward-pointing). The unit vectors  $(\mathbf{n}, \mathbf{t}, \mathbf{p})$  form an orthogonal set (basis). Furthermore,  $z$  denotes a representative length and  $\epsilon$  is an arbitrarily small number, such that if  $z \rightarrow 0$ , volume integrals in the conservation equations can be neglected.*

meaning that if  $\Gamma > 0$  it is implied that the wave speed increases with an increase in pressure and therefore an initially continuous compressive wave eventually coalesces into a compression shock wave, i.e., a shock wave whereby the pressure increases in the direction of the flow as seen by an observer moving with the discontinuity. On the other hand, if  $\Gamma < 0$  it is implied that the wave speed decreases with an increase in pressure and therefore an initially continuous expansive wave eventually coalesces into an expansion shock wave, i.e., a shock wave whereby the pressure decreases in the direction of the flow as perceived by an observer moving with the discontinuity.

Note that the analytical treatment of Riemann on shock-wave formation as just described, is only valid for weak shock waves and it is based on the implicit assumption that the shock wave is without structure. Furthermore, the Riemann description of shock-wave formation fails as soon as characteristics intersect, since this implies multivaluedness of properties. There exists no general solution at present that describes all successive stages during the formation of strong shock waves, whereby, for example, it may be necessary to account for relaxation effects in polyatomic vapors preceding the appearance of the geometric surface of discontinuity.

From the instant of shock-wave formation and onwards, the flow is no longer homentropic and further description of the flow field, if one is not interested in the structure of the shock wave, requires the use of the Hugoniot-Rankine jump conditions. The development of these relations between pre- and post-shock states A and B respectively, is based on the laws of conservation of mass, momentum and energy applied to a control volume which locally encloses the shock front and which moves with the shock velocity  $\mathbf{b}$ , see Fig. 2.2. The pre-shock state is indicated by A and the post-shock state by B. Under the supposition that the shock wave represents a discontinuity separating two regions of thermodynamic-equilibrium states, the control volume can be made arbitrarily thin. Furthermore, the area of the edges of the control volume which are perpendicular to the shock front, are negligible with respect to the surface-area parallel to the shock front. Applying the laws of conservation of mass, momentum and energy to the control volume, as seen by an observer moving with the shock wave, yields per unit area of shock-front-surface

$$-\rho_A w_{A\mathbf{n}} + \rho_B w_{B\mathbf{n}} = 0 \quad (2.8)$$

$$-\rho_A \mathbf{u}_A w_{A\mathbf{n}} + \rho_B \mathbf{u}_B w_{B\mathbf{n}} = -P_B \mathbf{n}_B - P_A \mathbf{n}_A \quad (2.9)$$

$$-\rho_A \left( e_A + \frac{u_A^2}{2} \right) w_{A\mathbf{n}} + \rho_B \left( e_B + \frac{u_B^2}{2} \right) w_{B\mathbf{n}} = -P_B \mathbf{n}_B \cdot \mathbf{u}_B - P_A \mathbf{n}_A \cdot \mathbf{u}_A, \quad (2.10)$$

where  $w_{A\mathbf{n}} \equiv -(\mathbf{u}_A - \mathbf{b}) \cdot \mathbf{n}_A$  and  $w_{B\mathbf{n}} \equiv (\mathbf{u}_B - \mathbf{b}) \cdot \mathbf{n}_B$  are the magnitudes of the relative velocities of the fluid normal to the shock-front surface in the pre- and post-shock states respectively,  $(P_A, \rho_A)$  and  $(P_B, \rho_B)$  are the pressure and density of the pre- and post shock states respectively, and  $e_{A,B}$  denotes the specific internal energy of the substance in the pre-, respectively post-shock state.

Following Thompson [198], the momentum and energy conservation equations can be simplified. With  $\mathbf{n}_A = -\mathbf{n}_B$  and by adding to the momentum equation, which is a vector equation,  $\mathbf{b}(\rho_A w_{A\mathbf{n}} - \rho_B w_{B\mathbf{n}}) = 0$ , Eq. (2.9) reduces to

$$-\rho_A (\mathbf{u}_A - \mathbf{b}) w_{A\mathbf{n}} + \rho_B (\mathbf{u}_B - \mathbf{b}) w_{B\mathbf{n}} = \mathbf{n}_A (P_B - P_A). \quad (2.11)$$

Taking the dot product of the momentum equation and the orthogonal set of unit vectors  $(\mathbf{n}, \mathbf{t}, \mathbf{p})$ , see Fig. 2.2, yields respectively

$$P_A + \rho_A w_{A\mathbf{n}}^2 = P_B + \rho_B w_{B\mathbf{n}}^2 \quad (2.12a)$$

$$w_{A\mathbf{t}} = w_{B\mathbf{t}} \quad (2.12b)$$

$$w_{B\mathbf{p}} = 0. \quad (2.12c)$$

Equation (2.12c) implies that the flow velocity in the post-shock state is in the plane of vectors  $\mathbf{n}$  and  $\mathbf{t}$  and Eq. (2.12b) states that locally, the component of the relative velocity which is parallel to the shock front is invariant. Combining Eq. (2.12a) with the continuity equation and multiplying both the left- and right-hand-side of the relation by  $\rho_A \rho_B$  gives

$$J^2 \equiv (\rho_A w_{A\mathbf{n}})^2 = (\rho_B w_{B\mathbf{n}})^2 = -\frac{P_B - P_A}{v_B - v_A}, \quad (2.13)$$

with  $J$  the mass flux. This equation represents a straight line in the  $P$ - $v$ -plane connecting the pre- and post-shock states with a slope of  $-J^2$  and it is referred to as the Rayleigh line.

The energy conservation equation can be simplified by addition of the term  $(P_B w_{B\mathbf{n}} - P_A w_{A\mathbf{n}})$  to both the left- and right-hand-side of Eq. (2.10) and by employing the continuity and momentum equations and the definition equation for enthalpy  $h \equiv e + P/\rho$ , yielding

$$h_B + \frac{u_B^2}{2} - \left( h_A + \frac{u_A^2}{2} \right) = \mathbf{b} \cdot (\mathbf{u}_A - \mathbf{u}_B). \quad (2.14)$$

Since  $\|\mathbf{u} - \mathbf{b}\|^2 = w_{\mathbf{n}}^2 + w_{\mathbf{t}}^2$  and according to Eq. (2.12b)  $w_{\mathbf{t}}$  is invariant across the shock front, the energy balance equation simplifies to

$$h_A + \frac{w_{A\mathbf{n}}^2}{2} = h_B + \frac{w_{B\mathbf{n}}^2}{2}. \quad (2.15)$$

Further symbolic manipulation finally results in

$$h_B - h_A = \frac{1}{2} (P_B - P_A) (v_B + v_A). \quad (2.16)$$

This equation, obtained independently by Rankine [167] and Hugoniot [97], is rather convenient since it contains only thermodynamic properties and it is independent of the reference frame. This so-called Hugoniot-Rankine (HR) shock adiabat applies to general shock discontinuities, and, for a given pre-shock state, say A, a locus of possible post-shock thermodynamic states can be drawn, say for example in a  $P$ - $v$ -diagram.

As a consequence of the abrupt changes of properties across the shock wave which bring about large temperature and velocity gradients, the transformation from state A to state B across the shock wave occurs irreversibly. The gradient in temperature for example results in irreversible heat flow and the gradient in velocity enhances viscous dissipation in the shock wave.<sup>3</sup> Additionally, relaxation of the vibrational degrees of freedom can become important, especially for polyatomic fluids, either immediately upstream or downstream of the

<sup>3</sup>Note that Riemann incorrectly assumed the flow to be isentropic even after shock wave formation.

shock wave. Ergo, apart from the principal shock conditions which stem from the conservation laws, the entropy must increase across a shock wave. Moreover, according to Lax [124] and Oleinik [158] a fifth condition (referred to as the (mechanical) stability criterium or speed-ordering condition) is required for admissible shock waves, namely that the pre-shock Mach number – defined as  $\text{Ma}_{\text{An}} \equiv w_{\text{An}}/c_{\text{A}}$  – must be greater than or at least equal to unity and that the post-shock Mach number, i.e.,  $\text{Ma}_{\text{Bn}} \equiv w_{\text{Bn}}/c_{\text{B}}$ , must be less than or at least equal to unity.<sup>4</sup> In summary, admissible shock waves must satisfy all of the following shock conditions:

$$[\rho w_{\text{n}}] = 0 \quad (2.17\text{a})$$

$$[P + J^2 v] = 0 \quad (2.17\text{b})$$

$$\left[ h - \frac{(v_{\text{A}} + v_{\text{B}})P}{2} \right] = 0 \quad (2.17\text{c})$$

$$[s] \geq 0 \quad (2.17\text{d})$$

$$\text{Ma}_{\text{An}} \geq 1 \geq \text{Ma}_{\text{Bn}}, \quad (2.17\text{e})$$

whereby the square brackets represent the jump of a quantity across the shock wave, e.g.,  $[\Upsilon] = \Upsilon_{\text{B}} - \Upsilon_{\text{A}}$ .

As was already mentioned, both the entropy condition and the stability criterium, unlike the conservation laws, impose a direction on the transformation that can occur in shock waves. By means of the purely mathematical treatment of Riemann, it was demonstrated that compression shock waves form if  $\Gamma > 0$  and that expansion shock waves form if  $\Gamma < 0$ . Moreover, the treatment of Riemann starts with an initially continuous disturbance which evolves in time into a discontinuity. Alternatively, it is also possible to distinguish admissible solutions from inadmissible solutions by performing a Taylor-series expansion of the HR shock adiabat with  $h(s, P)$ , which represents a fundamental EoS (see Duhem [57], Becker [12], and Bethe [14], and Courant and Friedrichs [39]). For weak shock waves the result is

$$\begin{aligned} \Delta s &= \overbrace{\left( \frac{\partial s}{\partial P} \right)_{\text{HR}_{\text{A},\text{A}}}}^{=0} \times (P - P_{\text{A}}) + \frac{1}{2!} \overbrace{\left( \frac{\partial^2 s}{\partial P^2} \right)_{\text{HR}_{\text{A},\text{A}}}}^{=0} \times (P - P_{\text{A}})^2 \\ &+ \frac{1}{3!} \left( \frac{\partial^3 s}{\partial P^3} \right)_{\text{HR}_{\text{A},\text{A}}} \times (P - P_{\text{A}})^3 + \mathcal{O} \left[ (P - P_{\text{A}})^4 \right] \Rightarrow \\ [s] &= (s_{\text{B}} - s_{\text{A}}) \approx \frac{\Gamma_{\text{A}} P_{\text{A}}^3}{6 T_{\text{A}} \rho_{\text{A}}^3 c_{\text{A}}^4} [P_{\text{B}}/P_{\text{A}} - 1]^3 \geq 0. \end{aligned} \quad (2.18)$$

Here, it has implicitly been assumed that  $\Gamma$ , defined in Eq. (1.1), does not change its sign as a result of the pressure disturbance due to the wave and that it is

<sup>4</sup>For strictly convex or hypothetically strictly concave isentropes, the entropy condition and the stability criterium are equivalent [114].

not equal to zero, and that there is thermodynamic equilibrium. In Eq. (2.18),  $(\partial^j s / \partial P^j)_{HR_{A,A}}$  is the short notation for the  $j$ -th order derivative ( $j = 1 \dots 3$ ) of entropy with respect to pressure along the HR shock adiabat of pre-shock state A, evaluated at state A. It is readily demonstrated that weak compression shock waves, these are shock waves with  $P_B/P_A \gtrsim 1$ , are admissible if  $\Gamma > 0$  and that weak expansion shock waves, namely shock waves with  $P_B/P_A \lesssim 1$ , are admissible if  $\Gamma < 0$ .<sup>5</sup> An in-depth analysis about the entropy jump across a shock wave featuring a change of sign of  $\Gamma$  as a result of the pressure wave is conducted by Cramer and Kluwick [48]. Additional results from the Taylor-series expansion are that at a pre-shock state A, the HR shock adiabat of state A and the isentrope through point A have the same slope and curvature in the  $P$ - $v$ -plane; formally,

$$\begin{cases} \left( \frac{\partial P}{\partial v} \right)_{HR_{A,A}} = \left( \frac{\partial P}{\partial v} \right)_{s,A} \\ \left( \frac{\partial^2 P}{\partial v^2} \right)_{HR_{A,A}} = \left( \frac{\partial^2 P}{\partial v^2} \right)_{s,A} \end{cases} \quad (2.19)$$

Hitherto, the structure of the shock waves has not been considered. This is not surprising since negligence of thermoviscous effects in the governing equations only allows for the admissibility of discontinuous solutions from a mathematical point of view. Consequently, dissipative effects are assumed to occur only in the discontinuity. The processes of dissipation represent a complex sequence of non-equilibrium transition from one thermodynamic equilibrium state to another thermodynamic equilibrium state, whereby the time which is required for completing the transition, determines the thickness of the shock wave [193]. Thermodynamic equilibrium implies the equilibrium distribution of energy over all molecular, atomic and electronic degrees of freedom. The structure of the shock wave is governed by the rate and type of relaxation process that occurs in it. The relaxation process is defined as that of establishing thermodynamic equilibrium and it is, for example, a result of a delay in energy transfer between various internal degrees of freedom. In the case of weak shock waves where the gradients of flow variables are sufficiently small, the structure of the wave can completely be described by the Navier-Stokes equations for a viscous and conducting fluid. In the case of strong shock waves the situation is very different. Strong shock waves contain a thin leading layer through which flow variables change quite abruptly. The thickness of this so-called shock front is of the order of the mean-free-path for translational relaxation, consequently, from a macroscopic viewpoint, this leading transitional layer is a gas-dynamic

<sup>5</sup>This procedure does not treat weak pressure disturbances that traverse the negative nonlinearity region, see Fig. 1.1; it is only intended as a demonstration that expansion shock waves are theoretically possible without violation of the second law of thermodynamics. Locally, the stability criterium is also satisfied because of local convexity or concavity of the strictly monotonous isentropes, depending on the sign of  $\Gamma_A$ .

discontinuity and at the discontinuity, the fluid is not a continuum. This results in a significant departure of thermodynamic equilibrium of the vapor immediately behind the shock front. A qualitative illustration of the relaxation zone behind a shock front is presented in Fig. 2.3. Thermodynamic equilibrium is attained through, as was previously mentioned, a succession of complex relaxation processes via excitation of rotational, vibrational and electronic degrees of freedom, each of which can be characterized by a relaxation time  $\tau$ . Generally,  $\tau_{\text{trans}} < \tau_{\text{rot}} \ll \tau_{\text{vib}}$ , i.e., the vibrational relaxation is much slower with respect to rotational relaxation and translational relaxation, or alternatively, the mean-free-path for vibrational relaxation is significantly greater than that for rotational relaxation and translational relaxation, respectively. This is the result of the low efficiency of energy transfer between vibrational and translational degrees of freedom on molecular collisions. Moreover, the majority of polyatomic molecules display a single relaxation process whereby the whole of the vibrational energy relaxes via the lowest mode, see Ref. [120] and Chap. 3, pg 64 of Ref. [121]. In this situation, the vibrational relaxation time is estimated from the Lambert-Salter plot [121] and the shock wave thickness can be estimated. Yet, exceptions have been found where nonlinear (vibrational) relaxation occurs, see for example Kiefer et. al. [108]. Under these circumstances it is then difficult or even impossible to estimate the shock wave thickness or to assess whether the hypothesis of thermodynamic equilibrium is valid.

Since the shock waves that are of interest herein are weak, the thickness can be determined by taking into account the dissipative processes under the provision that the continuum hypothesis is still valid. For this purpose, the second law of thermodynamics is employed. As derived by Thompson [198] (see also Borisov [17]), the entropy balance statement equals

$$\rho \frac{Ds}{Dt} = \frac{\Phi}{T} + \frac{1}{T} \nabla \cdot (\kappa \nabla T), \quad (2.20)$$

where  $\kappa$  is the thermal conductivity and the scalar  $\Phi$  is the dissipation function defined as

$$\begin{aligned} \Phi &= \frac{2}{3} \eta \left[ (D_{11} - D_{22})^2 + (D_{22} - D_{33})^2 + (D_{33} - D_{11})^2 \right] \\ &+ 4\eta (D_{12}^2 + D_{13}^2 + D_{23}^2) + \zeta (D_{11} + D_{22} + D_{33})^2. \end{aligned} \quad (2.21)$$

In Eq. (2.21),  $\eta$  is the dynamic viscosity,  $\zeta$  is the bulk (volume) viscosity,<sup>6</sup> and  $D_{ik} = D_{ki}$  is the so-called rate-of-deformation tensor defined as

$$D_{ik} \equiv \frac{1}{2} \left( \frac{\partial w_i}{\partial x_k} + \frac{\partial w_k}{\partial x_i} \right). \quad (2.22)$$

---

<sup>6</sup> $\zeta = \lambda + \frac{2}{3}\eta$ , where  $\lambda$  is the second viscosity coefficient.

States A and B are related via the HR-shock relations whereby it is assumed that the thermodynamic variables are equal to their values in the state of complete thermodynamic equilibrium.

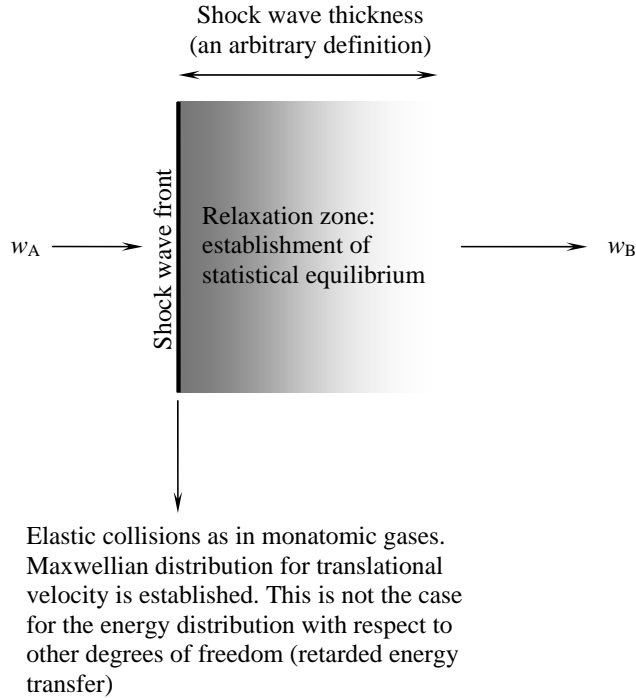


Figure 2.3: *Illustration of the relaxation zone behind a shock wave in a polyatomic gas. In the shock wave front equilibrium between the translational and rotational degrees of freedom is established (assuming that the time required for translational and rotational relaxation are of the same order of magnitude, the latter being greater), whereas the establishment of equilibrium over the vibrational degrees of freedom occurs behind the front.*

Noting that

$$\frac{1}{T} \nabla \cdot (\kappa \nabla T) = \nabla \cdot \underbrace{\frac{\kappa \nabla T}{T}}_{\ell} + \frac{\kappa}{T^2} (\nabla T)^2 \quad (2.23)$$

and assuming i) one-dimensional flow (or nearly so), ii) stationary conditions,

iii) fixed-valued transport properties, and accounting for the kinetic energy term, gives for Eq. (2.20),

$$T\rho w \left( \frac{ds}{dx} \right) = \left( \frac{4}{3}\eta + \zeta \right) \left( \frac{dw}{dx} \right)^2 + \frac{d}{dx} \left( \kappa \frac{dT}{dx} \right). \quad (2.24)$$

If  $dT/dx \approx [T]/\varepsilon$ ,  $ds/dx \approx [s]/\varepsilon$ , and  $dw/dx \approx [w]/\varepsilon$ , where  $\varepsilon$  is the shock thickness, and considering that (refer to Eq. (2.18))

$$[s] = \Gamma_A [P]^3 / (6T_A \rho_A^3 c_A^4), \quad (2.25)$$

and that vector  $\ell$  in Eq. (2.23) vanishes at the boundaries, then the shock wave thickness can be approximated by

$$\varepsilon = \left[ \left( \frac{4}{3}\eta + \zeta \right) [w]^2 + \frac{\kappa [T]^2}{T_A} \right] \frac{6\rho_A^2 c_A^3}{\text{Ma}_A \Gamma_A [P]^3}. \quad (2.26)$$

States A and B are chosen sufficiently far from the shock wave. It is seen that for a nonconducting, inviscid fluid, the shock wave thickness is equal to zero, as is to be expected. Also, if the shock wave is very weak such that  $P_B$  is less than but approximately equal to  $P_A$ , i.e., a rarefaction shock wave, or if  $\Gamma_A$  is very close to zero (and negative),  $\varepsilon$  becomes very large. The last example indicates the arbitrariness of this “definition” of shock wave thickness. Thompson and Lambrakis [201] for example use the criterium of 98.7 % of the overall speed change across the shock wave to determine its thickness. From this criterium and assuming that the bulk viscosity is of the same order of magnitude as the dynamic viscosity, Thompson and Lambrakis estimate the thickness of expansion shock waves to be of the order of 1  $\mu\text{m}$ . This approximate value for the shock wave thickness is sufficiently large and thus the continuum hypothesis is indeed valid.

## 2.2 Compression waves through the BZT-region

The determination of admissible solutions of the governing equations for shock waves, see Eqns. (2.17), is usually conducted graphically. As was demonstrated in Sec. 2.1, Eq. (2.13) for example represents a straight line in a  $P$ - $v$ -diagram connecting the pre-shock state with possible post-shock solutions. Similarly, the HR shock adiabat represented by Eq. (2.16) is invariant of the frame of reference and by approximation, it represents mathematical solutions of the energy conservation equation across a shock wave. Since the intersection of the HR shock adiabat and the Rayleigh line implies that there is conservation of mass, momentum and energy, the second law of thermodynamics and the stability criterium are used to distinguish between admissible solutions and mathematical solutions that are physically not allowed (inadmissible). Anticipating

the results outlined in detail by Kluwick [114] and summarized in the paragraphs hereinafter, an in-depth analysis of the relations developed in Sec. 2.1 has revealed that admissible solutions of the governing equations can be distinguished from inadmissible ones by employing geometrical arguments and by using visual information in a  $P$ - $v$ -diagram.

First, consider the HR shock adiabat of a pre-shock state denoted by A. Because of the fact that at the pre-shock state the HR shock adiabat of state A and the isentrope through point A have the same slope (and curvature), see Eq. (2.19),

$$\left(\frac{\partial P}{\partial v}\right)_{\text{HR}_{A,A}} = -\frac{c_A^2}{v_A^2}. \quad (2.27)$$

Here,  $(\partial P/\partial v)_{\text{HR}_{A,A}}$  is the short notation for the slope of the HR shock adiabat of state A, evaluated at state A. The equation for the Rayleigh line in combination with Eq. (2.27) gives for the pre-shock stability criterium  $\text{Ma}_A \geq 1$  that

$$\left(\frac{\partial P}{\partial v}\right)_{\text{HR}_{A,A}} \geq \frac{[P]}{[v]}. \quad (2.28)$$

*Thus, for admissible shock waves A–B, the absolute value of the slope of the HR shock adiabat of state A, evaluated at state A, is less than or at most equal to the absolute value of the slope of the Rayleigh line connecting states A and B.*

Next, the graphical interpretation of the  $\text{Ma}_B \leq 1$ -shock-admissibility criterium is illustrated. For this purpose consider the HR shock adiabat through pre-shock state A, and passing through a possible post-shock solution B. Application of the thermodynamic identity  $Tds = dh - vdP$  (Tds-equation) to post-shock state B gives

$$\begin{aligned} T_B ds_B &= dh_B - v_B dP_B \stackrel{\text{HR}_{A,B}}{=} \left( \frac{v_A + v_B}{2} dP_B + \frac{P_B - P_A}{2} dv_B \right) - v_B dP_B \\ &= -\frac{[v]}{2} dP_B + \frac{[P]}{2} dv_B, \end{aligned} \quad (2.29)$$

where  $\text{HR}_{A,B}$  is the short notation for the HR shock adiabat of state A, evaluated at state B. Furthermore, at state B, the variation of pressure can be expressed

according to

$$\begin{aligned}
 dP_B &= \left(\frac{\partial P}{\partial s}\right)_v(s_B, v_B) ds_B + \left(\frac{\partial P}{\partial v}\right)_s(s_B, v_B) dv_B \\
 &= T_B \left(\frac{\partial P}{\partial e}\right)_v(s_B, v_B) ds_B - \frac{c_B^2}{v_B^2} dv_B \Rightarrow \\
 T_B ds_B &= \frac{dP_B + \frac{c_B^2}{v_B^2} dv_B}{\left(\frac{\partial P}{\partial e}\right)_v(s_B, v_B)} \\
 &= \frac{dP_B + \frac{c_B^2}{v_B^2} dv_B}{G_B/v_B}, \tag{2.30}
 \end{aligned}$$

with  $G_B \equiv (\beta_P c^2 / \gamma C_v)_B$  and  $\beta_P \equiv (\partial \ln v / \partial T)_P > 0$  is the coefficient of volume expansion.<sup>7</sup> Equating the right-hand-sides of Eqns. (2.29) and (2.30) yields

$$\left(\frac{\partial P}{\partial v}\right)_{\text{HR}_{A,B}} - \frac{[P]}{[v]} = \frac{c_B^2}{v_B^2} \frac{(\text{Ma}_B^2 - 1)}{\left(1 + \frac{[v]}{2v_B} G_B\right)}. \tag{2.31}$$

The stability criterium applied to the post-shock state then gives

$$\left(\frac{\partial P}{\partial v}\right)_{\text{HR}_{A,B}} \leq \frac{[P]}{[v]}, \tag{2.32}$$

under the provision that: i)  $1 + [v] G_B / (2v_B) \neq 0$ , ii)  $\beta_P > 0$ , and iii) that the solution, viz. post-shock state B, in a  $P$ - $v$ -plane is located to the right of the singularity.

*Thus, for admissible shock waves A–B, it follows from condition (2.32) that the absolute value of the slope of the HR shock adiabat of state A, evaluated at state B, is greater than or at least equal to the absolute value of the slope of the Rayleigh line connecting states A and B.*

Because in the limit of down-stream sonic shock waves

$$\frac{[P]}{[v]} = \left(\frac{\partial P}{\partial v}\right)_{\text{HR}_{A,B}}, \tag{2.33}$$

---

<sup>7</sup>Cases where  $\beta_P \leq 0$  are excluded.

it can be inferred from Eq. (2.29) that at sonic point B on the shock adiabat of point A,

$$\left(\frac{\partial s}{\partial v}\right)_{\text{HR}_{A,B}} = 0. \quad (2.34)$$

If the Tds-equation is applied across the shock wave

$$\begin{aligned} \int_{\text{stateA}}^{\text{stateB}} T ds &= \int_{\text{stateA}}^{\text{stateB}} de + \int_{\text{stateA}}^{\text{stateB}} P dv = \Delta e + \int_{\text{stateA}}^{\text{stateB}} P dv \\ &= -\frac{P_A + P_B}{2} [v] + \int_{\text{stateA}}^{\text{stateB}} P dv = A_{\text{HR}_A} - A_{\text{R}_{A-B}} \geq 0, \end{aligned} \quad (2.35)$$

with  $A$  representing the area between  $v_A$  and  $v_B$  under either the HR shock adiabat or the Rayleigh line, depending on de subscript.

*This result together with Eq. (2.34) indicate that for admissible downstream sonic shock waves, the sonic point has a local extremum in entropy.*

In summary:

- According to the stability criterium, all admissible shock waves satisfy

$$\left(\frac{\partial P}{\partial v}\right)_{\text{HR}_{A,B}} \leq \frac{[P]}{[v]} \leq \left(\frac{\partial P}{\partial v}\right)_{\text{HR}_{A,A}}; \quad (2.36)$$

- An admissible downstream sonic post-shock state is a local maximum [114] in entropy;
- From Eqns. (2.17d), (2.35) and (2.36) it follows that the Rayleigh line must not intersect the HR shock adiabat at an interior point and therefore, the Rayleigh line connecting the pre- and post shock states must be located either completely above the HR shock adiabat (this means that compression shock waves are admissible) or completely below the HR shock adiabat (this means that expansion shock waves are admissible) [114, 124, 41].

To elucidate the use of the geometrical arguments, consider compressive waves originating from an upstream thermodynamic state 1 located in the dense-gas thermodynamic regime to the right of the region of negative nonlinearity, see Fig. 2.4, such that the isentrope through 1 exhibits a change of its curvature. As an example, consider a discontinuity leading from 1 to post-shock state 2. Discontinuity  $1 \rightarrow 2$  represents a classical admissible compression shock wave because the conservation equations and the stability criterium,  $(\partial P/\partial v)_{\text{HR}_{1,2}} <$

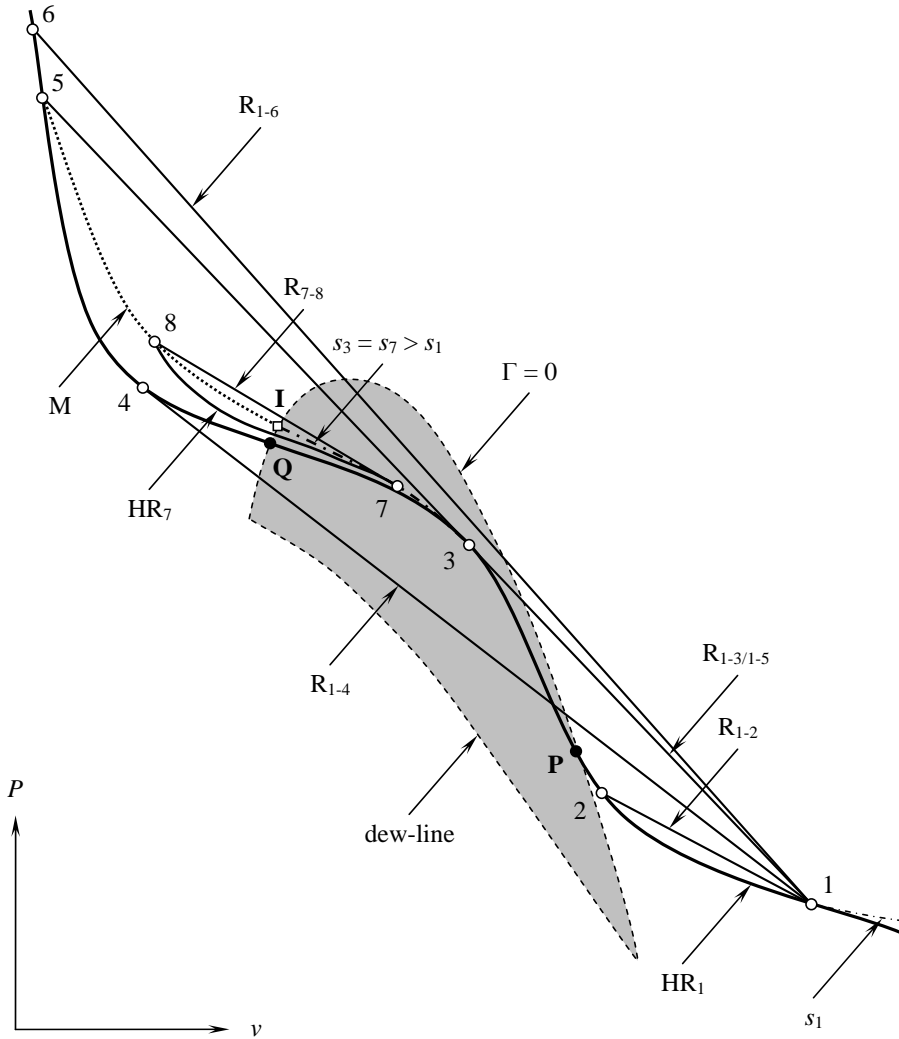


Figure 2.4: Qualitative chart illustrating thermodynamic states that are associated with compression waves that cross the region of negative nonlinearity, i.e., the region enclosed by the  $\Gamma = 0$ -line and the dew-line, in the  $P$ - $v$ -plane.  $R$ : Rayleigh line,  $HR$ : Hugoniot-Rankine shock adiabat, and  $s$ : isentrope. Points  $P$  and  $Q$  represent the inflection points of the Hugoniot-Rankine shock adiabat of state 1 and point  $I$  indicates the inflection point of the isentrope through point 3 (or 7).

$[P]/[v] < (\partial P/\partial v)_{\text{HR}_{1,1}}$  (which is more stringent than the entropy condition if the sign of the curvature of isentropes changes [114]), are satisfied. This can be concluded based solely on the fact that the Rayleigh line connecting states 1 and 2 is located completely above the HR shock adiabat of state 1 between points 1 and 2. The same arguments also apply to discontinuity  $1 \rightarrow 3$  representing a somewhat stronger (because  $P_3 - P_1 > P_2 - P_1$ ) *nonclassical* compression shock wave, because in this specific situation, the Mach number at the post-shock state 3 is unity due to the tangency of Rayleigh line  $R_{1-3}$  and  $\text{HR}_{1,3}$ . Accordingly, at state 3, the entropy is a local maximum because  $(\partial^2 s/\partial v^2)_{\text{HR}_{1,3}} < 0$ . Next, consider a configuration represented by jump  $1 \rightarrow 4$ . Discontinuity  $1 \rightarrow 4$  however, represents an inadmissible shock wave because the stability criterium is violated even though the conservation equations are satisfied. Remark that if point 4 is located very close to point 3 whereby  $v_4 < v_3$ , it is possible that the entropy condition is met, namely  $s_4 > s_1$ , however the stability criterium is violated and the HR shock adiabat is intersected by the Rayleigh line in an internal point. For jumps whereby the downstream pressure of the wave has a value between  $P_3$  and  $P_4$ , two situations can arise. In the first situation, the wave disintegrates into a nonclassical compression shock immediately followed by a nonclassical isentropic compression fan. Here the shock wave is nonclassical because the post-shock Mach number  $\text{Ma}_3 = 1$ . This occurs because, as was already shown, the entropy at a post-shock sonic point is a local extremum. Moreover, from thermodynamics it follows that

$$\left(\frac{\partial s}{\partial P}\right)_v = \frac{\rho C_P c^2}{\beta_P T} > 0 \quad (2.37)$$

signifying that at point 3, the isentrope is located above  $\text{HR}_1$  and because

$$\left(\frac{\partial^2 s}{\partial v^2}\right)_{\text{HR}_{1,3}} = -\frac{2[v]c_3^2\Gamma_3}{T_3v_3^3}, \quad (2.38)$$

the local extremum in entropy corresponds to a local maximum in entropy. Jump  $1 \rightarrow 7$  (whereby the downstream pressure corresponds to  $P_7$ ) represents such a phenomenon of shock wave splitting; the composite wave consists of a downstream sonic compression shock wave  $1 \rightarrow 3$  and an isentropic compression fan  $3 \rightarrow 7$ . This type of phenomenon arises for downstream pressures between  $P_3$  and  $P_I$ , where point **I** is located on the isentrope through point 3 ( $s_3$ ) and the  $\Gamma = 0$ -line. The second situation occurs if the downstream pressure is somewhat greater than  $P_I$ . If for example the downstream pressure is  $P_8$ , a nonclassical compression shock wave representing jump  $1 \rightarrow 3$  is formed ( $\text{Ma}_3 = 1$ ), followed by an isentropic nonclassical compression fan, and because the convected sound speed decreases with a decrease in specific volume if  $v < v_I$ , the compression fan develops a region of multivaluedness, i.e., the high-pressure part of the wave overtakes the low-pressure part, resulting in the formation of

a second nonclassical compression shock (the second shock wave is also nonclassical because the pre-shock Mach number,  $Ma_7 = 1$ ). Jump  $1 \rightarrow 3 \rightarrow 7 \rightarrow 8$  represents such a shock-fan-shock composite wave. Note that HR shock adiabat of point 7 is located beneath the isentrope through point 7 (or alternatively point 3) and  $R_{7-8}$  is located completely above  $HR_7$ . For downstream pressures corresponding to values between  $P_1$  and  $P_5$ , composite compressive shock-fan-shock waves are admissible, whereby the pressure jump across the second compression shock wave increases as the downstream pressure is increased, while the pressure change across the nonclassical compression fan, sandwiched between the two nonclassical compression shock waves, decreases. Line M is the locus of possible post-shock states of composite waves for downstream pressures between  $P_1$  and  $P_5$ . Finally, if  $P = P_5$ , the fan disappears completely and jump  $1 \rightarrow 5$  represents a single compression shock wave or alternatively, jump  $1 \rightarrow 5$  can be interpreted as representing a composite wave composed of a compression shock wave ( $1 \rightarrow 3$ , with  $Ma_3 = 1$ ) immediately followed by a second compression shock wave ( $3 \rightarrow 5$ ). For higher downstream pressures, e.g.,  $P = P_6$  only pure classical compression shock waves are admissible.

The previous discussion allows for delimiting the region of pure nonclassical compression fans. Making use of the geometrical relations whereby compression shock waves are admissible if and only if the Rayleigh line is located completely above the HR shock adiabat, implies that pure compression fans can be generated if and only if both the upstream and downstream thermodynamic states are located within the region of  $\Gamma \leq 0$ , whereby the up- and downstream states are connected via isentropes.

### 2.3 Expansion waves through the BZT-region

In this section, the focus is on expansion waves that either originate in the region of negative nonlinearity or have an upstream state located on an isentrope (or HR shock adiabat) that crosses the region of negative nonlinearity. The treatment outlined here summarizes the in-depth analysis of nonclassical gas-dynamic discontinuities of Kluwick [114] and Zamfirescu et. al. [226]. With reference to Fig. 2.5, consider a pre-shock state 1 which is located inside the negative nonlinearity region. Jump  $1 \rightarrow 2$  represents an admissible pure nonclassical expansion shock wave which satisfies both the entropy inequality and the mechanical stability condition since the Rayleigh line connecting states 1 and 2 is located completely below the HR shock adiabat of state 1 [124]. Similarly, jump  $1 \rightarrow 3$  represents a possible solution, whereby in this specific situation, the post-shock state is at sonic conditions, i.e.,  $Ma_3 = 1$ , because  $R_{1-3}$  is tangent to  $HR_{1,3}$ . Moreover, at sonic point 3, the entropy corresponds to a local maximum. Discontinuity  $1 \rightarrow 4$  however, is an inadmissible expansion shock wave because  $HR_1$  is intersected by  $R_{1-4}$  approximately at the middle. Nevertheless, if the downstream pressure is less than the value corresponding to  $P_3$ ,

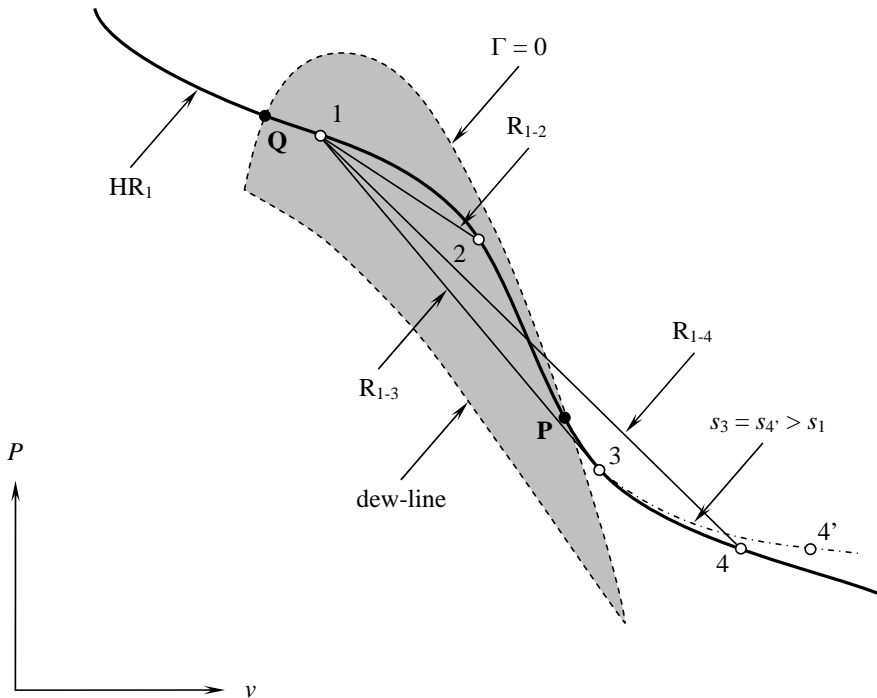


Figure 2.5: Qualitative chart illustrating thermodynamic states that are associated with expansion waves that originate in and possibly transverse the region of negative nonlinearity, i.e., the region enclosed by the  $\Gamma = 0$ -line and the dew-line, in the  $P$ - $v$ -plane.  $R$ : Rayleigh line,  $HR$ : Hugoniot-Rankine shock adiabat, and  $s$ : isentrope. Points  $P$  and  $Q$  represent the inflection points of the Hugoniot-Rankine shock adiabat of state 1; these are in close proximity to the  $\Gamma = 0$ -line.

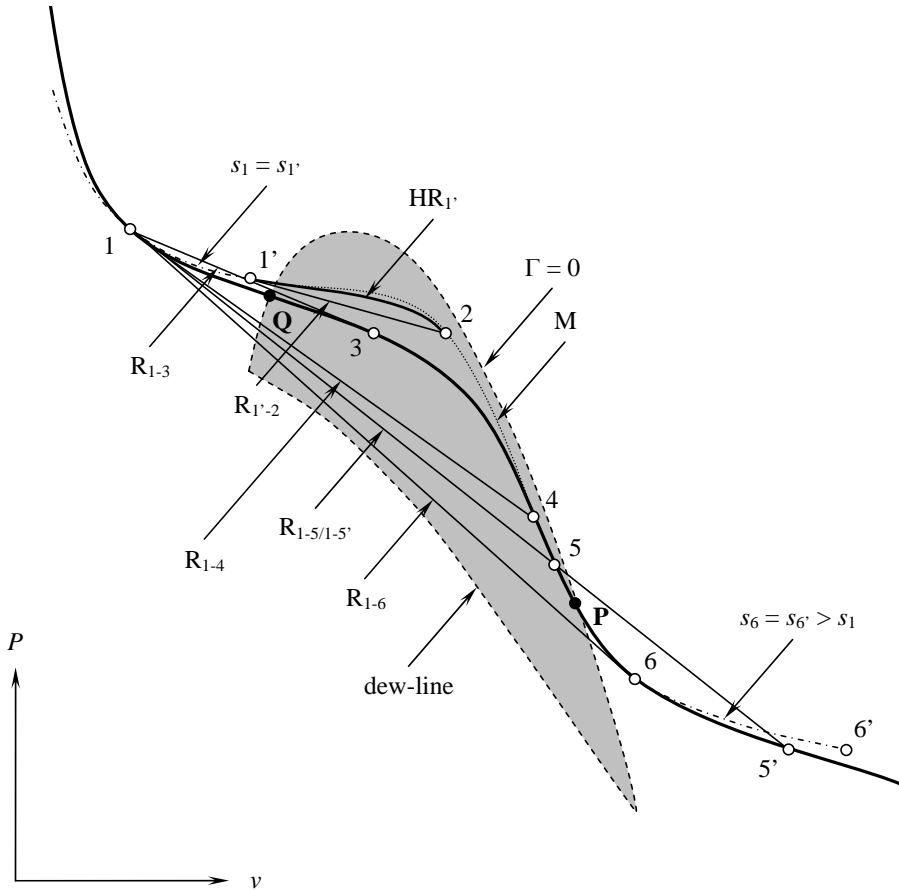


Figure 2.6: Qualitative chart illustrating thermodynamic states that are associated with expansion waves that cross the region of negative nonlinearity, i.e., the region enclosed by the  $\Gamma = 0$ -line and the dew-line, in the  $P$ - $v$ -plane. R: Rayleigh line, HR: Hugoniot-Rankine shock adiabat, and  $s$ : isentrope. Points **P** and **Q** represent the inflection points of the Hugoniot-Rankine shock adiabat of state 1.

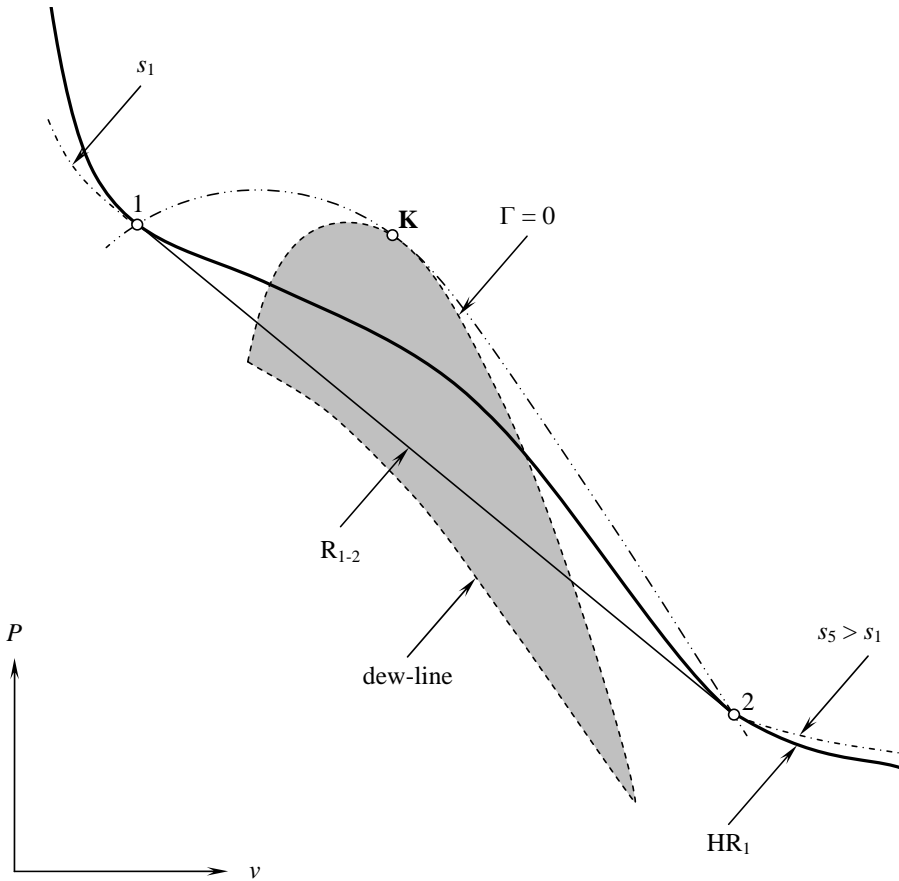


Figure 2.7: Qualitative chart illustrating thermodynamic states that are associated with double sonic shock waves. The dash-dot-dot line illustrates part of the double sonic locus.  $R$ : Rayleigh line,  $HR$ : Hugoniot-Rankine shock adiabat, and  $s$ : isentrope. Point  $K$  is the single inflection point of the isentrope through  $K$ .

shock splitting occurs, namely an expansion shock wave is formed connecting states  $1 \rightarrow 3$  with  $Ma_3 = 1$ ; the shock wave is immediately followed by an isentropic expansion fan which propagates with the convected sound speed. An example of shock splitting of the mentioned type, is indicated by  $1 \rightarrow 3 \rightarrow 4'$  in Fig. 2.5.

As a second case, consider an upstream state 1 which is located to the left of the region of negative nonlinearity on an isentrope that exhibits both convex and concave behavior, see Fig. 2.6. First consider the situation where the downstream pressure is slightly less than  $P_1$  and the specific volume at the downstream state is less than the value corresponding to the specific volume of the inflection point of the isentrope through point 1, i.e.,  $v_1 \leq v_I$  (point I is not shown). Because expansion shock waves are impossible due to violation of the second law of thermodynamics and the stability criterium, the wave necessarily evolves as an isentropic expansion fan. However, if  $v_1 > v_I$  and the downstream pressure has a value of say  $P_2$ , then, because of a sign-change of  $\Gamma$ , a composite wave is formed consisting of an isentropic expansion fan, in this example  $1 \rightarrow 1'$ , and an expansion shock wave  $1' \rightarrow 2$ , whereby  $Ma_{1'} = 1$ . This means that jump  $1 \rightarrow 3$  is inadmissible simply because the Rayleigh line connecting states 1 and 3 is located completely above the HR shock adiabat of state 1, therefore the stability criterium is violated, viz.  $Ma_1 < 1$ . Such a wave, namely one with a downstream pressure of  $P_3$ , would evolve as a fan-shock composite wave where the pre-shock Mach number equals unity. Line M in Fig. 2.6 is a locus of post-states of the expansion shock wave of the composite fan-shock-waves. If the downstream pressure is lower than that corresponding to  $P_3$ , pure expansion shock waves are still inadmissible because the HR shock adiabat of state 1 is intersected in an interior point by the Rayleigh line; instead, the mentioned composite waves are admitted. However, if the downstream pressure corresponds to  $P_4$ , the Rayleigh line connecting states 1 and 4 is located completely below  $HR_1$  and the stability and entropy criteria are not violated. Jump  $1 \rightarrow 4$  is the first pure nonclassical expansion shock wave that is admissible from pre-shock state 1; moreover,  $Ma_1 = 1$  because  $R_{1-4}$  is tangent to  $HR_{1,1}$ . Also jump  $1 \rightarrow 6$  represents an admissible expansion shock wave whereby here,  $Ma_1 > 1$  and  $Ma_6 = 1$  since at state 6,  $R_{1-6}$  is tangent to  $HR_{1,6}$ . For downstream pressures lower than  $P_6$ , shock splitting occurs because  $R_{1-6}$  intersects  $HR_1$  in an internal point. An example of shock splitting is represented by  $1 \rightarrow 6 \rightarrow 6'$  whereby the transformation from state 6 to state  $6'$  occurs isentropically along a fan propagating with the convected sound speed.

Apart from shock waves that feature a pre- or post-shock Mach number of unity, it is also possible to identify states  $(P_A, v_A; P_B, v_B)$  that display  $Ma_A = Ma_B = 1$ . These so-called double-sonic shock waves are expansion shock waves that feature the greatest jump in pressure for a given pre-shock state. Moreover, the pre-shock state must be located on an isentrope which displays both convex and concave behavior [43, 226]. Figure 2.7 gives a graphical description of such an admissible discontinuity in the  $P$ - $v$ -plane. Note that the Rayleigh line con-

necting states 1 and 2 is located completely below the HR shock adiabat of state 1 and that  $R_{1-2}$  is tangent at both state 1 and 2 of the HR shock adiabat. What is even more remarkable is that the pre- and post-shock states are both located outside the  $\Gamma < 0$ -region.

In summary, the following can be stated:

1. The uniqueness of both the pre- and post shock sonic points implies that there exists a geometrical locus, the so-called double-sonic locus, in the  $P$ - $v$  plane connecting these states (see Cramer [43] and Zamfirescu et. al. [226]).
2. All other expansion shock waves that can be admitted along a given isentrope, have a lower strength (in terms of pressure jump across the shock wave) than the double sonic shock. These single-phase pre-shock states are located between the double-sonic locus, specifically the dash-dotted line to the left of point **K** in Fig. 2.7, and the  $\Gamma = 0$ -line, viz. the dashed line to the right of point **K** in Fig. 2.7.
3. Expansion shock waves with a pre-shock state located between the double-sonic locus and the  $\Gamma = 0$ -line, as indicated in the previous item, have both upper and lower limits for their associated post-shock state. The upper limit corresponds to the expansion shock wave with sonic pre-shock conditions, e.g., jump  $1 \rightarrow 4$  in Fig. 2.6, and the lower bound corresponds to the expansion shock wave with sonic post-shock conditions, like jump  $1 \rightarrow 6$  in Fig. 2.6. However, expansion shock waves having a pre-shock state located inside the negative nonlinearity region only have a lower bound corresponding to shock waves whereby the post-shock conditions are sonic.
4. The domain delimiting the region of pre-shock states that allow for the admissibility of nonclassical gas-dynamic phenomena, is bounded by the left branch of the double sonic locus and the right branch of the  $\Gamma = 0$ -line.<sup>8</sup>
5. The maximum strength in terms of pressure jump for states inside the afore mentioned domain corresponds to the strength of downstream sonic shock waves.
6. For pre-shock states on the right branch of the  $\Gamma = 0$ -line in the  $P$ - $v$  plane, no expansion shock waves are admissible.

Apart from the intensity in terms of the pressure jump across expansion shock waves, it is also possible to identify pre-shock states along selected isentropes which display the highest pre-shock Mach number. More specifically,

<sup>8</sup>According to Fig. 2.7, left and right are considered with respect to point **K**, which corresponds to the single inflection point of the isentrope through **K**.

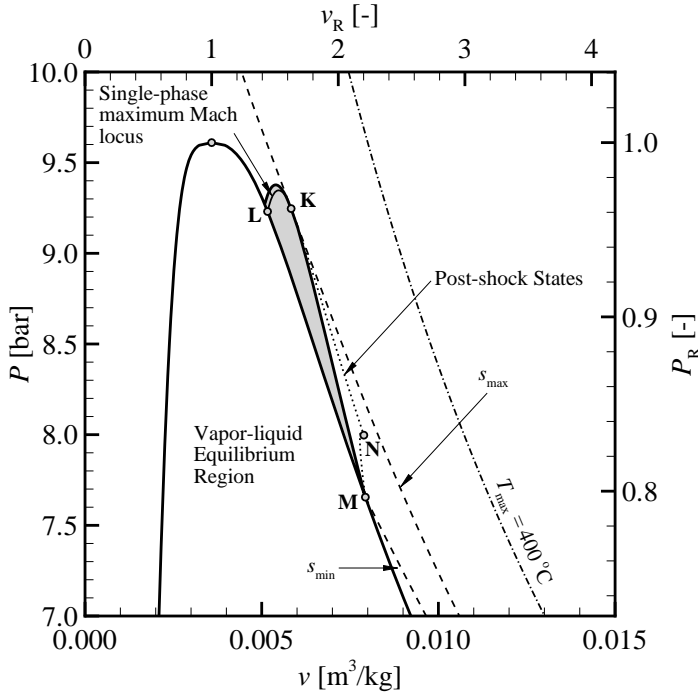


Figure 2.8: The  $P$ - $v$ -thermodynamic plane of  $D_6$  (the reduced pressure and specific volume, respectively  $P_R$  and  $v_R$ , are determined with respect to their critical point value). Shown are the vapor-liquid-equilibrium (VLE) region, the region of negative nonlinearity (highlighted), the maximum isotherm related to the thermochemical stability of  $D_6$  with respect to stainless steel as the containing material (dash-dotted line), the isentropes  $s_{\min}$  and  $s_{\max}$  (dashed lines), the locus of superheated-vapor thermodynamic states  $L$ - $K$  that allow for the highest pre-shock Mach number whereby the post-shock Mach number is unity (these associated post-shock states are located on the dotted-line  $N$ - $K$ ). Point  $O$  according to Fig. 2.9 is located on the dew-line somewhat to the right of point  $L$ .

the results presented hereinafter establish the existence of a locus of pre-shock states with the greatest supersonic-to-sonic transition across the shock wave. These results are useful in situations that give rise to unsteady expansion shock waves, as treated in Chap. 5. In this context, the maximum-Mach-locus is determined for dodecamethylcyclohexasiloxane ( $D_6$ ,  $[(CH_3)_2-Si-O]_6$ ), which is identified as a BZT fluid in Ref. [30]. Thermodynamic properties of this fluid are calculated with the EoS documented in Ref. [33] (see also Chap. 3 for details). The procedure is as follows:

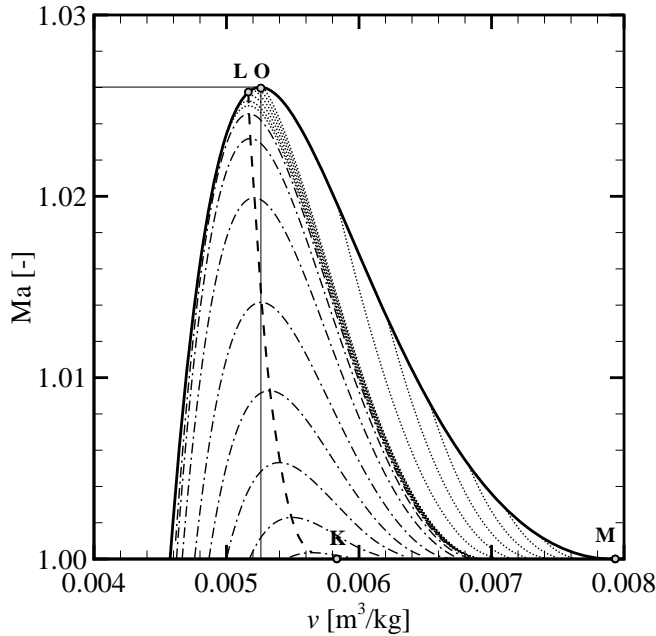


Figure 2.9: The pre-shock Mach number, associated with a post-shock Mach number of unity, as a function of the specific volume along selected isentropes of  $D_6$ . Thermodynamic properties are determined with the multiparameter EoS documented in Ref. [33] (see also Chap. 3). The solid line represents saturated-vapor states featuring a post-shock Mach number of unity, the dotted lines represent isentropes that intersect the dew-line of  $D_6$ , the dash-dotted lines are isentropes that are completely in the superheated-vapor regime, and the dashed line connects the maxima of the  $Ma$ - $v$ -curves for the latter isentropes. Point **O** represents the expansion shock wave with the highest possible pre-shock Mach number with a sonic post-shock state for  $D_6$ .

1. For the working fluid, determine the dew-line and the  $\Gamma = 0$ -locus in the dense-gas regime.
2. With reference to Fig. 2.8 compute and draw the isentropes  $s_{\min}$  and  $s_{\max}$ . All other isentropes  $s_i$  located in between  $s_{\min}$  and  $s_{\max}$  exhibit an interval of concavity in the dense-gas  $P$ - $v$ -thermodynamic plane.
3. Starting from the dew-line for a given isentrope  $s_{\min} \leq s_i \leq s_{\max}$ , determine by using the shock admissibility conditions, namely Eqns. (2.17),

the above-mentioned geometric arguments and the EoS of the fluid, both the pre-shock Mach number ( $Ma_A$ ) whereby the post-shock Mach number  $Ma_B = 1$ , and the pre-shock specific volume  $v_A$ . Next, increase the specific volume along the same isentropes  $s_i$  by  $\Delta v$  and again, for this newly assigned pre-shock state, determine  $Ma_A$  with the condition that  $Ma_B = 1$ .

- Application of the sequence of calculations outlined in the previous item results in the graph displayed in Fig. 2.9 illustrating the pre-shock Mach number, associated with a post-shock Mach number of unity, as a function of the pre-shock specific volume along selected isentropes of  $D_6$ . From this graph it is possible to identify for a given isentrope, a unique single-phase thermodynamic state with the greatest supersonic-to-sonic transition. Connecting these thermodynamic states gives the maximum-Mach locus, as indicated by the line connecting **M-L-K** in Fig. 2.8 (or the line connecting **M-L-O-K** in Fig. 2.9).

### Nomenclature

Symbol	Description
$A$	Area
$\mathbf{b}$	Speed-of-propagation vector of the shock wave with respect to a laboratory reference frame
$C_P$	Specific isobaric heat capacity
$C_v$	Specific isochoric heat capacity
$c$	Thermodynamic speed of sound
$D_{ik}$	Rate-of-deformation tensor
$e$	Specific internal energy
$F$	Thermodynamic function defined by Eq. (2.4) and valid only for isentropic flows
$G$	Grüneisen parameter
$h$	Specific enthalpy
$J$	Mass flux
$\mathcal{J}$	Riemann invariant for constant-area flows with negligible body force
$l$	Variable which appears after a particular coordinate transformation
$Ma$	Mach number
$\mathbf{n}$	Unit normal vector
$P$	Pressure

Continued on the next page...

Continued

Symbol	Description
$\mathbf{p}$	Unit vector tangential to a control-volume surface
$s$	Specific entropy
$T$	Absolute temperature
$\mathbf{t}$	Unit vector tangential to a control-volume surface
$t$	Time
$\mathbf{u}$	Fluid velocity vector with respect to a laboratory reference frame
$v$	Specific volume
$\mathbf{w}$	Fluid velocity vector with respect to a shock-related reference frame
$x$	Spatial coordinate
$x_0$	Variable which appears after a particular coordinate transformation
$\beta_P$	Coefficient of volume expansion
$\Gamma$	Fundamental derivative of gas dynamics
$\gamma$	Heat capacity ratio
$\varepsilon$	Shock-wave thickness
$\zeta$	Bulk viscosity
$\eta$	Dynamic (shear) viscosity
$\kappa$	Thermal conductivity
$\lambda$	Second viscosity coefficient
$\rho$	Density
$\sigma$	Wave speed
$\tau$	Time constant related to relaxation phenomena
$\Phi$	Dissipation function



“They underestimated me.”

President George W. Bush, Bentonville, Arkansas, November 6,  
2000

# 3

## Thermodynamic properties of selected dimethylsiloxanes

Selected contents from:

NANNAN, N. R. AND COLONNA, P. Improvement on multiparameter equations of state for dimethylsiloxanes by adopting more accurate ideal-gas isobaric heat capacities: supplementary to P. Colonna, N. R. Nannan, A. Guardone, and E. W. Lemmon, *Fluid Phase Equilib.* **244**, 193 (2006). *Fluid Phase Equilib.* (2009) in press.

COLONNA, P., NANNAN, N. R., AND GUARDONE, A. Multiparameter equations of state for siloxanes:  $[(\text{CH}_3)_3\text{-Si-O}_{1/2}]_2\text{-[O-Si-(CH}_3)_2]_{i=1\dots 3}$ , and  $[\text{O-Si-(CH}_3)_2]_6$ . *Fluid Phase Equilib.* **263**, 2 (2008), 115 - 130.

NANNAN, N. R., COLONNA, P., TRACY, C. M., ROWLEY, R. L., AND HURLY, J. J. Ideal-gas heat capacities of dimethylsiloxanes from speed-of-sound measurements and ab initio calculations. *Fluid Phase Equilib.* **257**, 1 (2007), 102 - 113.

COLONNA, P., NANNAN, N. R., GUARDONE, A., AND LEMMON, E. W. Multiparameter equations of state for selected siloxanes. *Fluid Phase Equilib.* **244**, 2 (2006), 193 - 211.

## Abstract

As is discussed in the subsequent chapters, Chaps. 4–6, the choice of appropriate initial conditions as well as the design of an experimental facility that can be used to generate and demonstrate the existence of nonclassical gas-dynamic phenomena, mandates the use and possibly development of good thermodynamic models. A good thermodynamic model in this context refers to its predictive capabilities and to the accuracy with which properties can be computed. The research activities that are documented in the following have been performed to obtain a better description of all thermodynamic properties of selected linear and cyclic dimethylsiloxanes in the entire range of pressure and temperature that is of interest for technical applications in general. In particular, this effort has been driven by the needs of the envisaged gas-dynamic experiment at the Delft University of Technology, see Chap. 6, aimed at proving the existence of nonclassical gas-dynamic phenomena in the thermodynamic region adjacent to the saturated vapor line at high reduced pressures and temperatures. Siloxanes have been chosen as test fluids, as motivated in Sec. 5.6. The selected functional form of the equations of state is that proposed by Span and Wagner for nonpolar and weakly polar substances, since this modern functional form uses a rather small number of parameters, provides sufficient accuracy from a technical viewpoint and has good extrapolation behavior. Because of scarcity of experimental thermal and caloric property data for most of these substances, estimation methods with reasonable uncertainty ( $\sim 2\text{--}5\%$ ) were employed, if necessary, to generate thermal-property data to be used for optimizing the fluid-specific parameters. Due to the unavailability of heat-capacity data however (hexamethyldisiloxane (MM,  $(\text{CH}_3)_3\text{-Si-O}_{1/2}$ ) is an exception), and particularly because of the large uncertainty associated with ad hoc estimation techniques if applied to organic silicon oils, namely  $\sim 25\%$ , a two-pronged approach was used to obtain molar ideal-gas heat capacity data ( $\bar{C}_p^0$ ) of selected siloxanes. Firstly, acoustic resonance measurements were made on gas-phase octamethylcyclotetrasiloxane ( $D_4$ ,  $[(\text{CH}_3)_2\text{-Si-O}]_4$ ) and decamethylcyclopentasiloxane ( $D_5$ ,  $[(\text{CH}_3)_2\text{-Si-O}]_5$ ) over the temperature range 450 K to 510 K. These new experimental data, along with previously published molecular vibrational frequency data for hexamethyldisiloxane, were used to develop an appropriate frequency scaling factor that can be used with *ab initio* frequency calculations to determine reliable ideal-gas heat capacities as a function of temperature. Ideal-gas heat capacities for both cyclic  $[(\text{CH}_3)_2\text{-Si-O}]_n$  (with  $3 \leq n \leq 8$ ) and linear  $(\text{CH}_3)_3\text{-Si-O-}[(\text{CH}_3)_2\text{-Si-O}]_n\text{-Si-(CH}_3)_3$  (with  $0 \leq n \leq 5$ ) siloxanes over a wide range of temperatures were determined by means of *ab initio* calculations. The collaboration with the process measurement division of the National Institute of Standards and Technology (NIST), Gaithersburg, MD and with DIPPR<sup>®</sup> thermodynamic properties laboratory at Brigham Young University, Provo, UT is acknowledged.

## 3.1 Introduction

Many energy conversion applications employ organic fluids as working media. Some of these organic compounds and their applications are listed in Table 3.1. Out of the class of organic fluids, siloxanes have many favorable characteristics – they feature good lubricating properties, are odorless, non-toxic, thermochemically stable up to high temperatures, scarcely flammable, and in the case of organic-Rankine-cycle (ORC) applications, these compounds are already employed because they exhibit good thermodynamic properties with respect to cycle design (see e.g., Refs. [7, 4, 6, 5]). Siloxanes are bulk-produced, mainly for the cosmetics industry. What is more is that, due to their molecular complexity, siloxanes are Bethe-Zel'dovich-Thompson (BZT) fluids [30] (see also Sec. 4.4) and may thus exhibit nonclassical gas-dynamic behavior in the dense-gas region close to saturation at high reduced pressures and temperatures.

Accurate and consistent predictions of thermodynamic properties are of the utmost importance both in the design of advanced process- and energy applications, e.g., high-temperature organic Rankine cycles, supercritical heat-pumps [8], process expanders and compressors in the (petro)chemical industry operating in the dense-gas thermodynamic regime [15, 111], as well as in nonclassical gas-dynamic investigations. A benchmark analysis documented in Chap. 4 shows that, at present, equations of state (EoS's) are the choice for the latter. References [37, 4] for example document the use of the Peng-Robinson [161], Stryjek and Vera modified [190], cubic EoS (PRSV) for siloxanes. The PRSV EoS allows for accurate predictions of vapor-pressures – for nonpolar fluids within 2 % of experimental data – and can be used with mixing rules to predict thermodynamic properties of mixtures [35, 4]. Physically based cubic EoS's however, are inherently rather inaccurate close to the critical region and for predicting saturated and sub-cooled liquid densities (especially for polar molecules) [1]. In the case of the PRSV EoS, thermodynamic properties also display a discontinuity at the critical temperature. With modern equations of state however, all thermodynamic properties of technical interest can be calculated with high accuracy and are thermodynamically consistent. The consistency of the thermodynamic model is a requirement if it is employed in computational fluid dynamics (CFD) programs [37, 35] or in dynamic systems simulations [207, 78].

Primarily, the documented work is related to the development of consistent technical equations of state for selected linear and cyclic siloxanes useful not only for nonclassical gas dynamic studies, but also for the design and analysis of technical applications in general. Referring back to the study performed by Colonna and Silva [37] where selected siloxanes were identified for the first time as BZT candidates, it was stated by the latter authors that the greatest source of uncertainty in the thermodynamic model was due to the rather large uncertainty in the estimation of the ideal-gas isobaric heat capacity, namely 25 %. For this reason, prior to the development of an EoS, as outlined in Sec. 3.3, a

Table 3.1: Energy conversion applications of organic fluids.

Fluid family	Applications
Hydrocarbons	Expanders and compressors in (petro)chemical processes, geothermal organic Rankine cycles (ORC's)
Fluorocarbons	Refrigeration and air conditioning, geothermal ORC's, low temperature heat recovery ORC's
Siloxanes	High temperature ORC's, heat transfer fluids as mixtures (possible future application: high-temperature heat pumps)

two-pronged approach was used to obtain accurate molar ideal-gas heat capacity data ( $\bar{C}_P^0$ ) of selected siloxanes. Using the new  $\bar{C}_P^0$  data documented in Sec. 3.2 which feature an estimated uncertainty of no more than 5–6 %, a multiparameter Helmholtz-energy-based EoS is established for selected siloxanes which allows for the prediction of all thermodynamic properties with an accuracy sufficient for technical applications, e.g., design of ORC engines.

## 3.2 Ideal-gas isobaric heat capacities of selected linear and cyclic dimethylsiloxanes

### 3.2.1 Overview

The work presented in this section is aimed at reducing the large uncertainty, namely  $\sim 25$  % according to DIPPR [172], in the estimate of the molar ideal-gas isobaric heat capacity ( $\bar{C}_P^0$ ) of linear and cyclic siloxanes. The only estimation method which is applicable to this family of fluids is the zeroth-order method by Harrison and Seaton [86] which was not specifically developed for these fluids, hence the large uncertainties. Knowledge of the temperature dependency of the (molar) ideal-gas isobaric heat capacity is essential for obtaining a comprehensive thermodynamic model, as discussed in Sec. 3.3.

To achieve the goal,  $\bar{C}_P^0$ 's for octamethylcyclotetrasiloxane ( $D_4$ ,  $[(CH_3)_2-Si-O]_4$ ) and decamethylcyclopentasiloxane ( $D_5$ ,  $[(CH_3)_2-Si-O]_5$ ) were determined using the acoustic resonance technique. The employed experimental apparatus available at NIST limited the temperature range from 450 K to 510 K. Information from the experiments was used to extend the estimation of  $\bar{C}_P^0$  from 298 K to the compound's decomposition temperature by using ab initio calculations and this computational method was also employed to provide estimates of  $\bar{C}_P^0$  for other selected members of the linear- and cyclic-siloxanes family.

The structure of this section is as follows: Ssec. 3.2.2 describes the experimental technique that was employed to measure the speed of sound in  $D_4$  and

D<sub>5</sub>. These data were correlated to get accurate temperature-dependent values of the ideal-gas isobaric heat capacity. The experimental speed-of-sound data and the derived data are reported in Appendix A and Ssec. 3.2.3, respectively. Remark that the speed-of-sound data can also be used to determine the second density virials of the fluids; these data however are reported elsewhere [154]. As described in Ssec. 3.2.4, information from speed-of-sound measurements can also be used to fine-tune the frequency scaling factor (FSF) in ab initio calculations. Ab initio calculations were used to obtain the  $\bar{C}_P^0$  as a function of temperature for six linear (MD<sub>n</sub>M; n = 0, 1, 2, 3, 4, and 5) and six cyclic members (D<sub>n</sub>; n = 3, 4, 5, 6, 7, and 8) of the siloxanes family. Subsection 3.2.4 also describes the results of the geometry optimization and examines the appropriate basis-set size for accurate determination of values.

### 3.2.2 Experimental section

Ideal-gas isobaric heat capacities can be determined by acoustic resonance techniques. These techniques measure the frequencies of resonance – and therefore the thermodynamic speed of sound – of sound in a gas sample contained within a cylindrical or spherical cavity. In the ideal-gas limit, i.e., when  $P \rightarrow 0$ , where  $P$  is the pressure, the thermodynamic speed of sound  $c^0$  is related to the isobaric heat capacity  $\bar{C}_P^0$  according to (where appropriate, superscript “0” denotes the ideal-gas limit and the overbar sign denotes molar-specific properties; if required, refer to the list at the end of this chapter explaining the adopted nomenclature)

$$(c^0)^2 = \gamma^0 \frac{\bar{R}T}{M} = \left( \frac{\bar{C}_P^0}{\bar{C}_P^0 - \bar{R}} \right) \frac{\bar{R}T}{M}. \quad (3.1)$$

Here,  $\gamma^0$  is the ratio of the isobaric to the isochoric heat capacity in the ideal-gas state, i.e.,  $\gamma^0 \equiv \bar{C}_P^0/\bar{C}_V^0$ ,  $\bar{R}$  is the universal gas constant ( $\bar{R} = 8314.472 \pm 0.014$  J/kmol-K and was determined by Moldover et. al. [149] using a spherical acoustic resonator),  $T$  is the temperature, and  $M$  is the molar mass of the substance. Therefore, provided that accurate data are available for the molar mass and for  $c^0$  at a specific temperature, the ideal-gas isobaric heat capacity can be computed from Eq. (3.1).

For dilute gases, the speed of sound smoothly departs from its ideal-gas value. Analogous to the density virial equation of state, namely

$$\frac{P}{\bar{\rho}\bar{R}T} = 1 + \bar{B}(T)\bar{\rho} + \bar{C}(T)\bar{\rho}^2 + \bar{D}(T)\bar{\rho}^3 + \dots, \quad (3.2)$$

which represents the departure of the molar density,  $\bar{\rho}$ , from ideal-gas behavior for low-to-moderate density gases, the acoustic virial equation of state, namely

$$c(T, P) = c^0(T) \left[ 1 + \left( \frac{\beta_a(T)}{\bar{R}T} \right) P + \left( \frac{\gamma_a(T)}{\bar{R}T} \right) P^2 + \left( \frac{\delta_a(T)}{\bar{R}T} \right) P^3 + \dots \right] \quad (3.3)$$

represents the speed of sound in dilute gases as a function of temperature and pressure. In Eq. (3.3),  $\beta_a(T)$ ,  $\gamma_a(T)$ , and  $\delta_a(T)$  are the second, third, and fourth acoustic virial coefficients, respectively. These only depend on the temperature as do the corresponding (density) virial coefficients  $\bar{B}(T)$ ,  $\bar{C}(T)$ , and  $\bar{D}(T)$  in Eq. (3.2). The second acoustic virial and the second density virial are connected by the thermodynamic relation

$$\beta_a(T) = 2\bar{B}(T) + 2(\gamma^0 - 1)T \frac{d\bar{B}(T)}{dT} + \frac{(\gamma^0 - 1)^2}{\gamma^0} T^2 \frac{d^2\bar{B}(T)}{dT^2}. \quad (3.4)$$

Expressions relating the higher-order acoustic virials to the higher-order density virials are also available [77, 76].

Values for the acoustic virial coefficients and the ideal-gas speed of sound are obtained by fitting Eq. (3.3) to experimental speed-of-sound and pressure data along isotherms. From the fitted values of  $c^0(T)$ , the ideal-gas isobaric heat capacity can be determined from

$$\bar{C}_P^0 = \frac{(c^0)^2 M}{T \left[ (c^0)^2 M / \bar{R}T - 1 \right]}. \quad (3.5)$$

A detailed description of the experimental equipment is given by Gillis [76]. In the following only a brief description of the resonator and of the measurement procedure is given.

### 3.2.2.1 The resonator

The resonator that was used for resonance frequency measurements was a cylinder with circular cross-section and was fabricated of a copper-nickel alloy. The height was approximately 14 cm and the width was about 6.5 cm (see Fig. 3.1). The internal surface of the resonator was polished to a mirror finish, therefore, the flat surface area was accurately known. To achieve good temperature stability and fast temperature equilibration, the cylinder was completely submerged in a continuously stirred liquid bath. This thermostated bath guaranteed that the temperature fluctuations in the gas sample were within 1 mK. The top plate of the cylinder contained a carefully designed port for charging and removal of the sample. The electro-acoustic transducers, these are the sound source and the microphone detector, were remote from the resonator because the high temperature of the thermostated bath was not compatible with these transducers. Instead, the sound waves generated at (received by) the source (microphone detector), were carried to (from) the resonator by waveguides. The waveguides are hollow cylindrical tubes with horn-shaped cross sections and were filled with argon. Apart from protecting the electro-acoustic transducers from the harsh environment of the thermostated bath and the gas in the resonator, the physical separation of the transducers by the waveguides reduces

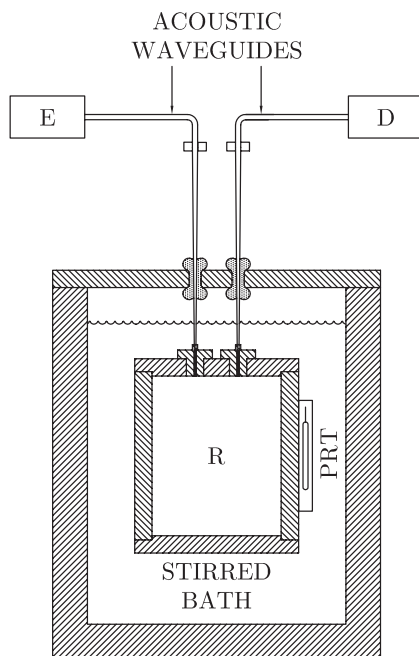


Figure 3.1: Schematic representation of the cylindrical resonator, the waveguides, and the electro-acoustic transducers (adapted from Ref. [76]). E: sound emitter, D: sound detector, R: resonator, and PRT: standard platinum resistance thermometer.

electro-magnetic and mechanical disturbances between the sound source and the microphone detector. A metal membrane separated the argon in the waveguides from the siloxane sample. To weaken resonances in the waveguides, which may complicate the resonance-frequency measurements in the sample, a metal screen was placed in both waveguides near the metallic membrane. The pressure of the sample was measured with a quartz-bourdon-tube pressure gauge in conjunction with a diaphragm-type differential pressure transducer (DPT). The pressure gauge measured the pressure of argon in the waveguides and the DPT, which was always kept at 230 °C, measured the pressure difference between the argon and the sample. To avoid pre-condensation,<sup>1</sup> the pressure of the test fluid

<sup>1</sup>this is a phenomenon whereby, if the thermodynamic state of the test fluid is close to saturation, evaporation and condensation occur at the resonator walls as a consequence of pressure and temperature variations caused by the acoustic cycle [142].

was kept to 80 % of the vapor pressure of the sample at the bath temperature or to that corresponding to 230 °C, whichever was lower. At the highest temperature that was reached, the DPT was relatively colder, so that was the limiting temperature.

### 3.2.2.2 Sample purity

A major source of uncertainty in  $\bar{C}_P^0$  derived from speed-of-sound data is sample impurity. For small levels of impurity, the fractional uncertainty in the derived ideal-gas isobaric heat capacity is approximately:

$$\frac{\sigma_u(\bar{C}_{P,t}^0)}{\bar{C}_{P,t}^0} \approx \left[ \underbrace{\left( \frac{\bar{C}_{P,i}^0}{\bar{C}_{P,t}^0} - 1 \right)}_{\text{first term}} + \underbrace{\left( \frac{M_i}{M_t} - 1 \right) \frac{1}{(\gamma_t^0 - 1)}}_{\text{second term}} \right] \bar{i} + \mathcal{O}(\bar{i}^2). \quad (3.6)$$

Subscripts “t” and “i” denote the fluid sample and the impurity, respectively,  $\sigma_u(\ )$  represents the absolute uncertainty of the property between the round brackets, and  $\bar{i}$  denotes the mole fraction of impurity in the sample. The term involving the ratio of the isobaric heat capacity of the impurity and that of the sample is usually small compared to the second term in Eq. (3.6). Complex fluids with many active vibrational degrees of freedom at the temperature of interest have large heat capacities and heat-capacity ratios,  $\gamma_t^0$ , very close to unity. For example,  $\gamma_t^0 \approx 1.017$  for D<sub>4</sub> at 500 K if  $\bar{C}_P^0$  is estimated using the Harrison-Seaton method. This means that if the D<sub>4</sub> sample contains impurities for which  $(M_i/M_t - 1)$  is of the order of unity, the fractional uncertainty in  $\bar{C}_{P,t}^0$  is of the order of 50 times the mole fraction of the impurity.

The test fluids were octamethylcyclotetrasiloxane (D<sub>4</sub>, [(CH<sub>3</sub>)<sub>2</sub>-Si-O]<sub>4</sub>) and decamethylcyclopentasiloxane (D<sub>5</sub>, [(CH<sub>3</sub>)<sub>2</sub>-Si-O]<sub>5</sub>) and had been supplied by the European branch of the Tokyo Chemical Industry Co, Ltd. These fluids were rated by the manufacturer as 99.9+ % pure; no gas-chromatographic analysis was done. The impurities that were present were most likely other siloxanes. Before the fluids were loaded into the resonator, they were thoroughly degassed to remove air and other volatilities by repeatedly freezing the fluid in liquid nitrogen and evacuating the space above the frozen sample.

### 3.2.2.3 Calibration

For accurate speed-of-sound measurements, the resonator needs to be calibrated. Calibration is necessary for determining the temperature-dependent dimensions of the cylinder. This was achieved by measuring the frequencies of resonance of different acoustic modes in argon in the temperature and pressure range of interest. Argon was chosen for the calibration, because it is inert

and because its transport properties and speed of sound are known with high accuracy.

For the cylinder that was used to measure the sound speed in the siloxanes, the following dimensions were obtained for temperatures between 350 K and 500 K:

$$\mathcal{L} = \mathcal{L}_0 [1 + \alpha (T - T_0)]. \quad (3.7)$$

Here,  $\mathcal{L}_0$  denotes the length of the cylinder at the reference temperature  $T_0 = 273.15$  K. From measurements with argon, it was inferred that  $\mathcal{L}_0$  equals 14.04 cm. The thermal expansion coefficient of the copper-nickel alloy was assumed to have a power-law dependence with temperature, i.e.,  $\alpha \propto T^{\mathfrak{B}}$ , whereby the proportionality constant was found to be equal to  $1.184 \cdot 10^4 \text{ K}^{-\mathfrak{B}-1}$  and  $\mathfrak{B} = 1.866$  ( $[\alpha] = \text{K}^{-1}$ ). The radius had the following temperature dependence:

$$\mathfrak{R} = \mathfrak{R}_0 [1 + \alpha (T - T_0)]. \quad (3.8)$$

The radius  $\mathfrak{R}_0$  at  $T_0 = 273.15$  K was determined from the calibration run with argon. From the obtained data it was inferred that  $\mathfrak{R}_0$  equals 3.279 cm. All pressure and temperature transducers were calibrated only once.

#### 3.2.2.4 Measurement procedure

The measurement procedure was as follows:

- At first, the thermostated bath was set to the desired measurement temperature. Once this temperature was reached, the resonator was charged with the gas sample. Acoustic measurements were made at pressures up to 80 % of the vapor-pressure at the thermostated temperature of either the bath or the DPT, whichever was lower. At pressures closer to the dew point, condensation at the walls due to the acoustic cycle can become a problem. This so-called pre-condensation lowers the apparent speed of sound [142]. The vapor-pressure was determined from the AIChE DIPPR<sup>®</sup> equation [172] using the substance specific parameters for the siloxanes  $D_4$  and  $D_5$ , given by Flaningam [69].
- After the temperature of the gas sample had equilibrated, selected purely longitudinal modes and one purely radial mode were measured. Redundant measurements were conducted to give confidence that the correct modes were measured. Because of the low speed of sound, it is important for the siloxanes considered herein to distinguish between pure and mixed modes. For example, the first purely longitudinal mode for  $D_4$  at 450 K occurs at a frequency of about 380 Hz. Because the experimental equipment (resonator and transducers) was not specifically designed (selected) to measure frequencies significantly below 1 kHz, it was necessary to measure higher modes (at low frequencies the signal to noise

ratio is small). Higher modes however, are spaced closer to each other than are, for example, the first and second purely longitudinal mode. It is therefore important to do redundant measurements in order to check (but also to distinguish) which modes are measured and whether they are pure modes or mixed modes. Additionally, redundant modes give a measure of the uncertainty in the resonance frequency  $f$ . To account for first-order drifts that can occur in temperature and pressure during a measurement cycle, each resonance frequency was measured three times. Furthermore, at each measurement, the interval sweep of the scan was in two directions, i.e., from  $f - g$  to  $f + g$  and then back from  $f + g$  to  $f - g$ . Here,  $g$  is the experimentally determined half-width, i.e., the width of the resonance frequency at  $2^{-1/2}$ -times the signal's maximum amplitude. Known contributions to the half-width (loss mechanisms) are: i) sound absorption at the metal-gas boundaries due to the formation of thermal and viscous boundary layers, ii) sound absorption in the bulk of the fluid as a consequence of the local rate of compression and fluid friction, iii) irreversible heat flows in the bulk of the fluid due to the periodic changes in temperature during the acoustic cycle, and iv) imperfections in the cylinder such as the fill duct and the gap at the O-ring seal.

- After the measurement sequence for each thermodynamic state, the pressure was reduced by about 10 kPa while the temperature was kept constant. Once pressure and temperature equilibrated (this required about 5 minutes), the resonance frequencies were measured again. The detected response of the measured resonance frequency is pressure dependent and attenuates with decreasing pressure. Consequently, the lowest pressure at which resonance frequencies were measured was 22 kPa.

### 3.2.3 Experimental results

#### 3.2.3.1 Experimental data for $D_4$

The speed of sound in  $D_4$  was measured along the isotherms of 450 K, 465 K, 480 K, and 495 K. The lower temperature limit was chosen based on the fact that for good speed-of-sound measurements in this apparatus, the pressure of the sample should approximately be greater than 30 kPa and less than about 80 % of the vapor pressure at the temperature of measurement. At lower pressures the signal-to-noise ratio is small and therefore it is difficult to measure the resonance frequency. The upper temperature limit is determined by the maximum allowed temperature of the liquid used in the thermostated bath and the highest temperature at which the DPT can operate.<sup>2</sup> The pressure spanned the range

---

<sup>2</sup>There is also an upper density limit: if superheated vapor densities are of the order of the critical density, speed-of-sound data determined with the acoustic resonance technique are not very accurate because of an increase of the coupling of the oscillations of the vapor enclosed in the resonator

Table 3.2: Derived values for the ideal-gas speed of sound and isobaric heat capacity of D<sub>4</sub>.

$T$ [K]	$c^0$ [m/s]	$\sigma_u(c^0)/c^0$ [%]	$\bar{C}_P^0$ [J/mol-K]	$\sigma_u(\bar{C}_P^0)/\bar{C}_P^0$ [%]
450	113.3	0.014	469.5	1.6
465	115.2	0.041	480.6	4.7
480	117.0	0.019	491.8	2.2
495	118.8	0.060	503.0	7.1

27 kPa - 225 kPa. The measured modes included the 5<sup>th</sup> and 7<sup>th</sup> purely longitudinal mode and the 1<sup>st</sup> purely radial mode. The experimental resonance frequency  $f^{\text{exp}}$  is slightly lower than the ideal resonance frequency  $f$  from which the true speed of sound should be determined. The shift in frequency,  $\Delta f$ , is the result of the viscous and thermal boundary layers at the walls of the resonator. The shift in frequency depends on the transport properties of the fluid sample, namely the shear viscosity, the bulk viscosity, and the thermal conductivity. Trusler [205] gives relevant equations that should be used to compute the frequency shift  $\Delta f$ ; moreover,  $\Delta f$  is related in part to the experimentally measured half-width of the signal (note that irreversible processes in the bulk of the sample contribute to the experimental half-width of a resonance frequency but are not responsible for the frequency shift). Because of the large uncertainty in transport-property estimates for siloxanes [172], this study uses the following simple correlation to determine the ideal resonance frequency:

$$f = f^{\text{exp}} + g^{\text{exp}}, \quad (3.9)$$

where  $g^{\text{exp}}$  denotes the half-width obtained from the measurements.

The speed-of-sound data obtained from these frequencies/modes were fitted to the acoustic virial equation of state, Eq. (3.3), to obtain the second and third acoustic virial coefficient at every temperature. Using the relationship between the second acoustic virial and the second density virial, as expressed by Eq. (3.4), values were also obtained for  $\bar{B}$  at the four temperatures [154]. From the speed-of-sound data, ideal-gas isobaric heat capacities were derived. Because of the relatively small temperature range of measurement, it was assumed that  $\bar{C}_P^0$  has a linear dependence on temperature. Table A.1 lists the experimental speed-of-sound data together with the uncertainties in  $c$  and Table 3.2 gives the derived  $c^0$ 's and ideal-gas isobaric heat capacities at each temperature of measurement. The uncertainties are calculated using the method documented by Taylor [195].

---

and the oscillations of the shell enclosing the vapor. Here, the upper density limit was not reached.

Table 3.3: Derived values for the ideal-gas speed of sound and isobaric heat capacity of D<sub>5</sub>.

$T$ [K]	$c^0$ [m/s]	$\sigma_u(c^0)/c^0$ [%]	$\bar{C}_P^0$ [J/mol-K]	$\sigma_u(\bar{C}_P^0)/\bar{C}_P^0$ [%]
485	105.1	0.025	563.3	3.3
500	106.7	0.042	574.5	5.7
510	107.7	0.054	581.9	7.5

The experimental  $\bar{C}_P^0$  data, which on average have a predicted experimental uncertainty of 3.9 %, are compared with the estimates determined from the Harrison-Seaton method. It is observed that the experimental  $\bar{C}_P^0$ 's are within the uncertainty assigned by DIPPR<sup>®</sup> [172]. Moreover, within the experimental temperature range, i.e., 450K <  $T$  < 495K, the Harrison-Seaton method gives values which are lower than the experimentally derived data by approximately 4 %.

### 3.2.3.2 Experimental data for D<sub>5</sub>

The speed of sound in D<sub>5</sub> was measured along the isotherms of 485 K, 500 K, and 510 K. The pressure spanned the range 22 kPa - 117 kPa. The measured modes were again the 5<sup>th</sup> and 7<sup>th</sup> purely longitudinal mode and the 1<sup>st</sup> purely radial mode. These experimental frequencies were corrected using Eq. (3.9). The speed-of-sound data and the experimental uncertainties are given in Table A.2 and the derived  $c^0$ 's and ideal-gas isobaric heat capacities are presented in Table 3.3. A comparison of the experimentally determined ideal-gas isobaric heat capacities (these have an average experimental uncertainty of 5.5 %) with estimates obtained from the Harrison Seaton method shows that although the experimental  $\bar{C}_P^0$ 's are within the uncertainty of the group-contribution method [172], the experimental  $\bar{C}_P^0$ 's are lower than values determined from the method of Harrison and Seaton and values obtained from the ab initio calculations (see Table 3.7). This is contrary to what was observed for D<sub>4</sub>. This discrepancy is a possible consequence of impurities in the D<sub>5</sub> sample: since the same resonator was used for resonance frequency measurements in both fluids, it is reasonable to assume that minute amounts of D<sub>4</sub> were present during the measurements in D<sub>5</sub>. This reasoning is consistent, since a lighter constituent in the sample of D<sub>5</sub> means that the speed of sound is greater with respect to a measurement not affected by impurities. Moreover, using Eq. (3.6) it is found that 0.07 % of D<sub>4</sub> as an impurity in D<sub>5</sub>, reduces the ideal-gas isobaric heat capacity by as much as 1 %. This level of impurity could have been measured using gas-chromatography (GC). However, no GC analyzer with the required sensitivity was available in the laboratory, therefore it was impossible to check whether cross-contamination

due to incomplete clean-out of the resonator had occurred. What is even more important is that only after the results from the *ab initio* computations became available, did it become a point of concern that contamination of the D<sub>5</sub> sample might have happened.

Remark that since the ideal-gas heat capacity ratio is close to unity, the presence of impurities can greatly influence the uncertainty in derived ideal-gas isobaric heat capacities. Furthermore, due to the low volatility of the siloxanes, the experiment had to be conducted at high temperatures. A viable approach to obtain accurate  $\bar{C}_P^0$ 's is the use of a buffer gas, e.g., argon, for which accurate thermodynamic properties are available. By measuring the shift in resonance frequency due to the addition of a small, but accurately known amount of siloxane in the buffer gas, one can obtain the value of the ideal-gas heat capacity ratio of the argon-siloxane mixture, from which  $\bar{C}_P^0$  of the siloxane can be determined. This approach has been used by Colgate et. al. [26] for measuring  $\bar{C}_P^0$ 's of n-butane, isobutane, and n-heptane. This technique will be considered for possible developments of this work, but it could not be adopted at the time of the measurements herewith documented because the available cylindrical resonator was not suitable and several modifications would have to be implemented.

### 3.2.4 *Ab initio* calculations

Several different families of siloxanes have been successfully studied with *ab initio* methods to help elucidate the relatively flexible Si-O backbone structure that is largely responsible for many of their useful properties [70]. Previous studies show that the Si-O bond is relatively short. This has been attributed to the high ionic character of the bond [90] and to partial transfer of electronic charge from the O lone electron pair to the Si atom [70]. The bending force constant for the Si-O-Si bond angle is very small, and the angle varies between 140–180° [70, 91, 68] for different molecules. For example, using HF calculations with modest basis sets for cyclo-n-trisilicic acids, Hill and Sauer [91] found Si-O-Si angles of 163.6°, 178.6°, and 166.4° for the n = 4, 5, and 6 rings, respectively. Freire et. al. [70] found considerable differences in the stable geometries of dimethyl- and diphenylsiloxane chains. The torsional barriers for rotations about the Si-O bonds are also quite low [70]. Thermodynamic measurements have shown that internal rotation about the Si-O bond in hexamethyldisiloxane (MM, [(CH<sub>3</sub>)<sub>3</sub>-Si-O<sub>1/2</sub>]<sub>2</sub>) is free, or nearly so [177]. Other experimental results, such as X-ray and electron diffraction [116], also agree quite well with the bond lengths and angles obtained from *ab initio* calculations.

The use of higher levels of theory and larger basis sets has been limited by the molecular size of these molecules and the number of electrons involved. However, Kudo et. al. [116] used 6-31G\* and 6-311G(d,p) basis sets with both HF and MP2 calculations for specific conformations of (H<sub>2</sub>-Si-O)<sub>n</sub> with n = 3, 4, 5. In most cases, the optimized geometries and energies were similar for the HF

and MP2 calculations, though the MP2 inclusion of electron correlation effects changed the stability order of some conformations of nearly equal energies.

Previous ideal-gas-heat-capacity determinations from ab initio frequency calculations on the siloxane family have not been found in the literature. In this study HF calculations were applied with basis sets similar to those used by Kudo et. al. on the dihydride siloxanes. The convergence of calculated  $\bar{C}_P^0$  values is initially determined with basis set size for MM. This basis set is then used for the geometry optimization and frequency calculations on twelve of the molecules studied here.

### 3.2.4.1 Basis-set dependence

The ideal-gas isobaric heat capacity is related to harmonic characteristic vibrational temperatures,  $\Theta_j$ , within the molecule by [171]

$$\frac{\bar{C}_P^0}{R} = 4 + \sum_{j=1}^{3m-6} \left( \frac{\Theta_j}{T} \right)^2 \left\{ \frac{\exp(\Theta_j/T)}{[\exp(\Theta_j/T) - 1]^2} \right\}, \quad (3.10)$$

where  $m$  is the number of atoms in the molecule and  $\Theta_j$  is related to the intramolecular vibrational frequencies,  $\nu_j$ , by

$$\Theta_j = \frac{h_P \nu_j}{k_B}. \quad (3.11)$$

Here  $h_P$  and  $k_B$  are Planck's and Boltzmann's constant, respectively. The derivation of Eq. (3.10) also assumes independence of the rotational and vibrational modes.

In this work, harmonic frequencies for the optimized geometry were obtained from frequency calculations using Gaussian 98 [73], and these were used in Eq. (3.10) to obtain  $\bar{C}_P^0$  values. Frequencies determined from ab initio calculations may differ from those measured experimentally due to the incomplete inclusion of electron correlation effects and the use of finite basis sets. In all cases, the same basis set was used for the frequency and optimization calculations, but  $\bar{C}_P^0$  values for MM were generated using increasingly larger basis sets to determine convergence of  $\bar{C}_P^0$  with the number of basis functions employed. MM is the only compound of those studied for which experimental frequency information is available [177]. The basis sets used and the corresponding number of basis functions are given in Table 3.4. While the 3-21G basis set is too small for accurate  $\bar{C}_P^0$  calculations, acceptable convergence is obtained for 6-31G(d) and larger basis sets. The addition of diffuse functions tends to lower  $\bar{C}_P^0$  values for the double zeta basis sets, but the use of 6-31G(d) gives values consistent with the largest basis set studied. HF/6-31G(d) and HF/6-31+G(d) were used for all subsequent calculations.

Geometry optimizations and frequency calculations were made using HF/6-31G(d) and HF/6-31+G(d) for six linear MD<sub>n</sub>M siloxanes ( $0 \leq n \leq 5$ ) and for six

Table 3.4: Basis set dependence of  $\bar{C}_P^0$  values [J/mol-K] for MM.

Basis set	Number of Basis Functions	$T$ [K]			
		273.15	500	1000	1500
3-21G	125	189.84	290.93	434.8548	512.5241
6-31G(d)	179	220.15	322.81	463.2236	539.1128
6-31+G(d)	215	213.50	315.91	455.6175	531.1374
6-31G(d,f)	242	221.72	324.65	464.3449	539.7807
6-31+G(d,f)	278	214.43	317.48	456.7552	531.8967
6-311G(d,f)	295	222.49	326.53	466.1793	541.1331
6-311+G(d,f)	331	222.57	326.77	466.3486	541.2369

cyclic  $D_n$  siloxanes ( $3 \leq n \leq 8$ ). All optimization calculations were performed without constraints. Several previous studies have restricted optimizations to investigate the relative energies of particular conformations. In the study of dihydride siloxanes, Kudo et. al. [116] found very close energies for the  $D_{5h}$ ,  $C_{5V}$  and  $C_1$  conformations with a minimum for the unconstrained  $C_1$  conformation. It has been chosen to use the unconstrained  $C_1$  optimized configuration, as did Hill and Sauer [91]. Evidence of the optimum geometry included convergence to the same minimum from different initial configurations and the absence of any imaginary frequencies. Average Si-O bond lengths and Si-O-Si angles, with the corresponding ranges of values observed within the molecule, are shown in Table 3.5. The O-Si-O bond angle is essentially tetrahedral and is not included in the table. Other bond lengths and angles are available but are not listed. Illustrative figures of the optimized geometries are shown for  $D_3$ ,  $D_4$ ,  $D_5$ , and  $MD_5M$  in Fig. 3.2. The results for  $D_3$ ,  $D_4$  and  $D_5$  are very similar to the  $C_1$  geometries reported by Kudo et. al. [116] for the corresponding dihydride cyclic compounds.  $D_3$  is planar,  $D_4$  is very nearly planar, and  $D_5$ ,  $D_6$  and  $D_7$  are puckered so that their geometries resemble the chair conformations of the corresponding cycloalkanes containing 5, 6 and 7 carbons, respectively. The geometry of  $D_8$  is more like a boat structure with the bow and stern bent toward each other. Again the Si-O-Si angle is seen to be relatively flexible and adjusts easily to steric constraints of the ring structure. The Si-O-Si bond angle is  $134.1^\circ$  in  $D_3$ ,  $157.9^\circ$  in  $D_4$ , and  $158.9^\circ$  in  $D_5$ . For the linear molecules, the Si-O-Si bond angle decreases from  $180^\circ$  for MM to  $160^\circ$  for the longer molecules. Interestingly, the larger linear  $MD_nM$  siloxanes tend to form a corkscrew shape as illustrated in Fig. 3.2 for  $MD_5M$ .

Table 3.5: Backbone Si-O bond lengths and Si-O-Si angles in the optimized geometries showing the average (Ave.) values and the minimum (Min.) and maximum (Max.) values within the molecule.

Siloxane	Si-O Bond [ $\text{\AA}=10^{-10} \text{ m}$ ]			Si-O-Si Angle [ $^\circ$ ]		
	Ave.	Min.	Max.	Ave.	Min.	Max.
	<b>Linear</b>					
MM	1.635	–	–	180.00	–	–
MDM	1.631	1.625	1.637	178.35	178.35	178.35
MD <sub>2</sub> M	1.630	1.625	1.639	168.65	168.47	169.01
MD <sub>3</sub> M	1.633	1.627	1.645	161.16	154.08	168.96
MD <sub>4</sub> M	1.633	1.626	1.643	160.06	158.76	160.77
MD <sub>5</sub> M	1.633	1.627	1.644	159.57	154.81	164.89
	<b>Cyclic</b>					
D <sub>3</sub>	1.648	–	–	134.05	–	–
D <sub>4</sub>	1.633	–	–	157.86	–	–
D <sub>5</sub>	1.632	1.630	1.635	158.90	153.95	167.35
D <sub>6</sub>	1.632	1.632	1.633	157.55	154.97	160.51
D <sub>7</sub>	1.631	1.629	1.634	159.48	154.65	163.28
D <sub>8</sub>	1.632	1.627	1.635	157.94	152.93	163.60

### 3.2.4.2 Frequency scaling factor

Currently, the determination of high-accuracy  $\bar{C}_P^0$  values from ab initio calculations requires use of an empirically determined frequency scaling factor (FSF) that adjusts harmonic frequencies, for use in Eq. (3.10), closer to the actual values. In so doing, it is assumed that the scaling factors compensate for anharmonic effects, errors resulting from the electronic structure calculations, and any lack of complete independence between vibrational and rotational modes. It has been found that such scaling factors are relatively uniform for specific combinations of theory and basis set, and considerable effort in obtaining FSF values is evident in the literature. Early on, Pople et. al [165] proposed an FSF of 0.89 for HF/3-21G, Hout and coworkers [96] suggested an FSF of 0.921 for MP2/6-31G(d), and DeFrees and McLean [52] recommended values of 0.96 for first-row molecules and 0.94 for second-row molecules. More recently, Scott and Radom [176] developed and tabulated FSF's for a large number of model chemistries. They recommend FSF = 0.8953 for HF/6-31G(d) and FSF = 0.8970 for HF/6-31+G(d). More recently Irikura et. al [101] reported an analysis of scaling factors based on 358 molecules using the Computational Chemistry Comparison and Benchmark Database (CCCBDB) maintained by the National Institute of Standards and Technology (NIST). These authors also performed careful

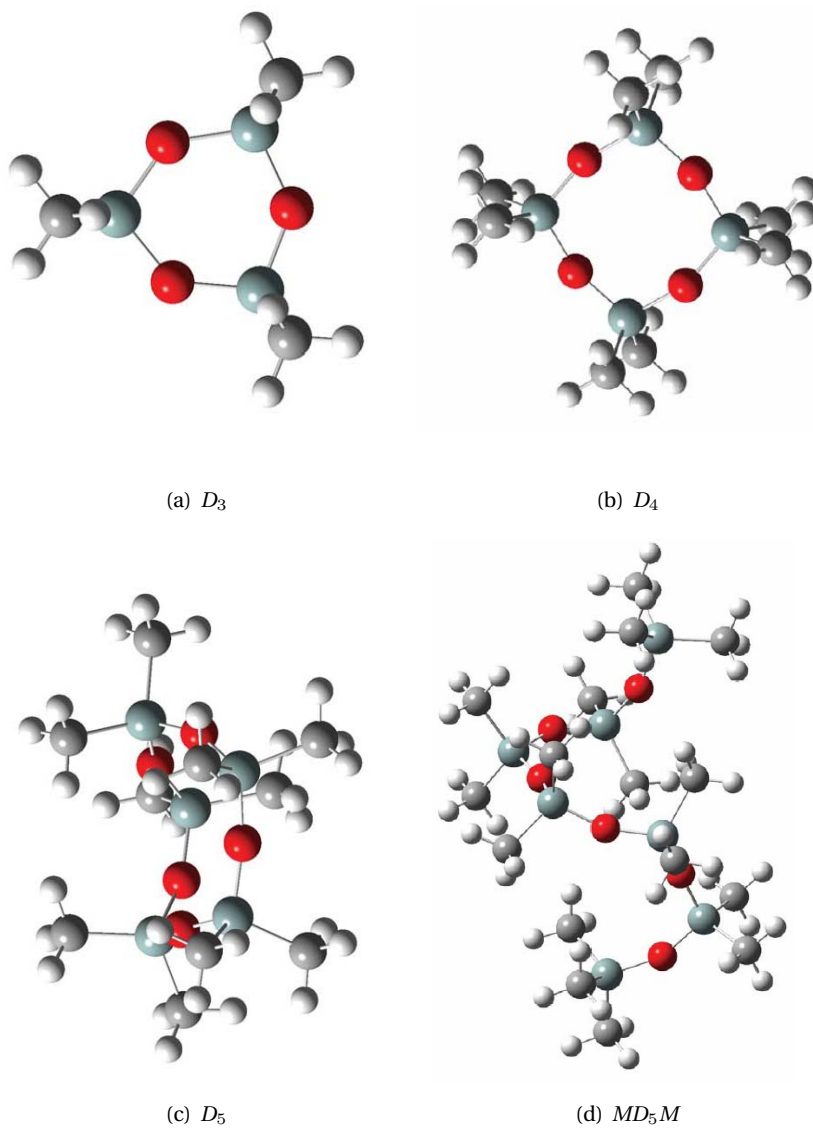


Figure 3.2: *Optimized structures of some of the considered siloxanes.*

Table 3.6: Recommended FSF values for siloxanes.

Compound	HF/6-31G(d)	HF/6-31+G(d)	MP2/6-31+G(d)
MM	1.0316	0.9898	1.0381
D <sub>4</sub>	1.0324	1.0077	–
Average	1.0320	0.9988	–

statistical analysis of the resultant frequency factors and determined uncertainties of their recommended values.

Because tabulated FSF values have been based on organic molecules containing primarily first- and second-row elements, it is unclear how effective these values are in correlation and prediction of siloxane thermochemical properties. Therefore, FSF values for siloxanes appropriate for the basis sets used in this work have been regressed from the experimental  $\bar{C}_p^0$  values for D<sub>4</sub> and from available thermochemical data for MM [177]. The resulting values, shown in Table 3.6, are consistent between the two compounds but closer to unity than the corresponding FSF values employed for non-Si compounds. The average values shown in Table 3.6 are used throughout this work to predict  $\bar{C}_p^0$  values for all of the remaining siloxanes. As an indication of possible electron correlation effects on the FSF, MP2/6-31+G(d) calculations on MM were also performed. The resultant  $\bar{C}_p^0$ 's were in excellent agreement with experimental values with an optimized FSF = 1.0381.

As mentioned, the FSF scaling of the frequencies attempts to compensate for deviations from the theoretical model. In this case these include deviations not only due to anharmonicity effects and mode coupling effects, but also deviations in  $\bar{C}_p^0$  due to the modeling of the fluid with the optimized geometry. The real fluid will be an equilibrium mixture of molecular conformers, but calculations of  $\bar{C}_p^0$  for a couple of different conformations indicates that the variation in  $\bar{C}_p^0$  values amongst conformers is likely very small and adequately accounted for by using the FSF.

### 3.2.4.3 Predicted ideal-gas isobaric heat capacities

Frequencies were obtained for the six linear and six cyclic siloxanes, adjusted using the average FSF shown in Table 3.6, and used with Eqns. (3.10) and (3.11) to obtain the values given in Table 3.7 at various temperatures. The listed values are predicted and, of course, only apply to the real-gas phase up to temperatures at which the fluids thermochemically decompose. Several low-frequency modes associated with Si-O-Si angle bending were consistent with the known flexibility of this angle. Similar calculations were made using HF/6-31+G(d) for

Table 3.7:  $\bar{C}_P^0$  values [J/mol-K] predicted for linear and cyclic siloxanes using HF/6-31G(d). Values given for temperatures above the decomposition temperatures are hypothetical.

Fluid	$T$ [K]									
	298	300	400	500	600	700	800	900	1000	1200
<b>Linear</b>										
MM	232	234	281	323	359	390	418	442	463	499
MDM	330	331	397	455	505	547	584	617	646	694
MD <sub>2</sub> M	403	405	489	562	625	679	726	767	804	865
MD <sub>3</sub> M	524	526	629	719	795	881	918	968	1012	1085
MD <sub>4</sub> M	621	624	745	851	941	1018	1084	1143	1194	1280
MD <sub>5</sub> M	718	721	861	983	1086	1174	1251	1318	1377	1476
<b>Cyclic</b>										
D <sub>3</sub>	273	274	331	379	420	454	484	509	532	570
D <sub>4</sub>	364	365	439	503	557	602	641	676	706	756
D <sub>5</sub>	469	471	564	643	710	768	817	860	897	960
D <sub>6</sub>	566	568	680	775	856	925	984	1035	1080	1155
D <sub>7</sub>	663	666	796	907	1001	1081	1150	1210	1263	1351
D <sub>8</sub>	759	762	911	1039	1146	1238	1317	1385	1446	1546

three MD<sub>n</sub>M and three D<sub>n</sub> compounds, and these results are shown in Table 3.8. Results are similar for the two basis sets although the predicted values are often slightly higher with the use of diffuse functions on the heavier nuclei. Figure 3.3 compares the D<sub>4</sub> experimental values measured here to the ab initio values predicted using the recommended average FSF value developed previously.

Figure 3.4 compares the experimental results for D<sub>4</sub> (see Ssec. 3.2.3.1) with values predicted by other means. Values predicted using the simple Harrison-Seaton group-contribution method are in very good agreement with the ab initio predicted values over the whole temperature range. Also shown in this figure are values of  $\bar{C}_P^0$  estimated using the approximate relationship,

$$\bar{C}_P^0 \approx \bar{C}_P^L + \left( \frac{d\bar{H}_{\text{vp}}}{dT} \right)_{\text{sat}} \quad (3.12)$$

with values for the saturated-liquid isobaric heat capacity,  $\bar{C}_P^L$ , and the molar-specific enthalpy of vaporization,  $\bar{H}_{\text{vp}}$ , obtained from the recommended correlations in the DIPPR<sup>®</sup> database [172]. Equation (3.12) neglects non-ideal vapor correction terms which can be significant at lower temperatures where the liquid heat capacity is usually more accurately known. Additionally, the correlation for  $\bar{H}_{\text{vp}}$  was obtained from the vapor pressure curve using the Clapey-

Table 3.8:  $\bar{C}_p^0$  values [J/mol-K] predicted for selected linear and cyclic siloxanes using HF/6-31+G(d). Values given for temperatures above the individual decomposition temperatures are hypothetical.

Fluid	$T$ [K]									
	298	300	400	500	600	700	800	900	1000	1200
<b>Linear</b>										
MM	231	232	280	322	358	390	417	441	462	498
MDM	338	339	406	465	515	557	594	627	656	704
MD <sub>3</sub> M	537	539	644	734	811	876	933	983	1026	1099
<b>Cyclic</b>										
D <sub>3</sub>	279	280	338	387	428	462	491	517	539	576
D <sub>4</sub>	364	366	441	506	559	605	644	678	708	758
D <sub>5</sub>	472	474	568	648	716	773	822	864	902	963

ron equation. This means that the second term in Eq. (3.12) is obtained from a second-order derivative of the experimental vapor-pressure data. Errors associated with this approximation are also worse at lower temperatures. One would therefore expect this approximate thermodynamic consistency check to be better at higher temperatures.

Within the accuracy of this test, Fig. 3.4 shows agreement with the available related thermodynamic data. A similar comparison of the ab initio results with the Harrison-Seaton method and the approximate thermodynamic consistency check of Eq. (3.12) was made for the other eleven siloxanes with results similar to those displayed in Fig. 3.5 for MM, MD<sub>3</sub>M, MD<sub>5</sub>M, and D<sub>5</sub>. Agreement of the ab initio values is within the expected uncertainty of the approximate thermodynamic consistency test. The Harrison-Seaton predictions exhibit similar trends, but they are often lower than the ab initio values.

The discrepancy between the measured D<sub>5</sub> values (see Ssec. 3.2.3.2) and the ab initio predictions is interesting. The thermodynamic consistency check also exhibits deviations from the ab initio results. These differences may be due to the difficulty in purifying D<sub>5</sub> and the large effect small amounts of impurities have on the speed-of-sound measurements as discussed in Ssec. 3.2.2.2.

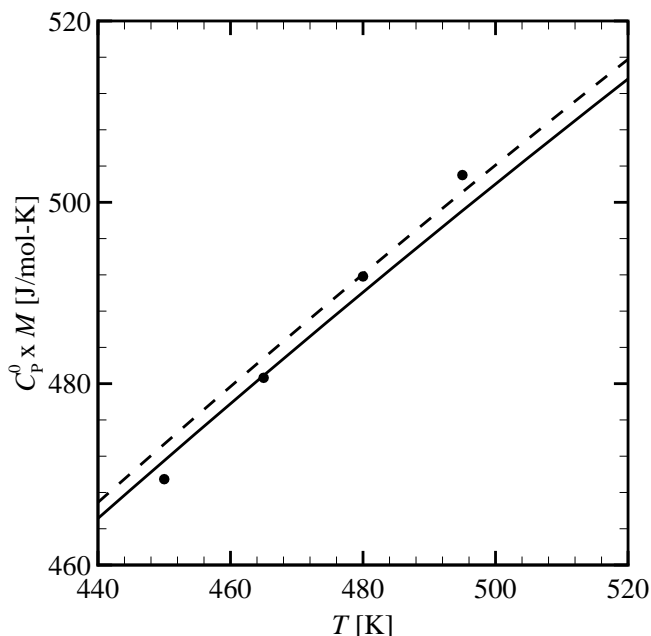


Figure 3.3: Experimental  $\bar{C}_p^0$  values for  $D_4$  (●) compared to *ab initio* values predicted by HF/6-31G(d) (solid line) and HF/6-31+G(d) (dashed line) calculations using the recommended FSF

### 3.3 Equations of state for selected linear and cyclic siloxanes

#### 3.3.1 Introduction

This section documents the development of short technical multiparameter EoS's for:

1. hexamethyldisiloxane (MM,  $[(CH_3)_3-Si-O_{1/2}]_2$ ),
2. octamethyltrisiloxane (MDM,  $[(CH_3)_3-Si-O_{1/2}]_2-[(CH_3)_2-Si-O]$ ),
3. decamethyltetrasiloxane (MD<sub>2</sub>M,  $[(CH_3)_3-Si-O_{1/2}]_2-[(CH_3)_2-Si-O]_2$ ),
4. dodecamethylpentasiloxane (MD<sub>3</sub>M,  $[(CH_3)_3-Si-O_{1/2}]_2-[(CH_3)_2-Si-O]_3$ ),
5. tetradecamethylhexasiloxane (MD<sub>4</sub>M,  $[(CH_3)_3-Si-O_{1/2}]_2-[(CH_3)_2-Si-O]_4$ ),

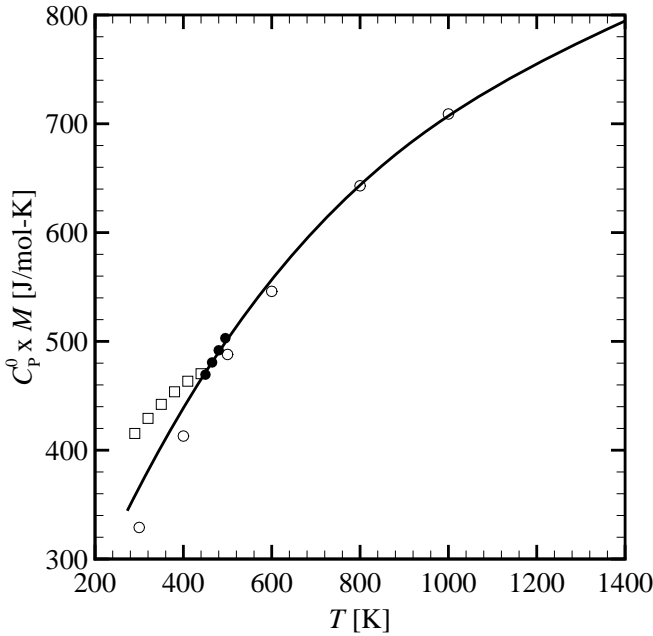


Figure 3.4: Comparison of experimental  $\bar{C}_P^0$  values for  $D_4$  (●) with those predicted with the Harrison-Seaton group contribution method (○), with Eq. (3.12) (□), and with HF/6-31G(d) (solid line).

6. octamethylcyclotetrasiloxane ( $D_4$ ,  $[(CH_3)_2-Si-O]_4$ ),
7. decamethylcyclopentasiloxane ( $D_5$ ,  $[(CH_3)_2-Si-O]_5$ ),
8. dodecamethylcyclohexasiloxane ( $D_6$ ,  $[(CH_3)_2-Si-O]_6$ ),

whereby, in order to be concise, only the development of the MDM EoS is discussed exhaustively.<sup>3</sup> To this purpose, the potentially very accurate Helmholtz-energy-based functional form developed by Span and Wagner [186, 187, 127] has been chosen, because it was determined from the simultaneous optimization of functional terms based on highly accurate sets of data for various fluids and fluid families. This is not the case for several other functional forms which are tailored to specific families of fluids, like the Starling EoS [189]. Secondly, the Span-Wagner functional form has qualitatively correct extrapolation behavior

<sup>3</sup>The reader is referred to Refs. [34, 33] documenting in detail the development of the EoSs for the other listed siloxanes.

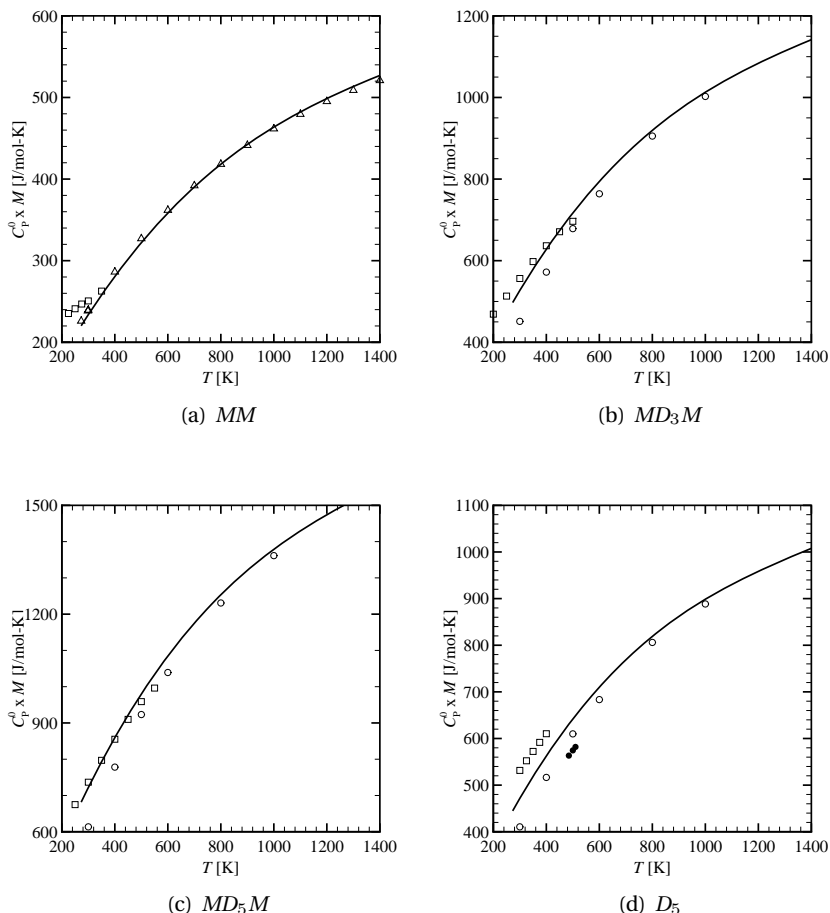


Figure 3.5: Comparison of  $\bar{C}_P^0$  values predicted with HF/6-31G(d) (solid line) calculations to those predicted using the Harrison-Seaton method ( $\circ$ ), Eq. (3.12) ( $\square$ ), experimental vibrational frequencies ( $\triangle$ ), and experimental measurements ( $\bullet$ ) for (a)  $MM$ , (b)  $MD_3M$ , (c)  $MD_5M$ , and (d)  $D_5$ .

outside the range where experimental data are available [187, 100]. The performance of EoS's in the 12-parameter Span-Wagner functional form is thoroughly discussed in quantitative terms in Ref. [186]. Thirdly, the Span-Wagner functional form uses a rather small set of substance-specific parameters, namely 12 (not considering the parameters of the ideal-gas heat capacity correlation). The 12-pSW FF therefore allows for fast and numerically stable computations of

thermodynamic data. Finally, as a last motivation, it is important to point out that the performance of these equations of state can easily be improved when in the future new information about the fluids becomes available.

This section is organized as follows: Sec. 3.3.2 presents a survey of available experimental data for MDM. Available data points have been assessed thoroughly for consistency and accuracy. Section 3.3.3 provides a review of the Span-Wagner functional form and presents the obtained substance-specific parameters for all the selected fluids mentioned in the previous paragraph. The performance of the established EoS for MDM is evaluated in Sec. 3.3.4.

### 3.3.2 Data survey – MDM, $[(\text{CH}_3)_3\text{-Si-O}_{1/2}]_2\text{-}[(\text{CH}_3)_2\text{-Si-O}]$

Available critical properties and relevant thermodynamic parameters of MDM, are listed in Table 3.9. The maximum difference among the reported critical pressures ( $P_C$ ) is 45 kPa (0.032 %); for the critical temperatures ( $T_C$ ), it is 2.5 K (0.004%) and for the critical specific volumes ( $\bar{v}_C$ ), it is 80 cm<sup>3</sup>/mol (0.097 %). The values of the critical temperature and density are possibly the most important data required for the development of EoS's having a fixed functional form. However, for all the siloxanes considered herein, critical density data are scarce; moreover, if experimental data for  $\rho_C$  are available, the uncertainty in the reported values is large. For this reason, in the optimization process, the critical specific volume has been left unconstrained, while the critical pressure and temperature in the case of MDM have been tightened to the experimental values reported by Lindley and Hershey [133]. These critical-point data have been preferred with respect to the data from other sources because Lindley and Hershey also report values for vapor-pressures and saturated vapor and liquid densities for states close to the critical point, namely at temperatures spanning the range 426 K up to the critical temperature, thus providing a region of coherently measured data. Remark that Lindley and Hershey do not indicate the absolute purity of their test samples, therefore it is difficult to assess if the critical properties are significantly influenced by impurities. In addition to the data listed in Table 3.9, another 260 experimental data have been found in the literature and are sorted by type in Table 3.10.

#### ★ Assessment of experimental vapor-pressures data

To assess the quality of the experimental vapor-pressures of MDM, the unweighted data are correlated with the Wagner-Ambrose [164] equation, i.e.,

$$P_R^{\text{sat}}(T_R) = \exp \left\{ \frac{\hat{a}(1 - T_R) + \hat{b}(1 - T_R)^{1.5} + \hat{c}(1 - T_R)^{2.5} + \hat{d}(1 - T_R)^5}{T_R} \right\}. \quad (3.13)$$

Table 3.9: Main thermodynamic property data for MDM available in literature. See also Ref. [172].

Property	Value <sup>3</sup>	Unit	$\sigma_u(Q)/Q$ [%] <sup>4</sup>	Source
$M$	236.53	kg/kmol	-	[102]
$P_C$	1415	kPa	0.5	[133]
	1420	kPa	3	[221] <sup>1</sup>
	1440	kPa	3	[69] <sup>1</sup>
	1460	kPa	1.3	[54]
$T_C$	562.9	K	3	[221] <sup>1,2</sup>
	564.1	K	0.02	[133]
	564.4	K	3	[69] <sup>1</sup>
	565.4	K	0.04	[54]
$\bar{v}_C$	828	cm <sup>3</sup> /mol	5	[54] <sup>1,2</sup>
	868	cm <sup>3</sup> /mol	5	[69] <sup>1</sup>
	882	cm <sup>3</sup> /mol	0.5	[133]
	908	cm <sup>3</sup> /mol	5	[140] <sup>1,2</sup>
$T_{BP}^5$	423.4	K	1	[191] <sup>1,2</sup>
	425.0	K	1	[98] <sup>1</sup>
	425.7	K	0.02	[133]
	425.7	K	0.02	[135]
	426.2	K	0.3	[159]
	425.7	K	0.03	[69] <sup>2</sup>
$T_{TP}^6$	187.2	K	1	[172] <sup>2</sup>
$\omega$	0.531	-	-	[133, 140] <sup>2</sup>
	0.533	-	-	[172] <sup>2</sup>

<sup>1</sup> The uncertainty was not indicated in the specified reference. The reported value is assigned by DIPPR® [172].

<sup>2</sup> The value of the property is computed in the specified reference.

<sup>3</sup> Pressures and temperatures have not been converted according to a particular standard, e.g., IPTS-90.

<sup>4</sup> Uncertainty in any thermodynamic property  $Q$ .

<sup>5</sup> Normal boiling point.

<sup>6</sup> Triple point temperature.

Here,  $\hat{a}$ ,  $\hat{b}$ ,  $\hat{c}$ , and  $\hat{d}$  are fluid-dependent parameters,  $P_R^{\text{sat}}$  is the reduced vapor-pressure, namely  $P^{\text{sat}}/P_C$  and  $T_R$  is the reduced temperature, i.e.,  $T/T_C$ . Figure 3.6 presents the experimental vapor-pressure data of MDM

Table 3.10: Available experimental thermodynamic data for MDM. See also Ref. [172].

Data type	Source	$T$ -range [K]	$P$ -range [kPa]	No. data points
$P^{\text{sat}}$	Stull [191]	280–424		10
	Lindley and Hershey [133]	322–564		74
	Wilcock [216]	339–425		3
	Skorokhodov et. al. [182]	344–417		7
	Flaningam [69]	346–437		12
	Voronkov et. al. [210]	423		1
	Voronkov et. al. [211]	423		1
	Waterman et. al. [213]	426		1
Thompson [203]	426		1	
$\rho^{\text{L}}$	Hurd [99]	273–353		5
	Lindley and Hershey [133]	426–564		26
$\rho^{\text{V}}$	Lindley and Hershey [133]	460–564		18
$P$ - $\rho$ - $T$	Waterman et. al. [213] <sup>2</sup>	293	101	1
	McLure et. al. [141] <sup>2</sup>	299–412	101	17
	Weissler [214] <sup>2</sup>	303	101	1
	Marcos et. al. [135] <sup>1</sup>	448–573	36–377	71
$\bar{B}$	Marcos et. al. [135] <sup>1</sup>	448–573		6
$c$	Waterman et. al. [213] <sup>2</sup>	293	101	1
	Weissler [214] <sup>2</sup>	303–323	101	2
$\kappa_T$	Weissler [214] <sup>3</sup>	303–323	101	2
	McLure et. al. [141]	303	101	1
$\kappa_s$	Weissler [214] <sup>3</sup>	303–323	101	2
$C_P$	McLure [139] <sup>3</sup>	303–323	101	2
$\beta_P$	McLure et. al. [141]	303	101	1

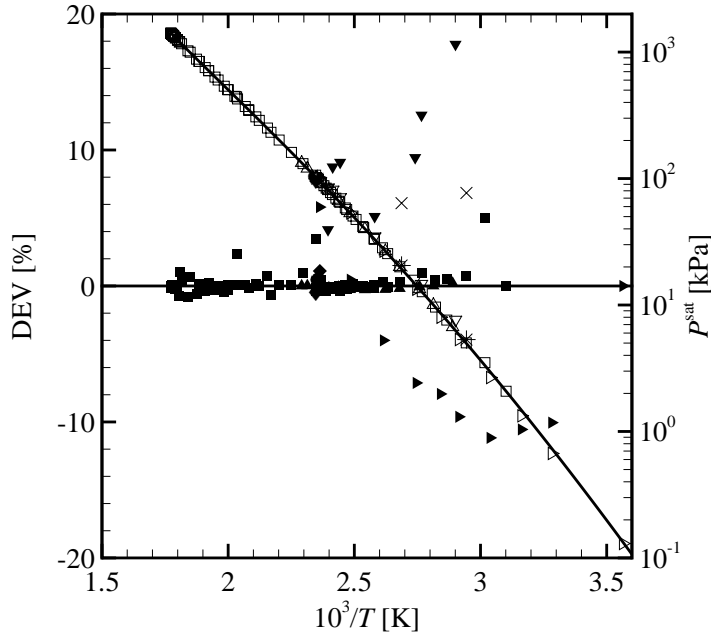
<sup>1</sup> (Superheated) vapor-phase data. Data were measured along 6 isotherms

<sup>2</sup> Sub-cooled liquid-phase data measured at 1 atm.

<sup>3</sup> Sub-cooled liquid-phase data derived from experimental values.

as a function of the inverse of the temperature. The deviations of the experimental data with respect to values determined from the correlated Wagner-Ambrose equation are also shown.

By inspecting the deviations of the experimental data with respect to values determined from the unweighted Wagner-Ambrose equation, the fol-



Data	DEV <sup>a</sup>	Source	Data	DEV	Source
□	■	Lindley and Hershey [133]	△	▲	Flaningam [69]
▽	▼	Skorokhodov et. al. [182]	▷	▶	Stull [191]
◁	◀	Voronkov et. al. [210]	◇	◆	Voronkov et. al. [211]
○	●	Thompson [203]	*	×	Wilcock [217]
♥	♦	Waterman et. al. [213]			

<sup>a</sup>The deviation is computed as  $DEV = 100 \cdot (P_{exp}^{sat} - P_{WA}^{sat}) / P_{exp}^{sat}$ , where superscript “sat” stands for saturated and subscripts “exp” and “WA” are the abbreviations for experimental, and Wagner-Ambrose [see Eq. (3.13)], respectively.

Figure 3.6: *Experimental vapor-pressure data for MDM as a function of the inverse of temperature. The unweighted data are correlated with the Wagner-Ambrose vapor-pressure equation [see Eq. (3.13)]. In addition, the deviations between the experimental data with respect to values computed from Eq. (3.13) are shown.*

lowing is observed: i) all of Flaningam’s experimental data [69] are represented within 0.3 %; ii) apart from three randomly located experimental points, all data from Ref. [133] have absolute deviations of less than

Table 3.11: Parameters  $\hat{a}$ – $\hat{d}$  of the Wagner-Ambrose vapor-pressure equation. These parameters were computed by fitting Eq (3.13) to critical properties from Table 3.15 and selected data sets. Results are only reported for MDM; parameters for the other siloxanes are presented in Refs. [34, 33].

Fluid name	$\hat{a}$	$\hat{b}$	$\hat{c}$	$\hat{d}$
MDM	-8.6693	2.2965	-4.4658	-8.4529

1 %; moreover, these deviations are randomly distributed around zero; iii) the deviations of data reported by Skorokhodov et. al. [182] progressively decrease starting from 18 % at the lowest temperature of measurement, viz. 344.7 K, to about 4 % at the highest experimental temperature, viz. 417.4 K. The average absolute deviation (AAD) of the data with respect to computed values is 9.5 %. Furthermore, all the values reported by Skorokhodov et. al. are greater than values computed from the correlated vapor-pressure equation; iv) the data reported by Stull do not display a peculiar trend and have an AAD of 6.7 %. The trend observed in the deviations of the data from Skorokhodov and coworkers [182] with respect to values obtained from the correlated Wagner-Ambrose equation may indicate that the data reported in the afore mentioned source contain a systematic error, possibly due to the presence of volatile impurities. Remark that the vapor-pressures reported in Refs. [191, 182] are very low, namely  $\sim 10$  kPa and are difficult to measure. Table 3.11 reports parameters  $\hat{a}$ – $\hat{d}$  obtained for the correlated Wagner-Ambrose equation. Using these fluid-dependent parameters, the selected data can be represented within 0.4 %. Based on these observations and using the same reasoning for vapor-pressure data contained in other sources listed in Table 3.10, it was decided that for the substance-specific-parameters optimization, only data reported by Flaningam and Lindley and Hershey should be used.

★ Assessment of experimental  $P$ - $\rho$ - $T$ -data for MDM

In Ref. [135], Marcos and coworkers report experimental vapor-phase  $P$ - $\rho$ - $T$  data of MDM for six isotherms. These data have compressibility factors in the range  $0.97 < Z < 1$ . Each isotherm is plotted in the  $P$ - $\rho$  diagram shown in Fig. 3.7 and is correlated with a second-order polynomial function which is constrained at the origin. This corresponds to fitting the data to the virial EoS up to the second density virial coefficient. Since all the data can be represented on average within 0.2 % by the polynomial function, it was decided to include all data points in the substance-specific-parameters optimization. The second density virial coefficient  $\bar{B}$  for each

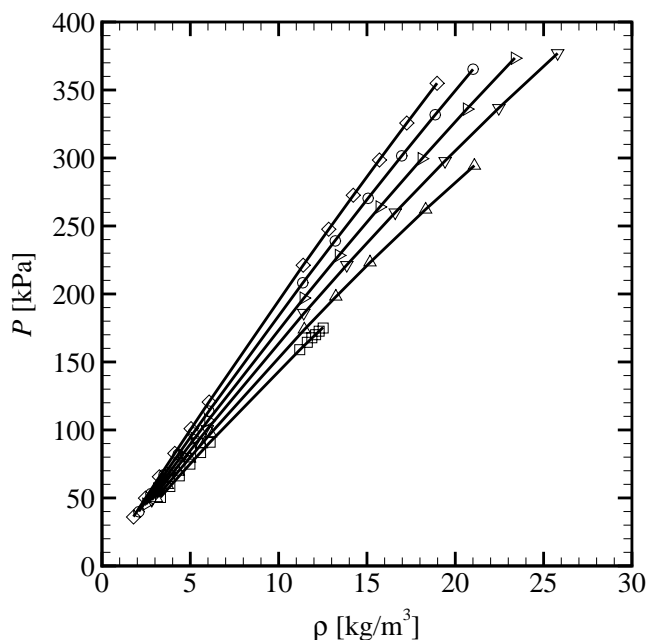


Figure 3.7: Isotherms in the vapor phase for MDM, experimentally determined from Marcos et. al. [135]. The data are correlated with second-order polynomial functions. The symbols indicate experimental data at the following temperatures:  $\square$ :  $T = 448.11$  K,  $\triangle$ :  $T = 473.11$  K,  $\nabla$ :  $T = 498.11$  K,  $\triangleright$ :  $T = 523.11$  K,  $\circ$ :  $T = 548.11$  K, and  $\diamond$ :  $T = 573.11$  K (these temperatures have been converted from ITS-68 to ITS-90).

isotherm is also obtained from all these data. These  $\bar{B}$  values are reported in Table 3.12. The second density virials are also reported by Marcos et. al. and they are based on a statistical F-test with a 95 % confidence level. The F-test was used to eliminate some of the highest pressure points until a quadratic fit with respect to density was satisfactory. The second density virials in Table 3.12 agree within  $0.03 \text{ m}^3/\text{kmol}$ , i.e., 2.8 %, with respect to the second density virials from Ref. [135].

$P$ - $\rho$ - $T$  data of MDM in the sub-cooled liquid phase are reported by Watterman et. al. [213], McLure et. al. [141], and Weissler [214]. Because all measurements were conducted at 1 atm., the data are plotted in the  $\rho$ - $T$ -plane in Fig. 3.8 and are fitted to a second-order polynomial function. This is a sufficient approximation of the correct exponential dependence,

Table 3.12: The second density virial coefficient  $\bar{B}$  for MDM. The temperatures have been converted from ITS-68 to ITS-90.

$T$ [K]	$\bar{B}$ [m <sup>3</sup> /kmol]	$T$ [K]	$\bar{B}$ [m <sup>3</sup> /kmol]	$T$ [K]	$\bar{B}$ [m <sup>3</sup> /kmol]
448.11	-2.03	498.11	-1.53	548.11	-1.17
473.11	-1.78	523.11	-1.35	573.11	-1.09

$\exp [f(T)]$ , with  $f(T)$  a smooth function of temperature, obtained from the definition of the coefficient of volume expansion. Figure 3.8 also contains data for fluids MD<sub>2</sub>M and MD<sub>3</sub>M and thus shows consistency of the experimental data for all the three fluids and the correct trend within the family. Based on the observations it was decided to use all data reported by Waterman et. al. [213], McLure et. al. [141], and Weissler [214].

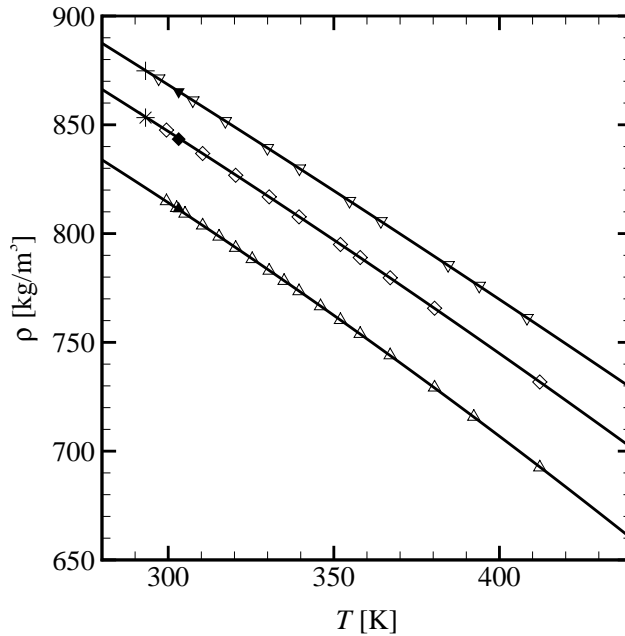
Table 3.10 lists some other derived properties reported in the previously mentioned references, namely the liquid-phase thermal properties  $\kappa_T$  (the isothermal compressibility) and  $\beta_P$  (the coefficient of volume expansion), and the caloric properties  $\kappa_s$  (the isentropic compressibility) and speed of sound, which were not used in the substance-specific-parameters optimization. These data are however considered in the evaluation of the performance of the EoS, as documented in Sec. 3.3.4.

★ Assessment of experimental saturated liquid density data for MDM

Only two sources reporting experimentally determined saturated liquid densities of MDM were found. The first set of data are reported in Ref. [99] at temperatures from about 273 K to about 353 K. More recent data at temperatures in the range 460 K to 564 K ( $T_C$ ) are reported in Ref. [133]. The equation proposed by Daubert et. al. [51] is used to further investigate the reported values. The Daubert equation can be written as

$$\rho^L = \frac{\hat{A}}{\hat{B} \left[ 1 + (1 - T/\hat{C})^{\hat{D}} \right]}, \tag{3.14}$$

where  $\rho^L$  is the saturated liquid density and  $\hat{A}$ ,  $\hat{B}$ ,  $\hat{C}$ , and  $\hat{D}$  are adjustable parameters which are obtained by fitting the functional form to the available experimental data. As initial guesses for the fitting procedure,  $\hat{C}$  is set equal to the critical temperature, and  $\hat{A}$ ,  $\hat{B}$ , and  $\hat{D}$  are set to  $P_C \cdot M/\bar{R}T_C$ , the critical compressibility factor  $Z_C$ , and 2/7, respectively. The universal gas constant  $\bar{R} = 8314.472$  J/mol-K [149]; this value is used throughout this study. Figure 3.9 shows the experimental data from Refs. [133, 99]



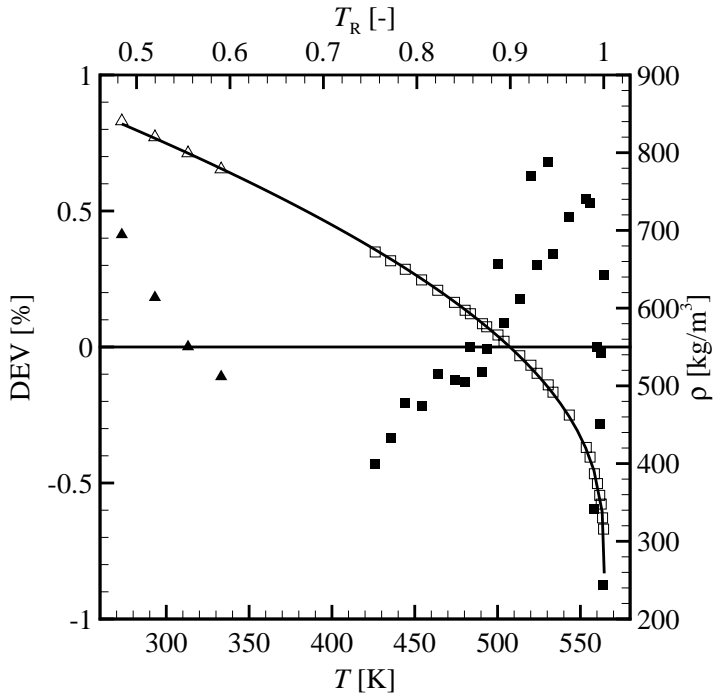
Data	Fluid	Source	Data	Fluid	Source
△	MDM	McLure et. al. [141]	*	MD <sub>2</sub> M	Waterman et. al. [213]
▲	MDM	Weissler [214]	▽	MD <sub>3</sub> M	McLure et. al. [141]
◇	MD <sub>2</sub> M	McLure et. al. [141]	▼	MD <sub>3</sub> M	Weissler [214]
◆	MD <sub>2</sub> M	Weissler [214]	+	MD <sub>3</sub> M	Waterman et. al. [213]

Figure 3.8: *Isobaric sub-cooled liquid-density data for MDM, MD<sub>2</sub>M, and MD<sub>3</sub>M as a function of temperature. All measurements were conducted at atmospheric pressure.*

and the deviations between the data and the correlated Daubert equation. Because all data points could be represented within 1 %, all points were selected for determining the parameters of the Span-Wagner functional form.

★ Assessment of experimental saturated vapor density data for MDM

Lindley and Hershey report 18 saturated vapor densities for temperatures between 460 K and 564 K ( $T_C$ ). These data are assessed by means of the Peng-Robinson, Stryjek-Vera modified, cubic EoS since it is known that



Data	DEV <sup>a</sup>	Source	Data	DEV	Source
□	■	Lindley and Hershey [133]	△	▲	Hurd [99]

<sup>a</sup>The deviation is computed as  $DEV = 100 \cdot (\rho_{exp}^L - \rho_D^L) / \rho_{exp}^L$ , where superscript “L” refers to saturated liquid and subscripts “exp” and “D” are the abbreviations for experimental and Daubert [see Eq. (3.14)], respectively.

Figure 3.9: Experimental saturated liquid-density data of MDM as a function of temperature (see also Ref. [172]). The data are correlated with the equation proposed by Daubert et. al. [51]. Additionally, the deviations between the experimental data and those obtained from the correlated Daubert et. al. equation are shown.

the PRSV EoS can be used to accurately predict vapor densities for reduced pressures  $P_R$  below 0.9 [1]. Using the selected critical properties and the acentric factor from Ref. [133], the average absolute deviation between predictions from the PRSV EoS and experimental data is 1.7 %. Figure 3.10 shows the deviations of experimental saturated vapor densities of MDM with respect to values computed from the PRSV EoS. The deviations are acceptable from a technical perspective and therefore, all data were selected for the parameters optimization.

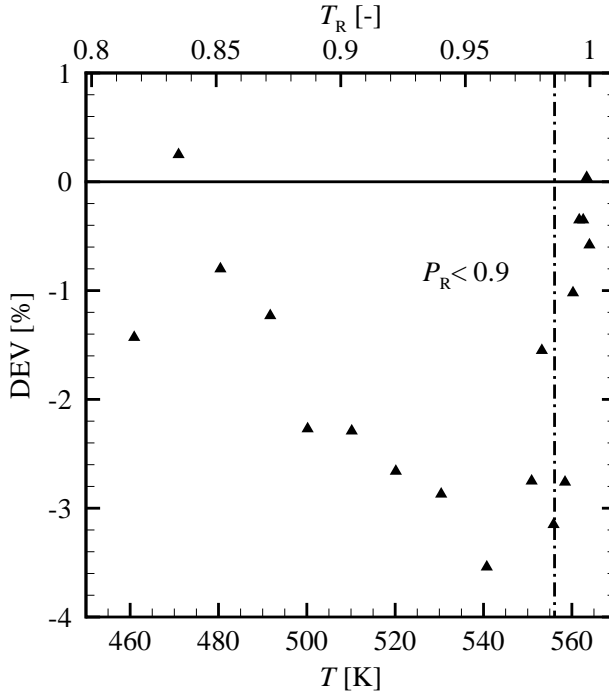


Figure 3.10: The deviations between the experimental saturated vapor densities of MDM from Ref. [133] and values obtained from the correlated PRSV EoS. The deviation is computed as  $DEV = 100 \cdot (\rho_{\text{exp}}^V - \rho_{\text{calc}}^V) / \rho_{\text{exp}}^V$ , where superscript “V” refers to saturated vapor and subscripts “exp” and “calc” are respectively, the abbreviations for experimental and calculated.

### 3.3.3 Substance-specific parameters for the equations of state

The functional form developed by Span and Wagner is expressed in terms of the reduced Helmholtz free energy,  $\Psi(T, \rho) / RT$  as a function of the reduced density,  $\delta \equiv \rho / \rho_C$ , and the inverse of the reduced temperature,  $\tau \equiv T_C / T$ . To take real-gas behavior into account, the Helmholtz free energy is decomposed in a term describing the ideal-gas contribution and a residual term, i.e.,

$$\frac{\Psi(T, \rho)}{RT} = \psi^0(\tau, \delta) + \psi^R(\tau, \delta), \quad (3.15)$$

where  $\psi^0$  and  $\psi^R$  represent the reduced ideal-gas and residual Helmholtz free energy, respectively. The ideal-gas Helmholtz free energy solely depends on the

isobaric heat capacity in the ideal-gas state, i.e.,  $\bar{C}_P^0$ , and is obtained from

$$\psi^0(\tau, \delta) = \frac{\bar{h}_0^0 \tau}{\bar{R} T_C} - \frac{\bar{s}_0^0}{\bar{R}} - 1 + \ln \left( \frac{\tau_0 \delta}{\delta_0 \tau} \right) - \frac{\tau}{\bar{R}} \int_{\tau_0}^{\tau} \frac{\bar{C}_P^0}{\tau^2} d\tau + \frac{1}{\bar{R}} \int_{\tau_0}^{\tau} \frac{\bar{C}_P^0}{\tau} d\tau \quad (3.16)$$

In Eq. (3.16),  $\delta_0 = \rho_0/\rho_C$  and  $\tau_0 = T_C/T_0$  are the reduced density and the inverse of the reduced temperature at a pre-defined or prescribed reference state  $(T_0, \rho_0)$ . Usually the reference state is prescribed in terms of  $T_0$  and  $P_0 = P(T_0, \rho_0)$ . Parameters  $\bar{h}_0^0$  and  $\bar{s}_0^0$  denote the ideal-gas enthalpy and entropy at  $(T_0, P_0)$ , and are chosen according to a common convention in industry or recommendations of, e.g., the International Institute of Refrigeration (IIR) or the International Union of Pure and Applied Chemistry (IUPAC) [127]. For hydrocarbons for example,  $\bar{h}_0^0$  and  $\bar{s}_0^0$  are chosen such that the enthalpy  $\bar{h}$  and entropy  $\bar{s}$  for the saturated liquid-phase at the normal boiling point are zero. This option is adopted in this work.

The reduced residual Helmholtz free energy for nonpolar and weakly polar fluids, i.e., the 12-pSW FE, is given by

$$\begin{aligned} \psi^R(\tau, \delta) = & n_1 \delta \tau^{0.250} & + & n_2 \delta \tau^{1.125} & + & n_3 \delta \tau^{1.500} \\ & + n_4 \delta^2 \tau^{1.375} & + & n_5 \delta^3 \tau^{0.250} & + & n_6 \delta^7 \tau^{0.875} \\ & + n_7 \delta^2 \tau^{0.625} e^{-\delta} & + & n_8 \delta^5 \tau^{1.750} e^{-\delta} & + & n_9 \delta \tau^{3.625} e^{-\delta^2} \\ & + n_{10} \delta^4 \tau^{3.625} e^{-\delta^2} & + & n_{11} \delta^3 \tau^{14.5} e^{-\delta^3} & + & n_{12} \delta^4 \tau^{12.0} e^{-\delta^3}, \end{aligned} \quad (3.17)$$

where  $n_1, \dots, n_{12}$  are substance-specific parameters. Equation (3.17) was developed by fitting a functional form, initially containing 583 terms, to high-accuracy experimental/reference data of various fluids of a certain group, in this case, nonpolar and weakly polar substances. Using a multi-property optimization algorithm that considered data of various fluids simultaneously, a 12-parameter equation, Eq. (3.17), was established, which provided the best functional form if applied to the considered data and fluids on which the EoS was based. Equation (3.17) is a fundamental equation – and consequently all thermodynamic properties can be computed from combinations of the Helmholtz free energy and its first and higher-order derivatives with respect to density and temperature.

The Aly-Lee equation [3],

$$\bar{C}_P^0(T) = \hat{\alpha} + \hat{\gamma} \left[ \frac{\hat{\chi}/T}{\sinh(\hat{\chi}/T)} \right]^2 + \hat{\varrho} \left[ \frac{\hat{\epsilon}/T}{\cosh(\hat{\epsilon}/T)} \right]^2, \quad (3.18)$$

was used to compute the reduced ideal-gas Helmholtz free energy. Parameters  $\hat{\alpha}$ - $\hat{\chi}$  were determined by fitting Eq. (3.18) to data reported in Table 3.7. The ideal-gas isobaric heat capacity correlation should be used for temperatures between 273 K and 673 K. The upper bound for the temperature range is approximately given by the decomposition temperature of the fluid in stainless steel, which is of practical interest.

Table 3.13: Parameters  $\hat{\alpha}$ - $\hat{\chi}$  of the Aly-Lee ideal-gas isobaric heat capacity correlation [see Eq. (3.18)]. The range of validity is for temperatures between 273 K and 673 K.

Fluid	$\hat{\alpha}$ [J/mol-K]	$\hat{\gamma}$ [J/mol-K]	$\hat{\chi}$ [K]	$\hat{\rho}$ [J/mol-K]	$\hat{\epsilon}$ [K]
MM	188.3	450.8	1770.6	292.6	774.0
MDM	275.1	612.9	1829.6	413.0	802.6
MD <sub>2</sub> M	331.9	777.1	1813.8	521.4	795.1
MD <sub>3</sub> M	463.2	957.2	2117.1	738.3	908.5
MD <sub>4</sub> M	508.6	1109.6	1778.2	752.9	776.5
MD <sub>5</sub> M	585.2	1274.8	1759.7	860.8	768.4
D <sub>4</sub>	292.7	657.0	1749.3	453.1	764.7
D <sub>5</sub>	377.2	821.7	1725.5	562.2	754.6
D <sub>6</sub>	468.7	981.2	1792.1	686.7	786.8

The calculation of the 12 parameters in Eq. (3.17) for a given substance is a nonlinear, multiparameter, constrained regression problem. The objective function is the weighted sum of the square of the deviations between selected thermodynamic data and values calculated with the equation of state. The overall accuracy of the obtained EoS depends on the accuracy of the experimental data that are used for its development. This requires that experimental data are assigned a weight, since accurate data should contribute more to the objective function than less accurate data. Consequently, experimental data with uncertainties larger than required should be discarded or should be weighted with their experimental or estimated uncertainties, and highly accurate data should be assigned a weight based on the required uncertainty of the EoS. For substances for which no (reliable) data are available in the critical region, two estimated experimental saturated points with low weights can be included in the regression process. Since the critical temperature is usually the most reliable critical property, Span and Wagner [186] propose

$$\begin{aligned}\rho^V &= 0.9 \cdot \rho_C, T = 0.9998 \cdot T_C \\ \rho^L &= 1.1 \cdot \rho_C, T = 0.9998 \cdot T_C.\end{aligned}$$

as good estimates. With these two points together with the experimental or estimated values for all three critical properties, the optimization procedure can be started. The computational procedure is not deterministic and requires a certain amount of judgement and trials. A well established program for multi-property fitting developed at NIST [127, 128] was used for the calculation of the parameters of the selected siloxanes.

Table 3.14 gives the 12 parameters of the siloxanes considered in this work.

Table 3.14: Parameters  $n_1, \dots, n_{12}$  in Eq. (3.17) for the selected fluids.

$i$	MDM	MD <sub>2</sub> M	MD <sub>3</sub> M	D <sub>6</sub>
1	1.1973537	1.3384033	1.2054039	1.6915619
2	-2.4038062	-2.6293939	-2.4291480	-3.3796257
3	0.3256564	0.4398383	0.6901643	0.3860904
4	-0.1997126	-0.5349672	-0.6926804	0.6459900·10 <sup>-1</sup>
5	0.1120628	0.1818844	0.1850605	0.1058901
6	0.1589400·10 <sup>-3</sup>	0.4077461·10 <sup>-3</sup>	0.3116144·10 <sup>-3</sup>	0.4545683·10 <sup>-4</sup>
7	0.5123432	1.1344451	0.9986252	0.7416928
8	-0.2066036·10 <sup>-1</sup>	0.5774631·10 <sup>-1</sup>	0.7422903·10 <sup>-1</sup>	-0.8810265·10 <sup>-1</sup>
9	-0.3897811	-0.5917498	-0.8025914	-0.1737334
10	-0.1186931	-0.1102023	-0.2086534	-0.1095137
11	-0.3720354·10 <sup>-1</sup>	-0.3494264·10 <sup>-1</sup>	-0.3646179·10 <sup>-1</sup>	-0.6269570·10 <sup>-1</sup>
12	0.1835998·10 <sup>-1</sup>	0.7646298·10 <sup>-2</sup>	0.1917405·10 <sup>-1</sup>	0.3745999·10 <sup>-1</sup>
$i$	MM	MD <sub>4</sub> M	D <sub>4</sub>	D <sub>5</sub>
1	1.0168601	1.1849242	1.0539241	1.4084473
2	-2.1971303	-1.8746564	-2.2298192	-2.2924804
3	0.7544319	-0.6571351·10 <sup>-1</sup>	0.7757392	0.4285161
4	-0.6800343	-0.6181269	-0.6937405	-0.7350638
5	0.1908216	0.1953580	0.1872156	0.1610381
6	0.1053013·10 <sup>-2</sup>	0.5067874·10 <sup>-3</sup>	0.4219333·10 <sup>-3</sup>	0.2964328·10 <sup>-3</sup>
7	0.6284595	1.2354408	0.7030184	0.8241248
8	0.3090304·10 <sup>-1</sup>	0.4946271·10 <sup>-1</sup>	0.4785189·10 <sup>-1</sup>	0.1521427
9	-0.8394873	-0.7368528	-0.8025348	-0.6849589
10	-0.2026238	-0.1999144	-0.1896887	-0.5570362·10 <sup>-1</sup>
11	-0.3513160·10 <sup>-1</sup>	-0.5511867·10 <sup>-1</sup>	-0.2221178·10 <sup>-1</sup>	0.1305539·10 <sup>-1</sup>
12	0.2590234·10 <sup>-1</sup>	0.28325890·10 <sup>-1</sup>	0.6010335·10 <sup>-2</sup>	-0.3185376·10 <sup>-1</sup>

The critical specific density and the critical temperature that are used for computing  $\delta$  and  $\tau$  are given in Table 3.15. The reference state where enthalpy and entropy are zero is the saturated liquid phase at the normal boiling point, which is also reported in Table 3.15.

### 3.3.4 Performance evaluation of the equation of state – MDM, [(CH<sub>3</sub>)<sub>3</sub>-Si-O<sub>1/2</sub>]<sub>2</sub>-[(CH<sub>3</sub>)<sub>2</sub>-Si-O] as an example

For an evaluation of the performance of the newly developed EoS's, predictions of various thermodynamic properties are compared with selected experimental data. The evaluated thermodynamic properties include vapor pressures, satu-

Table 3.15: Fixed parameters for the selected siloxanes.

Fluid	$M$ [kg/kmol]	$\omega$ [-]	$T_{BP}$ [K]	$T_C$ [K]	$P_C$ [kPa]	$v_C$ [dm <sup>3</sup> /kg]
MM	162.378	0.4176	373.40	518.70	1939	3.285
MDM	236.531	0.5297	425.68	564.09	1415	3.895
MD <sub>2</sub> M	310.685	0.6680	467.50	599.40	1227	3.519
MD <sub>3</sub> M	384.839	0.7218	503.03	628.36	945	3.789
MD <sub>4</sub> M	459.000	0.8249	532.72	653.20	877	3.501
D <sub>4</sub>	296.618	0.5926	448.50	586.49	1332	3.257
D <sub>5</sub>	370.773	0.6583	484.05	619.23	1161	3.418
D <sub>6</sub>	444.924	0.7361	518.14	645.78	961	3.583

rated liquid and vapor densities, densities in the sub-cooled liquid phase and superheated vapor phase, and selected caloric properties, e.g., sub-cooled liquid speed of sound, second density virials, etc.

Figures 3.11 and 3.12 show the  $P$ - $v$  and  $T$ - $s$  diagrams for MDM, respectively. The diagrams demonstrate the capability and consistency of the EoS regarding the computation of technically relevant thermodynamic properties. Note that due to the molecular complexity of siloxanes, the  $T$ - $s$  diagram exhibits retrograde behavior. For such substances the vapor remains dry upon expansion from saturated-vapor conditions, except for a small thermodynamic region close to the critical point (and, for some fluids, at very low pressures).

Figure 3.11 also contains the vapor-liquid equilibrium region and various isotherms computed with the PRSV EoS using the  $k_1$  value of 0.12634. As expected, the deviations of predictions of saturated liquid specific volumes from the PRSV EoS with respect to values computed from the multiparameter EoS of MDM progressively increase as the pressure increases; in fact at  $P_R = 0.5$ , the deviation is already greater than 5%. On the vapor side, the predictions of  $P$ - $\rho$ - $T$  data using the PRSV EoS are nearly superimposed over the predictions of the same data using the multiparameter EoS. However, the PRSV EoS cannot represent the flat curvature of the saturation line close to the critical point and it must be remarked that the new multiparameter EoS for MDM is also not intended for high accuracy in the critical region.

Table 3.16 gives a summary of the performance of the established EoS in the 12-pSW FF for MDM. The performance is indicated by means of the percentage average absolute deviation (AAD) of experimental data with respect to values computed from the EoS, i.e.,

$$\text{AAD} = \frac{100}{N} \cdot \sum_{i=1}^N (Q_{\text{exp},i} - Q_{\text{calc},i}) / Q_{\text{exp},i}, \quad (3.19)$$

where  $Q$  represents any thermodynamic property, and  $N$  is the total number of used data points.

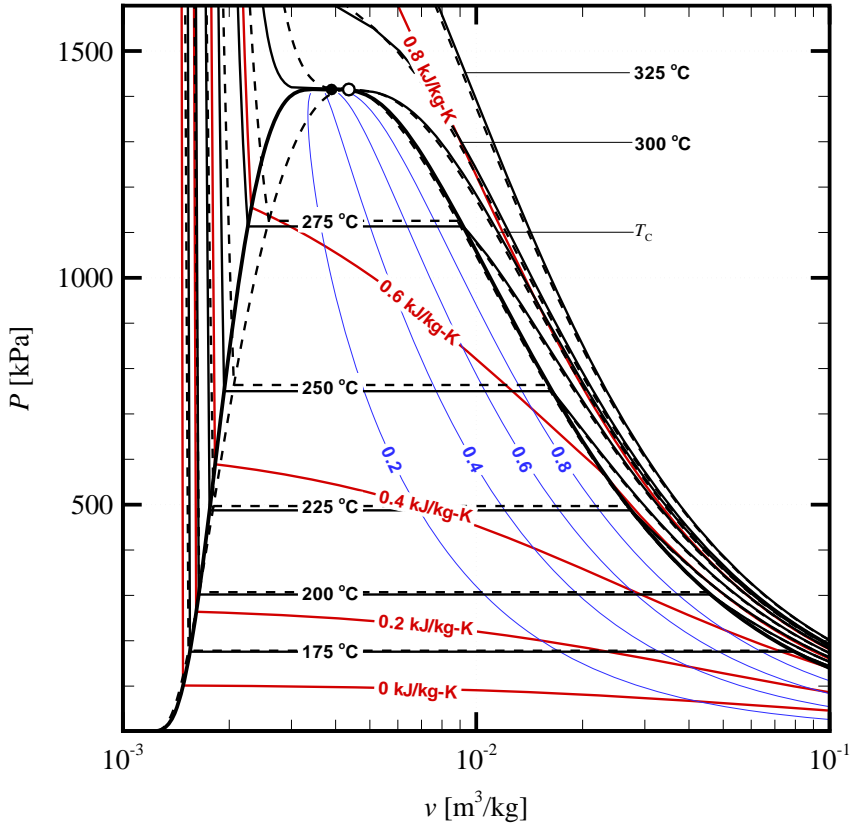


Figure 3.11: The  $P$ - $v$ -diagram of octamethyltrisiloxane ( $[(\text{CH}_3)_3\text{-Si-O}_{1/2}]_2\text{-[O-Si-(CH}_3)_2]$ , MDM) showing the coexistence region and several isotherms (black lines), isentropes (red lines) and iso-quality lines (blue lines), some of which have been labeled. Additionally, this diagram shows the difference between the prediction of thermal properties from the Peng-Robinson, Stryjek-Vera modified EoS (dashed lines) and those of the established EoS in the Span-Wagner functional form (continuous lines). ●: critical point from the Span-Wagner functional form; ○: critical point from the PRSV EoS.

- **Critical specific volume:**

The critical specific volume of MDM was determined simultaneously with

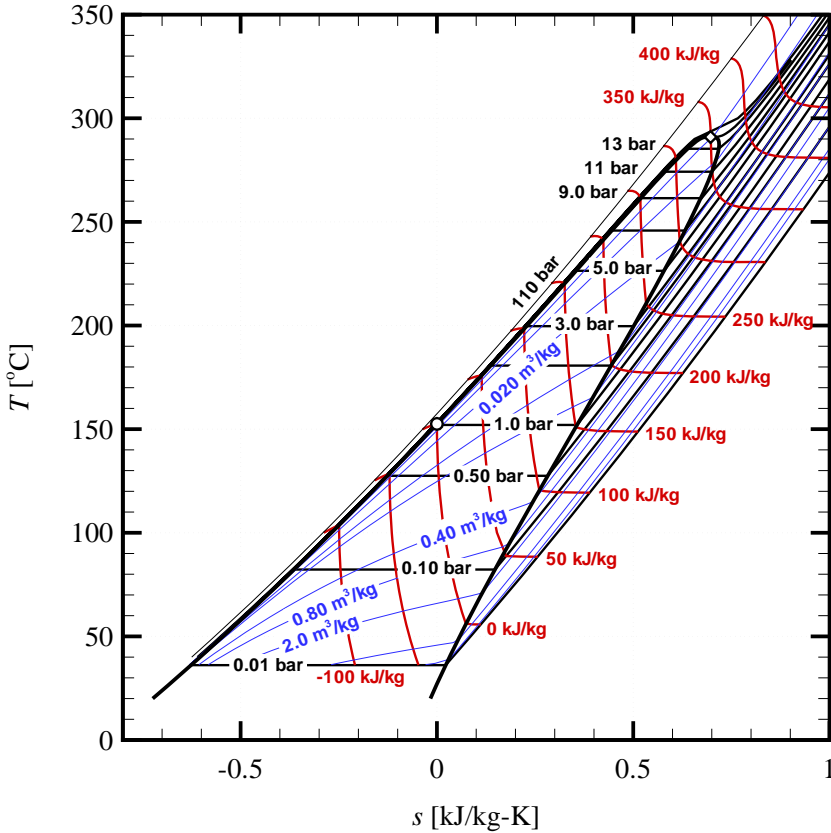


Figure 3.12: The  $T$ - $s$ -diagram of octamethyltrisiloxane ( $[(\text{CH}_3)_3\text{-Si-O}_{1/2}]_2\text{-[O-Si-(CH}_3)_2]$ , MDM) showing isobars (black lines), isenthalps (red lines) and isochors (blue lines). Thermodynamic properties are obtained from the established equation of state. ○: at the saturated liquid state corresponding to the normal boiling point,  $h = 0$  kJ/kg and  $s = 0$  kJ/kg-K, ◇: critical point from the Span-Wagner functional form.

the EoS parameters. For MDM, the value of  $v_C$  obtained from the EoS is  $3.895 \text{ dm}^3/\text{kg}$  ( $= 921 \text{ cm}^3/\text{mol}$ ). This value is greater than all critical specific volume data reported in Table 3.9. Taking the uncertainty in the experimental  $v_C$  data into account, the deviation between the EoS critical

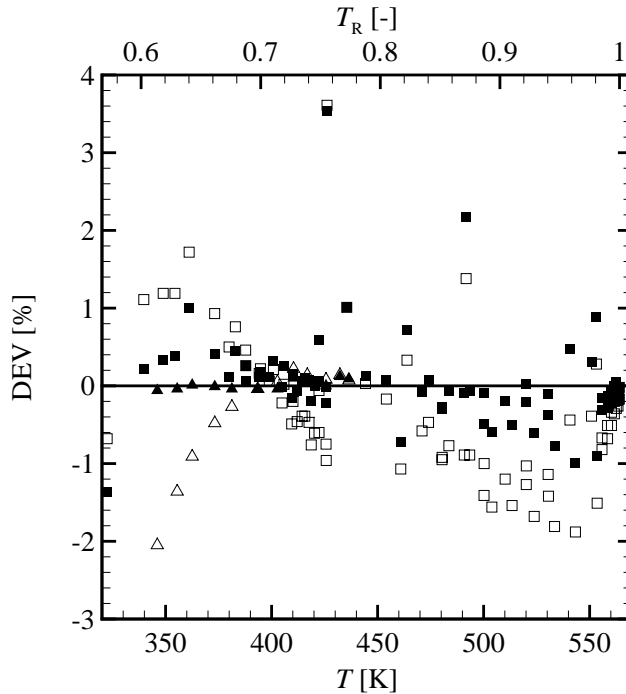
Table 3.16: Summary of comparisons between experimental data sets used for the development of the new EoS for MDM and calculated values.

Source	No. of data points	<i>P</i> and <i>T</i> range		AAD (%)	
		<i>T</i> [K]	<i>P</i> [kPa]	Gas / Liq.	Sat.
<b>Saturated Liquid Densities</b>					
Lindley and Hershey [133]	26	426-564	-	-	0.42
Hurd [99]	5	273-353	-	-	0.15
<b>Saturated Vapor Densities</b>					
Lindley and Hershey [133]	18	460-564	-	-	0.87
<b>Vapor pressure</b>					
Lindley and Hershey [133]	74	322-564	-	-	0.41
Flaningam [69]	12	346-437	-	-	0.06
<b><i>P</i>-<math>\rho</math>-<i>T</i> Data</b>					
McLure et. al. [141]	17	299-412	101	0.01	-
Weissler [214]	1	303	101	0.03	-
Waterman et. al. [213]	1	293	101	0.23	-
Marcos et. al. [135]	71	448-573	36-377	0.67	-
<b>Speeds of Sound</b>					
Weissler [214]	2	303-323	101	11.8	-
Waterman et. al. [213]	1	293	101	12.5	-
<b>Isobaric Heat Capacity</b>					
McLure [139]	2	303-323	101	2.55	-
<b>Liquid Coefficient of Volume Expansion</b>					
McLure et. al. [141]	1	303	101	0.33	-
Hurd [99]	1	303	101	1.19	-
<b>Second Density Virial Coefficient</b>					
Marcos et. al. [135]	6	448-573	-	6.05	-

specific volume and the median value of the experimental  $v_C$ 's is 5.5 %.

- **Vapor pressures:**

In addition to the newly developed EoS in the Span-Wagner functional form, the performance of the PRSV EoS regarding vapor-pressure predictions is also assessed. It can be observed that the PRSV EoS is able to represent the experimental data of Flaningam [69] and Lindley and Hershey [133] with an AAD of, respectively 0.54 % and 1.08 %, whereas the SW multiparameter EoS is capable of representing these data with an AAD of 0.06 % and 0.41 %, respectively. Remark that both EoS's provide sufficient



SW	PRSV	Source	SW	PRSV	Source
■	□	Lindley and Hershey [133]	▲	△	Flaningam [69]

Figure 3.13: Percentage deviations between predicted and selected experimental vapor-pressure data for MDM. The deviation is defined as  $DEV = 100 \cdot (P_{exp}^{sat} - P_{calc}^{sat}) / P_{exp}^{sat}$ .

accuracy regarding the prediction of vapor pressures, at least for the reduced temperature in the range 0.58–1.0, see Fig. 3.13.

- **Saturated vapor densities:**

Nearly all experimental data from Ref. [133] have a deviation of less than 2 % with respect to predictions of saturated vapor densities from the new multiparameter EoS (refer to Fig. 3.14). The largest deviations are observed near the critical point. The performance of the EoS in the Span-Wagner functional form is superior to that of the PRSV EoS, since the multiparameter EoS can predict saturated vapor densities with an AAD of 0.87 %, whereas the AAD of experimental data with respect to values computed from the PRSV EoS is around 2.4 %.

- **Saturated liquid densities:**

On average, the multiparameter EoS can represent the experimental data of Hurd [99], and Lindley and Hershey [133] with an average absolute deviation of 0.15 % and 0.42 %, respectively. The AAD between experimental data and predicted values for the PRSV EoS, is much greater than for the multiparameter EoS, because the PRSV EoS cannot adequately represent the bubble-line (see also Fig. 3.11). For  $T_R > 0.9$  the deviation between experimental data and values computed from the PRSV EoS increases to figures significantly in excess of 5 %. The deviations of experimental saturated liquid densities, reported by Hurd and Lindley and Hershey, with respect to values determined from the new multiparameter EoS are presented in Fig. 3.15.

- **Sub-cooled liquid densities:**

The sub-cooled liquid density data reported by McLure and coworkers [141], Waterman et. al. [213] and Weissler [214] are represented by the

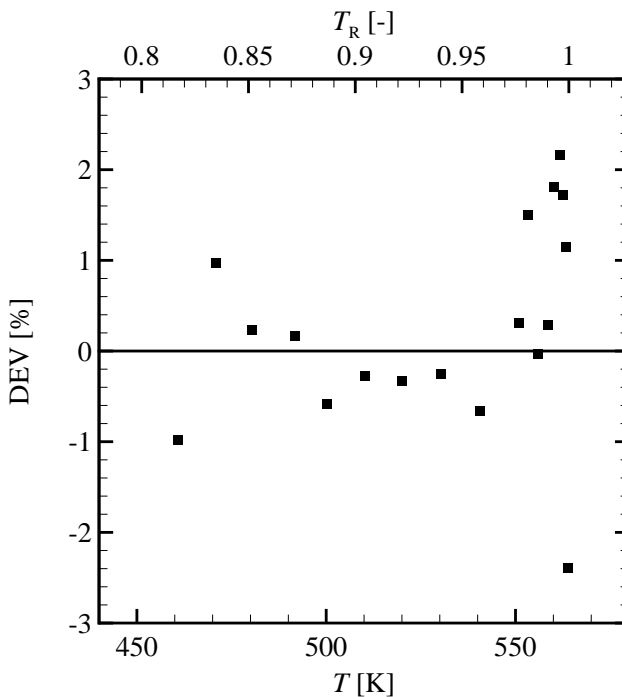


Figure 3.14: Percentage deviations between predicted and experimental saturated vapor-density data of MDM from Lindley and Hershey [133]. The deviation is defined as  $DEV = 100 \cdot (\rho_{exp}^V - \rho_{calc}^V) / \rho_{exp}^V$ .

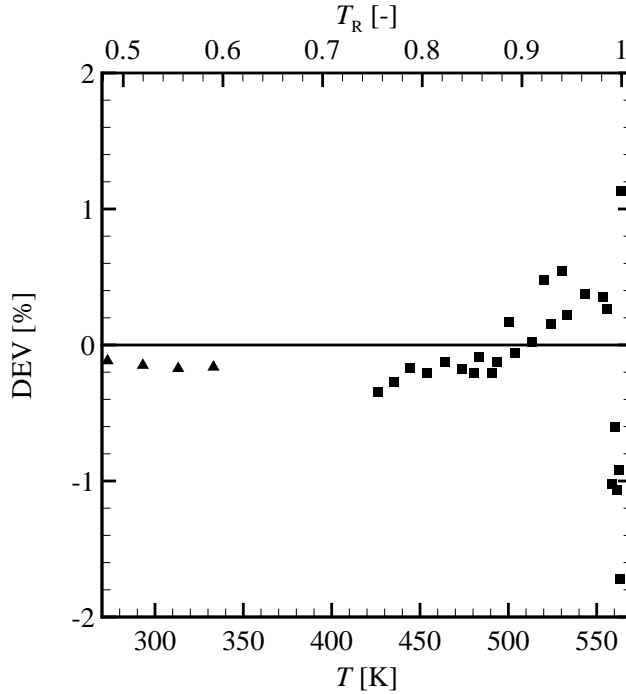


Figure 3.15: *Percentage deviations between predicted and experimental saturated liquid-density data of MDM. The deviation is defined as  $DEV = 100 \cdot (\rho_{exp}^L - \rho_{calc}^L) / \rho_{exp}^L$ .*

multiparameter EoS with an AAD of 0.01 %, 0.23 % and 0.03 %, respectively. The better performance of the multiparameter EoS with respect to the PRSV EoS is evident from Fig. 3.16.

- **Superheated vapor densities:**

The new EoS predicts all experimental superheated vapor densities, reported by Marcos et. al. [135], within 2 %; the PRSV EoS has a slightly poorer performance but can represent all experimental data within 2.5 %. These results are summarized in Fig. 3.17, which shows the deviations between experimental superheated vapor densities and values determined from the multiparameter EoS and the PRSV EoS.

- **Second density virials:**

The average absolute deviation of the predictions of the second density virial coefficient,  $\bar{B}$ , from the established 12-pSW EoS with respect to the experimentally derived data from Marcos et. al. [135], is 6.05 %. Devia-

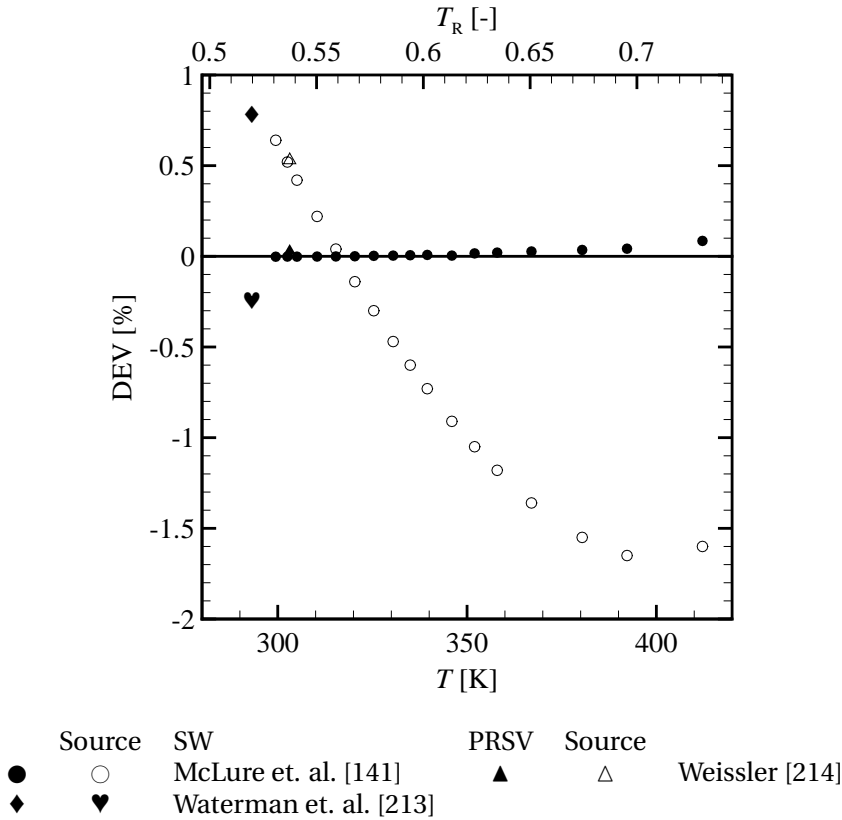


Figure 3.16: *Percentage deviations between predicted and experimental sub-cooled orthobaric liquid-density data of MDM. The deviation is defined as  $DEV = 100 \cdot (\rho_{exp} - \rho_{calc}) / \rho_{exp}$ .*

tions with respect to predictions from the PRSV EoS are not computed, because the PRSV EoS is highly inaccurate in this respect; moreover, as shown in Fig. 3.18, the physical behavior of the  $\bar{B}(T)$  values calculated with the PRSV EoS is incorrect due to the functional form of the attractive term.

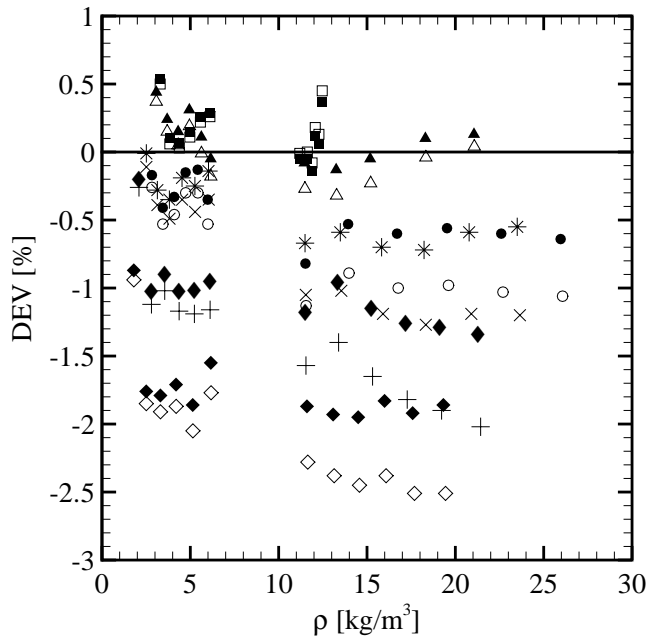


Figure 3.17: *The percentage deviations of experimental vapor-density data of MDM with respect to predicted data from the SW EoS and the PRSV EoS (experimental data are from Marcos et. al. [135]), i.e.,  $DEV = 100 \cdot (\rho_{exp} - \rho_{calc}) / \rho_{exp}$ . The symbols indicate the following temperatures, respectively (symbols between the brackets are for predictions from the PRSV EoS): ■ (□):  $T = 448.1119$  K, ▲ (△):  $T = 473.1104$  K, ● (○):  $T = 498.1100$  K, \* (×):  $T = 523.1102$  K, ◆ (+):  $T = 548.1107$  K, and ◇ (◇):  $T = 573.1109$  K.*

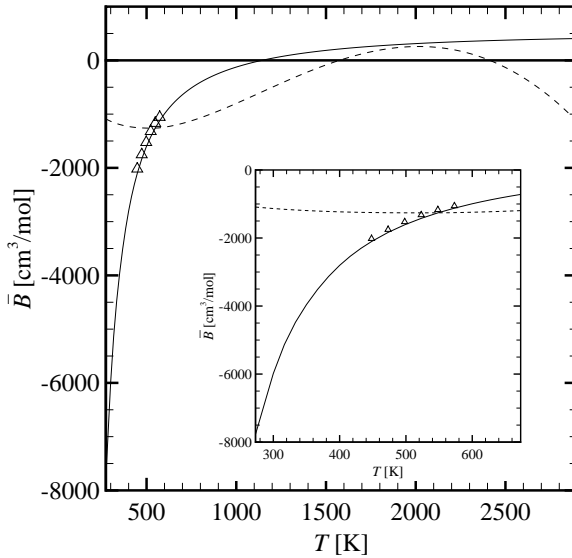


Figure 3.18: *The second density virial  $\bar{B}$ , obtained from the 12-pSW EoS (solid line) and the PRSV EoS (dashed line), as a function of temperature. Remark that the thermal decomposition temperature in stainless steel is  $\sim 400^\circ\text{C}$ ; higher temperatures are shown to illustrate the physical behavior of the  $\bar{B}$  function from both EoS's.*

## Nomenclature

Symbol	Description
$\hat{A}$	Substance-dependent parameter in the saturated liquid density correlation, Eq. (3.14)
$\hat{a}$	Substance-dependent parameter in the vapor-pressure correlation, Eq. (3.13)
$B$	Second density virial coefficient
$\mathfrak{B}$	Empirical parameter for use in Eq. (3.7)
$\hat{B}$	Substance-dependent parameter in the saturated liquid density correlation, Eq. (3.14)
$\hat{b}$	Substance-dependent parameter in the vapor-pressure correlation, Eq. (3.13)
$C$	Third density virial coefficient
$\hat{C}$	Substance-dependent parameter in the saturated liquid density correlation, Eq. (3.14)
$C_P$	Specific isobaric heat capacity
$C_v$	Specific isochoric heat capacity
$c$	Thermodynamic speed of sound
$\hat{c}$	Substance-dependent parameter in the vapor-pressure correlation, Eq. (3.13)
$D$	Fourth density virial coefficient
$\hat{D}$	Substance-dependent parameter in the saturated liquid density correlation, Eq. (3.14)
$\hat{d}$	Substance-dependent parameter in the vapor-pressure correlation, Eq. (3.13)
$f$	Resonance frequency
$g$	Half-width of a resonance signal
$H_{vp}$	Enthalpy of vaporization
$h$	Specific enthalpy
$h_P$	Planck's constant
$k_B$	Boltzmann's constant
$\mathcal{L}$	Resonator length
$M$	Molar mass
$N$	Number of data points
$n_i$	Substance-dependent parameter in the residual term of the EoS, Eq. (3.17)

Continued on the next page...

Continued

Symbol	Description
$P$	Pressure
$R$	Specific gas constant
$\mathfrak{R}$	Resonator radius
$s$	Specific entropy
$T$	Temperature
$v$	Specific volume
$Z$	Compressibility factor
$\alpha$	Thermal expansion coefficient
$\hat{\alpha}$	Substance-dependent parameter in the $\bar{C}_P^0$ correlation, Eq. (3.18)
$\beta_a$	Second acoustic virial coefficient
$\beta_P$	Coefficient of volume expansion
$\gamma$	Heat capacity ratio
$\hat{\gamma}$	Substance-dependent parameter in the $\bar{C}_P^0$ correlation, Eq. (3.18)
$\gamma_a$	Third acoustic virial coefficient
$\delta$	Reduced density
$\delta_a$	Fourth acoustic virial coefficient
$\hat{\epsilon}$	Substance-dependent parameter in the $\bar{C}_P^0$ correlation, Eq. (3.18)
$\Theta$	Characteristic vibrational temperature
$\iota$	Impurity fraction
$\kappa_s$	Isentropic compressibility
$\kappa_T$	Isothermal compressibility
$\nu$	Intermolecular vibrational frequency
$\rho$	Density
$\hat{\rho}$	Substance-dependent parameter in the $\bar{C}_P^0$ correlation, Eq. (3.18)
$\sigma_u ( )$	Uncertainty in the property between the round braces
$\tau$	Inverse reduced temperature
$\hat{\chi}$	Substance-dependent parameter in the $\bar{C}_P^0$ correlation, Eq. (3.18)
$\Psi$	Helmholtz free energy
$\psi$	Reduced Helmholtz free energy
$\omega$	Acentric factor

*“I want to tell you how proud I am to be the President of a nation that – in which there’s a lot of Philippine-Americans. They love America and they love their heritage. And I reminded the President that I am reminded of the great talent of the – of our Philippine-Americans when I eat dinner at the White House.”*

President George W. Bush, Washington, D.C., June 24, 2008

# 4

## On the computation of the fundamental derivative of gas dynamics in the dense-gas region

Selected contents from:

COLONNA, P, NANNAN, N. R., GUARDONE, A., AND VAN DER STELT, T. P. On the computation of the fundamental derivative of gas dynamics  $\Gamma$ , using equations of state. *Fluid Phase Equilib.* (2009) accepted for publication.

COLONNA, P, GUARDONE, A., AND NANNAN, N. R. Siloxanes: A new class of candidate Bethe-Zeldovich-Thompson fluids. *Phys. Fluids* 19, 086102 (2007), 12 pages.

### **Abstract**

*The fundamental derivative of gas dynamics,  $\Gamma$ , is a quantitative measure of the variation of the zero-frequency speed of sound with respect to density changes in isentropic transformations. The accurate computation of its value is a necessity for understanding and describing real-gas processes occurring in the dense-gas regime. Since  $\Gamma$  is a thermodynamic property related to the curvature of isentropes, it cannot arguably be determined directly from experiments. Several studies have documented the estimation of this caloric property for polyatomic fluids, notably BZT fluids, using relatively simple thermodynamic models. A re-*

view of these studies has revealed that the calculated values of  $\Gamma$  are affected by large uncertainties. Herein, under the presumption of local thermodynamic equilibrium, it is shown that: i) use of modern reference equations of state allows for the prediction of  $\Gamma$  with a level of accuracy which is suitable for the design and analysis of advanced technical applications operating in the dense-gas regime, and ii) that in the critical region analytic equations of state yield physically incorrect results for  $\Gamma$ . In fact, contrary to the results of analytic equations of state, scaled fundamental equations yield a weak divergence of  $\Gamma \rightarrow +\infty$  if the critical point is approached along the critical isochore from the single phase region, and a weak divergence to  $-\infty$  if the critical point is approached along the critical isochore from the vapor-liquid-equilibrium region.

## 4.1 Introduction

Accurate estimation of the thermodynamic domain featuring a negative value for the fundamental derivative of gas dynamics,  $\Gamma$  [see Eq. (1.1)], is a requirement for the design of experiments and processes or applications aimed at the generation and exploitation of nonclassical gas-dynamic effects (see for example Ref. [226]). Besides nonclassical gas dynamics, the study of dense-gas flows is relevant to several engineering applications: process expanders and compressors in the oil and chemical industries for example, often operate, at least partly, in the dense-gas region [15, 111]. Furthermore, the nozzle of organic-Rankine-cycle turbines expands the working fluid starting from superheated conditions close to the critical point [93, 32] and such turbines may benefit from nonclassical gas-dynamic effects [19, 150, 35].

The fundamental derivative of gas dynamics is a derived thermodynamic property of the caloric type. In principle,  $\Gamma$  can be obtained indirectly from measurable quantities, as can be clarified if  $\Gamma$  according to Eq. (1.1) is reformulated in terms of measurable quantities as

$$\Gamma(T, P) = 1 + c\rho \left( \frac{\partial c}{\partial P} \right)_T + \frac{\beta_P c T}{C_P} \left( \frac{\partial c}{\partial T} \right)_P. \quad (4.1)$$

Each of the thermodynamic properties in Eq. (4.1) can be measured either directly, e.g., densities, speeds of sound and isobaric heat capacities, or indirectly like  $(\partial c/\partial P)_T$ ,  $(\partial c/\partial T)_P$  and the coefficient of volume expansion  $\beta_P$ . Furthermore, the functional relation expressed by Eq. (4.1) makes it possible to assign an uncertainty to  $\Gamma$  under the provision that the uncertainty in each thermodynamic property is known. Unfortunately the availability of these data, e.g.,  $\beta_P$  and speed-of-sound along isobars, is insufficient even for well-measured fluids like methane.<sup>1</sup> The value of  $\Gamma$  is therefore determined from equations of

---

<sup>1</sup>It must be mentioned that values of  $\Gamma$  can be derived from published experimental data for the heat capacity ratio,  $\gamma^0$ , in the ideal-gas state. However, to the knowledge of the author, no experi-

state (EoS's). The accuracy of these predictions however, among other things, depends on both the accuracy of the thermodynamic properties on which the model is based, like critical-point values, the acentric factor, but also experimental property data in the case that the substance-specific parameters of the EoS are determined from a fit. Also the functional form of the EoS [84] is important, because uncertainties effecting for example  $P$ - $\rho$ - $T$ -data on the basis of which the EoS is optimized, are amplified in the case of derived properties.

Earlier studies treating the evaluation of the fundamental derivative of gas dynamics (see Sec. 4.2) are concerned mainly with the identification of BZT fluids. Only recently the problem of the correctness of the predicted values has been pointed out [84, 30, 31]. On the one hand, BZT fluids are necessarily composed of polyatomic molecules<sup>2</sup> and therefore thermodynamic modeling of candidate BZT fluids requires the use of rather simple functional relations for the EoS, e.g., cubic EoS's. The application of simple model EoS's is unavoidable because heavy polyatomic compounds which classify as BZT fluids are not well-measured since experiments would have to be conducted at quite high temperatures, or if few data are available, these are affected by comparatively large uncertainties with respect to data for simple fluids as for example methane. On the other hand, reference EoS's which possess the capability of representing thermal and caloric property data within the uncertainty with which these data can be measured, are available only for fluids composed of simple molecules, because these compounds are very well-measured (e.g., number of data points are of the order of thousands for simple fluids compared to tens or hundreds of data points for potential BZT fluids). Therefore, in order to assess the quality of simple EoS's with respect to predictions of  $\Gamma$ , the fundamental derivative of gas dynamics is firstly computed from reference EoS's for simple fluids. The obtained results for the simple fluids are then used as a benchmark; the performance of the simple EoS's can then be assessed, in this context, with respect to the benchmark. Moreover, the benchmark analysis allows for assigning an estimated uncertainty to predictions of  $\Gamma$  obtained from simple EoS's, e.g., the Peng-Robinson cubic EoS.

This chapter is structured as follows. After a review of previous work, see Sec. 4.2, Sec. 4.3 firstly treats the calculation of  $\Gamma$  for several, mainly simple, hydrocarbons by means of the reference EoS and either one or two accurate multiparameter technical EoS's for each fluid, with the purpose of assessing the uncertainty of such calculations. Next, the reference EoS's of the simple hydrocarbons are used as a benchmark against which the performance of the Peng-Robinson [161] Stryjek-Vera-modified [190] cubic EoS and the multiparameter Martin-Hou technical EoS can be evaluated. A simple cubic EoS has been taken into consideration because, as was mentioned, simple EoS's are currently the

---

ment is reported in literature with the specific aim of measuring the fundamental derivative of gas dynamics.

<sup>2</sup>To give an example, a molecules of BZT fluid dodecamethylcyclohexasiloxane ( $D_6$ ,  $[(CH_3)_2-Si-O]_6$ ) consists of 60 atoms [30].

only available option for fluids composed of polyatomic molecules classifying as BZT fluids; the Martin-Hou EoS has been considered because it was used in previous studies to identify BZT fluids. Results demonstrate that appreciable differences between the various EoS's are only observed near the critical point (in this context it must be indicated that cubic EoS's are inherently inaccurate in the critical region). The behavior of  $\Gamma$  in the critical region is analyzed in detail in Sec. 4.5 by application of so-called scaled fundamental equations. These scaled fundamental equations are only available for simple fluids, like methane and water, nevertheless, the qualitative behavior of properties in the critical region is universal and consequently, the results can be generalized.

## 4.2 Critical review of previous studies

Thompson and Lambrakis were the first to address the computation of the fundamental derivative of gas dynamics, specifically with the aim of identifying fluids with an embedded region of  $\Gamma < 0$  [122, 201]. In their work of 1972 they calculated the value of the fundamental derivative of gas dynamics along the critical isotherm for 16 organic compounds using two different methods. The first method consisted of interpolating published thermodynamic data in order to draw isentropes on a  $P$ - $v$  diagram. If the obtained isentrope exhibits a finite interval of concavity, this implies a region of a negative value of  $\Gamma$ . This method is clearly subjected to large uncertainties, as the computation of a second-order derivative from not-so-accurate primary thermodynamic data, leads to values of  $\Gamma$  which heavily depend on the data selected for the interpolation, the interval size and the interpolation type. The second method involved the direct computation of  $\Gamma$  from a complete thermodynamic model of the compound. In this case, Thompson and Lambrakis employed the virial (up to the fourth virial coefficient), the Hirschfelder-Buehler-McGee-Sutton (HBMS) [92] the Benedict-Webb-Rubin (BWR) [13] and the Martin-Hou (MH) [136] multiparameter EoS's. However, many relevant properties (e.g., the critical pressure  $P_C$ , the critical temperature  $T_C$ , the critical specific volume  $v_C$ , the acentric factor  $\omega$ , and the normal boiling point  $T_{BP}$ ) which are required for the computation of the fluid-specific parameters of the EoS, together with the ideal-gas heat capacities, had to be determined using estimation techniques, because accurate and reliable experimental information was not available at that time. Depending on the estimation method and the substance itself, uncertainties in estimated critical properties can be as high as 10 % [172, 164] and up to 25 % for heat capacities [172, 164]. Moreover, the estimated critical properties can be inconsistent. No sensitivity analysis was performed, but it can be inferred that the calculated values of  $\Gamma$ , as well as the correct identification of BZT fluids, are affected by large uncertainties [84]. Table 4.2 reports the fluids selected in these studies and the method employed to determine  $\Gamma$ . The results presented by Lambrakis and Thompson indicated that all 16 fluids exhibit a region of negative nonlinearity,

i.e., a region of  $\Gamma < 0$ . As an indication of the inaccuracy of such estimations, it can be noted that computations performed with the most recent and accurate thermodynamic EoS's for hydrocarbons (refer to Sec. 4.3) show that the minimum value of the fundamental derivative of gas dynamics ( $\Gamma_{\min}^V$ ), which is along the dew-line, is 0.68 for n-butane (the thermodynamic model is that of Buecker and Wagner [22]), whereas for n-decane, employing the EoS of Lemmon and Span [127],  $\Gamma_{\min}^V = 0.29$ . Consequently, it can be asserted, based on the law of corresponding states, that (n)-alkanes with a molecular complexity lower than or equal to that of n-decane, are not BZT fluids.

In the following study of BZT fluids [201], Thompson and Lambrakis analyzed the influence of the functional form of the EoS on the estimation of  $\Gamma$  in more detail, although the reliability of the input thermodynamic data was still left untreated. Using the Van der Waals, Redlich-Kwong [169], Clausius, and Abbott cubic EoS's [1], and the HBMS, the MH, and the BWR multiparameter EoS's, they reported the minimum value of  $\Gamma$  along the critical isotherm for the same fluids as in Ref. [122] and additionally for 5 fluorinated ethers (also included in Table 4.2). They noted that the minimum value of  $\Gamma$  in the vapor phase and far from the critical-point region lies on the dew line, nonetheless they calculated  $\Gamma$  only along the critical isotherm, most likely for simplicity, as phase-equilibrium computations can be avoided. From these results they concluded that values reported in Ref. [122] for  $\Gamma_{\min}$  (the reported values were obtained from the HBMS EoS) were too negative and that, if compared to the results of the cubic EoS's and the other multiparameter EoS's considered in Refs. [122, 201], the predictions of  $\Gamma$  from the Martin-Hou EoS were preferable. Thompson and Lambrakis also indicated that because the HBMS EoS has incorrect functional form if the critical compressibility  $Z_C$  is less than 0.302, it should not be used for calculating  $\Gamma$  (note that all potential BZT fluids have a  $Z_C < 0.302$ ).

The list of possible BZT fluids was extended in subsequent studies. Cramer [44] adopted the MH EoS complemented by an ideal-gas isochoric heat capacity correlation expressed as a power-law of the reduced temperature,  $T/T_C$ , and valid only for temperatures close to  $T_C$ . All the necessary fluid constants were estimated, therefore the accuracy of the model is possibly low. Incidentally, it is worthwhile noting that the MH EoS has a quite limited validity range if the model data are all computed from few fluid parameters, namely a single vapor-pressure data point and critical point data [60]. Cramer reports negative values for  $\Gamma$  along the saturated-vapor line for perfluorocarbons of the FC and PP families (see Table 4.2). However, the properties which were necessary for the computation of the substance-specific parameters of the MH EoS, e.g., critical and saturation properties, were provided by the fluid manufacturers and were not published in the open literature. It is therefore neither known if the fluid data were measured or estimated, nor can their accuracy be assessed; it can be inferred from common practice that the manufacturers estimated the data with ad hoc techniques, since measuring these data for fluids of low volatility is very challenging, even nowadays. Estimation techniques for these data can

be affected by large uncertainties, as previously indicated. In the concluding remarks, Cramer suggests that the predictions of  $\Gamma$  from the Martin-Hou EoS are too conservative with respect to negative values of  $\Gamma$ . Anticipating the results of section 4.3, this hypothesis is contrary to what has been observed herein.

In 2003, Colonna and Silva [37] considered cyclic and linear siloxanes as candidate BZT fluids and determined the value of  $\Gamma$  along the critical isotherm using the Peng-Robinson cubic EoS, modified by Stryjek and Vera in order to obtain accurate estimates of vapor pressures [190]. The employed EoS was based on measured vapor pressures, critical values extrapolated from vapor-pressure measurements and on ideal-gas isobaric heat capacities obtained with a group contribution method [86], the latter being possibly the major source of uncertainty. The authors were also the first to test substance-specific multiparameter EoS's based on large experimental data sets and they reported results of estimates of  $\Gamma$  in the vapor phase for water, nitrogen and n-octane. As expected, none of these substances can be classified as a BZT fluid, but comparisons of values of  $\Gamma$  along the critical isotherm calculated with various thermodynamic models, clearly showed to which extent the functional form of the EoS influences the results. Based on their preliminary results, Colonna and Silva anticipated that dodecamethylpentasiloxane (MD<sub>3</sub>M, C<sub>12</sub>H<sub>36</sub>O<sub>4</sub>Si<sub>5</sub>) and linear siloxanes of greater complexity, and octamethylcyclotetrasiloxane (D<sub>4</sub>, C<sub>8</sub>H<sub>24</sub>O<sub>4</sub>Si<sub>4</sub>) and cyclic siloxanes of greater complexity might have a region of negative nonlinearity in the single-phase region. In this work they also examined for the first time values of  $\Gamma$  for mixtures calculated by means of the mixing rules of Wong and Sandler [218] in combination with the PRSV EoS. The exemplary results showed that equimolar mixtures of cyclic siloxanes might have an embedded region of negative nonlinearity.

More recently, a study concerning the identification of BZT fluids was carried on by Guardone and Argrow [81]. They analyzed the influence of fluid constants, namely the acentric factor, critical compressibility, fluid complexity, etc., on the calculation of  $\Gamma$  using six different thermodynamic EoS's. The selected EoS's were: Van der Waals, Redlich-Kwong [169], Soave-Redlich-Kwong [183], Clausius II [59], Peng-Robinson [161], and that of Martin and Hou according to Ref. [137], herein denoted by mMH EoS. As for the ideal-gas heat capacity correlation, they chose the same functional form as the one adopted by Cramer [44]. In addition to the perfluorocarbons investigated by Cramer in Ref. [44], they included in their analysis PP-5, PP-9, FC-72, and FC-75. Also in this study, most of the relevant fluid parameters were obtained from manufactures or from the previously indicated references [44, 122]. The reported results indicated that PP-5 and PP-9 feature a region where  $\Gamma < 0$ ; FC-72 and FC-75 display a BZT region only if rather simple EoS's are used, namely the Van der Waals, Redlich-Kwong, and Clausius II EoS's. These models are known to be quantitatively inaccurate in the dense-gas region.

Finally, the study by Colonna et. al. [30] shows an investigation on siloxanes as candidate BZT fluids. In this work, the authors employed state of the art

multiparameter EoS's [34, 33] fitted on numerous and heterogenous data, either experimental or carefully estimated. As stated by all other studies, the ideal-gas heat capacity is a major source of uncertainty in the estimation of the fundamental derivative of gas dynamics. The thermodynamic model adopted in this study is based on the most accurate data for the ideal-gas isobaric heat capacity of siloxanes [153], i.e., data obtained from acoustic resonance-frequency measurements and ab initio calculations. The results show that linear and cyclic siloxanes, namely dodecamethylpentasiloxane (MD<sub>3</sub>M, C<sub>12</sub>H<sub>36</sub>O<sub>4</sub>Si<sub>5</sub>) and dodecamethylcyclohexasiloxane (D<sub>6</sub>, C<sub>12</sub>H<sub>36</sub>O<sub>6</sub>Si<sub>6</sub>), respectively (and fluids of the same family but of greater complexity) display a vapor region where  $\Gamma$  becomes negative. A sensitivity analysis to the estimation of the ideal-gas heat capacity is also included, while the authors point out that other sources of uncertainty still remain due to lack of information.

One last important remark is that, apart from Refs. [30] and [37], none of the previous studies on fluids that might exhibit a region of negative nonlinearity address the problem of the thermal stability of the fluid. This issue was first highlighted by Thompson and Lambrakis [201]. The thermodynamic region where  $\Gamma$  might be negative for some fluids composed of complex polyatomic molecules lies in a range of temperatures for which organic molecules tend to decompose if, for instance, they are in contact with metals (refer to, for example, Ref. [28]) or if they are not thoroughly degassed. For most of the fluids listed in Table 4.2, no information on their thermal stability is available, and therefore the negative- $\Gamma$  region might be located at temperatures for which the molecules decompose, if the fluid is contained in metal or if it is not completely degassed and dehydrated. Some preliminary experimental results indicate that siloxanes in contact with stainless steel are indeed thermally stable at the temperatures characterizing states with negative  $\Gamma$ , if the fluid is sufficiently purified [7, 27]. For siloxanes purification is very important because minute amounts of oxygen and water can trigger thermochemical decomposition.

## 4.3 The fundamental derivative of gas dynamics for selected alkanes

### 4.3.1 Reference equations of state

As the prediction of  $\Gamma$  by means of EoS's currently appears to be the only viable option, reference EoS's, which are the most accurate and complete thermodynamic models, are used to calculate the fundamental derivative of gas dynamics and to assess the accuracy that can be obtained with respect to the evaluation of  $\Gamma$ . Reference EoS's exist only for few simple molecules, like water, argon, nitrogen and simple hydrocarbons [184]. Methane, ethane, propane, n-butane, and isobutane are the fluids selected for this study. To provide an indication of the

accuracy of these thermodynamic models, the reference EoS for methane [181] is able to predict densities with an uncertainty of 0.03 % for pressures below 12 MPa. For the speed of sound in the vapor phase the uncertainty is 0.03 %. Iso-baric heat capacities may generally be calculated within an uncertainty of 1 % (higher uncertainties can be expected in the close-to-critical region) [181, 129].

The functional form of the reference equations is expressed in terms of the reduced Helmholtz free energy,  $\psi \equiv \Psi(T, \rho) / RT$ , as a function of the reduced density  $\delta \equiv \rho / \rho_C$  and the inverse of the reduced temperature  $\tau \equiv T_C / T = 1 / T_R$ . To take real-gas behavior into account, the Helmholtz free energy is decomposed in a part describing the ideal-gas contribution (indicated by superscript “0”), namely

$$\psi^0(\tau, \delta) = \frac{h_0^0 \tau}{RT_C} - \frac{s_0^0}{R} - 1 + \ln\left(\frac{\tau_0 \delta}{\delta_0 \tau}\right) - \frac{\tau}{R} \int_{\tau_0}^{\tau} \frac{C_P^0}{\tau^2} d\tau + \frac{1}{R} \int_{\tau_0}^{\tau} \frac{C_P^0}{\tau} d\tau, \quad (4.2)$$

which only depends on the ideal-gas (isobaric) heat capacity of the substance, and a residual part which takes the intermolecular forces into account. In Eq. (4.2),  $\delta_0 = \rho_0 / \rho_C$  and  $\tau_0 = T_C / T_0$  represent the reduced density and the inverse of the reduced temperature, respectively at a pre-defined or prescribed reference state  $(T_0, \rho_0)$ . The residual part can again be separated in two sets of terms, namely a set of regular terms that describes the thermodynamic behavior in the far-field region and a set of critical-point terms which is intended to describe the thermodynamics of the region in the vicinity of the critical point. For the alkanes selected for this study, the residual reduced Helmholtz free energy has the functional form

$$\begin{aligned} \psi^R = & \underbrace{\sum_{i=1}^j n_i \delta^{d_i} \tau^{t_i} + \sum_{i=j+1}^k n_i \delta^{d_i} \tau^{t_i} \exp(-\delta^{c_i})}_{\text{Regular terms}} \\ & + \underbrace{\sum_{i=k+1}^m n_i \delta^{d_i} \tau^{t_i} \exp\left(-\alpha_i (\delta - \Delta_i)^2 - \beta_i (\tau - \gamma_i)^2\right)}_{\text{Critical-point terms}}. \end{aligned} \quad (4.3)$$

Here,  $n_i$  are substance-specific parameters and are determined by fitting the functional form of the EoS to weighted experimental or estimated data. Parameters  $d_i$ ,  $t_i$  and  $c_i$ , the Gaussian-curve parameters  $\alpha_i$ ,  $\beta_i$ ,  $\gamma_i$  and  $\Delta_i$ , and the total number of terms, namely  $j$ ,  $k$  and  $m$ , are specific to an EoS. In the case of propane, n-butane, and isobutane, the EoS's have the same functional relation for the reduced Helmholtz free energy [22].

To assess the behavior of the functional form with respect to the estimation of  $\Gamma$ , values calculated with the reference EoS's are compared with one or two accurate multiparameter technical EoS's (depending on the availability) for each

of the selected fluids. These additional EoS's are the functional relations formulated by Miyamoto and Watanabe, Span and Wagner, and Friend, Ingham and Ely, and they are also expressed in terms of the Helmholtz free energy, whereby

$$\psi^R = \sum_{i=1}^j n_i \delta^{d_i} \tau^{t_i} + \sum_{i=j+1}^k n_i \delta^{d_i} \tau^{t_i} \exp(-\delta^{c_i}). \quad (4.4)$$

For the functional form proposed by Span and Wagner,  $j = 6$  and  $k = 12$ , for the functional form proposed by Miyamoto and Watanabe,  $j = 8$  and  $k = 19$ , and for the functional form used by Friend et. al.,  $j = 13$  and  $k = 32$ . The interested reader is referred to the respective papers for the parameters  $d_i$ ,  $t_i$  and  $c_i$ . Contrary to the reference EoS's where the entire functional form (thus including the EoS-parameters) can be optimized for a specific fluid, the functional form of the Span-Wagner (SW), Miyamoto-Watanabe (MW), and the Friend et. al. technical EoS's is fixed and the substance-specific parameters  $n_i$  are determined by fitting the equation to weighted experimental or estimated data. Consequently, the technical EoS's are applicable to a certain group of fluids, e.g., non-polar fluids, although this is only rigorously tested for the Span-Wagner functional form.

The procedure for obtaining  $\Gamma$  from a thermodynamic model, for example, formulated in terms of the reduced Helmholtz free energy as a function of its canonical variables temperature and density (or specific volume), necessitates a reformulation of Eq. (1.1) as (see e.g., Colonna and Silva [37])

$$\Gamma = \frac{v^3}{2c^2} \left\{ \left( \frac{\partial^2 P}{\partial v^2} \right)_T - 3 \frac{T}{C_v} \left( \frac{\partial P}{\partial T} \right)_v \left( \frac{\partial^2 P}{\partial v \partial T} \right) + \left[ \frac{T}{C_v} \left( \frac{\partial P}{\partial T} \right)_v \right]^2 \times \right. \\ \left. \left[ 3 \left( \frac{\partial^2 P}{\partial T^2} \right)_v + \frac{1}{T} \left( \frac{\partial P}{\partial T} \right)_v \left( 1 - \frac{T}{C_v} \left( \frac{\partial C_v}{\partial T} \right)_v \right) \right] \right\}. \quad (4.5)$$

Each of the thermodynamic functions in Eq. (4.5) can be obtained from the EoS using standard mathematical operations, like exact differentials, and the Maxwell relations, particularly  $(\partial \Psi / \partial v)_T = -P$  and  $(\partial \Psi / \partial T)_v = -s$ . Results are reported in Appendix B.

Figure 4.1 shows the results of calculations of the fundamental derivative of gas dynamics along the dew-line ( $\Gamma^V$ ) for methane as predicted by the reference EoS [181], by the Span-Wagner technical EoS [187], and by the Friend-Ingham-Ely technical EoS [71]. Values are calculated from the triple point ( $-182.46$  °C) up to the critical point ( $-82.59$  °C). It can be noted that the  $\Gamma^V$ -lines superimpose to an excellent degree. The minute difference between the values of  $\Gamma^V$  calculated with the Friend-Ingham-Ely EoS and the values calculated with the other two EoS's at low temperature is due to the difference in the prediction of the ideal-gas heat capacity; the correlations employed by the two more recent EoS's are to be preferred.

Figures 4.2-4.5 display similar results for fluids propane, ethane, n-butane and isobutane. The reference EoS and the other multiparameter technical EoS's

Table 4.1: The minimum value of fundamental derivative of gas dynamics along the dew-line and the corresponding reduced temperature, as predicted by the reference EoS and the multiparameter technical EoS's for several alkanes. Note: SW: Span-Wagner functional form, MW: Miyamoto-Watanabe functional form, FIE: Friend-Ingham-Ely functional form.

	Reference EoS		SW EoS		MW/FIE EoS	
	$T_R$ [-]	$\Gamma_{\min}^V$ [-]	$T_R$ [-]	$\Gamma_{\min}^V$ [-]	$T_R$ [-]	$\Gamma_{\min}^V$ [-]
CH <sub>4</sub>	0.75	1.15	0.77	1.14	0.76	1.15
C <sub>2</sub> H <sub>6</sub>	0.90	1.00	0.89	1.00	0.90	1.00
C <sub>3</sub> H <sub>8</sub>	0.93	0.82	0.93	0.83	0.94	0.83
C <sub>4</sub> H <sub>10</sub>	0.95	0.68	0.95	0.70	0.95	0.70
HC-(CH <sub>3</sub> ) <sub>3</sub>	0.95	0.68	0.95	0.69	0.96	0.68

predict practically the same  $\Gamma^V$  from the triple point up to temperatures very close to  $T_C$ . In the close vicinity of the critical point, where the variation of  $\Gamma^V$  is very large, the differences between the calculated  $\Gamma^V$  values tend to become comparatively larger. A quantitative indication of the difference in the calculated  $\Gamma^V$  is provided in Table 4.1, which lists the minimum value of the fundamental derivative of gas dynamics and the corresponding reduced temperature for the selected alkanes, as calculated by the reference EoS and the mentioned multiparameter technical EoS's.

Based on the considered EoS's, the first important observation is that the functional form does not significantly influence, from both a quantitative and qualitative viewpoint, the prediction of  $\Gamma$  in the (dense) vapor phase. Worded differently, for a given thermodynamic state,  $\Gamma$  values from the thermodynamic models differ at most by only a few of a hundredth, except for the region very near the critical point. Therefore, if reference EoS's were available for fluids made of polyatomic molecules that are complex enough for  $\Gamma$  to be negative, it can be asserted that the predictions of  $\Gamma$  made with these models would be accurate enough for the design and interpretation of nonclassical gas dynamic experiments, see, e.g., Refs. [66, 35, 226, 31], and processes, see, e.g., Refs. [19, 175, 150, 35]. As was mentioned before, the only limitation is the unavailability or scarcity of experimental data (and the fact that the fluid may decompose at the thermodynamic states where  $\Gamma < 0$ ).

To assess the uncertainty of the values of  $\Gamma$  in the vapor phase if calculated with reference EoS's, it can be observed that predictions of  $\Gamma$  deviate from the true values due to two aspects, namely i) the uncertainty in the experimental data on which the parameters of the functional form are fitted (formulated differently, this implies that the substance-specific parameters of the EoS have an uncertainty), and ii) the bias introduced by the functional form. The influence of the functional form of the EoS on predictions of  $\Gamma$ , i.e., the estimation of the

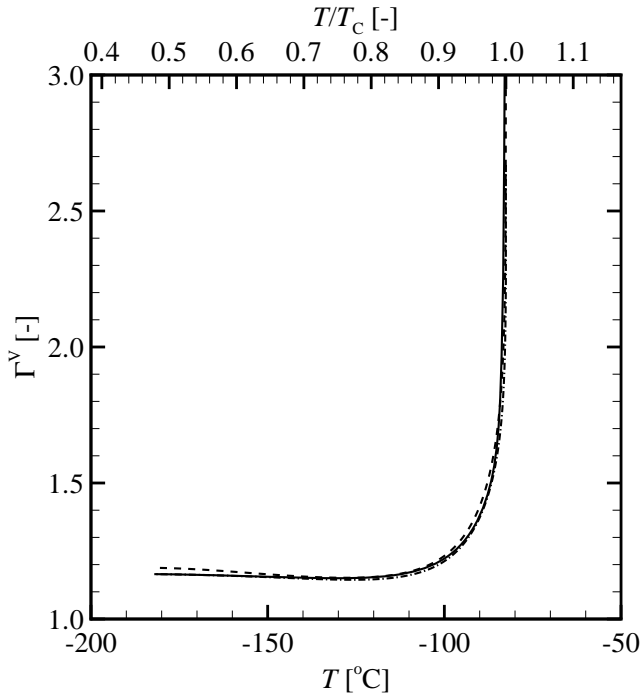


Figure 4.1: *The fundamental derivative of gas dynamics along the saturated vapor line of methane ( $\text{CH}_4$ ) as a function of  $T$  and  $T/T_C$ , where  $T_C$  is the critical temperature. Results of computations performed with the Wagner-Setzmann reference equation of state [181] (solid line) are in excellent agreement with  $\Gamma^V$  computed with the Span-Wagner EoS [187] (dash-dotted line) and with the Friend-Ingham-Ely EoS [71] (dashed line), from the triple point ( $-182.46^\circ\text{C}$ ) up to almost the critical point ( $-82.59^\circ\text{C}$ ).*

bias error, can be analyzed by applying the procedure illustrated in the following, valid only under the assumption that: 1) the reference EoS is truly capable of predicting thermal and caloric properties within their experimental uncertainty (this is a necessary assumption only if the reference EoS is used to simulate experimental data; if sufficient experimental data are available, this assumption can be abandoned), 2) that the single-phase thermodynamic surface in the  $P$ - $T$ -plane is smooth, and 3) the analyzed thermodynamic state is outside the so-called critical region as delimited by Anisimov et. al. [9].

First of all, the reference EoS is used to simulate experimental data for densities, speeds of sound, and isobaric heat capacities. Experimental data, like for example the speed of sound, are computed from the reference EoS at a given

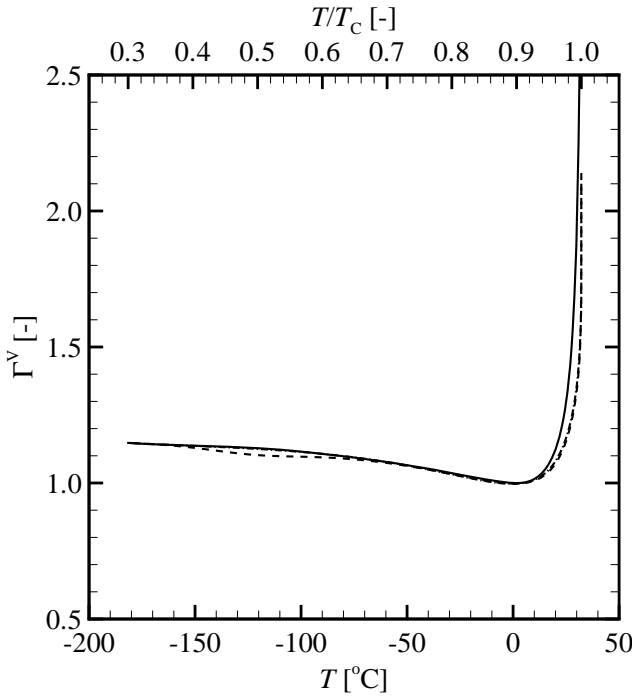


Figure 4.2: The fundamental derivative of gas dynamics along the saturated vapor line of ethane ( $\text{C}_2\text{H}_6$ ) as a function of  $T$  and  $T/T_c$ , where  $T_c$  is the critical temperature. Values calculated with the Buecker-Wagner reference EoS [21] (solid line) are almost coincident with those computed with the Span-Wagner EoS [187] (dash-dotted line) and with the Friend-Ingham-Ely EoS [72] (dashed line) from the triple point ( $-182.78^\circ\text{C}$ ) up to almost the critical point ( $32.17^\circ\text{C}$ ).

pressure  $P$  and temperature  $T$ , and then randomly – according to a uniform distribution function – perturbed based on the maximum expected deviation that the EoS exhibits with respect to experimental data. For the Wagner-Setzmann reference EoS for methane for example, speeds of sound, densities and isobaric heat capacities display a deviation with respect to experimental data of, on average, 0.03%, 0.03%, and 1% respectively. Figure 4.6 shows a collection of data points for which  $\rho$ ,  $c$  and  $C_P$  are simulated; these data-points are indicated by an “\*”-symbol. The simulated data are then fitted to the following Taylor series

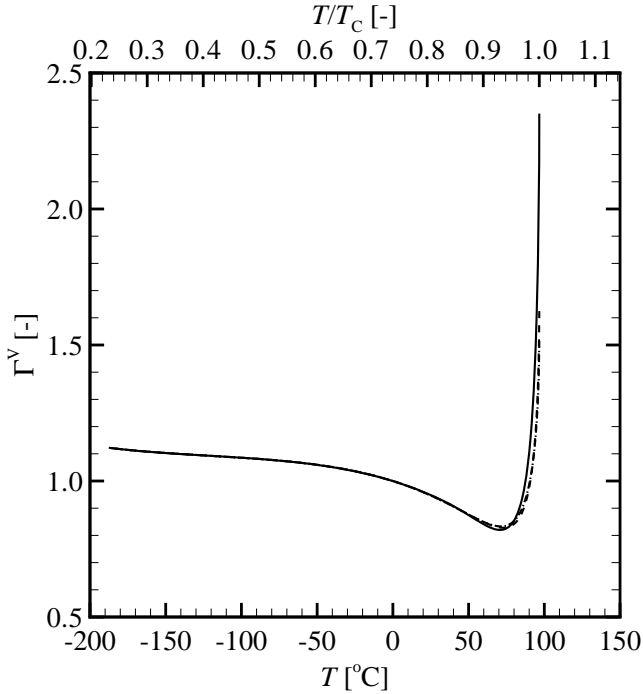


Figure 4.3: *The fundamental derivative of gas dynamics along the saturated vapor line of propane ( $C_3H_8$ ) as a function of  $T$  and  $T/T_C$ , where  $T_C$  is the critical temperature. Results of computations performed with the Buecker-Wagner reference EoS [22] (solid line) are in excellent agreement with  $\Gamma^V$  computed with the Span-Wagner EoS [187] (dash-dotted line) and with the Miyamoto-Watanabe EoS (dashed line) [146], from the triple point ( $-187.67$  °C) up to almost the critical point ( $96.68$  °C).*

expansion around  $(P^\bullet, T^\bullet)$  to second-order of smallness<sup>3</sup>

$$\begin{aligned} \rho(T, P) = & \rho^\bullet(T^\bullet, P^\bullet) + \left(\frac{\partial \rho}{\partial P}\right)_{T^\bullet, P^\bullet} \Delta P + \left(\frac{\partial \rho}{\partial T}\right)_{T^\bullet, P^\bullet} \Delta T + \quad (4.6) \\ & \frac{1}{2} \left[ \left(\frac{\partial^2 \rho}{\partial P^2}\right) \Delta P^2 + 2 \left(\frac{\partial^2 \rho}{\partial P \partial T}\right) \Delta P \Delta T + \left(\frac{\partial^2 \rho}{\partial T^2}\right) \Delta T^2 \right]_{T^\bullet, P^\bullet} \end{aligned}$$

<sup>3</sup>Note that it is in fact unnecessary to perform a Taylor series expansion to second-order of smallness, since these higher-order derivative properties are not required for Eq. (4.1). Fortunately however, it can be verified numerically that the higher-order contributions are small with respect to the first-order terms.

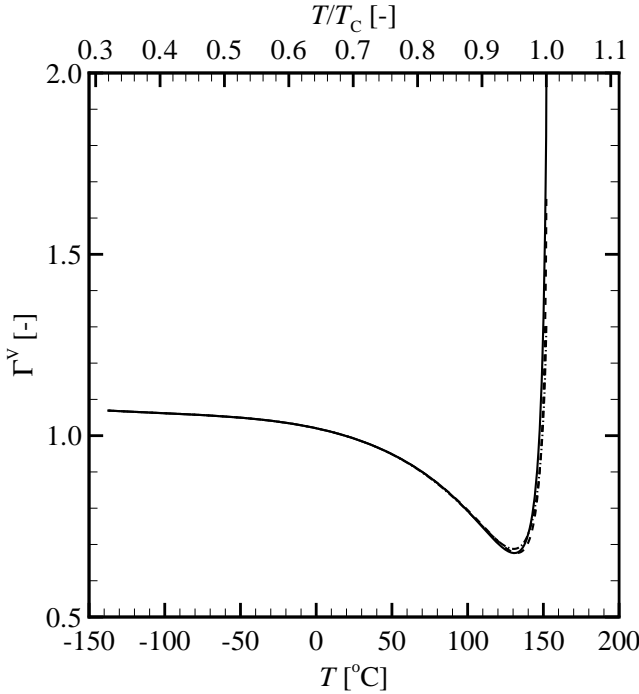


Figure 4.4: The fundamental derivative of gas dynamics along the saturated vapor line of *n*-butane ( $C_4H_{10}$ ) as a function of  $T$  and  $T/T_C$ , where  $T_C$  is the critical temperature. Values calculated with the Buecker-Wagner reference EoS [22] (solid line) are almost coincident with those computed with the Span-Wagner EoS [187] (dash-dotted line), and with the Miyamoto-Watanabe EoS (dashed line) [147], from the triple point ( $-138.26^\circ\text{C}$ ) up to almost the critical point ( $151.98^\circ\text{C}$ ).

$$C_P(T, P) = C_P^\bullet(T^\bullet, P^\bullet) + \left(\frac{\partial C_P}{\partial P}\right)_{T^\bullet, P^\bullet} \Delta P + \left(\frac{\partial C_P}{\partial T}\right)_{T^\bullet, P^\bullet} \Delta T + \quad (4.7)$$

$$\frac{1}{2} \left[ \left(\frac{\partial^2 C_P}{\partial P^2}\right) \Delta P^2 + 2 \left(\frac{\partial^2 C_P}{\partial P \partial T}\right) \Delta P \Delta T + \left(\frac{\partial^2 C_P}{\partial T^2}\right) \Delta T^2 \right]_{T^\bullet, P^\bullet}$$

$$c(T, P) = c^\bullet(T^\bullet, P^\bullet) + \left(\frac{\partial c}{\partial P}\right)_{T^\bullet, P^\bullet} \Delta P + \left(\frac{\partial c}{\partial T}\right)_{T^\bullet, P^\bullet} \Delta T + \quad (4.8)$$

$$\frac{1}{2} \left[ \left(\frac{\partial^2 c}{\partial P^2}\right) \Delta P^2 + 2 \left(\frac{\partial^2 c}{\partial P \partial T}\right) \Delta P \Delta T + \left(\frac{\partial^2 c}{\partial T^2}\right) \Delta T^2 \right]_{T^\bullet, P^\bullet}$$

and the thermodynamic properties necessary for Eq. (4.1) and therefore  $\Gamma$ , are

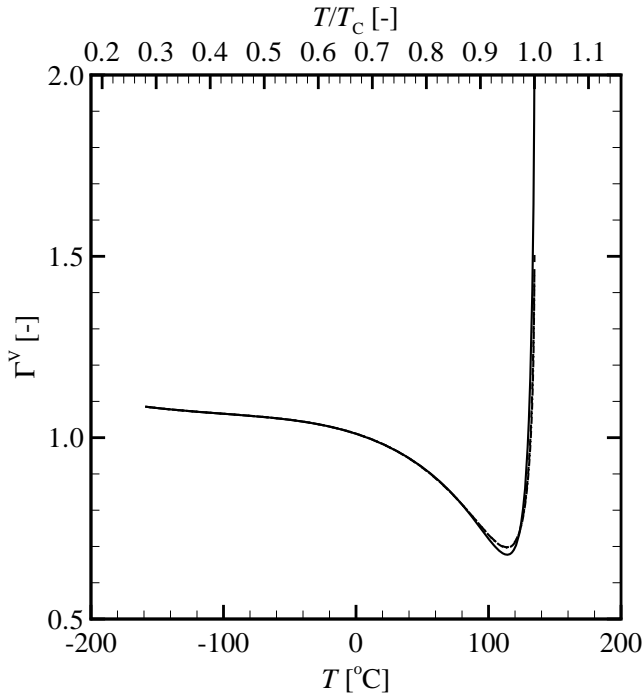


Figure 4.5: The fundamental derivative of gas dynamics along the saturated vapor line of isobutane ( $\text{HC}-(\text{CH}_3)_3$ ) as a function of  $T$  and  $T/T_C$ , where  $T_C$  is the critical temperature. Results of computations performed with the Buecker-Wagner reference EoS [22] (solid line) are in excellent agreement with  $\Gamma^V$  computed with the Span-Wagner EoS [187] (dash-dotted line) and with the Miyamoto-Watanabe EoS (dashed line) [148], from the triple point ( $-159.42$  °C) up to almost the critical point ( $134.66$  °C).

determined. This method allows for predicting  $\Gamma$  without a prescribed functional form for an EoS. Moreover, the difference between  $\Gamma$  from an EoS with respect to  $\Gamma$  from the fit to simulated data can be considered as an estimate of the precision of the EoS for this specific collection of points. To get an unbiased estimate of the precision, more than one configuration of data points has to be considered. Herein, five configurations of data 40 points (indicated by “\*”) per each center-point (indicated by “•”) were considered. Moreover, three center-points which are all located in the vapor region, were considered for methane, namely

$$- (P^\bullet = 2002.5, T^\bullet = 192.62), \text{ with } Z = 0.84,$$

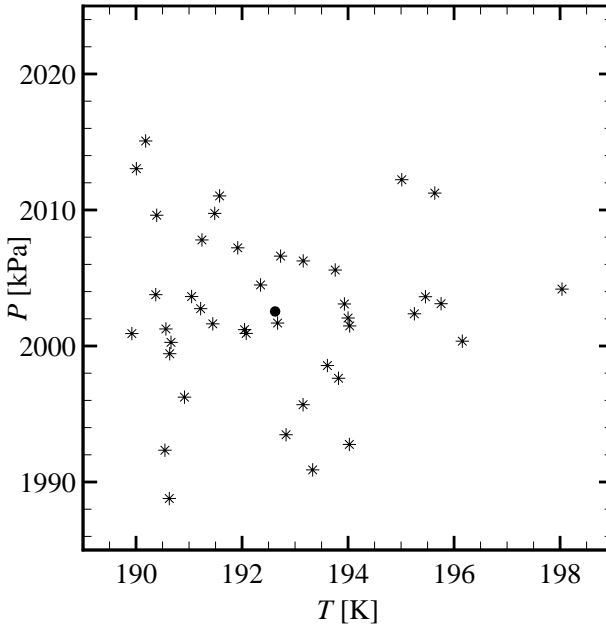


Figure 4.6: An example of a collection of  $(P, T)$ -points of methane for which  $\rho$ -,  $c$ - and  $C_P$ -data are simulated. •: represents the center-point of the simulated data.

- ( $P^\bullet = 3487.3, T^\bullet = 192.65$ ), with  $Z = 0.68$  and
- ( $P^\bullet = 3405.0, T^\bullet = 192.70$ ), with  $Z = 0.62$  (the pressures are expressed in kPa and temperatures in K).

For all these points it was found that the bias of the estimation of  $\Gamma$  randomly varied between  $\pm 0.01$ . Computations performed with ethane yielded a similar result.

### 4.3.2 Simpler equations of state

For the vast majority of fluids, reference EoS's are not available. Roughly speaking, the availability of accurate multiparameter EoS's is inversely proportional to the molecular complexity characterizing the fluid. In all previous studies related to the evaluation of the fundamental derivative of gas dynamics, except for Ref. [30], simpler and comparatively inaccurate thermodynamic models were

adopted, primarily because this was the only option. It is interesting to evaluate the performance of simpler EoS's with respect to the computation of  $\Gamma$ , in comparison with reference EoS's. This assessment provides an indication with regard to the accuracy that can be expected from simpler functional relations for the EoS. To this purpose, the cubic PRSV EoS and the multiparameter MH EoS are selected, because these thermodynamic models were adopted in many of the previous studies on nonclassical gas dynamics (see Sec. 4.2). It should be noted that the PRSV EoS is inconsistent at the critical temperature since derivative properties exhibit a discontinuity at the critical isotherm [190], and that the MH EoS has poor performance at reduced temperatures below 0.9 if it is only fitted to critical-point and normal-boiling-point data.

Figure 4.7 presents a comparison between the values of  $\Gamma$  along the dew line calculated with the PRSV and MH EoS's with respect to values calculated with reference EoS's for ethane, propane, n-butane and n-octane. A relevant remark is that the EoS of n-octane is that of Kunz and Wagner [117] and it classifies as a technical EoS rather than a reference EoS, therefore, although accurate, it does not fulfill all the requirements of a reference EoS [184, 188]. Note that the  $\Gamma^V$  curve calculated with the MH EoS is truncated at a temperature higher than the triple point, because the saturation calculations performed with this EoS at temperatures lower than indicated, do not converge to meaningful values. Inspection of Figure 4.7 yields that, while the performance of the PRSV EoS is very satisfactory, and only in the case of n-octane it slightly underpredicts the minimum value of  $\Gamma$ , the MH EoS displays fairly large deviations in the lower temperature range.

Figure 4.8 reports the same lines as Fig. 4.7, but an appropriate scale has been chosen for the horizontal axis in order to amplify the difference between the computed values close to the critical point. The reference EoS's contain critical-point terms [see Eq. (4.3)] to achieve good accuracy in the estimation of primary properties, while cubic EoS's are known to be inaccurate close to the critical point. Nonetheless, even reference EoS's, which are analytic in the Helmholtz free energy at the critical point, fail to correctly predict many critical anomalies [131, 132, 180] and therefore, also the trend of  $\Gamma$  along the dew-line is inaccurate/incorrect; in fact,  $\Gamma$  should diverge at the critical point [61].

## 4.4 The fundamental derivative of gas dynamics for selected siloxanes

The estimation of the value of the fundamental derivative of gas dynamics is of special interest in the case of fluids made of complex molecules, because for these fluids the inversion of gas dynamic phenomena is predicted in the thermodynamic region where  $\Gamma$  is negative. As an example, the results of the calculation of  $\Gamma^V$  as a function of  $T/T_C$  for MDM, MD<sub>2</sub>M and MD<sub>3</sub>M made with the

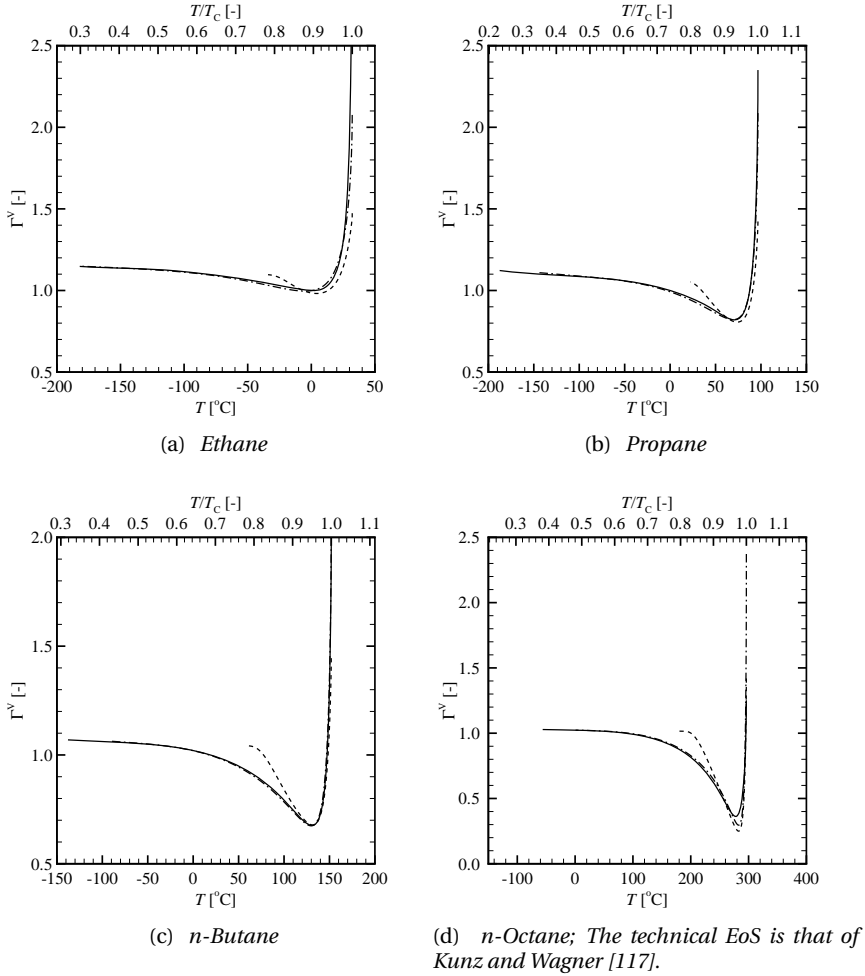


Figure 4.7: The fundamental derivative of gas dynamics along the dew-line of selected n-alkanes. Continuous lines represent computations with the reference EoS (see Ssec. 4.3.1), dashed lines represent computations with the MH EoS, and the dash-dotted lines represent computations with the PRSV EoS.

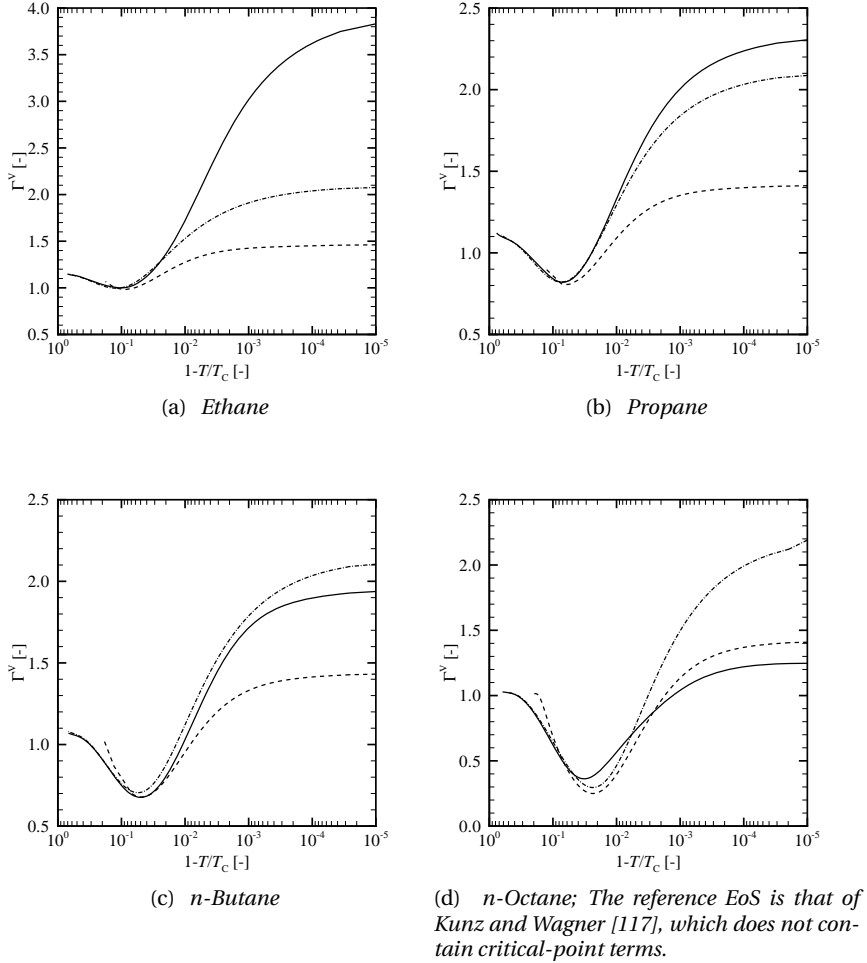


Figure 4.8: The fundamental derivative of gas dynamics along the dew-line of selected *n*-alkanes whereby the horizontal axis is adapted to better visualize the region close to the critical point. The solid line represents computations with the reference EoS, the dashed line represents computations with the MH EoS, and the dash-dotted line represents computations with the PRSV EoS. Note that  $1 - T/T_C = 10^{-2}$  corresponds to approximately 3 to 4 K.

SW, the PRSV and the MH EoS's are shown in Figure 4.9. Figures 4.10 and 4.11 respectively display the iso- $\Gamma$ -lines computed with the EoS's in the Span-Wagner functional form (see Ssec. 3.3.3) in the  $P$ - $T$  thermodynamic plane of cyclic and linear siloxanes. It can be observed that the MH EoS consistently predicts a significantly lower value of  $\Gamma_{\min}^V$  compared to the PRSV and the technical EoS [33], respectively. Finally, for all siloxanes it can be noted that  $\Gamma_{\min, \text{MH EoS}}^V < \Gamma_{\min, \text{Ref. EoS}}^V$ . This is the case also for all alkanes considered herein.

As a last remark, it is interesting to assess the influence of molecular complexity on the estimation of the fundamental derivative of gas dynamics. Note that  $\Gamma$  can be written as the summation of three terms as

$$\Gamma = \frac{v^3}{2c^2} (\bar{\Gamma}_1 + \bar{\Gamma}_2 + \bar{\Gamma}_3), \quad (4.9)$$

where,

$$\bar{\Gamma}_1 = \left( \frac{\partial^2 P}{\partial v^2} \right)_T \quad (4.10a)$$

$$\bar{\Gamma}_2 = -3 \frac{T}{C_v} \left( \frac{\partial P}{\partial T} \right)_v \left( \frac{\partial^2 P}{\partial v \partial T} \right)_{T,v} \quad (4.10b)$$

$$\bar{\Gamma}_3 = \left[ \frac{T}{C_v} \left( \frac{\partial P}{\partial T} \right)_v \right]^2 \times \left[ 3 \left( \frac{\partial^2 P}{\partial T^2} \right)_v + \frac{1}{T} \left( \frac{\partial P}{\partial T} \right)_v \left( 1 - \frac{T}{C_v} \left( \frac{\partial C_v}{\partial T} \right)_v \right) \right] \quad (4.10c)$$

In the dense-gas region, but outside the critical region, it can be shown that, as the isochoric heat capacity increases, the contribution of  $\bar{\Gamma}_2$  (due to the factor  $C_v^{-1}$ ) and in particular the contribution of  $\bar{\Gamma}_3$  (due to the factor  $C_v^{-2}$ ) to the value of  $\Gamma$ , relative to the contribution of  $\bar{\Gamma}_1$ , i.e., the curvature of isotherms, decreases. For this reason, in the case of a complex molecule, the estimation of  $\Gamma$  is more sensitive to the accuracy of  $P$ - $v$ - $T$  experimental data (because of the  $\bar{\Gamma}_1$ , and to a lesser extent,  $\bar{\Gamma}_2$  terms) rather than to the term affected by  $C_v^{-2}$ .

Recent work on the estimation of the ideal-gas heat capacity of siloxanes [153] (or refer to Sec. 3.2) demonstrated that, by combining experimental measurements with ab initio calculations, ideal-gas isobaric heat capacities of molecularly complex fluids can be determined with approximately 5–6 % uncertainty. The availability of accurate  $P$ - $v$ - $T$  data in the dense-gas region of molecularly complex fluids and the correct estimation of their critical parameters remains an issue, as far as accurate values of  $\Gamma$  are concerned.

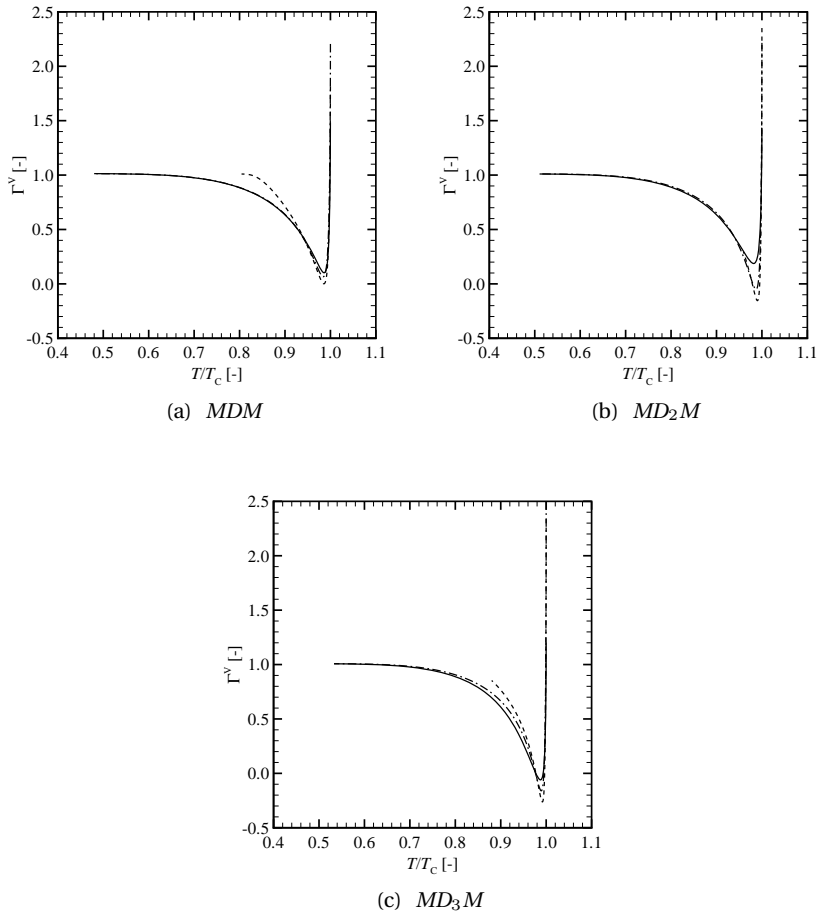


Figure 4.9: *The fundamental derivative along the dew-line of selected linear siloxanes. The solid line represents computations with the multiparameter EoS using the SW functional form [33], the dashed line represents computations with the MH EoS, and the dash-dotted line represents computations with the PRSV EoS.*

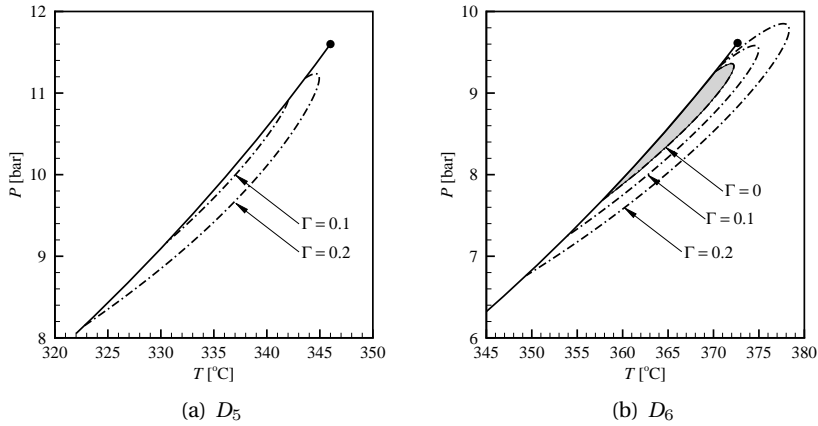


Figure 4.10: Iso- $\Gamma$  lines in the  $P$ - $T$  plane for cyclic siloxanes. Thermodynamic properties are obtained from the Span-Wagner EoS. (•) critical point. The shaded area represents the  $\Gamma < 0$  region.

## 4.5 The fundamental derivative of gas dynamics in the vapor-liquid critical region of pure fluids

### 4.5.1 Introduction

The critical region is delimited by Anisimov et. al. [9] as the domain approximately bounded by  $0.96 < T/T_C < 1.04$  along the critical isochore and at least  $\pm 50\%$  from the critical density  $\rho_C$ . In this thermodynamic regime, fluids near the vapor-liquid critical point feature anomalous behavior in many transport and thermodynamic properties – see for example the experimental data of the thermal conductivity [143] and of the isochoric heat capacity [58] for carbon dioxide ( $\text{CO}_2$ ). The observed anomalies are usually the result of the divergence of some thermodynamic properties, for instance the divergence of the isothermal compressibility,  $\kappa_T \equiv -(\partial v / \partial P)_T / v$ .

Using Anisimov's [9] criterium, it can be verified that part of the domain featuring a negative value for  $\Gamma$  in the single-phase dense-gas regime, i.e., the region approximately bounded by  $1.4 < v/v_C < 2.5$ ,  $0.96 < T/T_C < 1.01$ ,  $0.75 < P/P_C < 1$  (see Guardone et. al. [79, 84]), is located in the critical region. It is therefore plausible that predictions of  $\Gamma$  from cubic and/or multi-parameter EoS's, as described in the previous section, are inaccurate or even incorrect, particularly because the previously treated EoS's assume analyticity of the Helmholtz free energy at the critical point whereas experimental obser-

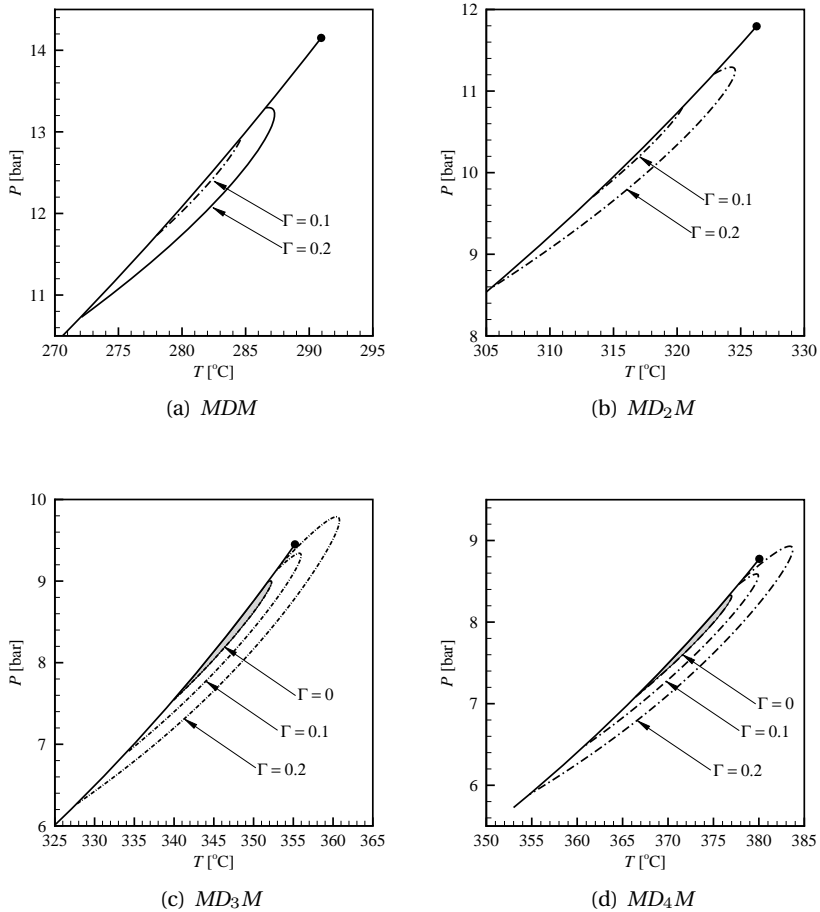


Figure 4.11: Iso- $\Gamma$  lines in the  $P$ - $T$  plane for linear siloxanes. Thermodynamic properties are obtained from the Span-Wagner EoS. (●) critical point. The shaded area represents the  $\Gamma < 0$  region.

vation of the divergence of the isochoric heat capacity,  $C_v$ , as the critical point is approached, is a direct indication of the nonanalyticity of the Helmholtz free energy. Moreover,  $\Gamma$  is a second-order derived caloric property and it is even more sensitive to critical-point anomalies than thermal properties like the density. It is the aim of this section to investigate the behavior of  $\Gamma$  in the critical region.

The divergence of properties near the critical point is usually described in

terms of so-called scaling laws, see for example the scaling laws described by Levelt-Sengers and collaborators [131, 130, 104, 132]. Two types of scaling – also referred to as classical and nonclassical scaling – can be identified. The method using classical scaling is based on the assumption that the Helmholtz free energy is analytic at the critical point, hence it can be expanded in Taylor series in terms of the canonical properties density and temperature. Moreover, classical scaling ignores critical fluctuations and predicts a finite value for the isochoric heat capacity at the critical point. Although the method can be used to illustrate the concept of scaling, the obtained critical exponents do not agree with experimental data. The method of nonclassical scaling is based on the nonanalyticity of the Helmholtz free energy at the critical point and in this case, the analysis of the singular part is treated with other concepts, e.g., renormalization group theory applied to 3-dimensional Ising-like systems.

Using the method of nonclassical scaling, Balfour et al. [10] formulated an equation of state to determine properties in the near-critical state of pure fluids in terms of  $P/T$  as a function of  $1/T$  and  $\mu/T$ , where  $P/T$  is referred to as the potential and  $\mu$  is the chemical potential. With the aid of the critical-point values the equation of state is made dimensionless. Using the definition of the following dimensionless quantities, namely

$$\tilde{P} \equiv \frac{P}{T} \frac{T_C}{P_C}, \quad \tilde{T} \equiv -\frac{T_C}{T}, \quad \tilde{\mu} \equiv \frac{\mu}{T} \frac{\rho_C T_C}{P_C}, \quad (4.11)$$

the functional form of the scaled fundamental equation reads

$$\tilde{P} = 1 + \sum_{i=1}^3 \tilde{P}_i (\Delta\tilde{T})^i + \Delta\tilde{\mu} (1 + \tilde{P}_{11} \Delta\tilde{T}) + \Delta\tilde{P}. \quad (4.12)$$

Here,  $\tilde{P}_{i=1\dots 3}$  and  $\tilde{P}_{11}$  are so-called pressure background parameters and are fluid-specific,

$$\Delta\tilde{T} = \tilde{T} + 1, \quad \Delta\tilde{\mu} = \tilde{\mu} - \tilde{\mu}_C - \sum_{i=1}^4 \tilde{\mu}_i (\Delta\tilde{T})^i, \quad (4.13)$$

whereby  $\tilde{\mu}_{i=1\dots 4}$  and  $\tilde{\mu}_C$  are the fluid-specific thermal background parameters. The singular part of the scaled fundamental equation, namely

$$\Delta\tilde{P} = \alpha r^{\bar{\beta}(\bar{\delta}+1)} \left[ k_0 \hat{p}_0(\theta) + r^{\bar{\Delta}_1} k_1 \hat{p}_1(\theta) \right], \quad (4.14)$$

is expressed as a function of the parametric variables  $r$  and  $\theta$  (which conform to the asymptotic behavior and symmetry of the Ising model), auxiliary functions  $\hat{p}_0(\theta)$  and  $\hat{p}_1(\theta)$ , universal critical exponents  $\bar{\beta}$ ,  $\bar{\delta}$  and  $\bar{\Delta}_1$ , and substance-specific parameters  $\alpha$ ,  $k_0$  and  $k_1$  (refer also to Tables C.1, C.2 and C.3 in Appendix C). The variable denoted by  $r$  gives the distance of a thermodynamic state with respect to the critical point and the variable denoted by  $\theta$  gives the location of the

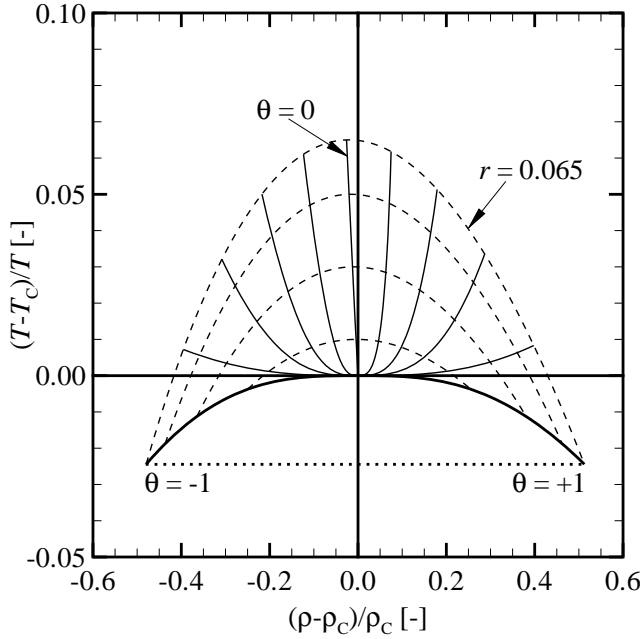


Figure 4.12: The parametric distance ( $r$ ) and the contour ( $\theta$ ) variables in the density-temperature plane of methane. The solid lines represent iso- $\theta$  contours, some of which have been labeled, and the dashed lines represent iso- $r$  contours. For this specific fluid, namely methane ( $\text{CH}_4$ ), the  $r = 0.065$ -line and the horizontal dotted line delimit the domain of validity of the scaled fundamental equation [118] for the single- and vapor-liquid equilibrium (VLE) region. Properties in the VLE region can be determined using the law of mass conservation, e.g.,  $s = \varpi s^{\text{V}} + (1 - \varpi) s^{\text{L}}$ , where  $\varpi$  is the vapor fraction. Remark that

$$\lim_{\Delta\tilde{T} \downarrow 0} \left( \frac{\partial \Delta\tilde{T}}{\partial \tilde{\rho}} \right)_{\theta=0} = 0.$$

thermodynamic state on a line of constant  $r$ , such that  $\theta = -1$  represents the dew-line and  $\theta = +1$  represents the bubble-line ( $-1 \leq \theta \leq +1$ ). Figure 4.12 displays the parametric plot for methane in order to elucidate the meaning of the parametric distance and contour variables. Along the  $\theta = 0$ -line, as the critical point is approached from the supercritical region, i.e.,  $\Delta\tilde{T} \downarrow 0$ ,  $\left( \frac{\partial \Delta\tilde{T}}{\partial \tilde{\rho}} \right)_{\theta} = 0$ . With  $r$  and  $\theta$  now introduced, the parametric equations for  $\Delta\tilde{\mu}$  and  $\Delta\tilde{T}$  are

$$\Delta\tilde{\mu} = \alpha r^{\bar{\beta}\bar{\delta}} \theta (1 - \theta^2) \quad (4.15)$$

and

$$\Delta\tilde{T} = r(1 - \bar{b}^2\theta^2) - c\Delta\tilde{\mu}, \quad (4.16)$$

with  $\bar{b}^2$  representing a universal constant and  $c$  being a fluid-specific parameter.

From the EoS represented by Eq. (4.12), all other thermodynamic properties can be determined. To exemplify this, consider firstly the following relationship for a scaled fundamental equation formulated as  $\tilde{P}(\tilde{T}, \tilde{\mu})$ . Then the corresponding thermodynamic differential relation is

$$d\tilde{P} = \left(\frac{\partial\tilde{P}}{\partial\tilde{T}}\right)_{\tilde{\mu}} d\tilde{T} + \left(\frac{\partial\tilde{P}}{\partial\tilde{\mu}}\right)_{\tilde{T}} d\tilde{\mu}. \quad (4.17)$$

According to Maxwell's relation,  $(d\mu/dP)_T = \rho^{-1}$ , therefore it can be demonstrated that

$$\left(\frac{\partial\tilde{P}}{\partial\tilde{\mu}}\right)_{\tilde{T}} = \frac{\rho}{\rho_C} \equiv \tilde{\rho}. \quad (4.18)$$

Furthermore,

$$\left(\frac{\partial\tilde{P}}{\partial\tilde{T}}\right)_{\tilde{\mu}} = \frac{T}{P_C} \left[ \left(\frac{\partial P}{\partial T}\right)_{\tilde{\mu}} - \frac{P}{T} \right]. \quad (4.19)$$

Equation (4.19) can be simplified by using the chain rule for partial differentiation, the triple-product rule and  $(d\mu/dT)_P = -s$ , yielding

$$\left(\frac{\partial P}{\partial T}\right)_{\tilde{\mu}} = -\frac{\left(\frac{\partial P}{\partial\tilde{\mu}}\right)_T}{\left(\frac{\partial T}{\partial\tilde{\mu}}\right)_P} = -\frac{\left(\frac{\partial P}{\partial\mu}\right)_T \left(\frac{\partial\mu}{\partial\tilde{\mu}}\right)_T}{\left(\frac{\partial\mu}{\partial\mu}\right)_P \left(\frac{\partial\tilde{\mu}}{\partial\tilde{\mu}}\right)_P} = \rho s \left(1 + \frac{\mu}{Ts}\right). \quad (4.20)$$

Since  $\mu = e + P/\rho - Ts$ , where  $e$  is the specific internal energy, it is found that

$$\left(\frac{\partial\tilde{P}}{\partial\tilde{T}}\right)_{\tilde{\mu}} = \frac{e\rho}{P_C} \equiv \tilde{e}, \quad (4.21)$$

ergo

$$d\tilde{P} = \tilde{e}d\tilde{T} + \tilde{\rho}d\tilde{\mu}. \quad (4.22)$$

Coming back to Eq. (4.18), the density is computed from the following expression, which is derived by differentiating Eq. (4.12) with respect to  $\tilde{\mu}$  along an isotherm:

$$\frac{\rho}{\rho_C} = \left[ 1 + \tilde{P}_{11}\Delta\tilde{T} + \left(\frac{\partial\Delta\tilde{P}}{\partial\Delta\tilde{\mu}}\right)_{\Delta\tilde{T}} \right]. \quad (4.23)$$

From Eq. (4.13) and the fact that

$$\left(\frac{\partial\Delta\tilde{P}}{\partial\Delta\tilde{\mu}}\right)_{\Delta\tilde{T}} = \left(\frac{\partial\Delta\tilde{P}}{\partial r}\right)_{\theta} \left(\frac{\partial r}{\partial\Delta\tilde{\mu}}\right)_{\Delta\tilde{T}} + \left(\frac{\partial\Delta\tilde{P}}{\partial\theta}\right)_r \left(\frac{\partial\theta}{\partial\Delta\tilde{\mu}}\right)_{\Delta\tilde{T}}, \quad (4.24)$$

application of the triple-product rule and the chain rule for partial differentiation gives

$$\left(\frac{\partial\Delta\tilde{P}}{\partial\Delta\tilde{\mu}}\right)_{\Delta\tilde{T}} = r^{\bar{\beta}} \left[k_0 + r^{\bar{\Delta}_1} k_1\right] \theta + c \left(\frac{\partial\Delta\tilde{P}}{\partial\Delta\tilde{T}}\right)_{\Delta\tilde{\mu}}, \quad (4.25)$$

whereby

$$\left(\frac{\partial\Delta\tilde{P}}{\partial\Delta\tilde{T}}\right)_{\Delta\tilde{\mu}} = \alpha r^{\bar{\beta}(\bar{\delta}+1)-1} \left[k_0 \hat{s}_0(\theta) + r^{\bar{\Delta}_1} k_1 \hat{s}_1(\theta)\right]. \quad (4.26)$$

In these two parametric equations for the singular terms,  $\alpha$ ,  $k_0$ ,  $k_1$ , and  $c$  are the previously mentioned substance-dependent scaling-function constants,  $\hat{s}_0(\theta)$ , and  $\hat{s}_1(\theta)$  are auxiliary functions and depend only on  $\theta$ . In a similar way as outlined for the density, an expression can be derived for the specific internal energy  $e$  by differentiating Eq. (4.12) with respect to  $\tilde{T}$  at constant  $\tilde{\mu}$ .

Using the same procedure as described in the previous paragraph, Albright et. al. [2] derive and present thermodynamic relationships that can be used to determine commonly used thermal and caloric properties. For example, successive use of the chain rule for differentiation and

$$\left(\frac{\partial F}{\partial\Delta\tilde{\mu}}\right)_{\Delta\tilde{T}} = \frac{\left(\frac{\partial F}{\partial r}\right)_{\theta} \left(\frac{\partial\Delta\tilde{T}}{\partial\theta}\right)_r - \left(\frac{\partial F}{\partial\theta}\right)_r \left(\frac{\partial\Delta\tilde{T}}{\partial r}\right)_{\theta}}{\left(\frac{\partial\Delta\tilde{\mu}}{\partial r}\right)_{\theta} \left(\frac{\partial\Delta\tilde{T}}{\partial\theta}\right)_r - \left(\frac{\partial\Delta\tilde{\mu}}{\partial\theta}\right)_r \left(\frac{\partial\Delta\tilde{T}}{\partial r}\right)_{\theta}} \quad (4.27)$$

and

$$\left(\frac{\partial F}{\partial\Delta\tilde{T}}\right)_{\Delta\tilde{\mu}} = \frac{\left(\frac{\partial F}{\partial r}\right)_{\theta} \left(\frac{\partial\Delta\tilde{\mu}}{\partial\theta}\right)_r - \left(\frac{\partial F}{\partial\theta}\right)_r \left(\frac{\partial\Delta\tilde{\mu}}{\partial r}\right)_{\theta}}{\left(\frac{\partial\Delta\tilde{\mu}}{\partial\theta}\right)_r \left(\frac{\partial\Delta\tilde{T}}{\partial r}\right)_{\theta} - \left(\frac{\partial\Delta\tilde{\mu}}{\partial r}\right)_{\theta} \left(\frac{\partial\Delta\tilde{T}}{\partial\theta}\right)_r}, \quad (4.28)$$

with  $F(r, \theta)$  being any parametric function, gives

$$\begin{aligned} \left(\frac{\partial P}{\partial \rho}\right)_T &= -\frac{P_C}{\tilde{T}} \left(\frac{\partial \tilde{P}}{\partial \rho}\right)_T = -\frac{P_C}{\tilde{T}\rho_C} \left(\frac{\partial \tilde{P}}{\partial \tilde{\rho}}\right)_{\tilde{T}} = -\frac{P_C}{\tilde{T}\rho_C} \frac{\left(\frac{\partial \tilde{P}}{\partial \Delta \tilde{\mu}}\right)_{\Delta \tilde{T}}}{\left(\frac{\partial \tilde{\rho}}{\partial \Delta \tilde{\mu}}\right)_{\Delta \tilde{T}}} \\ &= -\frac{P_C}{\rho_C} \left[ \frac{\tilde{\rho}}{\tilde{T} \left(\frac{\partial^2 \tilde{P}}{\partial \Delta \tilde{\mu}^2}\right)_{\Delta \tilde{T}}} \right] = -\frac{P_C}{\rho_C} \left[ \frac{\tilde{\rho}}{\tilde{T} \left(\frac{\partial^2 \Delta \tilde{P}}{\partial \Delta \tilde{\mu}^2}\right)_{\Delta \tilde{T}}} \right], \quad (4.29) \end{aligned}$$

where

$$\begin{aligned} \left(\frac{\partial^2 \Delta \tilde{P}}{\partial \Delta \tilde{\mu}^2}\right)_{\Delta \tilde{T}} &= \left( \frac{\partial \left( \frac{\partial \Delta \tilde{P}}{\partial \Delta \tilde{\mu}} \right)_{\Delta \tilde{T}}}{\partial \Delta \tilde{\mu}} \right)_{\Delta \tilde{T}} \\ &\stackrel{\text{Eq. (4.27)}}{=} \alpha^{-1} r^{\bar{\beta}(1-\bar{\delta})} \left[ k_0 \hat{u}_0(\theta) + r^{\bar{\Delta}_1} k_1 \hat{u}_1(\theta) \right] + \\ &\quad 2cr^{\bar{\beta}-1} \left[ k_0 \hat{v}_0(\theta) + r^{\bar{\Delta}_1} k_1 \hat{v}_1(\theta) \right] + \\ &\quad c^2 \left( \frac{\partial^2 \Delta \tilde{P}}{\partial \Delta \tilde{T}^2} \right)_{\Delta \tilde{\mu}} \quad (4.30) \end{aligned}$$

and

$$\left(\frac{\partial^2 \Delta \tilde{P}}{\partial \Delta \tilde{T}^2}\right)_{\Delta \tilde{\mu}} \stackrel{\text{Eq. (4.28)}}{=} \alpha r^{\bar{\beta}(\bar{\delta}+1)-2} \left[ k_0 \hat{w}_0(\theta) + r^{\bar{\Delta}_1} k_1 \hat{w}_1(\theta) \right]. \quad (4.31)$$

Computation of  $\Gamma$  additionally requires expressions for the following derivatives, viz.  $(\partial^2 P / \partial \rho^2)_T$ ,  $(\partial^2 P / \partial T^2)_\rho$ ,  $(\partial^2 P / \partial \rho \partial T)_{\rho, T}$ , and  $(\partial C_v / \partial T)_\rho$ . Moreover, terms containing derivatives with respect to the specific volume in the expression for  $\Gamma$  must be converted into density-based derivatives, that is

$$\Gamma = 1 + \frac{\rho}{c} \left( \frac{\partial c}{\partial \rho} \right)_s \Leftrightarrow \Gamma = \frac{1}{2c^2 \rho^3} (\bar{\Gamma}_1 + \bar{\Gamma}_2 + \bar{\Gamma}_3), \quad (4.32)$$

where

$$\bar{\Gamma}_1 = \rho^4 \left( \frac{\partial^2 P}{\partial \rho^2} \right)_T + 2\rho^3 \left( \frac{\partial P}{\partial \rho} \right)_T \quad (4.33a)$$

$$\bar{\Gamma}_2 = 3 \frac{T\rho^2}{C_v} \left( \frac{\partial P}{\partial T} \right)_\rho \left( \frac{\partial^2 P}{\partial \rho \partial T} \right)_{T,\rho} \quad (4.33b)$$

$$\bar{\Gamma}_3 = \left[ \frac{T}{C_v} \left( \frac{\partial P}{\partial T} \right)_\rho \right]^2 \times \left[ 3 \left( \frac{\partial^2 P}{\partial T^2} \right)_\rho + \frac{1}{T} \left( \frac{\partial P}{\partial T} \right)_\rho \left( 1 - \frac{T}{C_v} \left( \frac{\partial C_v}{\partial T} \right)_\rho \right) \right], \quad (4.33c)$$

and the thermodynamic speed of sound,  $c$ , is computed from

$$c^2 = \left( \frac{\partial P}{\partial \rho} \right)_T + \frac{T}{\rho^2 C_v} \left( \frac{\partial P}{\partial T} \right)_\rho^2. \quad (4.33d)$$

The procedure to determine the above-mentioned missing functions is not complicated yet laborious and by using the same procedure as outlined for  $(\partial P/\partial \rho)_T$ , the missing thermodynamic relationships have been determined and are provided in Appendix C.

### 4.5.2 Previous work related to compressible dynamics in the critical region

From a gas-dynamic viewpoint, the anomalous behavior of near-critical fluids entails a variety of interesting fluid dynamic phenomena. Examples include the inversion of reflection rules for acoustic waves in near-critical fluids [230] and the so-called piston effect – hereby, in spite of the fact that the thermal diffusivity of near-critical substances is very low and under micro-gravity conditions buoyant convection is absent, the thermal boundary layer formed near a heated wall of a confined cavity, due to the high compressibility of the fluid, expands within the acoustic time-scale as a piston, thereby heating-up the bulk of the fluid [228, 18, 227, 229, 23, 126]. Moreover, strong temperature gradients near the wall can even result in the formation of shock waves [20].

Regarding the study of near-critical shock waves, the experimental study of Borisov et. al. [17] reports the observation of a rarefaction shock wave of non-negligible thickness in the single-phase of near-critical freon-13 (chlorotrifluoromethane, Cl-C-F<sub>3</sub>) generated using an approximately 3-meter-long thermostated shock tube. The results reported by Borisov et. al. are particularly interesting, since the admissibility of rarefaction shock waves requires, as indicated in Chap. 2, the nonlinearity coefficient  $\Gamma$  to be negative (at least in a finite thermodynamic region) or change sign. Indeed, Borisov and coworkers do present a, be it brief, demonstration that the nonlinearity coefficient  $\Gamma$  diverges as the critical point is approached: in their paper, Borisov et. al. [17] present in Fig. 7 therein, that along the critical isotherm  $\Gamma \rightarrow +\infty$  as  $(P - P_C) \downarrow 0$  and

that  $\Gamma \rightarrow -\infty$  as  $(P - P_C) \uparrow 0$ , that is to say that there exists a region of negative nonlinearity to the right of the critical point in the  $P$ - $v$  thermodynamic plane.

Borisov's results on the divergence of  $\Gamma$  near the critical point are corroborated in a theoretical/numerical study conducted by Gulen et. al. [85] in the late 80s. By employing an extended Benedict-Webb-Rubin-type multiparameter equation of state with an improvised switching function to better describe the critical singularities, Gulen and coworkers demonstrate that the fundamental derivative of gas dynamics in the single-phase region diverges to either  $+\infty$  or  $-\infty$  depending on the direction of approach of the critical point.

However, the results of these two earlier computations on  $\Gamma$  in the critical region are contrary to the outcome of computations performed by Emanuel [61], where the application of the scaling methods, as reviewed in Ssec 4.5.1, yielded that  $\Gamma$  diverges to  $+\infty$  in the single-phase region of a single-component fluids independent of the direction of approach of the critical point (see also Ref. [174] although therein,  $\Gamma$  is computed numerically using a finite difference method applied to the cross-over scaled fundamental equation of SF<sub>6</sub> [219]).

These two different outcomes on the behavior of the fundamental derivative of gas dynamics, i.e., on the one hand the results of Borisov et. al. [17] and Gulen et. al. [85] and on the other hand Emanuel's [61] results, justifies further study in this field. For this purpose, using the scaled fundamental equation outlined in Ssec 4.5.1,  $\Gamma$  is computed in the critical region for methane, water and carbon dioxide. Moreover, these substances do not exhibit a negative nonlinearity region as identified in Fig. 1.1, because within the context of nonclassical gas dynamics, these fluids are not sufficiently molecularly complex. As a final remark it should be stated that near-critical behavior is universal and consequently, from a qualitative point of view, the results for the behavior of  $\Gamma$  are similar for all pure compounds which have a vapor-liquid critical point according to the 3-dimensional Ising universality class.

In terms of thermodynamic properties that are more meaningful than  $(r, \theta)$ , Fig. 4.13 shows the  $P$ - $\rho$ -plane of methane with selected iso- $\Gamma$ -lines, isotherms and isentropes. It is evident from the results that as the critical point is approached from the single-phase region,  $\Gamma$  tends to increase to large values, where for a given  $r$ ,  $\Gamma^L > \Gamma^V$ . Furthermore, Figs. 4.14 and 4.15 show the fundamental derivative of gas dynamics along the saturated-vapor line and the critical isochore, respectively, of methane in the single-phase critical region as a function of  $|\Delta\tilde{T}| \equiv |T - T_C|/T$ . It is readily demonstrated that along the dew-line as  $\Delta\tilde{T} \uparrow 0$ ,  $\Gamma^V \propto |\Delta\tilde{T}|^{1-\bar{\beta}\bar{\delta}-\bar{\beta}} \rightarrow +\infty$ , and that along the critical isochore as  $\Delta\tilde{T} \downarrow 0$ ,  $\Gamma \propto (\Delta\tilde{T})^{\bar{\alpha}-1} \rightarrow +\infty$ . Note that  $\bar{\alpha} - 1 = 1 - \bar{\beta}\bar{\delta} - \bar{\beta} \approx -0.89$  (see e.g., Levelt-Sengers et. al. [132]).

To illustrate the universality of the observed behavior of the fundamental derivative of gas dynamics in the single-phase region, Fig. 4.16 presents the re-

sults of computations performed with water and carbon dioxide along the critical isochore and the dew-line (calculations were also performed for ethylene and isobutane with qualitatively similar results for  $\Gamma$ ). For both water and carbon dioxide it is found that as  $\Delta\tilde{T} \uparrow 0$   $\Gamma^V \propto |\Delta\tilde{T}|^{1-\beta\delta-\beta} \rightarrow +\infty$  along the dew-line, and that as  $\Delta\tilde{T} \downarrow 0$ ,  $\Gamma \propto (\Delta\tilde{T})^{\alpha-1} \rightarrow +\infty$  along the critical isochore.

The results obtained up to now for the fundamental derivative of gas dynamics in the single-phase critical region clearly demonstrate that  $\Gamma$  is positive and diverges to  $+\infty$  independent of the direction of approach of the vapor-liquid critical point and can be viewed as a verification of the results of Emanuel [61].

Based on the outcome that  $\Gamma$  is positive in the near-critical state, it can therefore be stated that the phenomenon observed by Borisov and coworkers [17]

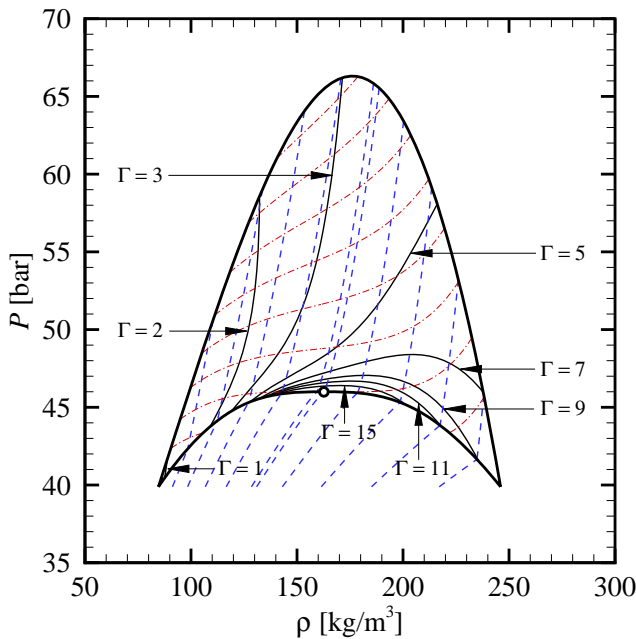


Figure 4.13: The pressure-density plane of methane in the critical region. Properties are computed with the scaled fundamental equation reported by Kurumov et al. [118]. The solid lines indicate iso- $\Gamma$  lines (all of which are labeled), the dashed lines indicate isentropes and the dash-dotted lines represent isotherms.  $\circ$ : critical point of methane.

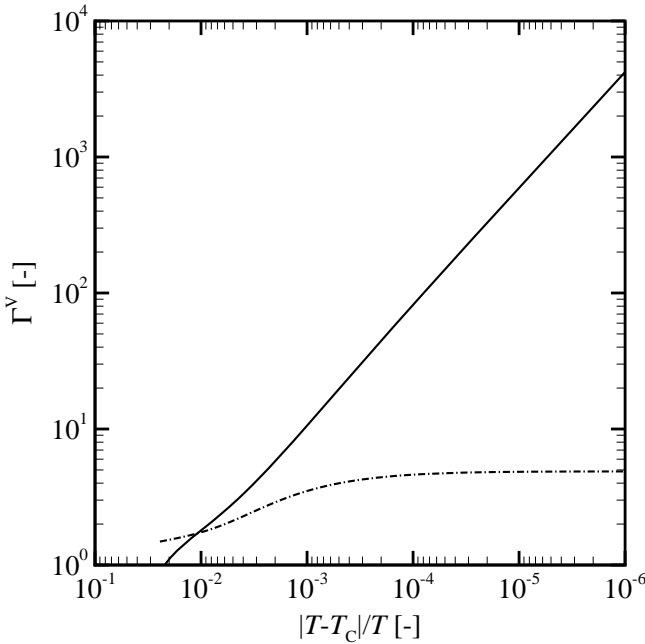


Figure 4.14: *The fundamental derivative of gas dynamics along the saturated-vapor line of methane as a function of  $|\Delta\tilde{T}| \equiv |T - T_C|/T$ . The solid line is obtained from application of the scaled fundamental equation of Kurumov et. al. [118] and the dashed line is obtained from application of the Wagner-Setzmann reference EoS [181]. Remark that  $\lim_{\Delta\tilde{T} \uparrow 0} \Gamma^V \propto |\Delta\tilde{T}|^{1-\tilde{\beta}\delta-\tilde{\beta}} \rightarrow +\infty$ .*

cannot be a nonclassical expansion shock wave in the single-phase regime. This is also pointed out by Ferguson [65], whereby numerical simulations have shown that the expansion process across the wave studied by Borisov et. al. is partly conducted in the two-phase regime. Also Kluwick [114] points out using the results of Piechór [162], that the post-shock state of the wave created by Borisov et. al. was influenced by capillary forces. Nevertheless, the fact that the wave generated by Borisov et. al. featured a steady profile in time also has to be taken into consideration. The main idea here is that  $\Gamma$  can be negative in the two-phase region of the test fluid, thereby causing the wave created by Borisov et. al. to be a rarefaction shock wave, be it one with vapor-liquid transition. This is investigated in the subsequent subsection.

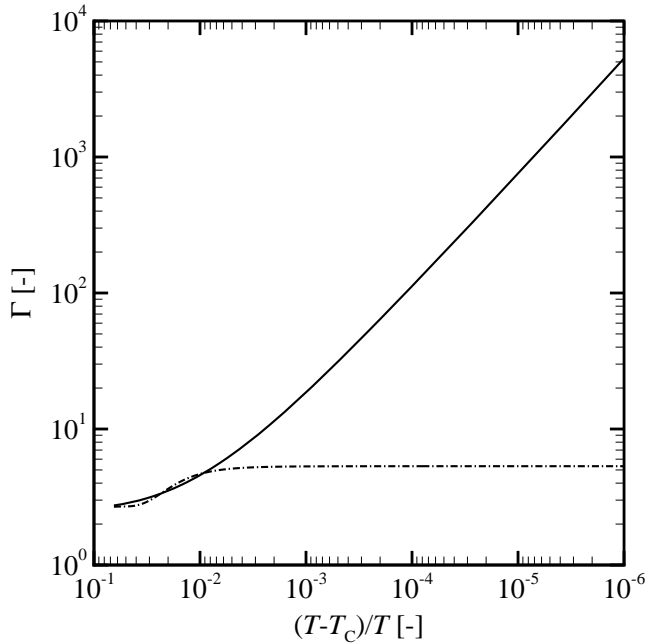
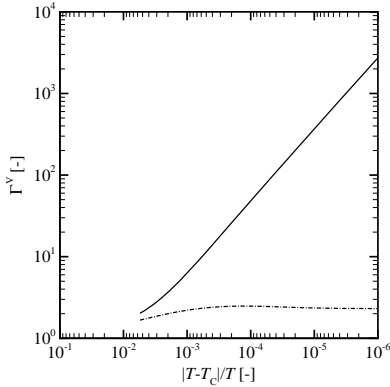


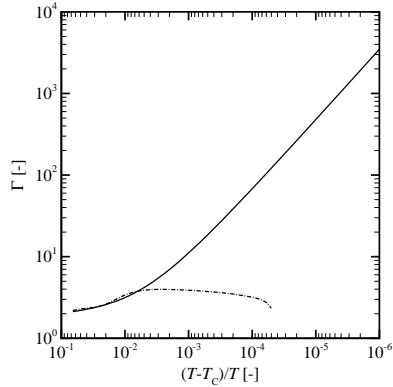
Figure 4.15: The fundamental derivative of gas dynamics along the critical isochore of methane as a function of  $\Delta\tilde{T} \equiv (T - T_C)/T$ . The solid line is obtained from application of the scaled fundamental equation of Kurumov et. al. [118] and the dashed line is obtained from application of the Wagner-Setzmann reference EoS [181]. Remark that  $\lim_{\Delta\tilde{T} \downarrow 0, \rho_C} \Gamma \propto (\Delta\tilde{T})^{\bar{\alpha}-1} \rightarrow +\infty$ , where  $\bar{\alpha} - 1 = 1 - \bar{\beta}\bar{\delta} - \bar{\beta}$  (see e.g., Levelt-Sengers et. al. [132]).

### 4.5.3 The fundamental derivative of compressible dynamics in the two-phase critical region

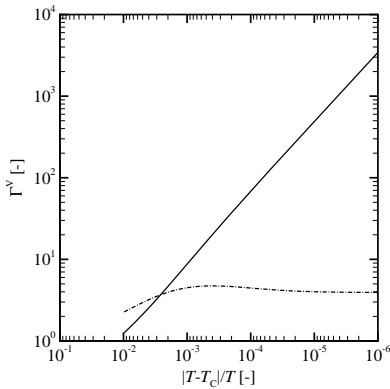
The motivation for studying the behavior of the fundamental derivative of gas dynamics in the critical vapor-liquid equilibrium region is twofold. In the first place, within the context of this study, the steady rarefaction wave created and observed by Borisov, as discussed in the previous subsection, may be a shock wave featuring two-phase transition. This would mandate  $\Gamma$  to be negative in part of the critical VLE region. It should be noted that expansion evaporation shock waves featuring liquid-to-vapor transition in retrograde fluids due to  $\Gamma = -\infty$  at the phase-boundary (see e.g., Thompson et. al. [202, 199, 200]) are



(a)  $\Gamma$  along the dew-line of water.



(b)  $\Gamma$  along the critical isochore of water.



(c)  $\Gamma$  along the dew-line of carbon dioxide.



(d)  $\Gamma$  along the critical isochore of carbon dioxide.

Figure 4.16:  $\Gamma$  in the critical region of water and carbon dioxide. The solid line is obtained by using the scaled fundamental equation: relevant system-dependent parameters for water are found in Ref. [179] and for carbon dioxide in Ref. [2]. The dash-dotted line is determined with the reference EoS of the fluid: see details in Ref. [212] for water and in Ref. [185] for carbon dioxide. Remark that there are minor discrepancies between the  $T_C$  and  $\rho_C$  of the reference EoS and the scaled fundamental equations.

not considered herein. Secondly, on the basis of an unreferenced steam table, Novikov [156] reports that water exhibits a region of negative nonlinearity in the

two-phase critical region; a claim which is confirmed by Kahl and Mylin [107] (see Fig. 3 therein) within the context of the admissibility of rarefaction shock waves. This means that it is possible according to conventional multiparameter EoS to have negative- $\Gamma$  values in the VLE region.

The scaled fundamental equation can be used to determine properties in the vapor-liquid-equilibrium (VLE) region under validity of the hypothesis of thermodynamic equilibrium; meta-stable states are therefore excluded. What is more is that as far as two phases are concerned, i) these form a homogeneous mixture, and ii) the influence of surface-tension is negligible and the size of droplets or bubbles is negligibly small. To elucidate the use of the scaled fundamental equation in the VLE region consider a closed system with a vapor fraction of  $\varpi$ . Then the corresponding entropy at temperature  $T'$  is determined from the law of mass conservation, namely  $s(T') = \varpi s^V(T') + (1 - \varpi) s^L(T')$ , where  $s^V(T')$  and  $s^L(T')$  are the saturated vapor and liquid entropy respectively, evaluated at  $T'$ . Since here the scaled EoS is formulated in terms of parametric variables  $r$  and  $\theta$ , saturated vapor properties are evaluated along the  $\theta = -1$ -line whereas saturated liquid properties are evaluated along the  $\theta = +1$ -line and the corresponding value of  $r$  at a given saturation temperature is computed from Eq(ns). ((4.15) and) (4.16).

Using a similar procedure as outlined in the previous subsection, successive use of the triple product rule and the chain rule for partial differentiation allows for computing  $\Gamma$  in the VLE region. Relevant equations for this purpose are given in Appendix D. In the following, an example is presented to determine the expression for the speed of sound in the VLE region (under the hypothesis of a two-phase homogeneous equilibrium mixture with negligibly small surface-tension effects). From the definition of the thermodynamic speed of sound, it follows that

$$c^2 = -v^2 \left( \frac{\partial v}{\partial P} \right)_s^{-1} \quad (4.34)$$

Since from the law of mass conservation,  $v = \varpi v^V + (1 - \varpi) v^L$ , then

$$\left( \frac{\partial v}{\partial P} \right)_s = \varpi \left[ \left( \frac{dv^V}{dP} \right) - \left( \frac{dv^L}{dP} \right) \right] + (v^V - v^L) \left( \frac{\partial \varpi}{\partial P} \right)_s + \left( \frac{dv^L}{dP} \right). \quad (4.35)$$

Using  $s = \varpi s^V + (1 - \varpi) s^L$ ,

$$\left( \frac{\partial \varpi}{\partial P} \right)_s = \left( \frac{\varpi - 1}{s^V - s^L} \right) \left( \frac{ds^L}{dP} \right) - \left( \frac{\varpi}{s^V - s^L} \right) \left( \frac{ds^V}{dP} \right). \quad (4.36)$$

Here,  $(ds^{V,L}/dP)$  can be computed by employing the composite derivative rule for partial differential equations as follows

$$\left( \frac{ds^{V,L}}{dP} \right) = \left( \frac{\partial s}{\partial T} \right)_P \frac{1}{\left( \frac{dP}{dT} \right)^{\text{sat}}} + \left( \frac{\partial s}{\partial P} \right)_T, \quad (4.37)$$

where

$$\left(\frac{dP}{dT}\right)^{\text{sat}} = \frac{s^{\text{V}} - s^{\text{L}}}{v^{\text{V}} - v^{\text{L}}} \quad (4.38)$$

is Clapeyron's equation, and  $(\partial s/\partial T)_P$  and  $(\partial s/\partial P)_T$  are properties evaluated along an isobar and isotherm respectively, as the saturation lines are approached from the single-phase region. By further using standard thermodynamic relations, it is found that

$$\left(\frac{ds^{\text{V,L}}}{dP}\right) = \frac{C_P^{\text{V,L}}}{T^{\text{sat}}} \frac{1}{\left(\frac{dP}{dT}\right)^{\text{sat}}} + \frac{\left(\frac{\partial P}{\partial T}\right)_{v^{\text{V,L}}}}{\left(\frac{\partial P}{\partial v}\right)_{T^{\text{sat}}}}. \quad (4.39)$$

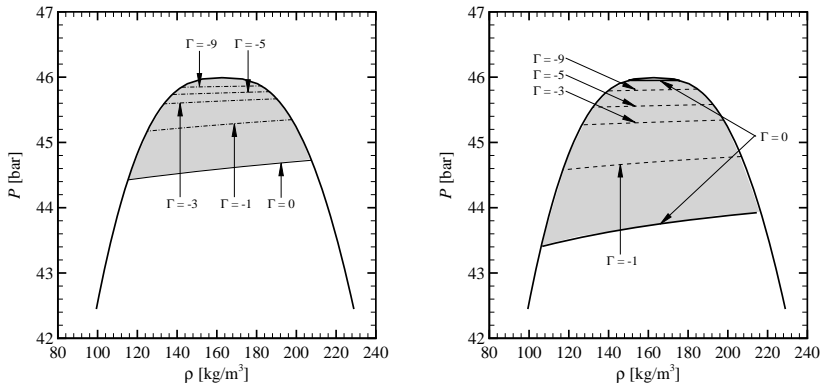
Here,  $C_P^{v=v^{\text{V,L}}}$  is the isobaric heat capacity of either the saturated vapor or liquid phase in the limit that the saturated state is approached from the single-phase region. Results to determine  $\Gamma$  in the VLE region is similar to what has been outlined for the two-phase sound speed and the necessary equations are presented in Appendix D (for further details see Ref. [152]).

Figure 4.17 gives the results of calculations performed in the two-phase critical region of methane using both the scaled fundamental equation of Kurumov et. al. and the Wagner-Setzmann reference EoS. It is observed that both EoS's predict a region of  $\Gamma < 0$  in the two-phase critical region. According to the scaled fundamental equation, as the critical point is approached from  $(T - T_C) \uparrow 0$  along the two-phase critical isochore,  $\Gamma \propto \left(\Delta\tilde{T}\right) \left|\Delta\tilde{T}\right|^{\bar{\alpha}-2} \rightarrow -\infty$  with a power of  $\bar{\alpha} - 1 \approx -0.89$ . However, the Wagner-Setzmann reference EoS predicts a finite and positive value of  $\Gamma$  in the close vicinity of the critical point if it is approached from the VLE-region. The entire critical region of methane is shown in Fig. 4.18 in the  $P$ - $\rho$ -plane of methane together with the local value of  $\Gamma$ , assuming thermodynamic equilibrium.

Just as for the single-phase critical region, due to scale invariance one can conclude based on the universal nature of thermodynamic behavior in the critical region, that a wide class of fluids exhibit a  $\Gamma < 0$ -region in a portion of the two-phase critical region.

## 4.6 Concluding remarks

Herein, the possibility of calculating the fundamental derivative of gas dynamics by means of equations of state has been assessed. At present,  $\Gamma$  cannot be obtained by direct measurements, being a higher-order derivative of primary thermodynamic properties. Previous studies have shown a high degree of uncertainty, if relatively simple thermodynamic models are employed.



(a) The shaded area highlights the  $\Gamma < 0$ -region. Thermodynamic properties are computed with the scaled fundamental equation puted with the Wagner-Setzmann reference reported by Kurumov et. al. [118].  
 (b) The shaded area highlights the  $\Gamma < 0$ -region. Thermodynamic properties are computed with the Wagner-Setzmann reference EoS [181].

Figure 4.17: The fundamental derivative of gas dynamics in the critical region of methane. Here,  $\Gamma$  is computed in the vapor-liquid equilibrium region using both the scaled fundamental equation and the Wagner-Setzmann reference EoS. The shaded area represents the region of  $\Gamma < 0$ . The left and right boundaries of the  $\Gamma < 0$ -region is formed by the iso-quality lines ( $\varpi = \text{constant}$ ) in the limit that  $\varpi \uparrow 1$ , respectively  $\varpi \downarrow 0$ .

In order to obtain the most accurate values of the fundamental derivative of gas dynamics, reference equations of state were employed. In order to test the performance of these equations with respect to the estimation of the fundamental derivative of gas dynamics, values of  $\Gamma$  were calculated along the dew line for several alkanes and compared to values calculated with other highly accurate thermodynamic models. The accuracy of the obtained predictions has been assessed under several assumptions. Furthermore, simpler thermodynamic models adopted in the past for the computation of  $\Gamma$  of more complex fluids were used to perform the same calculations, using reference equations as a benchmark. This allows for an indication of the uncertainty involved in the use of simpler models. Also the calculation of  $\Gamma$  for fluids made of complex molecules was addressed by comparing values calculated with three different thermodynamic models. The influence of molecular complexity on the accuracy of  $\Gamma$  has been shortly discussed. The following conclusions can therefore be drawn:

1. If highly accurate EoS's are employed, the value of  $\Gamma$  can be calculated with

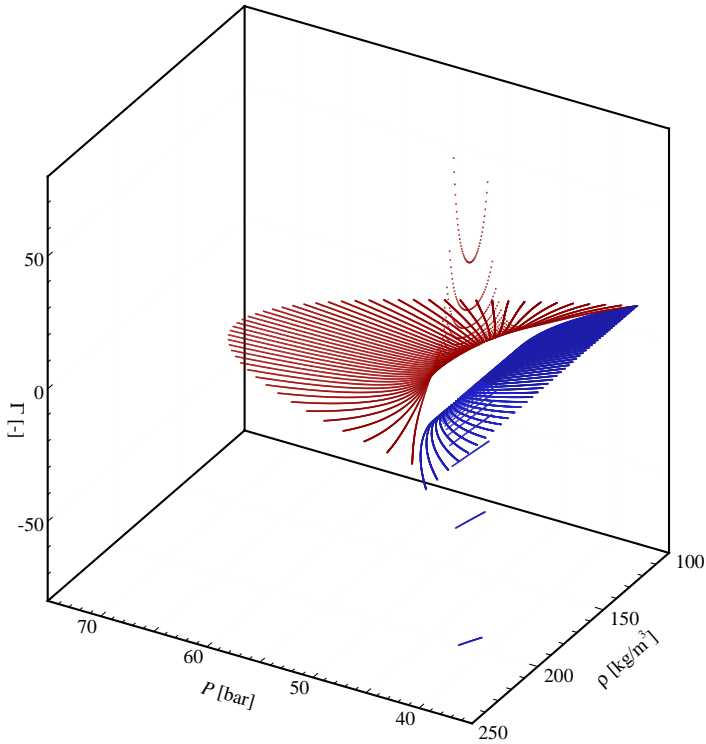


Figure 4.18: *The fundamental derivative of gas dynamics in the critical region of methane computed with the scaled fundamental equation of Kurumov et. al. [118].*

a degree of uncertainty that is suitable for dense-gas applications, namely the study and design of processes involving dense gases and of nonclassical gas dynamic experiments and processes.

2. The PRSV cubic equation of state has shown a better performance with respect to the calculation of  $\Gamma$ , if compared to the MH multiparameter model. Moreover, predictions of the minimum value of  $\Gamma$  with the PRSV equation of state are conservative with respect to predictions from the MH equation of state.
3. For fluids made of complex molecules, it is possible to achieve a comparatively higher level of accuracy in the estimation of  $\Gamma$  with respect to molecularly simpler fluids, if experimental data are available. If a sufficient number of accurate experimental data are available, multiparameter

technical equations of state can be developed and lead to an appreciable improvement with respect to the uncertainty of the estimation of  $\Gamma$ .

Finally, computations of  $\Gamma$  using scaled fundamental equations have shown that:

1. The high-pressure side of the region of negative nonlinearity in single-component fluids is located in the critical region; this can be concluded based on the universal behavior of critical phenomena.
2. There exists a region of negative- $\Gamma$  values in the two-phase critical region.
3. Reference EoS's yield physically incorrect results for  $\Gamma$  in the critical region.

As a last remark it must be mentioned that due to the lack of sufficient experimental thermodynamic property data, reference EoS's for potential BZT fluids are not available. This implies that out of necessity, model EoS's like the PRSV cubic EoS must be employed. Moreover, model EoS's are physically based, and as opposed to (semi-)empirical multiparameter EoS's, model EoS's have a limited number of substance-specific parameters. There exists the risk that in the case of multiparameter EoS's, it is always possible to tune the fluid-parameters such as to fit the functional form to all available experimental data, whilst physically correct behavior is lost. Using the multiparameter EoS's documented in Chap. 3 and the Peng-Robinson Stryjek-Vera modified cubic EoS, it is found that MD<sub>3</sub>M and linear dimethylsiloxanes of greater complexity and D<sub>6</sub> and cyclic dimethylsiloxanes of greater complexity are BZT fluids, even if the uncertainty in the heat capacity correlation is taken into consideration (see Ref. [30]).

Table 4.2: Previous studies on the identification of BZT fluids. All these fluids are indicated as exhibiting a region of negative nonlinearity according to the employed thermodynamic model. Legend: BWR: Benedict-Webb-Rubin EoS [13], HBMS: Hirschfelder-Buehler-McGee-Sutton EoS [92], MH: Martin-Hou EoS [136], mMH: modified Martin-Hou EoS [137], PRSV: Peng-Robinson EoS [161] modified by Stryjek and Vera [190], VdW: Van der Waals EoS, RK: Redlich-Kwong EoS [169], SRK: Soave-Redlich-Kwong EoS [183], CII: Clausius II EoS [59], WS: Wong-Sandler mixing rule [218], and SW: Span-Wagner functional form for the EoS [187].

Reference	Formula	Name	Thermodynamic Model
Lambrakis and Thompson [122]	$C_4H_{10}$	n-butane	Tabulated data <sup>1</sup> ; Virial
	$C_5H_{12}$	n-pentane	Tabulated data <sup>1</sup> ; Virial
	$C_6H_{14}$	n-hexane	Tabulated data <sup>1</sup> ; Virial
	$C_7H_{16}$	n-heptane	HBMS
	$C_8H_{18}$	n-octane	HBMS; BWR
	$C_9H_{20}$	n-nonane	HBMS; BWR
	$C_{10}H_{22}$	n-decane	HBMS; BWR; MH
	$C_6F_{14}$	perfluoro-n-hexane	Tabulated data <sup>2</sup> ; HBMS
	$C_{10}F_{22}$	perfluoro-n-decane	HBMS; MH
	$C_8F_{16}$	1,3-perfluorodimethylcyclohexane	Tabulated data <sup>2</sup> ; HBMS; MH
	$C_7F_{14}$	perfluoromethylcyclohexane	Tabulated data <sup>2</sup> ; HBMS
	$C_6F_6$	perfluorobenzene	Tabulated data <sup>2</sup> ; HBMS
	$C_{10}F_{18}$	perfluorodecalin	Tabulated data <sup>2</sup> ; HBMS; MH
	$C_{11}F_{20}$	perfluoromethyldecalin	Tabulated data <sup>2</sup> ; HBMS; MH
	$C_{15}H_{16}$	4-isopropylbiphenyl	Tabulated data <sup>3</sup> ; HBMS; MH
	$C_8F_{16}O$	perfluoro-2-butyltetrahydrofuran	Tabulated data <sup>4</sup>
Thompson and	$C_8F_{17}HO_2$	fluorinated ether E-2	HBMS; MH
Continued on the next page...			

Table 4.2 – Continued

Reference	Formula	Name	Method
Lambrakis [201]	C <sub>11</sub> F <sub>23</sub> HO <sub>3</sub>	fluorinated ether E-3	HBMS; MH
	C <sub>14</sub> F <sub>29</sub> HO <sub>4</sub>	fluorinated ether E-4	HBMS; MH
	C <sub>17</sub> F <sub>35</sub> HO <sub>5</sub>	fluorinated ether E-5	HBMS; MH
Cramer [44]	C <sub>12</sub> F <sub>27</sub> N	FC-43, pf-tributylamine	MH
	C <sub>15</sub> F <sub>33</sub> N	FC-70, pf-tripentylamine	MH
	C <sub>18</sub> F <sub>39</sub> N	FC-71, pf-trihexylamine	MH
	C <sub>13</sub> F <sub>22</sub>	PP-10, pf-perhydrofluorene	MH
	C <sub>14</sub> F <sub>24</sub>	PP-11, pf-perhydrophenanthrene	MH
	C <sub>16</sub> F <sub>26</sub>	PP-24, pf-fluoranthrene	MH
	C <sub>17</sub> F <sub>30</sub>	PP-25, pf-benzyltetralin	MH
Colonna and Silva [37]	C <sub>12</sub> H <sub>36</sub> O <sub>4</sub> Si <sub>5</sub>	MD <sub>3</sub> M, dodecamethylpentasiloxane	PRSV
	C <sub>14</sub> H <sub>42</sub> O <sub>5</sub> Si <sub>6</sub>	MD <sub>4</sub> M, tetradecamethylhexasiloxane	PRSV
	C <sub>8</sub> H <sub>24</sub> O <sub>4</sub> Si <sub>4</sub>	D <sub>4</sub> , octamethylcyclotetrasiloxane	PRSV
	C <sub>10</sub> H <sub>30</sub> O <sub>5</sub> Si <sub>5</sub>	D <sub>5</sub> , decamethylcyclopentasiloxane	PRSV
	C <sub>12</sub> H <sub>36</sub> O <sub>6</sub> Si <sub>6</sub>	D <sub>6</sub> , dodecamethylcyclohexasiloxane	PRSV
	Equimolar mixtures containing cyclic siloxanes of D <sub>i&gt;4</sub>		PRSV+WS
Guardone and Argrow [81]	C <sub>12</sub> F <sub>27</sub> N	FC-43, pf-tributylamine	VdW; RK; CII; PR; SRK; mMH
	C <sub>15</sub> F <sub>33</sub> N	FC-70, pf-tripentylamine	VdW; RK; CII; PR; SRK; mMH
	C <sub>18</sub> F <sub>39</sub> N	FC-71, pf-trihexylamine	VdW; RK; CII; PR; SRK; mMH
	C <sub>6</sub> F <sub>14</sub>	FC-72, perfluorohexane	VdW; RK
	C <sub>8</sub> F <sub>16</sub> O	FC-75	VdW; RK; CII
	C <sub>10</sub> F <sub>18</sub>	PP-5, perfluorodecalin	VdW; RK; CII; PR; SRK; mMH
	C <sub>11</sub> F <sub>20</sub>	PP-9, perfluoromethyldecalin	VdW; RK; CII; PR; SRK; mMH
	C <sub>13</sub> F <sub>22</sub>	PP-10, pf-perhydrofluorene	VdW; RK; CII; PR; SRK; mMH
	C <sub>14</sub> F <sub>24</sub>	PP-11, pf-perhydrophenanthrene	VdW; RK; CII; PR; SRK; mMH
C <sub>16</sub> F <sub>26</sub>	PP-24, pf-fluoranthrene	VdW; RK; CII; PR; SRK; mMH	

Continued on the next page...

Table 4.2 – Continued

Reference	Formula	Name	Method
	$C_{17}F_{30}$	PP-25, pf-benzyltetralin	VdW; RK; CII; PR; SRK; mMH
	$C_{11}F_{23}HO_3$	fluorinated ether E-3	VdW; RK; CII; PR; SRK; mMH
	$C_{14}F_{29}HO_4$	fluorinated ether E-4	VdW; RK; CII; PR; SRK; mMH
	$C_{17}F_{35}HO_5$	fluorinated ether E-5	VdW; RK; CII; PR; SRK; mMH
Colonna et. al. [30]	$C_{12}H_{36}O_4Si_5$	MD <sub>3</sub> M, Dodecamethylpentasiloxane	SW
	$C_{14}H_{42}O_5Si_6$	MD <sub>4</sub> M, Tetradecamethylhexasiloxane	SW
	$C_{12}H_{36}O_6Si_6$	D <sub>6</sub> , Dodecamethylcyclohexasiloxane	SW
1		L. N. Canjar and F. S. Manning. <i>Thermodynamic Properties and Reduced Correlations for Gases</i> . Gulf Publishing Company, Houston, Texas, 1967	
2		Imperial Smelting Corporation, Ltd. <i>Tables of Thermodynamic Properties for Flutec</i> . Bristol, England	
3		Monsanto Chemical Company. <i>Computer Tables of Thermodynamic Properties for CP 9</i> . St. Louis, Missouri, 1965	
4		R. M. Yarrington and W. B. Kay. Thermodynamic Properties of Perfluoro-2-Butyltetrahydrofuran. <i>J. Chem. Eng. Data.</i> , 5(1): 24-29, 1960	

## Nomenclature

Symbol	Description
$\alpha$	Scaling-field parameter in Eq. (4.14)
$\bar{b}^2$	Universal constant in Eq. (4.16)
$C_P$	Specific isobaric heat capacity
$C_v$	Specific isochoric heat capacity
$c$	Speed of sound
$\mathbf{c}$	Scaling-field parameter in Eq. (4.16)
$c_i$	EoS-specific parameter in Eq. (4.3)
$d_i$	EoS-specific parameter in Eq. (4.3)
$e$	Specific internal energy
$h$	Specific enthalpy
$k_0$	Scaling-field parameter in Eq. (4.14)
$k_1$	Scaling-field parameter in Eq. (4.14)
$n_i$	Fluid-specific parameter in Eq. (4.3)
$P$	Pressure
$\tilde{P}_i$ or $\tilde{P}_{11}$	Pressure background parameters
$\hat{p}_0$	Auxiliary function in Eq. (4.14) (see Table C.3)
$\hat{p}_1$	Auxiliary function in Eq. (4.14) (see Table C.3)
$R$	Specific gas constant
$r$	Parametric distance variable
$s$	Specific entropy
$\hat{s}_0$	Auxiliary function in Eq. (4.26) (see Table C.3)
$\hat{s}_1$	Auxiliary function in Eq. (4.26) (see Table C.3)
$T$	Temperature
$t_i$	EoS-specific parameter in Eq. (4.3)
$\hat{u}_0$	Auxiliary function in Eq. (4.30) (see Table C.3)
$\hat{u}_1$	Auxiliary function in Eq. (4.30) (see Table C.3)
$v$	Specific volume
$\hat{v}_0$	Auxiliary function in Eq. (4.30) (see Table C.3)
$\hat{v}_1$	Auxiliary function in Eq. (4.30) (see Table C.3)

Continued on the next page...

Continued

Symbol	Description
$\hat{w}_0$	Auxiliary function in Eq. (4.31) (see Table C.3)
$\hat{w}_1$	Auxiliary function in Eq. (4.31) (see Table C.3)
$Z$	Compressibility factor
$\bar{\alpha}$	Critical exponent of Ising-like systems defined along the critical isochore
$\alpha_i$	EoS-specific parameter in Eq. (4.3)
$\bar{\beta}$	Critical exponent of Ising-like systems defined along the saturation line
$\beta_P$	Coefficient of volume expansion
$\beta_i$	EoS-specific parameter in Eq. (4.3)
$\Gamma$	Fundamental derivative of gas dynamics
$\gamma_i$	EoS-specific parameter in Eq. (4.3)
$\bar{\Delta}_1$	Gap exponent of Ising-like systems
$\Delta_i$	EoS-specific parameter in Eq. (4.3)
$\delta$	Reduced density
$\bar{\delta}$	Critical exponent of Ising-like systems defined along the critical isotherm
$\theta$	Parametric contour variable
$\kappa_T$	Isothermal compressibility
$\mu$	Chemical potential
$\tilde{\mu}_i$ or $\tilde{\mu}_C$	Thermal background parameters
$\varpi$	Vapor fraction
$\rho$	Density
$\tau$	Inverse reduced temperature
$\Psi$	Helmholtz free energy
$\psi$	Reduced Helmholtz free energy
$\omega$	Acentric factor

*“And so the fact that they purchased the machine meant somebody had to make the machine. And when somebody makes a machine, it means there’s jobs at the machine-making place.”*

President George W. Bush, Mesa, Arizona, May 27, 2008

# 5

## Methods for the experimental investigation of nonclassical gas-dynamic phenomena

### **Abstract**

*Theoretically, a variety of viable experimental options are available for the investigation of nonclassical gas-dynamic phenomena. In particular, emphasis is placed on setups that allow for the generation and detection of expansion shock waves in molecularly complex substances, e.g., dimethylsiloxanes. After a thorough assessment of many possible options, each of which is treated in detail in this chapter, a facility is proposed which incorporates the operational ease, modularity and versatility of both the variable-cross-section shock tube and the Ludwig tube. The so-called Flexible Asymmetric Shock Tube (FAST) is used for creating a pure rarefaction shock wave in the charge-tube section and, in order to increase the availability of the facility, it is equipped with a specially designed fast-opening valve.*

### **5.1 Introduction**

Hitherto, the emphasis was placed on the fundamentals of nonclassical gas dynamics and relevant aspects of the affiliated thermodynamic property, viz. the nonlinearity coefficient  $\Gamma$ . Herein, experimental options are presented that the-

oretically allow for generating and studying nonclassical wave fields which originate and persist in the single-phase dense-gas thermodynamic regime of a single component fluid. More specifically, the nonclassical phenomenon which is at the focal point is the rarefaction shock wave. The reasons for choosing a rarefaction shock wave instead of a compression fan, are threefold. First of all, shock waves in general are more exotic phenomena compared to fans and speak more to the imagination. Secondly, two earlier experiments, namely one conducted in 1983 and one in 2001 in two different laboratories, have also focussed on the generation of rarefaction shock waves, albeit not explicitly. In this context, the results of the experiment of Borisov et. al. [17] are disputed by Ferguson [65] and in the second attempt at the University of Colorado at Boulder, many technical difficulties were encountered, like thermochemical decomposition of the working fluid, just to mention one problem. Thirdly, the admissibility region of rarefaction shock waves in terms of pressure and temperature is larger than that of compression fans, as demonstrated by Zamfirescu et. al. [226], therefore choosing and setting the initial states of an experiment to create a nonclassical shock wave is comparatively simpler.

The options for experiments are subdivided into unsteady and steady types. The following sections provide an overview of each category (an exhaustive discussion on possible experimental options is presented in Chaps. 4–6 of Zamfirescu et. al. [224]). Firstly, the associated experimental facility is described, followed by a treatment of the procedure to determine the initial states of such an experiment. Moreover, emphasis is placed on how the phenomenon under scrutiny is to be obtained, what is to be measured and how such a measurement is to be performed with the greatest reliability and the highest (acceptable) accuracy. Secondly, relevant issues related to the design of the facility are discussed. Finally, the part on experimental options to study BZT effects is concluded with a comparative analysis whereby arguments for and against each experimental option/strategy are discussed. Based on these arguments, a setup is chosen that aims at the production of an unsteady rarefaction shock wave with maximal supersonic-to-sonic speed change; the experimental facility incorporates both the operational aspects of a simple shock tube and a Ludwig tube. The last section of this chapter treats the selection of the test fluid.

## 5.2 Unsteady experiments

### 5.2.1 The triple-discontinuity experiment

#### 5.2.1.1 The shock tube

There are many methods available for generating both classical and nonclassical shock waves. These methods include the creation of explosions, e.g., spherical shock waves, and shock waves that are formed due to a supersonic flow

past a body. However, for the study of the physical and chemical aspects of shock waves, a simple shock tube is often used because the wave fields are nearly planar and one-dimensional. The shock tube is a comparatively cheap and simple device that is commonly employed in aerodynamic and physics laboratories and it has applications in the study of combustion, e.g., in Refs. [209, 16, 234], nucleation and droplet growth [53, 160, 215, 134], and the study of the kinetics of non-equilibrium phenomena, e.g., vibrational relaxation and dissociation [193, 74, 173, 109, 157, 56]. The conventional shock tube consists of a pipe of constant cross section which is separated into a high- and low-pressure compartment by a diaphragm. Variations to the standard design are common and include, for example, the diaphragmless shock tube [105, 206, 50] and the variable-cross-section shock tube [222, 194, 115]. The high-pressure gas, i.e., the driver gas, and the gas at low pressure, viz. the driven gas, can be chemically different fluids. When the diaphragm is ruptured, a compressive wave travels into the low-pressure section of the tube and an expansive wave propagates into the high-pressure compartment (see Fig. 5.2). Furthermore, a contact surface (CS) – this is a geometric surface of discontinuity which physically separates the driver gas from the driven gas because there is no mass flow through an ideal contact surface – moves in the direction of the compressive wave. The diaphragm requires some hundreds of microseconds to open. During the opening process a jet of driver gas flows out and forms a succession of compressive waves. These compressive waves superimpose nonlinearly and eventually coalesce into a shock wave. The initially distorted shock wave front becomes planar due to the interaction with the tube wall. Behind the shock wave the flow velocity is uniform. The compression shock wave (CSW) propagates at supersonic velocity with respect to the quiescent medium upstream of the wave, whereas the expansion wave spreads out in time (this wave is known as a rarefaction fan (RF)) as it moves into the high-pressure compartment. A picture of a transonic shock tube facility at the shock wave laboratory of the RWTH Aachen University is shown in Fig. 5.1.

Two methods are available for detecting and recording changes occurring in, due to, and beyond the geometric surfaces (CSW, CS and RF). One method uses instruments which continuously record the state of the substance with respect to time as the wave moves past the instruments (here the resolution in time is relevant). Alternatively, less intrusive visualization techniques are used which give an instantaneous image of the flow-field variables (here the spatial resolution is important). The choice of either method is governed by what quantities have to be measured, the physicochemical process(es) of interest, and the experimental facility itself.

The features of the above-mentioned wave fields are of the classical type and are observed, for example, in air under atmospheric conditions. Alternatively, Ferguson and collaborators [64] have demonstrated by numerically solving the shock conditions for perfluoro-tripentylamine (FC-70,  $C_{15}F_{33}N$ ) as test fluid and under validity of the Martin-Hou equation of state (MH EoS), that it is

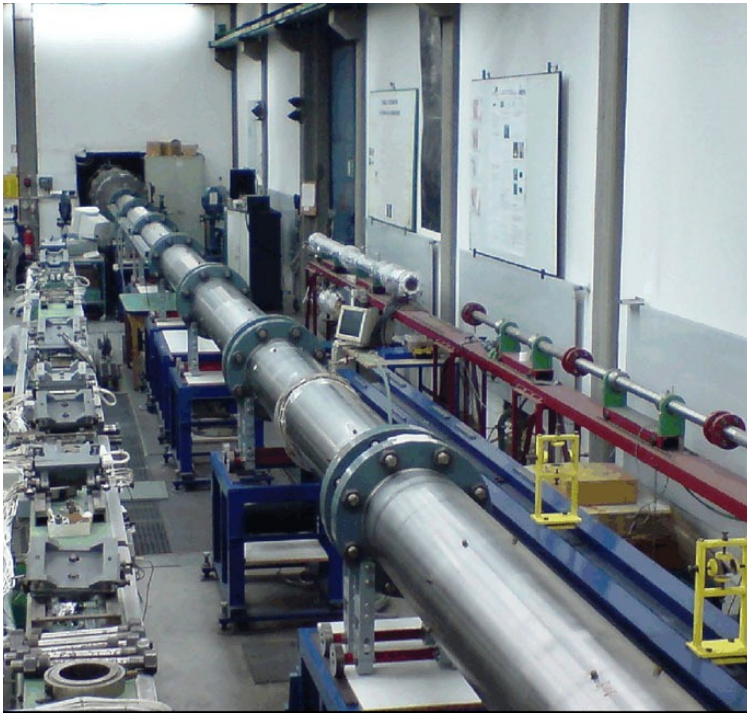


Figure 5.1: *Picture of a transonic shock tube at the Shock Wave Laboratory of the RWTH Aachen University.*

in principle possible to choose the initial fluids states such as to generate three geometric surfaces of discontinuity in a shock tube, namely a conventional CS and CSW and an unconventional RSW. The results of these numerical calculations of Ferguson et. al. were verified by means of two-dimensional CFD simulations whereby the fluid viscosity was set to zero (inviscid approximation). Although Ferguson et. al. did not follow a systematic approach to calculate the initial fluid states, the initial states were determined such as to maximize the strength of the RSW in terms of the pressure jump across it, i.e., the fluid states corresponded to that of a double sonic shock wave. An attempt to conduct such a triple discontinuity experiment was made at the University of Colorado at Boulder, however, the experiment proved unsuccessful due to the onset of decomposition of the perfluorocarbon test fluid at the high experimental temperature (which was of the order of 300–350 °C).

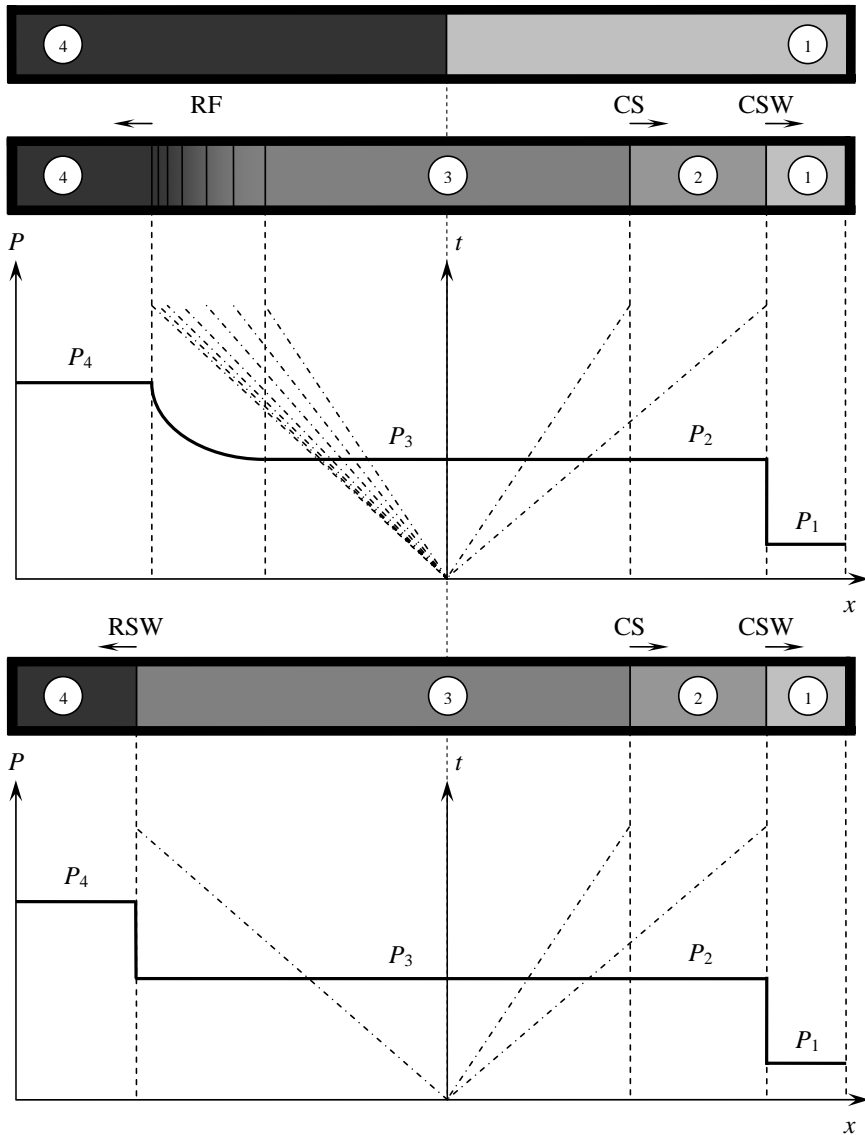


Figure 5.2: Upper: sketch of  $P-x$ - and  $t-x$ -diagrams of a conventional shock tube featuring classical wave fields: here, a left-moving RF, a right-moving CS and a right-moving CSW are observed. Lower: sketch of  $P-x$ - and  $t-x$ -diagrams of a shock tube featuring nonclassical wave fields: here, a left-moving RSW, a right-moving CS and a right-moving CSW are observed. Adapted from Ref. [64]

### 5.2.1.2 Initial fluid-states for a triple-discontinuity experiment

The initial states for a triple-discontinuity experiment can be chosen in order to either maximize the pressure jump across the RSW, i.e., via a unique double-sonic expansion shock wave, or to maximize the supersonic-to-sonic transition through the unsteady wave, which is an original idea that was proposed during the first year of this research project. An experiment maximizing the pressure jump across the discontinuity was proposed by Ferguson et. al. [64]. The RSW was to be identified by observing an abrupt pressure decrease as the wave passed the dynamic pressure instruments which are flush-mounted on the pipe wall of the high-pressure compartment, and its speed-of-propagation was to be measured using a time-of-flight technique. Yet, in the case of a double sonic RSW, it may be potentially difficult to unambiguously assert from the results of a measurement of the pressure drop and the wave speed, whether or not the observed expansive wave is a nonclassical expansion shock wave or a classical expansion fan. This is a point of concern primarily because a double sonic shock wave moves at sonic speed with respect to a shock-related frame of reference, just as the front runner wave of an expansion fan. Secondly, expansion shock waves necessarily feature a rather small jump in pressure, namely  $\mathcal{O}([P]) = 1$  bar, and, due to i) a low value of  $\Gamma$  which can be of the order of 0.1, ii) the influence of thermoviscous effects, and iii) thermal relaxation effects (since BZT fluids are necessarily molecularly complex), the shock thickness can be significant. In air for example under ideal-gas conditions, the shock-wave thickness for a shock-Mach number of about unity, is of the order of  $0.1 \mu\text{m}$ . However, in  $D_6$  in the dense-gas regime, the thickness of a nonclassical RSW can be of the order  $1\text{--}10 \mu\text{m}$  depending on the ratio of the bulk viscosity with respect to the shear (dynamic) viscosity, which can be in the range  $\mathcal{O}(\zeta/\eta) = 1 - 10^2$  [62] (see also Chap. 6, Table 6.1). It is also known from experiments with carbon dioxide, for example, that weak shock waves can be fully dispersed and therefore rather thick (refer to Fig. 232 on pg. 140 of Van Dyke [208] showing an 8-mm thick shock wave in  $\text{CO}_2$  with a shock Mach number of 1.04; the dispersed structure is due to slow vibrational relaxation). Consequently, the dynamic-pressure instruments may not detect a rather sharp decrease of pressure in time as one might have anticipated based on measurements/experience of/with weak shock waves in air. Additional complications can arise if the expansion wave features shock-fan composite behavior, or if the dynamic pressure instruments (which have a finite response time) are not well synchronized, and/or if crude noise-filtering is used, thereby potentially being the cause of a misinterpretation of the measurements.

The arguments presented in the previous paragraph against an experiment featuring a double-sonic RSW however, do not rule-out the effectiveness of performing a triple-discontinuity experiment in a shock tube. In fact, an experiment using a time-of-flight method whereby an expansion shock wave which displays the highest supersonic-to-sonic transition, may be used to unequivocally

cally demonstrate nonclassical RSW's. Here, a unique interpretation of the experimental pressure signals is possible. Due to the fact that only shock waves, independent of their nature, propagate at supersonic speed,<sup>1</sup> whereas the front runner wave of fans move at sonic speed, nonclassical RSW's displaying the highest supersonic-to-sonic transition, move the fastest with respect to the still fluid. Therefore, a time-of-flight method can be used to determine the wave speed and the wave-Mach number; if and only if the obtained wave Mach number, taking the uncertainties into account, is greater than unity can it be claimed that the expansive wave is a nonclassical RSW.

With reference to Fig. 5.2, the initial states ( $P_1, v_1, u_1 = 0$ ) and ( $P_4, v_4, u_4 = 0$ ) that admit three discontinuities in a conventional shock tube with the same fluid as driver and driven gas, can be determined as indicated in the following. The delineated procedure is valid if: i) the entire tube is maintained at a constant temperature, i.e.,  $T_1 = T_4$ , ii) the fluid is inviscid, iii) the waves are planar, iv) the flow is nearly one-dimensional, v) the geometric surfaces of discontinuity are instantaneously formed (meaning that if a diaphragm is employed, the opening time is effectively zero), and vi) the flow is rotation free.

1. Since a time-of-flight method is to be used, the aim is to create an RSW which features a transition from state 4 to 3 with a post-shock Mach number of unity whereby the pre-shock Mach number,  $Ma_4$ , is maximized. For dodecamethylcyclhexasiloxane ( $D_6$ ) as the test fluid or alternatively for tetradecamethylhexasiloxane ( $MD_4M$ ), it follows from the  $Ma$ - $v$ -plot depicted in Figs. 2.9 and 5.3 respectively, that the thermodynamic properties of state 4 correspond to saturated-vapor conditions, namely to that of point **O**.
2. The properties of post-shock state 3 are located on line **M-N** in Figs. 2.8 and 5.5 for fluids  $D_6$  and  $MD_4M$ , respectively. The values of  $v_3$ ,  $P_3$  and  $u_3$  are determined iteratively from

$$h_3(P_3, v_3) = h_4 + \frac{1}{2}(P_3 - P_4)(v_3 + v_4), \quad (5.1a)$$

$$J_{RSW} \equiv \frac{w_3}{v_3} = \frac{w_4}{v_4} = \sqrt{-\left(\frac{P_3 - P_4}{v_3 - v_4}\right)}, \quad (5.1b)$$

$$\mathbf{u}_3 = \mathbf{w}_3 - \mathbf{w}_4, \quad (5.1c)$$

taking into account that

$$Ma_3 \equiv \frac{w_3}{c_3} = 1, \quad (5.2a)$$

$$Ma_4 \equiv \frac{w_4}{c_4} > 1, \quad (5.2b)$$

$$[s] = s_3 - s_4 \geq 0. \quad (5.2c)$$

<sup>1</sup>double-sonic and RSW's with a pre-shock Mach number of unity are an exception.

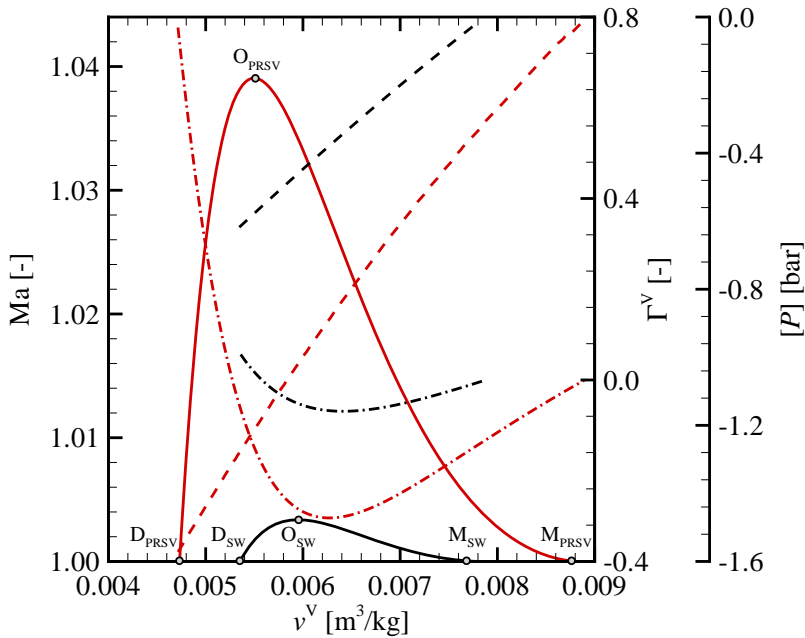


Figure 5.3: The pre-shock Mach number (solid lines) – whereby the post-shock Mach number is equal to unity – as a function of the saturated vapor specific volume ( $v^V$ ) of MD<sub>4</sub>M. Thermodynamic properties are determined with the EoS documented in Ref. [33] (black lines) and the PRSV EoS (red lines). The dashed lines give the pressure jump  $[P]$  across the RSW and the dash-dotted lines represent the value of  $\Gamma$  in the pre-shock state. The points labeled “D” indicate shock states with a pre- and post-shock Mach number of one, the points labeled “M” represent the limiting RSW’s with  $[P] = 0$ , and points “O” give the pre-shock state with the greatest supersonic-to-sonic speed change.

The equality sign for the entropy jump is only valid for infinitely weak shock waves satisfying  $[s] \downarrow 0$ .

3. The results obtained from the shock admissibility conditions when applied to the RSW, facilitate the computation of the properties behind and ahead of the CSW, i.e., states 2 and 1 respectively, by considering that: i) the change of velocity across a CS is purely tangential, i.e., there is no mass flow through an ideal CS, and ii) that for an inviscid fluid, the pressures on

both sides of the CS are equal, namely

$$\mathbf{u}_2 = \mathbf{u}_3, \quad (5.3a)$$

$$P_2 = P_3. \quad (5.3b)$$

4. Using an iterative scheme, the properties of state 1 are obtained from

$$h_2(P_2, v_2) = h_1 + \frac{1}{2}(P_2 - P_1)(v_1 + v_2) \quad (5.4a)$$

$$J_{\text{CSW}} \equiv \frac{w_1}{v_1} = \frac{w_2}{v_2} = \sqrt{-\left(\frac{P_2 - P_1}{v_2 - v_1}\right)} \quad (5.4b)$$

$$\mathbf{u}_2 = \mathbf{w}_2 - \mathbf{w}_1 \quad (5.4c)$$

as follows:

- Guess the value of  $P_1 < P_2$  and determine  $v_1$  using the EoS of the working fluid and the fact that  $T_1 = T_4$  is imposed.
- Using the equation for the shock adiabat through state 1, compute  $v_2$ .
- Using the Rayleigh equation, calculate  $\mathbf{w}_1$ ,  $\mathbf{w}_2$  and  $\mathbf{u}_2$ .
- Check that  $\text{Ma}_2 \equiv \frac{w_2}{c_2} < 1$ ,  $\text{Ma}_1 \equiv \frac{w_1}{c_1} > 1$ , and  $s_2 - s_1 > 0$ .
- If the new value of  $\mathbf{u}_2$  differs significantly from the value obtained via the shock admissibility conditions applied to the RSW, make a new guess for  $P_1$  and iterate until convergence is obtained.

The described successive steps are applied to BZT fluid MD<sub>4</sub>M [30] whereby thermodynamic properties are computed with the Peng-Robinson, Stryjek and Vera modified, cubic (PRSV) EoS using the fixed fluid parameters documented in Table 3.15. The PRSV EoS was selected for the calculations because, as was indicated in Sec. 4.6, model EoS's, although less accurate than multiparameter EoS's, do correctly account for the thermodynamic and physical behavior of the fluid with the least number of parameters possible. This is important if a thermodynamic model is applied to a fluid for which only a limited number of experimental data are available.

The initial states 1 and 4 of the triple-discontinuity experiment and the properties of the intermediate states 2 and 3 are listed in Table 5.1. These values are confirmed with one-dimensional CFD simulations of the triple-discontinuity experiment using version 1.00 of the software zFlow [36], a CFD solver using real-gas properties. The computational grid contains 400 cells with a node-spacing of  $x/L = 0.0025$ , the time integration is done with a 2<sup>nd</sup>-order Runge-Kutta scheme and the CFL number is 0.5. Furthermore, it is assumed that the diaphragm ruptures instantaneously. Results of these computations are displayed in Fig. 5.4. An important note is that these calculations were performed

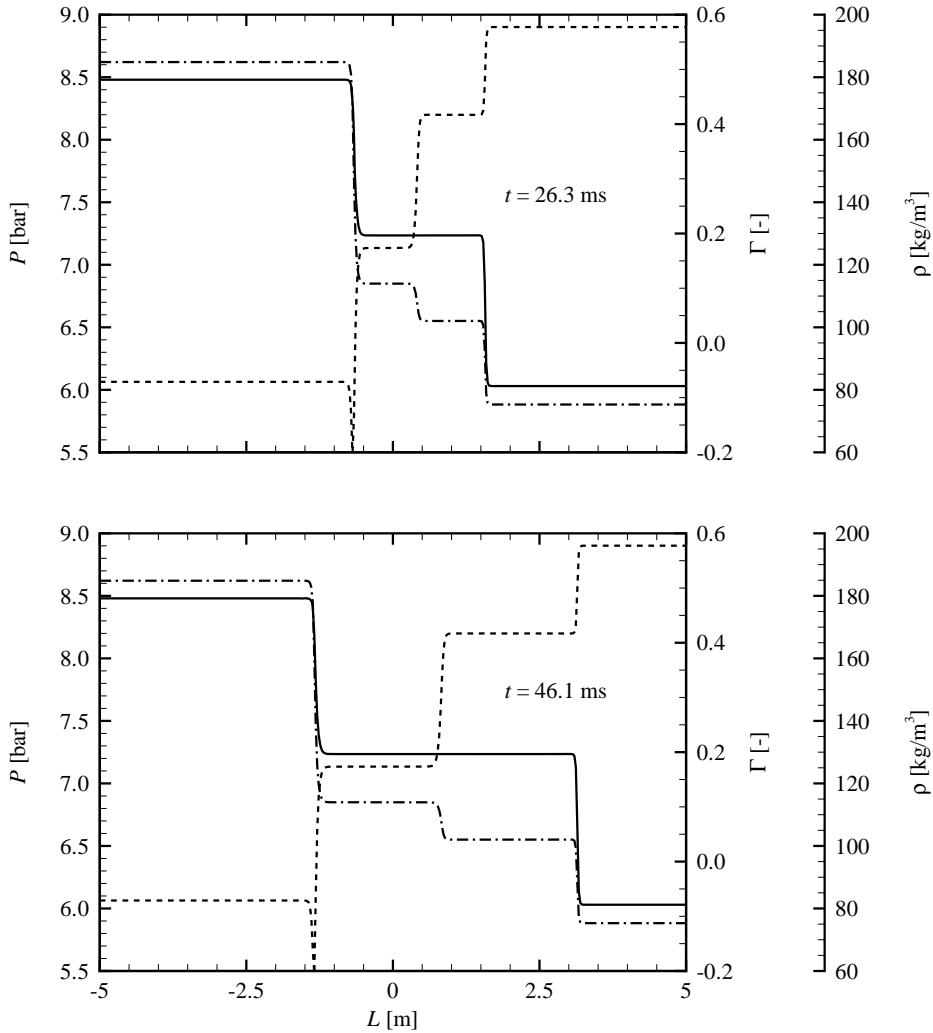


Figure 5.4: *zFlow* simulation of the triple-discontinuity experiment in a conventional shock tube using BZT fluid MD<sub>4</sub>M. Thermodynamic properties are calculated with the Peng-Robinson EoS with the Stryjek and Vera modification. The solid line represents the pressure profile and the dashed and dash-dotted lines represent the  $\Gamma$ - and density profile, respectively.

Table 5.1: States 1–4 according to Fig. 5.2 of a triple discontinuity experiment conducted with MD<sub>4</sub>M as working fluid. Thermodynamic properties are calculated in the PRSV EoS. A positive (negative) velocity indicates fluid flow towards the right (left) with respect to the laboratory frame of reference. Note  $[P] = 121.1$  kPa.

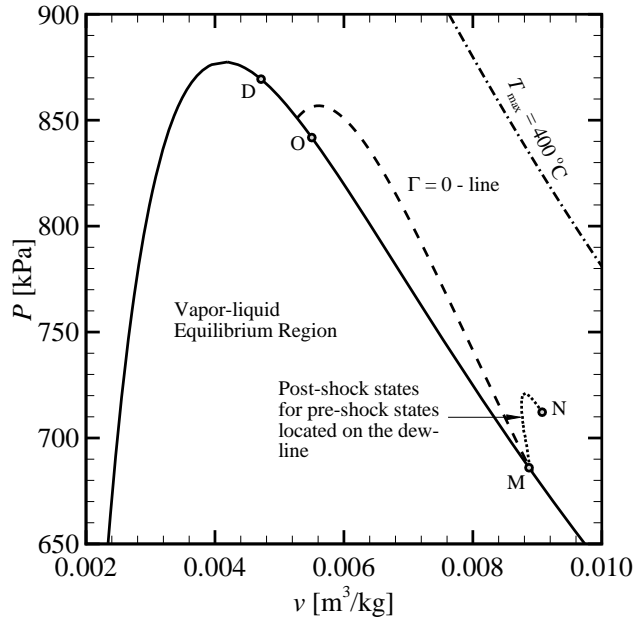
State	$P$ [kPa]	$\rho$ [kg/m <sup>3</sup> ]	$T$ [°C]	$u$ [m/s]	$w$ [m/s]	$c$ [m/s]	$ \text{Ma} $ [-]
1	602.9	75.5 <sub>7</sub>	377.2	0	-77.5 <sub>8</sub>	77.8 <sub>2</sub>	1.08 <sub>0</sub>
2	720.7	102.0	380.2	+20.0 <sub>9</sub>	-57.5 <sub>0</sub>	61.7 <sub>6</sub>	0.931 <sub>0</sub>
3	720.7	113.2	371.4	+20.0 <sub>9</sub>	+53.2 <sub>7</sub>	53.2 <sub>7</sub>	1.00 <sub>0</sub>
4	841.8	181.8	377.2	0	+33.1 <sub>9</sub>	31.9 <sub>4</sub>	1.03 <sub>9</sub>

in 2005 employing the older ThermoProp fluid properties library, therefore the flow properties reported in Table 5.1 are slightly different than the values displayed in the respective figures, however, qualitatively, the flow features are unchanged.

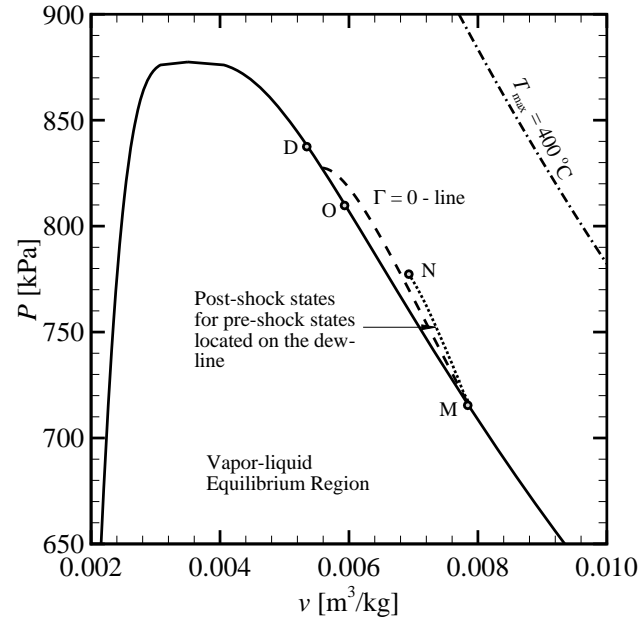
### 5.2.1.3 Influence of secondary effects on shock-tube experiments

The following items, although some are mostly based on experimental and numerical studies of classical flows of simple fluids (see references herein), these are qualitatively applicable also to nonclassical flows of dense gases. From a quantitative viewpoint, it is still an unanswered question whether or not accounting for these secondary effects, even yields numerically correct results, particularly because of the lack of experiments conducted with molecularly complex dense gases.

In the determination of the initial states of a triple-discontinuity experiment in a shock tube, it was assumed that the discontinuities are planar, the flow is quasi one-dimensional and that the flow past the discontinuities is a potential flow. In the case of BZT fluids however, the following aspects must be accounted for and the validity of the assumptions must be assessed (see Chap. 6 where the below-mentioned aspects have been considered during the preliminary design of the test facility).



(a) Results from the PRSV EoS



(b) Results from the multiparameter EoS of Ref. [33]

Figure 5.5: The  $\Gamma < 0$ -region of  $MD_4M$  in the  $P$ - $v$ -plane calculated with two EoS's. The dotted line indicates post-shock states with a Mach number of one, point **O** represents the thermodynamic state on the dew-line that displays the greatest supersonic-to-sonic transition and point **D** gives the thermodynamic state on the dew-line which features both a pre- and post-shock Mach number of unity (the sonic post-shock state of point **D** is point **N**). Point **M** is the limiting case of an RSW with  $[P] = 0$ .

- **Incomplete rupture of the diaphragm:**

In the case that a diaphragm is used in the shock tube, complications may arise due to its incomplete rupture. See for example the experimental and numerical study conducted by Gaetani et. al. [75] where results show that the shock intensity is lower in the case of incomplete diaphragm rupture compared to when the diaphragm ruptures completely, and multi-dimensional disturbances are generated due to shock diffraction from the diaphragm edges and results in a complex unsteady flow field behind the leading shock wave. The numerical study by Gaetani et. al. was done employing an unsteady Euler solver documented in Ref. [83] and assuming negligible viscosity, thermal conductivity, and a polytropic ideal gas. Also refer to Ferguson's PhD thesis [65] where pictures are included, namely Fig. 7.6 therein, showing incomplete rupture of a scorched metallic diaphragm; the test fluid was nitrogen gas at 350 °C and a low pressure difference, i.e., between 0.6–0.7 atm. similar to that of the foreseen experiment with the provisional working fluid, was used to rupture the diaphragm. Moreover, the experimenter has little control over the moment of rupture and the opening time, especially because the experiments have to be conducted at elevated temperatures (300–400 °C). Also, because of the high temperatures involved and purity requirements of the test fluid, the availability of the shock tube equipped with a diaphragm is low. Finally, it must be indicated that due to the fact that the moment at which and the manner that the diaphragm breaks are difficult to control, the repeatability and the reproducibility of the experiments is poor.

- **The effect of the boundary layer:**

The boundary layer which is formed behind the shock wave results in a loss of homogeneity of the flow. Consequently, a non-negligible portion of the mass contained in the plug, i.e., the region between the shock wave and the CS, gets accumulated in the boundary layer and intermixing of the driver and driven gas takes place through the CS which becomes non-planar [193]. Additionally, weakening of the pressure jump across the shock wave and the shock speed take place during propagation.

There are numerous investigations devoted to the numerical and experimental study of boundary layers in shock tubes. Notable studies are that of Donaldson and Sullivan [55], Hollyer [94], Mirels [144, 145], and Trimpi and Cohen [204]. Donaldson and Sullivan for example, determined the deceleration of a shock wave due to the formation of an incompressible boundary layer, therefore, their model is only valid for weak shock waves, e.g., nonclassical RSW's. Trimpi and Cohen [204] on the other hand reduce the problem to a one-dimensional flow and apply a correction to the incompressibility assumption of the boundary layer. They provide an equation for determining the attenuation across the shock wave in terms of the pressure jump. Interestingly enough, if linear attenuation is accounted for,

it was found that for a specific range of shock pressure ratios, strengthening of the wave occurred and that the larger the shock-tube Reynolds number, i.e.,  $Re_D = u_2 D / \nu_2$ , where  $D$  is the shock tube diameter, the lower the pressure jump attenuation. Experimental studies on classical flows of simple fluids have shown that for shock waves with a shock-Mach number less than 4, the transition from a laminar to a turbulent boundary layer occurs at Reynolds numbers  $Re_x$  of  $2 \cdot 10^5$  (see Refs. [87, 88]) –  $3 \cdot 10^6$  (see Ref. [138]), where the lower limit was found in shock tubes with rough walls.<sup>2</sup>

- **The effect of the uncertainty in the prediction of thermodynamic properties:**

The thermodynamic description of the fluid significantly influences the qualitative and quantitative prediction of the flow features and flow variables. In this respect the sensitivity of the results due to the uncertainty in the ideal-gas isobaric heat capacity prediction, which can be quantified (see Sec. 3.2), is investigated. Although  $P$ - $v$ - $T$ -properties are left uninfluenced by the uncertainty in the predicted values of  $C_p^0$ , the caloric properties do change. As a consequence of the uncertainty in  $C_p^0$  values of 5 % for siloxanes, if the same pressure and temperature listed in Table 5.1 are used for states 1 and 4 of a triple-discontinuity experiment, the following can occur: i) either the rarefaction shock wave splits into a composite shock-fan; in this case the post-shock Mach number is still unity, on the other hand the pressure jump can be less than the 121.1 kPa computed using the values listed in Table 5.1, or ii) the rarefaction shock wave does not feature a supersonic-to-sonic transition, but rather a supersonic-to-subsonic transition. In the most extreme situation, e.g., if  $C_p^0$  values are significantly overpredicted, it is also possible that the rarefaction wave does not steepen into a shock front but evolves as an isentropic rarefaction fan instead. The results of an exemplary calculation for MD<sub>4</sub>M taking the 5 % uncertainty in  $C_p^0$  predictions into account, are presented in Tables 5.2 and 5.3 where the PRSV EoS is used. Figures 5.6 and 5.7 display the sensitivity of the results given in Fig. 5.3 to the uncertainty in  $C_p^0$ . As a remark it should be mentioned that the quantitative prediction of the flow features and flow variables are also sensitive to the uncertainty in thermal property data, however, only the uncertainty in  $C_p^0$  can be rigorously justified (see also the concluding remarks of Chap. 4).

- **The influence of non-equilibrium effects:**

Non-equilibrium effects cause the density and temperature profile behind the discontinuities to be non-negligibly different than their equilibrium counterparts. The pressure profile however is only slightly affected, although this is only confirmed for substances composed of rather simple

---

<sup>2</sup>In this context,  $Re_x = x \rho_2 (w_2^2) / (\eta_2 u_2)$ , and  $x$  is the distance from the shock front [193]. Note that Trimpi and Cohen [204] define  $Re_x = x \rho_2 u_2 / \eta_2$ .

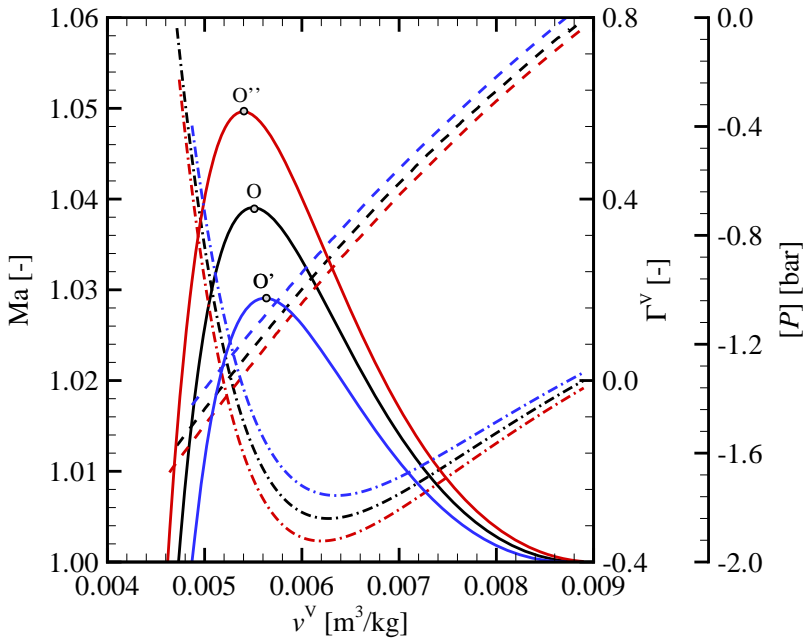


Figure 5.6: Sensitivity of the results displayed in Fig. 5.3 for  $MD_4M$  to the 5 % uncertainty in the isobaric-heat-capacity prediction, see Sec. 3.2. Note that only the PRSV EoS is considered; these results are qualitatively similar to those obtained with the SW EoS. Legend: the red lines are the result of an over-predicted value for  $C_P^0$ , whereas the blue lines are the result of an under-predicted value for  $C_P^0$ . The reference  $C_P^0$  values are determined with Eq. (3.18) using the parameters listed in Table. 3.13. The solid lines represent the pre-shock Mach number, the dashed lines give the pressure drop over the predicted rarefaction shock wave and the dash-dotted lines give the value of  $\Gamma$  along the dew-line for relevant pre-shock states. Points **O**, **O'** and **O''** represent the maxima in the pre-shock Mach number for admissible RSW's.

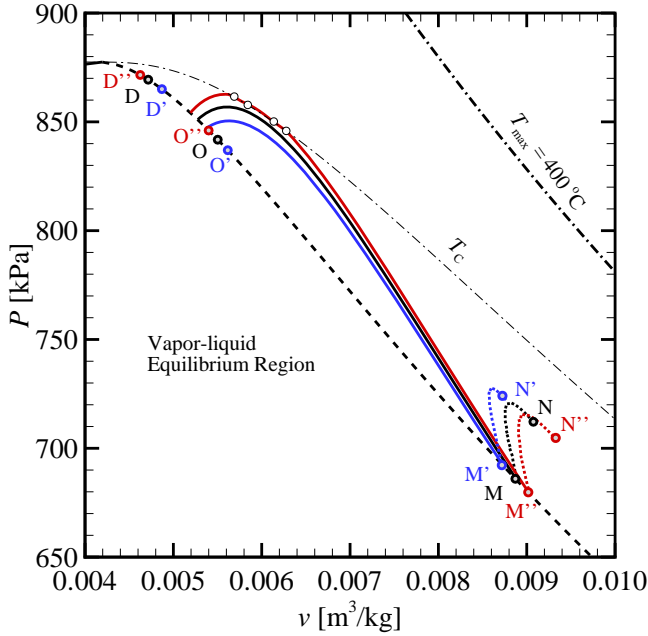


Figure 5.7: Sensitivity of the size of the  $\Gamma < 0$ -region of  $MD_4M$  due to the 5 % uncertainty in the isobaric-heat-capacity prediction, see Sec. 3.2. Only the PRSV EoS is considered. Legend: the red lines are the result of an over-predicted value for  $C_p^0$ , whereas the blue lines are the result of an under-predicted value for  $C_p^0$ . The reference  $C_p^0$  values are determined with Eq. (3.18) using the parameters listed in Table. 3.13. The solid line delimits the vapor-liquid equilibrium region, the dashed lines give the  $\Gamma = 0$ -line in the superheated vapor region, the dotted lines indicate the post-shock states featuring a Mach number of unity, whereby the pre-shock Mach number is maximized; moreover, pre-shock states are located on the dew-line, and the dash-dotted lines indicate isotherms. Points **O**, **O'** and **O''** represent the maxima in the pre-shock Mach number for admissible RSW's, as identified in Fig. 5.6, points **D**, **D'** and **D''** represent the pre-shock states with a Mach number of one (the associated post-shock states are indicated by points **N**, **N'** and **N''**, respectively), and points **M**, **M'** and **M''** represent limiting sonic RSW's with a pressure jump of zero. Note the discontinuity in the slope of the  $\Gamma = 0$ -line at  $T = T_C$  due to the inconsistency of the PRSV EoS.

Table 5.2: Properties 1–4 of the triple-discontinuity experiment whereby the pressure and temperature of states 1 and 4 are the same as the values listed in Table 5.1, however increasing the  $C_P^0$  prediction by 5 %. Note that the RSW features a pressure jump of 121 kPa.

State	$P$ [kPa]	$\rho$ [kg/m <sup>3</sup> ]	$T$ [°C]	$u$ [m/s]	$w$ [m/s]	$c$ [m/s]	Ma  [-]
1	602.9	75.5 <sub>7</sub>	377.2	0	-77.3 <sub>8</sub>	71.7 <sub>2</sub>	1.07 <sub>9</sub>
2	720.8	102.2	380.0	+20.1 <sub>6</sub>	-57.2 <sub>2</sub>	61.4 <sub>3</sub>	0.931 <sub>6</sub>
3	720.8	112.9	371.7	+20.1 <sub>6</sub>	+53.1 <sub>9</sub>	53.3 <sub>6</sub>	0.99 <sub>7</sub>
4	841.8	181.8	377.2	0	+33.0 <sub>4</sub>	31.4 <sub>9</sub>	1.04 <sub>9</sub>

Table 5.3: Properties 1–4 of the triple-discontinuity experiment whereby the pressure and temperature of states 1 and 4 are the same as the values listed in Table 5.1, however decreasing the  $C_P^0$  prediction by 5 %. Note that the RSW features a pressure jump of 114.4 kPa. The RSW is immediately followed by a rarefaction fan featuring transition 3–3’.

State	$P$ [kPa]	$\rho$ [kg/m <sup>3</sup> ]	$T$ [°C]	$u$ [m/s]	$w$ [m/s]	$c$ [m/s]	Ma  [-]
1	602.9	75.5 <sub>7</sub>	377.2	0	-77.4 <sub>7</sub>	71.9 <sub>2</sub>	1.07 <sub>7</sub>
2	714.6	100.3	380.1	+19.0 <sub>8</sub>	-58.3 <sub>9</sub>	62.5 <sub>8</sub>	0.933 <sub>0</sub>
3’	714.6	111.6	370.9	+19.0 <sub>8</sub>	N.A	53.9 <sub>6</sub>	N.A.
3	727.4	116.1	371.4	+18.8 <sub>7</sub>	+52.2 <sub>3</sub>	52.2 <sub>3</sub>	1.00 <sub>0</sub>
4	841.8	181.8	377.2	0	+33.3 <sub>6</sub>	32.4 <sub>3</sub>	1.02 <sub>9</sub>

molecules like Ar and O<sub>2</sub> [192]. This means that because the time-of-flight method uses pressure instruments to detect when the leading wave reaches the sensors, non-equilibrium effects will probably not be detected. However, the flow field itself can be radically different than what follows from equilibrium relations depending on the severity of the departure from equilibrium. In the case of polyatomic gases, such as BZT fluids, vibrational relaxation is the main point of concern, since contrary to translational and rotational equilibrium, which is achieved in only few collisions, the achievement of vibrational equilibrium may require thousands of collisions [121]. Moreover, polyatomic gases have several modes of molecular vibration – each of which can, in principle, relax independently – and are structurally flexible. Consequently they can change their shape, both during normal vibration and during collision, the latter being probably more relevant. The majority of polyatomic gases exhibit a single vibrational relaxation process, which involves the entire vibrational energy content of the molecule. This is based on the assumption that vibrational-vibrational energy transfer is faster than vibrational-translational energy

transfer, therefore the total vibrational energy content of a molecule relaxes by vibrational-translational energy transfer via the lowest mode. For estimating the time for vibrational relaxation, the mode of the lowest frequency of vibration is required. These data were determined from ab initio calculations, as treated by Nannan et. al. [153]. The computed lowest frequency of vibration for all the siloxanes considered in Chap. 3 (this includes  $D_6$ ) is lower than  $40 \text{ cm}^{-1}$  (data provided by Prof. Richard Rowley of BYU, UT). By using the Lambert-Salter plot, documented in Chap. 3, pg. 64 of Ref. [121], for molecules containing more than two hydrogen atoms, the vibrational relaxation time is estimated to be of the order of 0.1 nanoseconds, i.e.,  $10^{-10}$  sec at 300 K. The fact that the pre- and post shock states for rarefaction shock waves are at a higher pressure and temperature, should not have a significant effect on the estimation of the order of magnitude of the vibrational relaxation time [121]. As in Ref. [201], the rarefaction shock thickness for  $D_6$  can be computed based on: i) the calculated viscosity using the method of Chung et. al., ii) the assumption that the bulk viscosity is of the same order of magnitude as the shear viscosity, and iii) that the ratio of the isobaric with respect to the isochoric heat capacity is of the order of 1. This results in an estimated shock thickness of the order of micrometers and therefore the residence time of the molecule – for a speed of sound of about 40 m/s – is of the order of  $10^{-8}$  sec. According to these calculations, the relaxation time is at least two orders of magnitude smaller than the residence time of a molecule in the shock. Equilibrium of the internal energy can therefore be assumed past the shock wave.

## 5.2.2 Point explosions in dense gases

Sufficiently far from the source of a disturbance, as for example are the pressure waves caused by supersonic aircrafts or resulting from explosions, spherical waves are perceived as weak N-waves, so-named due to the shape of the pressure profile as a function of the distance from the center of origin [178]. Under laboratory conditions, N-waves are created in simple spherical cavities often containing air, by using sparks, exploding wires, or a pulsed laser.

The possibility of using point explosions and thus the resulting N-waves as a means to provide experimental proof for the existence of nonclassical wave fields, particularly nonclassical compression waves, is numerically investigated and discussed by Guardone and Colonna [82]. This idea of employing point explosions to study phenomena associated with nonclassical gas dynamics was initiated based on earlier tests conducted at the University of Maryland by Dr. F. Ferioli [67] related to Laser-Induced Breakdown Spectroscopy (LIBS) measurements in hydrocarbons.<sup>3</sup> In the experimental facility at the University of Mary-

---

<sup>3</sup>LIBS can be used for quick gas composition measurements.

land, a focusing pulsed laser was used to create a hot plasma expanding in an initially still, cold gas confined in a spherical cavity.

In the classical case, e.g., if diatomic nitrogen is used as test medium, and if dissociation and ionization do not occur due to the localized energy input, concentration of a fixed amount of thermal energy at the center of the spherical cavity results in the formation of classical N-waves. In fact, the localized release of energy results in the formation of a succession of compression and rarefaction waves. The compression waves steepen into a shock wave and move further from the point of origin, whereas the rarefaction waves move towards the center. As the distance between the leading compression shock wave and the center increases, the amplitude of the pressure profile of the CSW attenuates and the wave speed gradually decreases (the observed attenuation and dispersion depend on the magnitude of the energy input). Furthermore, the focussing rarefaction waves eventually admit a second compression shock wave which propagates away from the center. In between the initial CSW and the RE, a CS is present.

Due to the difficulty of the prediction of the formation of N-waves from sparks or exploding wires and the additional complications caused by relaxation phenomena, often the theoretical study of point explosions is conducted by means of numerical simulation whereby the energy input/explosion is appropriately modeled. In Ref. [95] for example, the formation of an N-wave due to a localized explosion in air is studied assuming a pressurized sphere of small radius at room temperature separated from the outside air by an imaginary diaphragm, see Fig. 5.8. Initially, the temperature is uniform and the absolute fluid velocities are zero. The simulation starts by removing the diaphragm and solving the fully compressible Navier-Stokes governing equations assuming spherical symmetry and constant-valued transport properties. Moreover, energy transfer related to relaxation phenomena can be taken into account in the governing equations.

A similar approach utilizing an imaginary diaphragm is used by Guardone and Colonna [82] in their study of nonclassical N-waves in fluid  $D_6$ . Contrary to the procedure adopted by Honma and Glass documented in Ref. [95] whereby the initial temperature is the same on both sides of the imaginary spherical diaphragm, Guardone and Colonna assume the density of the fluid contained in the inner sphere to be equal to that contained in the outer sphere. Furthermore, relaxation phenomena are not modeled, thermoviscous effects are not considered, however, real-gas behavior is accounted for by employing the Martin-Hou EoS to  $D_6$ . Moreover, the initial pressure and density on the low-pressure side (i.e., the fluid contained in the outer sphere) is slightly supercritical whereas the initial thermodynamic state on the high-pressure side of the imaginary diaphragm is located inside the negative nonlinearity region ( $\Gamma < 0$ -region). Ad-

ditionally, the fluid velocity is zero everywhere. In brief,

$$\begin{aligned}
 \frac{\rho(r)}{\rho_C} &= 0.47169 && \forall r \\
 \frac{u(r)}{u_C} &= 0 \text{ m/s} && \forall r \\
 \frac{P(r)}{P_C} &= \begin{cases} 0.8700 & \text{if } R_i < r \leq R_o \\ 1.200 & \text{if } 0 \leq r \leq R_i, \end{cases} && (5.5)
 \end{aligned}$$

where inner radius  $R_i = 1$  mm and the inner radius of the outer sphere  $R_o = 150$  mm. The critical density and pressure adopted by Guardone and Colonna were respectively,  $276 \text{ kg/m}^3$  and  $9.6$  bar.

The results of the simulation with  $D_6$  show that indeed the compression wave spreads out in time as an isentropic compression fan. The rarefaction wave on the other hand does not coalesce into an expansion shock wave. Additionally, numerically simulated Schlieren images of the point explosion demonstrate that the use of an optical arrangement does not allow for a detection of the compression fan. Therefore, the spreading of the compression fan has to be measured by using total pressure probes positioned at various distances, say  $R_1$  and  $R_2$ , from the center of origin. Provided that the probes themselves do not influence the flow field – although this must be investigated in more detail, e.g., by using CFD analysis – a nonclassical wave yields for  $R_2 > R_1 \Rightarrow \Delta t(R_2) > \Delta t(R_1)$ , where  $\Delta t = t' - t''$ , and  $t'$  and  $t''$  being the times at which the compression profile starts and ends, respectively.

### 5.3 Steady experiments

Steady experiments are classified as those having a steady flow field and where the nonclassical gas-dynamic phenomenon under scrutiny remains steady with respect to a laboratory reference frame. Two steady experiments can be envisaged for studying flow phenomena which are the result of  $\Gamma$  being (locally) less than zero, namely: i) an experiment which creates a steady nonclassical rarefaction shock wave or a series of both nonclassical and classical shock waves which are typical only of BZT fluids in a classical converging-diverging nozzle, or ii) an experiment whereby a nonclassical two-dimensional wave field is created due to turning of a supersonic flow over a body. Both of these options are discussed in the following.

#### 5.3.1 Nonclassical shock waves in a classical nozzle

##### 5.3.1.1 Overview – steady isentropic flows of BZT fluids in one dimension

A numerical investigation into the occurrence of shock waves, be it classical or nonclassical, in steady, inviscid flows of a BZT fluid in classical converging-

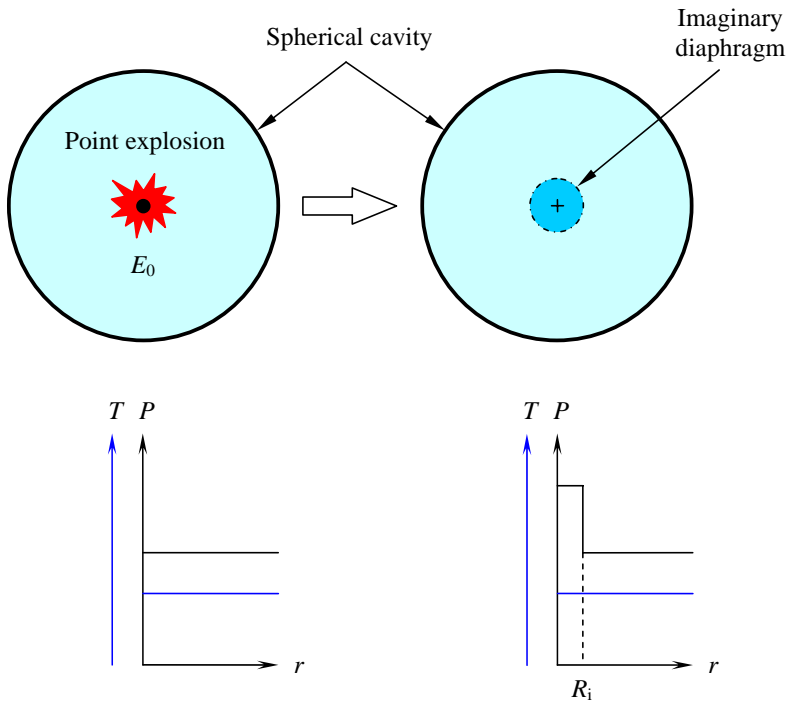


Figure 5.8: *Top left: point explosion occurring in the center of the spherical cavity releasing a concentrated amount of energy  $E_0$ . Bottom left: the pressure and temperature as a function of the radial coordinate at  $t = 0$ . Top right: Model of the point explosion. Here, an imaginary diaphragm separates the high- and low-pressure sides. The diaphragm instantaneously disappears at  $t = 0$ . Bottom right: the pressure and temperature as a function of the radial coordinate at  $t = 0$  where  $R_i$  is the radius of the inner spherical cavity.*

diverging nozzles is documented by Cramer and Fry [41]. Their study is an extension of earlier works of Chandrasekar and Prasad [24] and Kluwick [112].

Consider a classical converging-diverging nozzle. From a control-volume perspective, if the flow is one-dimensional, inviscid, single-phase, isentropic, steady and free of body forces, then the governing equations are (subscript “0” indicates stagnation (total) properties)

$$\begin{cases} \dot{m} = \rho u A & = \text{constant} \\ h_0 = h + \frac{u^2}{2} & = \text{constant} \\ s_0 = s & = \text{constant} \end{cases} \quad (5.6)$$

Using the differential form of Eqns. (5.6), namely

$$\frac{1}{A} \frac{dA}{dx} + \frac{1}{u} \frac{du}{dx} + \frac{1}{\rho} \frac{d\rho}{dx} = 0 \quad (5.7a)$$

$$\frac{dh}{dx} + u \frac{du}{dx} = 0 \quad (5.7b)$$

$$\frac{ds}{dx} = 0 \quad (5.7c)$$

and the fact that  $Tds = dh - dP/\rho = 0$ ,  $Ma = u/c$ ,  $dP = c^2 d\rho$ , and  $dc = c(\Gamma - 1) d\rho/\rho$  because of Eq. (5.7c), it can be demonstrated with Eq. (5.7b) that [196]

$$\frac{dMa}{d\rho} = \frac{Ma}{\rho} \underbrace{\left(1 - \Gamma - \frac{1}{Ma^2}\right)}_{\varphi}. \quad (5.8)$$

Or, by using the differential form of the mass conservation equation, namely Eq. (5.7a), it is found that

$$\frac{1}{Ma} \frac{dMa}{dx} = \frac{1 + (\Gamma - 1) Ma^2}{(Ma^2 - 1)} \frac{1}{A} \frac{dA}{dx}, \quad (5.9)$$

and

$$\frac{1}{\rho} \frac{d\rho}{dx} = \left( \frac{Ma^2}{1 - Ma^2} \right) \frac{1}{A} \frac{dA}{dx}. \quad (5.10)$$

Starting from a specific stagnation state on an isentrope, Figs. 5.9 and 5.10 illustrate the local Mach number computed using Eq. (5.8), with respect to the reduced density of fluid  $D_6$ . Thermodynamic properties are obtained with the PRSV EoS. As demonstrated by Cramer and Best [47], the results presented in these figures show that, depending on the choice of the stagnation conditions, steady isentropic expansion of a BZT fluid in the dense-gas regime to supersonic conditions results in the occurrence of at least one, and at most three

sonic points. What is more is that passage of the first sonic point is necessarily a state with  $\Gamma > 0$ . All of the stagnation states for which the trend lines are drawn in Fig. 5.9 for example, exhibit only one sonic point. Figure 5.10 shows the  $\text{Ma}-\rho$ -plot for two stagnation states selected along the isentrope which is tangential along to the VLE region on the dew-line of  $D_6$  ( $s = s_{\text{max}}^V$ ), which exhibit three sonic points. As a last remark, it is observed that in Fig. 5.9 the dashed line, i.e., the line connecting states with  $\wp = 0$  as defined in Eq. (5.8), intersects the sonic ( $\text{Ma} = 1$ ) line twice. This only occurs if the isentrope along which the fluid is expanded from stagnation to supersonic conditions exhibits  $\Gamma_{\text{min}} < 0$ . Isentropes with  $0 < \Gamma_{\text{min}} < 1$  display a qualitatively similar trend as shown in Fig. 5.9, however for these isentropes, the  $\wp = 0$ -line is located completely above the sonic line, since  $\text{Ma}_{\text{min}, \wp=0} = (1 - \Gamma_{\text{min}})^{-1/2} > 1$ , see Ref. [47]. Consequently, isentropes with  $0 < \Gamma_{\text{min}} < 1$  feature, depending on the stagnation state, non-monotonous  $\text{Ma}-\rho$ -trend lines which can have two extremes; these extremes occur at supersonic conditions and because of this, these isentropes only have a single sonic point. Finally, isentropes with  $\Gamma_{\text{min}} > 1$  display monotonous  $\text{Ma}-\rho$  lines and admit a single sonic point in the case of steady isentropic expansion from stagnation to supersonic conditions, because  $\wp < 0$ .

Utilizing the results displayed in Figs. 5.9 and 5.10, one can either compute, using Eqns. (5.9) and (5.10), for a given stagnation state on a specific isentrope, the area variation. Alternatively, which within the context of this chapter is more interesting, for a given area as a function of the spatial coordinate  $x$ , the local flow variables can be determined and the shock admissibility conditions can be used to identify steady shock waves.

### 5.3.1.2 Creating steady nonclassical shock waves in classical nozzles

Based on the fact that – and depending on the choice of the stagnation (reservoir) conditions – steady, isentropic expansion of a BZT fluid can result in the occurrence of at least one, and at most three sonic points (see Figs. 5.9 and 5.10), three types of flow can be distinguished. Numerical calculations [41], confirmed by mathematical and physical reasoning and computations (see e.g., Ref. [24, 112]), have shown the admissibility of two nonclassical types of flow which feature, among a variety of nonclassical gas dynamic discontinuities, rarefaction shock waves, and one classical type featuring well-known compression shock waves which can be generated downstream of the throat. All the stagnation states displayed in Fig. 5.9 for example, give rise to purely classical compression shock waves past the nozzle's throat. This is also what theoretically occurs for steady isentropic expansion of dense gases if  $0 < \Gamma_{\text{min}} < 1$  everywhere in the flow (that is in fluids which are molecularly complex, but which do not classify as BZT fluids). Stagnation states which admit three sonic points, such as illustrated in Fig. 5.10, theoretically permit the above-mentioned nonclassical flows; Cramer and Fry [41] refer to these nonclassical flows as type I and II flows. More specifically, according to Cramer and Fry, type I flows occur if

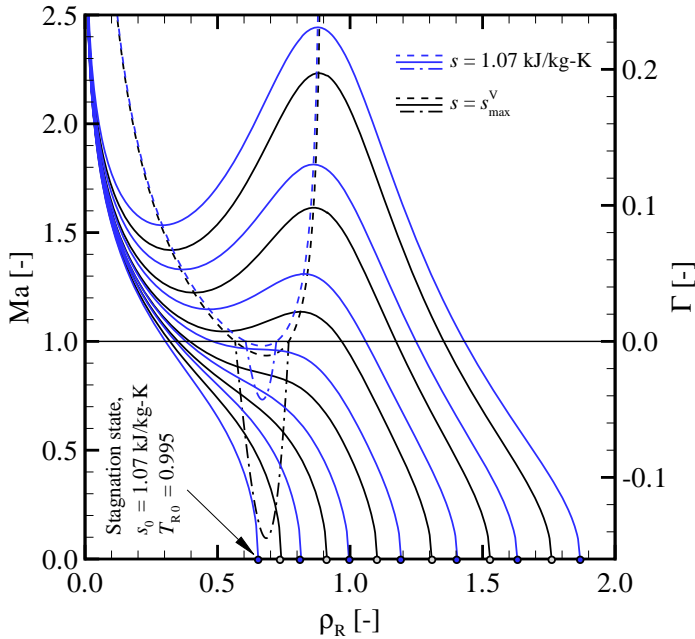


Figure 5.9:  $Ma$ - $\rho$ -plot for fluid  $D_6$  assuming isentropic expansion from various stagnation states (reservoir conditions) ( $\rho_0(T_0), s_0, u_0 = 0$ ). The blue lines are results for the isentrope which is tangential to the VLE region on the dew-line for various stagnation temperatures ( $T_{R0} \equiv T_0/T_C = 0.995, 1.00, \dots, 1.02$ ), whereas the black lines are results for an isentrope ( $s = 1.07 \text{ kJ/kg-K}$ ) which is completely located in the superheated dense-gas region for 7 different stagnation temperatures ( $T_{R0} = 0.995, 1.00, \dots, 1.025$ ). The solid lines indicate the functional relation between the local flow Mach number and the local reduced fluid density (i.e.,  $\rho_R \equiv \rho/\rho_C$ ), the dashed lines, where  $\varphi = 0$  [see Eq. 5.8], connect the extremes of the individual  $Ma$ - $\rho$ -lines for the isentropes affiliated with them and the dash-dotted lines indicates the value of  $\Gamma$  (only for the range of densities where  $\Gamma \leq 0$ ) along the considered isentropes. Remark that the selected isentropes exhibit positive and negative nonlinearity. Thermodynamic properties are computed with the PRSV EoS.

the sonic points labeled  $\rho_2^I$  and  $\rho_3^I$  in Fig. 5.10 are closer to each other than sonic points  $\rho_1^I$  and  $\rho_2^I$ , whereas type II flows are found if the sonic points labeled  $\rho_1^{II}$  and  $\rho_2^{II}$  in Fig. 5.10 are closer to each other than sonic points  $\rho_2^{II}$  and  $\rho_3^{II}$ .

First consider the type II flows. For a given area variation  $A(x)$ , Eqns. (5.9)

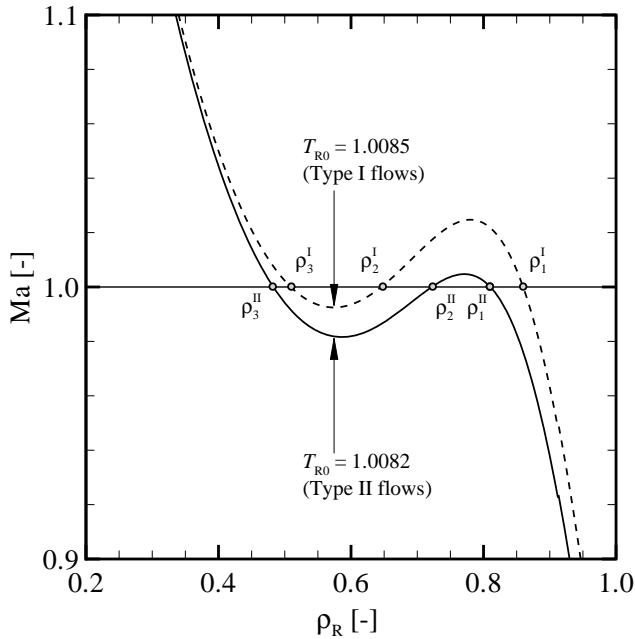


Figure 5.10:  $Ma$ - $\rho$ -plot for fluid  $D_6$  assuming expansion from two different stagnation states (not shown) along the isentrope which is tangential to the VLE region on the dew-line. Observe three sonic points for each line compared to only one along each  $Ma$ - $\rho$ -trend line in Fig. 5.9. Thermodynamic properties are computed with the PRSV EoS.

and (5.10) are just ordinary differential equations as a function of the spatial coordinate  $x$ . Thus, if the area variation corresponding to that of a classical converging-diverging nozzle is specified, then with appropriate boundary conditions, Eq. (5.10) for example, can be solved numerically. The results can be conveniently displayed in so-called phase-plane plots, which, depending on an integration constant which among other things, is related to the mass flow through the nozzle, represents the graphical solution of Eq. (5.10) under the validity of an equation of state (EoS). With reference to Fig. 5.10, Fig. 5.11 gives an example of a phase-plane plot representing (some of the) mathematical solutions of a one-dimensional, steady isentropic expansion through a converging-diverging nozzle whereby the  $Ma$ - $\rho$ -trend line exhibits three sonic points such that the points labeled  $\rho_1^{\text{II}}$  and  $\rho_2^{\text{II}}$  are closer to each other than  $\rho_2^{\text{II}}$  and  $\rho_3^{\text{II}}$ . Also illustrated are admissible, so-called type II, discontinuities. Details are to be

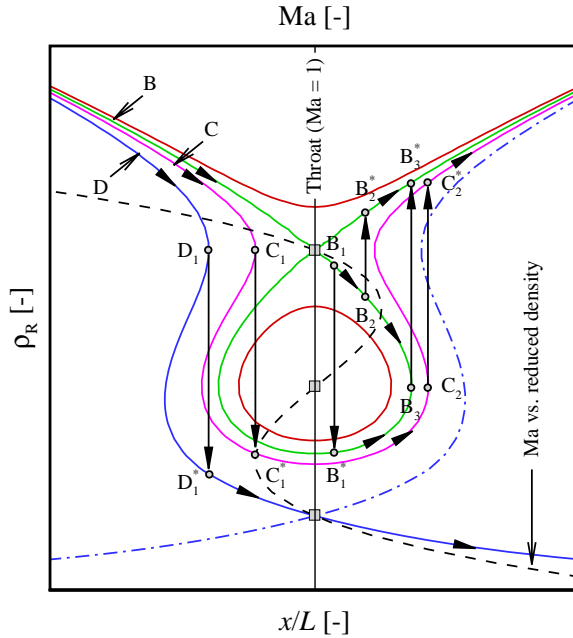


Figure 5.11: The phase-plane diagram that can be used to analyze the admissibility of type II shock waves in a conventional converging-diverging nozzle. The flow is from left to right. Remark that all phase-plane lines are for a single isentropie ( $s = s^*$ ) and the same stagnation state, although the mass flow is different between the various lines. Note that it was implicitly assumed that the shock waves are weak and therefore density jumps are nearly isentropic. Also sketched is the  $Ma$ - $\rho$  variation (black dashed line) in the case of steady expansion of the fluid along  $s^*$  from one specific stagnation condition.

presented in the subsequent paragraphs, following Cramer and Fry.

Note that for each individually colored curve in Fig. 5.11 (three of which are labeled B, C and D), the entrance conditions, the mass flow and the throat area for a given entrance area are the same, however, the mentioned conditions are different among the differently colored curves. For a single curve, the main difference in the actual physical flow is the entropy and pressure at the exit of the nozzle. Consider firstly curve B (green curve) in Fig. 5.11 representing the solution of an isentropic flow from left to right starting from subsonic conditions. As the fluid passes through the convergent section of the nozzle, the flow is accelerated from subsonic to sonic velocity in the throat. From the sonic throat

onward (and assuming that the shock waves are weak), the following can occur:

- The flow expands to a supersonic speed and at a certain location, a non-classical RSW is admissible (labeled  $B_1-B_1^*$ ). A discontinuity such as  $B_1-B_1^*$  can also occur in the nozzle's throat. Past the RSW, the flow is sped up further to finally give rise to the formation of a nonclassical sonic-to-subsonic CSW which exhibits the maximum strength in terms of pressure jump (labeled  $B_3-B_3^*$ ). Past the CSW, the flow expands further but remains subsonic.
- The flow expands to supersonic speed and eventually, a normal classical CSW is admissible (labeled  $B_2-B_2^*$ ). Also here, the flow expands further downstream of the CSW but remains subsonic.
- The flow expands to supersonic speed, then it slows down to sonic speed, and eventually, a nonclassical upstream sonic CSW is permissible (labeled  $B_3-B_3^*$ ).

Next, consider the curve labeled C, which is a solution if the mass flow is increased somewhat or if the throat-area-inlet-area ratio  $A_T/A_{\text{inlet}}$  is slightly decreased with respect to curve B. As the fluid passes through the convergent section of the nozzle, the flow is accelerated from subsonic to sonic velocity, however, due to the increased mass flow for example (with respect to the value corresponding to curve B), the sonic state is obtained upstream of the throat. Consequently, a nonclassical upstream sonic RSW is admitted (labeled  $C_1-C_1^*$ ) upstream of the nozzle's throat. Past the RSW, the flow speeds up to sonic conditions downstream of the nozzle's throat and finally admits a sonic-to-subsonic nonclassical CSW (labeled  $C_2-C_2^*$ ).

Finally, for an even larger mass flow (or more reduced nozzle throat area), the flow evolves along the curve labeled D. Also here, starting from subsonic stagnation conditions, the flow reaches sonic conditions upstream of the throat of the convergent-divergent nozzle. For the flow to continue further, a nonclassical upstream sonic RSW is admitted (labeled  $D_1-D_1^*$ ). Past the shock wave, the flow accelerates, becomes sonic at the nozzle's throat and accelerates to supersonic conditions downstream of the throat. Then, depending on the conditions in the low-pressure reservoir and the nozzle design, the following can occur, namely: i) a classical CSW is admitted: past this first CSW, the flow is accelerated to sonic conditions and finally admits a nonclassical upstream sonic CSW, or ii) the flow simply expands to supersonic conditions without admitting any discontinuity, or iii) the flow expands to supersonic velocity in the divergent section of the nozzle and eventually admits a classical CSW.

Of the mentioned gas dynamic discontinuities that can appear in expansion flows through nozzles, the most interesting phenomenon is the admissibility of a nonclassical RSW in the convergent part of the classical nozzle. From an experimental point of view, notwithstanding that apart from the RSW, also a

variety of additional (compression) shock waves are admissible, all of these second shock waves occur downstream of the nozzle's throat. The major drawback of such a proposed experiment using a converging-diverging nozzle interposed between two reservoirs is flow stability. Moreover, it is also noticed that slight changes of state in the high- and/or low-pressure reservoir can significantly complicate the flow field since more than one discontinuity surface is permissible (not persé along a specific curve B, C or D). Therefore, such an experiment is not to be recommended to provide experimental evidence of nonclassical gas dynamic phenomena.

Similar to what was shown for type II flows using the phase-plane plot, type I flows can permit, depending on the reservoir conditions (see Cramer and Fry [41], Kluwick [112] and Chandrasekar and Prasad [24]):

- No discontinuities if the Mach number in the throat is less than unity, however, if the throat is choked then,
- A pure nonclassical downstream sonic RSW is admissible past the nozzle's throat: downstream of the shock wave, depending on the nozzle-area variation and the thermodynamic state in the low-pressure reservoir, the fluid can either expand to supersonic velocity or undergo a supersonic-to-subsonic transition via a classical compression shock wave.
- A pure nonclassical downstream sonic RSW is admissible, succeeded by a first compression shock wave and a second upstream sonic compression shock wave, i.e., three shock waves are observed in the flow past the throat of the nozzle.
- A pure nonclassical RSW is admissible succeeded by an upstream sonic compression shock wave, i.e., two shock waves are observed in the flow past the throat of the nozzle.
- A nonclassical upstream sonic compression shock wave is admissible.
- A classical compression shock wave is admissible.

The previously mentioned type I and II flows can be visualized in an experimental facility and therefore, allow for a method for experimentally demonstrating nonclassical gas dynamic phenomena. Figure 5.12 shows a conceptual drawing of an experimental facility in which a high-pressure supercritical single-component fluid is expanded into a low-pressure reservoir. The complete system, apart from the balance of plant of charging and discharging the facility (the balance of plant is not shown), is placed in an oven for accurate temperature control. Also equipment for Schlieren imagery is needed to visualize the flow field, and are placed outside the oven. Because a visualization technique is used, the nozzle must be made of quartz glass or other high-temperature glass. Two parallel quartz glass windows equipped with obtura-

tors are also required. The obturators open the windows only during measurements. It is also proposed to place at various axial locations along the nozzle, static pressure measurements which can be useful in the interpretation of the visualized flow field. Note that for such an experiment flow stability is a major point of concern, because due to the change of pressure in both reservoirs due to the flow, also the admissible shock waves are different and therefore various shock waves would appear in the flow field. This would complicate the interpretation of the experimental results. Note that it is *theoretically* also possible to use a high-pressure reservoir with the fluid thermodynamic state located in the vapor-liquid equilibrium region, i.e., saturated vapor is expanded via the nozzle. However, in this case, if the saturated vapor state has a negative value of the fundamental derivative, then according to theory, the first part of the nozzle must have a nonclassical diverging-converging shape to first accelerate the flow from subsonic to supersonic conditions [196]. The nonclassical nozzle is immediately followed by a classical nozzle. Moreover, as the saturated vapor expands via the classical nozzle into the low-pressure reservoir, the liquid contained in the high-pressure reservoir flashes. Due to the temperature control, the flashing liquid allows for maintaining a nearly constant pressure in the high-pressure reservoir during the experimental run.

### 5.3.2 Supersonic flow in two dimensions - oblique shock waves

The turning of a (homentropic) supersonic flow is well documented (see e.g., Thompson [198]). If a supersonic flow of, say air, passes over a sharp compression corner, a classical oblique compression shock wave is formed, whereas a so-called centered Prandtl-Meyer expansion fan is observed for a supersonic flow of air over a sharp expansion corner. Using the Prandtl-Meyer function  $\omega$ ,<sup>4</sup> viz.

$$d\omega = \frac{\sqrt{\text{Ma}^2 - 1}}{1 + (\Gamma - 1)\text{Ma}^2} \frac{d\text{Ma}}{\text{Ma}}, \quad (5.11)$$

Thompson [196] demonstrated that if  $\Gamma < 0$  and remains so across the wave, turning of a supersonic flow over an expansion corner must occur via a nonclassical rarefaction shock wave. Conversely, turning of a homentropic supersonic flow past a compression corner is achieved by a centered Prandtl-Meyer compression fan. As was detailed in Sec. 2.3, nonclassical waves, e.g., sonic expansion shock waves, can (must necessarily) feature a change of sign of  $\Gamma$  across the wave. Consequently, expansion corners for example – under the provision that the thermodynamic state of the working fluid is located in the “rarefaction-shock region (RSR)” as delimited by Zamfirescu et. al. [226] (see Fig. 13 therein)

---

<sup>4</sup> $\omega$  has an analogous interpretation as the thermodynamic function  $F(\rho(x, t)) \equiv \int_{\rho_0}^{\rho} cd(\ln \rho)$  in Sec. 2.1.

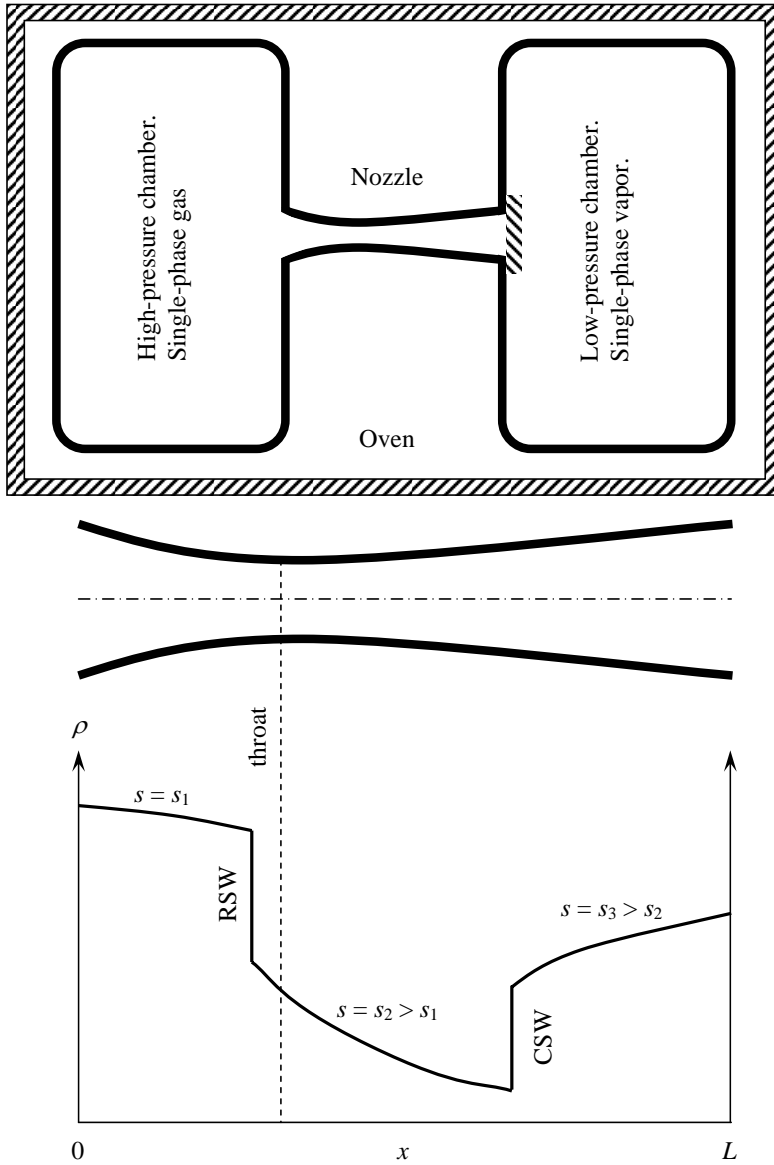


Figure 5.12: *Experimental facility to generate nonclassical shock waves in a classical nozzle. Here, the nozzle is to be equipped with static pressure instruments and Schlieren imagery is employed to visualize the flow field.*

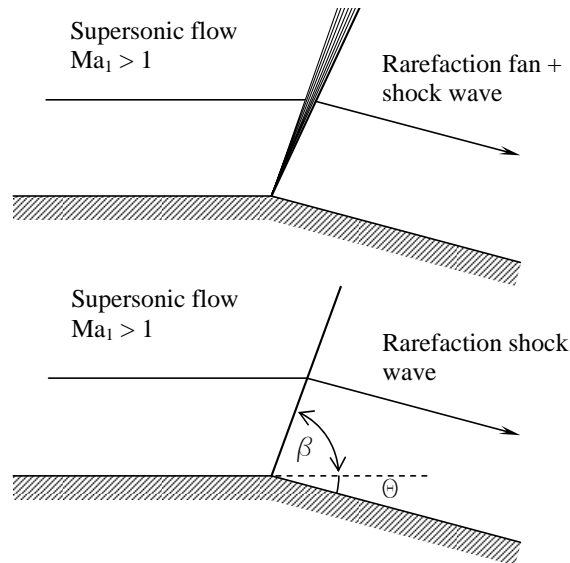


Figure 5.13: *Above: The formation of a centered Prandtl-Meyer expansion fan followed by an oblique rarefaction shock wave over an expansion corner (i.e.,  $\theta < 0$ ). Below: The formation of an oblique pure rarefaction shock wave over an expansion corner. Remark:  $\beta$  is the shock angle and  $\theta$  is the turning angle.*

– do not only permit the admissibility of oblique pure RSW's, but also composite waves like expansive fan-shocks or fan-shock-fans (see Fig. 5.13). Caveat: Cramer [40] has shown that not only the fundamental derivative of gas dynamics is important in the analysis of oblique shock waves but also the magnitude of the isentropic variation of  $\Gamma$  with density. This being stated, if the flow Mach number  $Ma_1$  is appropriately chosen, it can straightforwardly be demonstrated that not all thermodynamic states located within the RSR permit the admissibility of oblique (pure) RSW's.

From an experimental viewpoint where the main objective is to give proof of nonclassical gas-dynamic effects, two possibilities exist. On the one hand, an experiment can be performed which is aimed at creating a pure centered Prandtl-Meyer compression fan. In this situation, calculations should be aimed at maximizing the spreading angle of the centered compression fan. On the other hand, an oblique rarefaction shock wave can be generated in an experiment where a supersonic flow passes over a body with an expansion corner. In the following, an investigation is conducted for test fluid  $D_6$ , where, for a given

pre-shock state in terms of  $(P_1, \rho_1, Ma_1)$ , the shock-angle-turning-angle combination is determined; this results in a so-called  $\theta$ - $\beta$ - $Ma_1$ -plot (or oblique-shock chart). Moreover, only the near-sonic regime is considered. In this context, the presented work is similar to the study reported by Cramer [40], however herein, the weak-shock approximation is abandoned. It is worthwhile to mention that Cramer found from use of the weak-shock approximation, that not only the value of  $\Gamma_1$  but also that of its isentropic change with density, formulated as  $\Lambda_1 \equiv \Gamma_1 (\Gamma_1 - 2) + \rho_1 (\partial\Gamma/\partial\rho)_{s1}$ , plays an important role in the qualitative study of nonclassical oblique shock waves. In order to perform the computations, use is made of the shock admissibility conditions given by Eqns. (2.17) in Sec. 2.1. The computational procedure is as follows:

- Firstly,  $(P_1, \rho_1)$  and the flow Mach number  $Ma_1$  are chosen. Note that  $(P_1, \rho_1)$  is a thermodynamic state located in the RSR. Note that in choosing the combination of  $P_1$  and  $\rho_1$ , account has to be taken also of the value of  $\Gamma_1$  and  $\Lambda_1$ . Within the RSR, from high density to low density, isentropes exhibit successive intervals with  $\Gamma_1 > 0$  and  $\Lambda_1 > 0$ ,  $\Gamma_1 < 0$  and  $\Lambda_1 > 0$ ,  $\Gamma_1 < 0$  and  $\Lambda_1 < 0$ , and  $\Gamma_1 > 0$  and  $\Lambda_1 < 0$ , respectively. This implies that four cases of  $(P_1, \rho_1)$ -combinations are distinguishable.
- Next,  $\beta_{\min}$ , i.e., the smallest shock angle which can in principle result in the formation of an oblique shock wave (either compressive or expansive), is computed. The minimum shock angle is obtained from

$$\beta_{\min} = \arcsin (Ma_1^{-1}). \quad (5.12)$$

- For values of  $\beta$  varying from  $\beta_{\min} - 90^\circ$ , the post-shock states are determined using Eqns. (2.17), these are the shock admissibility conditions, and the equation of state of the test fluid. Remark that admissible shock waves satisfy  $Ma_{2n} \leq 1$ , however  $Ma_2 \begin{matrix} \leq \\ \geq \end{matrix} 1$ .
- Using geometrical arguments and taking into consideration that: i) the component of the flow velocity parallel to the oblique shock wave is invariant across the discontinuity, ii) that the normal component of the flow velocity undergoes a (super)sonic-to-(sub)sonic speed change, and the boundary conditions of the wall(s), it can be demonstrated that

$$\frac{[P]}{\rho_1 (c_1 Ma_1)^2} = \frac{\tan \theta}{\cot \beta + \tan \theta}. \quad (5.13)$$

This represents one equation with a single unknown, namely the turning angle  $\theta$ . From the data obtained in the previous two steps,  $\theta$  can be solved and the oblique-shock chart can be drawn.

Applying the above-mentioned procedure to fluid D<sub>6</sub> and using the EoS documented in Sec. 3.3,  $\theta$ - $\beta$ - $Ma_1$ -plots are calculated and displayed in Figs. 5.14–5.16 for three different combinations of  $(P_1, \rho_1)$  located on the same isentrope.

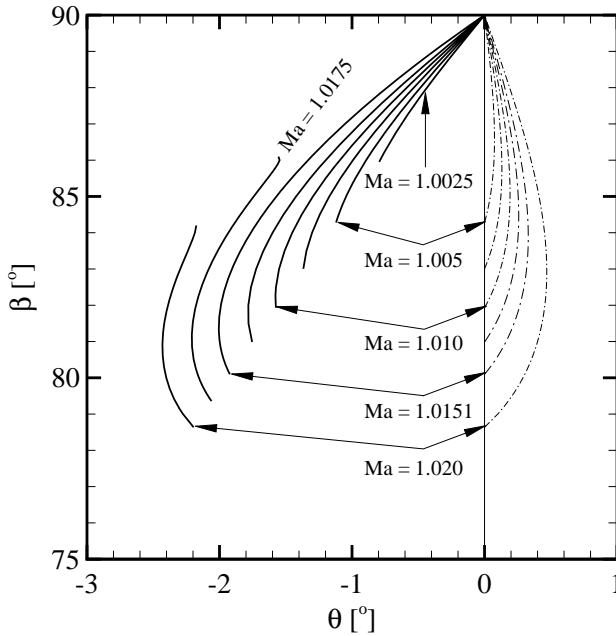


Figure 5.14: The shock angle  $\beta$  as a function of the turning angle  $\theta$  for various values of  $Ma_1$ . Negative values of  $\theta$  imply expansion corners and positive values imply compression corners. Here,  $P_1 \approx 9.40$  bar,  $\rho_1 = 208.82$  kg/m<sup>3</sup>,  $\Gamma_1 > 0$ , and  $\Lambda_1 > 0$ . Observe that for values of  $Ma_1 > 1.0151$  there exists a range of negative- $\theta$ -angles where oblique pure RSW's are inadmissible. This can be explained by means of the results presented in Fig. 2.9 where it is seen that along a superheated isentrope there exists a maximum pre-shock Mach number. For Mach numbers greater than this threshold value, a pure RSW is not possible because of violation of the shock admissibility conditions (geometrically, this would imply that the slope of the Rayleigh line is greater than the value which gives rise to a sonic post-shock state).

Just for the sake of completeness, it should be mentioned that the selected isentrope exhibits two inflection points in the dense-gas thermodynamic regime. The combination of  $(P_1, \rho_1)$  where  $\Gamma_1 > 0$  and  $\Lambda_1 < 0$  is not chosen because an (oblique) RSW is never admissible for this case.

For the results presented in Figs. 5.14–5.16 it is observed that steep RSW's are admissible even for very small turning angles, not that this would be the cause of specific difficulties like flow instabilities. Furthermore, the range of

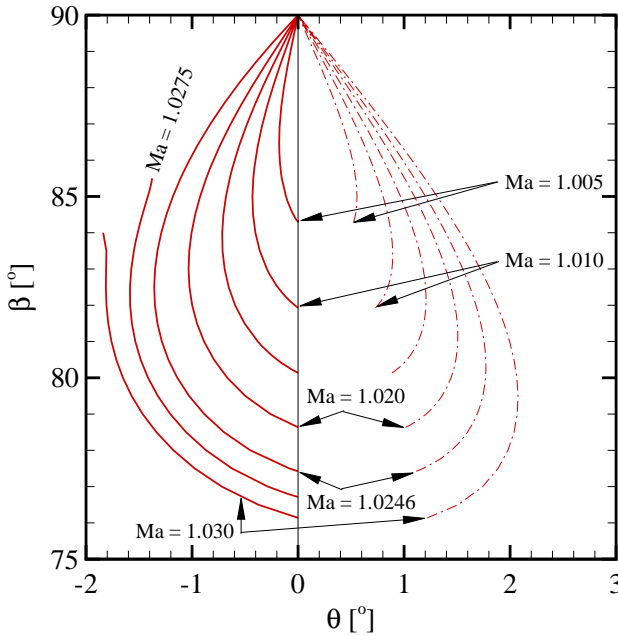


Figure 5.15: The shock angle  $\beta$  as a function of the turning angle  $\theta$  for various values of  $Ma_1$ . Here,  $P_1 \approx 9.20$  bar,  $\rho_1 = 190.45$  kg/m<sup>3</sup>,  $\Gamma_1 < 0$ , and  $\Lambda_1 > 0$ .

upstream pressures is rather large and the local upstream Mach number does not necessarily need to be very close to unity. Taking these considerations into account, an experiment where an oblique pure RSW is created seems feasible. In this case, a steady supersonic flow has to be created and visualization techniques should be used to measure the angle of the oblique discontinuity, which is formed near an expansion corner of a body. Here, for example, a LASER source, a CCD camera, and a high frequency oscilloscope can be used for both pulse measurements and synchronization purposes. Two parallel quartz glass windows equipped with obturators are required. The obturators open the windows only for a very short period of time, namely when the measurement is conducted. In this way the glass is kept at an approximatively constant temperature and therefore, the formation of thermal stresses in it is reduced. Remark that complications can arise due to non-equilibrium phenomena, like relaxation.

To obtain a steady supersonic flow of a timescale of tens of milliseconds, use can be made of a Ludwieg tube equipped with a fast-opening valve (or a diaphragm). Conceptually the Ludwieg tube is similar to the variable-cross-

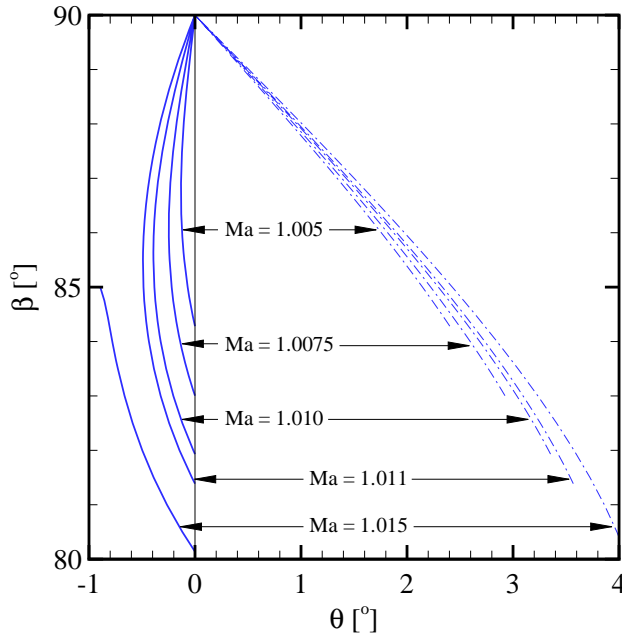


Figure 5.16: The shock angle  $\beta$  as a function of the turning angle  $\theta$  for various values of  $Ma_1$ . Here,  $P_1 \approx 8.90$  bar,  $\rho_1 = 168.59$  kg/m<sup>3</sup>,  $\Gamma_1 < 0$ , and  $\Lambda_1 < 0$ .

section shock tube; it consists of a long, high-pressure charge tube, a nozzle, either a diaphragm or a fast opening valve, and a large-volume low-pressure dump-tank where for example a body can be placed around which the flow has to be investigated. If the fast opening valve is opened, commonly, an expansion wave propagates into the charge tube. The high-pressure fluid upstream the expansion wave is accelerated through it and flows towards the nozzle at a constant Mach number, total pressure and temperature. These conditions can be maintained during the whole experiment run time, since the thermodynamic states in the facility are chosen to choke the nozzle. Moreover, the flow at the exit of the nozzle is supersonic.

## 5.4 Comparison between the experimental options

In the following, the pros and cons of each of the experimental options to investigate nonclassical phenomena associated with BZT fluids, as described in

the previous sections, are presented. To do this in a systematic manner, first of all, the presented experimental options are briefly recalled. Afterwards, criteria are presented on the basis of which each option and/or facility is judged. The experimental options described in the previous sections are:

- **Triple discontinuity shock tube**

The experiment is aimed at creating a nonclassical rarefaction shock wave in a constant-cross-section shock tube. The discontinuity is created by rupturing a diaphragm which separates the driver and driven gas; alternatively, a fast-opening valve can be used instead of a diaphragm. A time-of-flight method is used to determine the speed of propagation of the expansive wave. Only if the measured wave speed is greater than the local speed of sound of the quiescent medium in the high-pressure side, can it be claimed that the expansive wave is a rarefaction shock wave. The time-of-flight method requires the use of dynamic pressure sensors which are placed at accurately known distances along the pipe wall.

- **Laser induced point explosion**

A point explosion is induced in a BZT fluid in a spherical chamber to produce a spherical compression/rarefaction/compression wave combination. The fluid is at rest in a thermodynamic state located inside the negative nonlinearity region; the energy necessary to generate the spherical waves is provided by either an electrical discharge or by focusing a laser beam at the center of a small inner sphere. Total-pressure measurements of the leading nonclassical compression wave are to be performed to demonstrate that the wave is indeed a nonclassical isentropic wave of which the thickness is increasing in time. The pressure probes however should not severely perturb the flow field. Alternatively, visualization techniques can be used to estimate the thickness of the compression wave at different times.

- **Creating steady nonclassical shock waves in a convergent-divergent nozzle**

By expanding a BZT fluid through a classical convergent-divergent nozzle, the numerical calculations have shown that a variety of discontinuities are admissible which do not have counterparts according to classical gas dynamics, e.g., the formation of nonclassical RSW's in the throat or even upstream of the throat of a convergent-divergent nozzle. Such an experiment would probably focus on creating the last mentioned discontinuity and optical measurements are used to visualize the shock wave and static pressure measurements are used as a validation that the shock wave is expansive.

- **Oblique rarefaction shock waves over bodies**

Calculations have shown that expansion of a supersonic BZT fluid over

a sharp expansion corner, permits the formation of oblique rarefaction shock waves. By using visualization techniques, the discontinuity can be analyzed.

An assessment of the different outlined experimental options is to be based on suitably defined criteria. These criteria are:

- **Flow field complexity**

The flow field to be observed has to be as simple as possible, i.e., nonclassical phenomena to be observed must be clearly visible and distinguishable from the rest of the flow field. This is necessary in order to simplify the measurements and to avoid possible confusion in the interpretation of the observed and measured phenomena. In this respect, a “simple” flow field simplifies the design of the facility. As an example, consider the shock tube and the steady nozzle flow experiments. The shock tube can be designed by means of CFD simulations or analytical approaches relying on the inviscid flow approximations.

- **Manufacturing and operating simplicity**

If less instruments and parts are used, less errors are introduced in the measurement chain. Also trouble shooting is easier.

- **Versatility**

The selected experimental option and the associated facility must allow for changing both the operating conditions and the working fluid with ease. The operating conditions are for example computed from thermodynamic models, which have a certain accuracy. It is therefore reasonable to expect that the preliminary experimental phase will involve trial and error. The choice of a suitable fluid is subjected to both thermochemical stability constraints and BZT characteristics, e.g., the size of the region of negative nonlinearity. Prior to the experiment, this information is only partially known. The possibility of changing the working fluid is therefore considered a significant amenity of the setup.

- **Modularity**

Besides the primary goal of proving the existence of nonclassical phenomena in the dense gases of molecularly complex substances, the proposed experimental setup must be designed taking into account the possibility of making modifications in the future. This is necessary in case of failure of the facility or if different nonclassical wave fields not considered during the design stage, are to be investigated. Moreover, every experiment is in itself a learning experience and the knowledge acquired in the experiment can be directly applied to improve it.

- **Intrusiveness**

Due to the very limited range of operating conditions allowing for nonclas-

sical behavior, the measurement technique is required not to be intrusive, namely to keep the disturbances in the flow as small as possible.

- **Accuracy requirements**

Any given measurement technique poses accuracy constraints on thermodynamic and gas-dynamic models. These constraints are to be consistent with the actual capability of the models. Consider as an example the triple discontinuity experiment. In this experiment, the speed of sound in the unperturbed state is to be known within approximately 2 % of uncertainty for distinguishing between a nonclassical rarefaction shock and a classical isentropic rarefaction fan. In this case, a high-accuracy EoS should be used which is also validated extensively with experimental data, or the speed of sound should be measured on site.

- **Sensitivity to operating conditions**

The quantities to be measured (e.g., shock position, shock speed) must be nearly insensitive to small changes in the operating conditions. Consider for example a shock wave inside a nozzle. If the curvature of the nozzle walls is very small, a small change in the back pressure results in a large change in the shock position (it is even possible that multiple shock waves are observed), thus making the measurements (and the interpretation of the results) more difficult.

- **Availability**

The experimental facility should be characterized by high availability. The above is true in the preliminary phase of the investigations, where numerous experiments are to be carried out to verify the operating conditions. Availability here includes maintenance turnaround times but particularly the time elapsed between different runs.

- **Repeatability**

Repeatability is critical in that differences between runs may lead to large uncertainties in the results.

- **Cost**

Cost are of course to be included in the evaluations.

Based on the above-mentioned criteria, arguments for and against each of the options delineated in Secs. 5.2 and 5.3, are given.

- **The triple discontinuity experiment**

The flow field is rather simple and can be simulated by means of simple one-dimensional inviscid computations, provided that an estimate is given on the boundary layer effects in the shock tube. The modularity is also very high if for example the tube is made of pipe segments and sufficient measurement stations are available along the pipe wall. Intrusiveness of the pressure probes is almost negligible if they are flush mounted.

Accuracy requirements are well within the capabilities of the thermodynamic models – although this should always be verified for molecularly complex substances, especially in the region which is of interest for BZT-experiments – and of measuring techniques. From the cost perspective, the price is higher than that of a simple shock tube mainly because of the high temperatures involved. There are however some drawbacks (at least when it concerns BZT experiments). If a diaphragm is used, a time-consuming trial & error process is required to determine the scorch-depth which allows for a complete rupture of the diaphragm at the required pressure (difference) and temperature. Moreover, previous experiments at the University of Colorado at Boulder have shown that the diaphragm can still rupture incompletely, thereby disturbing the flow field. These aspects related to the diaphragm reduce the repeatability and reproducibility of the experiments and seriously limits the availability of the setup, and would jeopardize fluid purity. Many of the highlighted complications are eliminated if a fast-opening valve is employed instead.

- **Laser induced point explosion**

The flow field is more complex than for example for the shock tube. The facility however, is believed to be very small, namely consisting of a sphere with a diameter of less than 50 cm. Manufacturing and operating the facility are believed to be quite simple. Operating conditions can be varied in a simple way by changing the duration of the laser impulse and/or its power and the initial conditions. The sensitivity of the resulting flow field to operating conditions is higher than in the case of the triple discontinuity experiment because here, the goal is to generate a nonclassical compression fan; the admissibility region of compression fans is somewhat smaller in terms of pressures and temperatures compared to that of rarefaction shock waves. Accuracy requirements are within the range of available thermodynamic models. However, the fluid in the excited state is expected to thermally decompose if the localized energy input is too high. This implies that the fluid is to be changed after each trial or after few trials, thus the availability is very poor. If total pressure measurements are conducted, the flow field can be disturbed significantly, due to probe intrusion. Furthermore, because of the peculiar design, the versatility of the setup is limited. Also the costs are potentially high, if the working fluid is expensive and if a laser for optical measurements is unavailable in the laboratory. Note that if visualization techniques are used, potential relaxation effects can be detected. This provides additional information of the flow field, but complicates the interpretation of the results.

- **Expansion of a BZT fluid through a classical nozzle**

The flow field in an experiment where a BZT fluid is expanded in a classical nozzle is rather complex and in fact very much sensitive to both the

high- and low-pressure-reservoir conditions. For example, the calculations by Cramer demonstrate that for a given stagnation state, as many as three shock waves (expansive and compressive) can appear depending on the thermodynamic state of the low-pressure reservoir. Furthermore, obtaining a steady flow can be rather problematic and the repeatability is expected to be low. As was mentioned however, if a steady flow is possible, creating a discontinuity in the convergent section of a classical nozzle does provide an unambiguous proof of a BZT effect. The availability of the setup is similar to that of a shock tube equipped with a balance of plant (the balance of plant consists of auxiliary equipment which allows the user to set and control the required operating conditions of the facility; in this framework, the balance of plant consists of a vapor-generator, a condenser, pumping equipment, etc.). Moreover, by equipping the low-pressure reservoir with optical equipment and windows, it is possible to study the admissibility of oblique nonclassical wave fields, like oblique rarefaction shock waves and compression fans. In this situation however, the size of the region of negative nonlinearity should be large enough to encompass the critical isotherm, so that it is rather easier to obtain the required upstream Mach number.

- **Oblique rarefaction shock wave in two dimensions**

Such an experiment would require the use of, for example, Schlieren imagery or shadowgraphy to visualize the flow field along a 2-D geometry (gradual processes as for example fans are difficult to detect using shadow methods). In this case, the shape of the body itself can complicate the flow field, since additional discontinuities can be observed. Furthermore, relaxation phenomena can be observed which complicate the interpretation of the results. Also in such an experiment, the size of the region of negative nonlinearity should be large enough to encompass the critical isotherm, so that it is rather easier to obtain the required upstream Mach number in a simple Ludwig tube. Such an experiment may be rather costly however, because it would be necessary to not only have/build a high-temperature Ludwig tube, but also to purchase optical instruments. Also various 2-D bodies are required. Repeatability is not a major point of concern if the Ludwig tube is equipped with a fast-opening valve. However, the results of calculations show that the flow field is very sensitive to the uncertainty in the thermodynamic EoS. The experiment is non-intrusive.

## 5.5 The proposed experimental facility

From the information presented in the previous section, it can be argued that the goal of the experiment which is to be performed, is to create and detect a rarefaction shock wave. Comparison of various experimental strategies sug-

gests that, as a first step, an unsteady experiment using a variable cross-section shock tube equipped with a fast-opening valve and a nozzle is the most suitable facility to start with. The experimental facility is flexible and modular and can be expanded and/or modified in successive phases of the project (see the technical report by Zamfirescu et. al. [224]), therefore the acronym **FAST**, i.e., **Flexible Asymmetric Shock Tube**, is used. The fast-opening valve is used because it greatly increases the availability of the setup; it is placed in the low-pressure compartment of the setup. Moreover, a fast-opening valve with technically feasible opening times can be designed and manufactured because of the comparatively low speeds of sound involved in the case of substances classifying as BZT fluids. The nozzle is located in between the high- and low-pressure side of the shock tube in order to stabilize the flow in the charge tube, but mainly to block disturbances which can be initiated by the opening of the fast-opening valve from propagating into the charge tube and thereby complicating the measurement of the RSW. Details about the conceptual design of the facility can be found in Chap. 6. Chapter 7 treats the commissioning of the setup.

## 5.6 Working fluid selection

The choice of a working fluid for the experiment is of the utmost importance, as the previous failed attempts to experimentally demonstrate nonclassical gas-dynamic effects in superheated vapors have shown. In the experiment conducted by Borisov et. al. [17], the working fluid R13 does not display a region of negative nonlinearity in the single-phase thermodynamic plane, therefore it is in theory impossible to create RSW's. The experiment of Ferguson [65] encountered major problems due to thermochemical decomposition of the fluid, which was a heavy perfluorocarbons (PP10).

The choice of the working fluid for the experiment is to be based on several considerations: firstly, a number of fluid parameters related to the strength of potential BZT effects must be assessed, e.g., the value of  $\Gamma_{\min}$  and the sensitivity of, for example, the pressure jump across an RSW to the value of the dimensionless isochoric heat capacity. Secondly, other important fluid characteristics, like thermochemical stability and availability of thermodynamic properties must be duly considered. Finally, safety concerns must be addressed. These criteria are intimately linked: the strength of nonclassical gas-dynamic effects is related on a microscopic level to the capacity of the molecule to store energy, i.e., to its specific heat [29]. The more complex is a molecule the higher is its isochoric specific heat but also the lower is its thermochemical stability. High temperature is closely related to the risk of explosions and thermal decomposition can be the cause of the formation of toxic gases. Currently, three fluid families can be taken into consideration, namely hydrocarbons, perfluorocarbons and siloxanes. In all cases the experiments have to be carried out at elevated temperatures, therefore complex hydrocarbons that could potentially exhibit BZT

effects, have to be ruled out because of the risk of explosions. Complex perfluorocarbons are potentially very attractive because they have a high isochoric specific heat but a lower critical temperature with respect to siloxanes. The high specific heat is due to the molecular content of fluor atoms which contribute, in terms of rotational and vibrational energy, to the specific heat more than hydrogen and silicon atoms in siloxanes. The comparably lower critical temperature of perfluorocarbons implies that the  $\Gamma < 0$ -region lies also at lower temperature if compared to siloxanes. As an example, using the PRSV EoS, PP5 has a  $\Gamma_{\min} = -0.11$  at  $T = 284.4 \text{ }^\circ\text{C}$  ( $T_C = 291.85 \text{ }^\circ\text{C}$ ), whereas  $D_5$  has comparatively the same  $\Gamma_{\min} = -0.14$ , however at  $T = 338.9 \text{ }^\circ\text{C}$  ( $T_C = 346 \text{ }^\circ\text{C}$ ), so at about  $55 \text{ }^\circ\text{C}$  higher than that of PP5. It should be noted that thermodynamic-properties calculations for PP5 are affected by much larger uncertainties than for siloxanes. Perfluorocarbons are also known to be extremely thermally stable among organic fluids. Assuming that siloxanes and perfluorocarbons have similar thermochemical stability, the safety margin with respect to decomposition would be greater for perfluorocarbons. On the other hand decomposition products of perfluorocarbons are highly aggressive, e.g. hydrofluoric acid (HF) and possibly other very toxic compounds. Moreover, the knowledge of their thermodynamic properties is at a far lower stage if compared to siloxanes and this makes the design of the experiment and the setting of the operating conditions much more problematic. Siloxanes can theoretically exhibit BZT effects as demonstrated in Ref. [30]. These results are linked to the current estimation of the specific heat for this family, which has an uncertainty of 5–6 %. Anyhow, thermodynamic modeling of siloxanes is in an advanced stage and their thermal stability in conditions similar to the foreseen experiment has been tested [27]. Thermal decomposition of siloxanes leads to polymerization and the polymer product is not toxic. Flammability of siloxanes is far lower than hydrocarbons. The siloxanes, e.g., MM and MDM, are currently utilized in organic Rankine cycle engines, which is the first applications proposed for the envisaged results of the current research project. All the mentioned reasons leads to choose siloxanes as the first working fluids to be tested in the proposed experiment.

**Nomenclature**

Symbol	Description
$A$	Flow area
$C_P^0$	Specific ideal-gas isobaric heat capacity
$c$	Speed of sound
$D$	Shock tube diameter
$h$	Specific enthalpy
$J$	Mass flux
Continued on the next page...	

Continued

Symbol	Description
$L$	Shock tube length
Ma	Mach number
$\dot{m}$	Mass flow
$P$	Pressure
$R$	Radius of a spherical cavity
$r$	radial coordinate in a spherical coordinate system
Re	Reynolds number
$s$	Specific entropy
$T$	Temperature
$t$	Time
$u$	Fluid velocity with respect to a laboratory reference frame
$v$	Specific volume
$w$	Fluid velocity with respect to a shock-related reference frame
$x$	Spatial coordinate
$\beta$	Shock angle
$\Gamma$	Fundamental derivative of gas dynamics
$\zeta$	Bulk viscosity
$\eta$	Dynamic (shear) viscosity
$\theta$	Turning angle
$\Lambda$	Isentropic variation of the fundamental derivative of gas dynamics
$\nu$	Kinematic viscosity
$\rho$	Density
$\omega$	Prandtl-Meyer function



*“We’re going to – we’ll be sending a person on the ground there pretty soon to help implement the malaria initiative, and that initiative will mean spreading nets and insecticides throughout the country so that we can see a reduction in death of young children that – a death that we can cure.”*

President George W. Bush, Washington, D.C., October 18, 2007

# 6

## Rarefaction-shock-wave experiments in the flexible asymmetric shock tube (FAST)

From:

COLONNA, P., GUARDONE, A., NANNAN, N. R., AND ZAMFIRESCU, C. Design of the dense gas Flexible Asymmetric Shock Tube. *J. Fluids Eng.-T. ASME* 130, 034501 (2008), 6 pages.<sup>1</sup>

### **Abstract**

*Herein, the conceptual design of the flexible asymmetric shock tube (FAST) facility for the experimental verification of the existence of nonclassical expansion shock waves in vapors of BZT fluids, is discussed. The FAST facility is a Ludwieg tube setup composed of a charge tube which is separated from a discharge vessel by a fast-opening valve. Furthermore, a nozzle with adjustable throat-area is placed in between the valve and the charge tube. The nozzle is intended to be choked during stationary operation and therefore it prevents disturbances which can be initiated in the discharge vessel, from propagating into the tube. The speed of the generated expansion wave is measured by means of high-resolution dynamic-pressure transducers using a time-of-flight technique. The provisional working fluid is dodecamethylcyclohexasiloxane ( $D_6$ ,  $C_{12}H_{36}O_6Si_6$ ).*

---

<sup>1</sup>Numerical data have changed slightly.

*To support the preliminary design, numerical simulations of the experiment are conducted using real-gas thermodynamic properties and the results are presented. Additionally, the sensitivity of the results due to the uncertainty of the thermodynamic equation of state of the fluid is assessed. The preliminary design is confirmed to be feasible and construction requirements are found to be within technical limits.*

## 6.1 Introduction

The existence of nonclassical rarefaction shock waves (RSW's) is to be proved by measuring the speed of propagation of the surface of the discontinuity in a quiescent fluid, as attempted first at the University of Colorado at Boulder (see Ferguson et. al. [63, 65, 66] and Guardone [80]). From the knowledge of the speed of sound in the unperturbed state – which has to be measured on site prior to the experiment – one can compute the expansion-wave Mach number. If this wave Mach number is greater than unity, i.e., supersonic, the wave is a nonclassical one (refer to Chap. 2). Conversely, if the wave Mach number is sonic with respect to unperturbed conditions, then it is either a classical expansion fan or an upstream or double sonic expansion shock wave.

Herein, the preliminary design of the experimental facility to generate and measure expansion shock waves is described. The preliminary design is validated by means of numerical simulations. The dependence of the results on the chosen thermodynamic model is also assessed. Furthermore, the wave velocity measurement technique is discussed. Finally, an overview is given of the measurement system and the experimental strategy.

## 6.2 Preliminary design

The concept of the flexible asymmetric shock tube (FAST) facility is depicted in Fig. 6.1. The Ludwieg-tube setup is composed of a high-pressure charge tube connected to a low-pressure reservoir (also referred to as a dump tank or discharge vessel). The charge tube and the reservoir are separated by a fast-opening valve (FoV). The fluid is initially at rest everywhere and the temperature is kept uniform by a suitable temperature-control system. The experiment starts when the FoV is opened, thereby connecting the fluid in the charge tube to that contained in the reservoir. For suitable initial states A in the charge tube and R in the reservoir, an RSW is expected to form and to propagate into the charge tube. Through the RSW, the fluid is accelerated from rest conditions A to post-shock conditions B. The fluid flows into the reservoir through a nozzle. Under stationary conditions, the nozzle is designed to operate in choked conditions, namely at sonic conditions S at the nozzle throat. Consequently, disturbances initiated during the opening process or formed in the reservoir do not

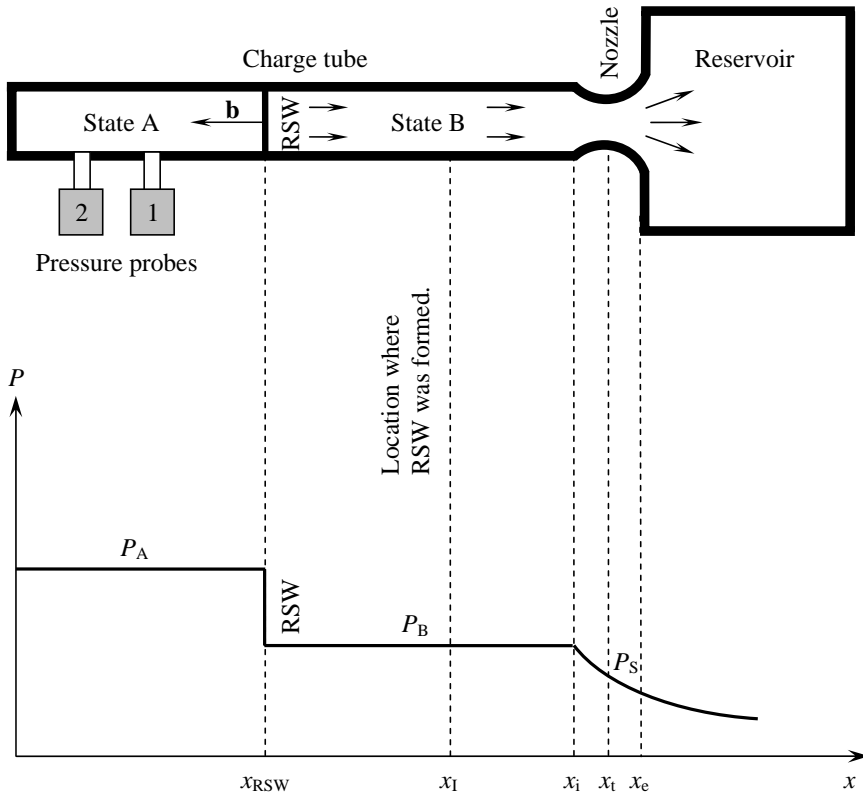


Figure 6.1: *The dense-gas Ludwieg tube: a qualitative description elucidating the operation of the facility and the pressure profile after the opening of the FoV (not shown) which separates the fluid in the charge tube from that contained in the reservoir. Coordinates  $x_i$  and  $x_e$  refer to the nozzle inlet and exit, respectively.  $P$ - $x$ -snapshot: an expansion (rarefaction) shock wave (RSW) propagates into the charge tube at (super)sonic speed with respect to the quiescent medium ahead of the wave. Past the RSW, the fluid is accelerated from rest conditions A to post-shock conditions B and flows into the reservoir through the nozzle. At the nozzle throat, the flow Mach number as perceived according to an inertial reference frame, is unity.*

propagate into the charge tube. Four dynamic-pressure transducers are flush-mounted on the charge tube (only two are shown in Fig. 6.1) and they are used in pairs to measure the incident RSW using a predetermined high data-sampling rate. A time-of-flight method is used to determine the speed of the rarefaction wave; as was indicated previously, if the speed is greater than the local speed

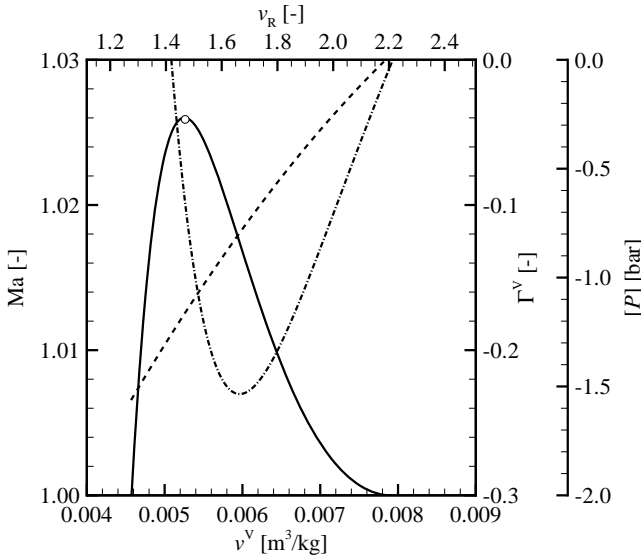


Figure 6.2: The maximum pre-shock Mach number  $M_A$  (solid line) of admissible pure nonclassical RSW's in  $D_6$  as a function of the pre-shock (reduced) saturated vapor specific volume  $v^V$  ( $v_R \equiv v^V/v_C$ ), whereby the post-shock Mach number  $M_B = 1$ . Also displayed are the value of the fundamental derivative of gas dynamics along the dew-line ( $\Gamma^V$ ; dash-dotted line) and the pressure change  $[P]$  across the admissible RSW's (dashed line). The maximum in Mach number, namely 1.026, occurs at  $P^{sat} \approx 9.18$  bar. Calculations are conducted with the EoS documented in Sec. 3.3.

of sound, then the wave propagates at supersonic speed with respect to unperturbed conditions and it is indeed a nonclassical shock wave of the expansive type.

The working fluid is dodecamethylcyclohexasiloxane ( $D_6$ ,  $C_{12}H_{36}O_6Si_6$ ) and it is chosen as a compromise between thermochemical stability and the size of the thermodynamic region – in terms of the pressure and temperature range – in which nonclassical gas-dynamic phenomena can possibly occur according to current thermodynamic equations of state (EoS's) (see also Sec. 5.6). Pre- and post-shock conditions leading to the RSW with maximum Mach number have been computed according to the procedure presented in Ref. [223] and are reported in Fig. 6.2 and in Table 6.1. Anticipating the outcome of the computations to be outlined in the following subsections, Fig. 6.3 shows an RSW and the expansion process up to the nozzle throat in the reduced volume-pressure plane and the Mach profile along the charge tube at a time  $t = t_I$  (the plotted data are taken from Tables 6.1 and 6.2).

Table 6.1: Pre- and post-shock states A and B computed analytically using the EoS in the Span-Wagner functional form for  $D_6$  (refer to Sec. 3.3). Remark that the pre-shock state is located on the dew-line, whereby the corresponding saturated vapor specific volume is slightly less than that giving rise to the maximum Mach number shown in Fig. 6.2 as indicated by  $\circ$ . The RSW is downstream sonic.

		Value	Units
RSW	$b$	36.12	m/s
	$Ma_b$	1.026	–
State A	$P_A$	9.126	bar
	$\rho_A$	186.11	kg/m <sup>3</sup>
	$T_A$	369.19	°C
	$\Gamma_A$	-0.1421	–
	$u_A$	0.0	m/s
	$c_A$	35.22	m/s
	$Ma_A$	0.0	–
State B	$P_B$	8.017	bar
	$\rho_B$	127.54	kg/m <sup>3</sup>
	$T_B$	364.05	°C
	$\Gamma_B$	0.1576	–
	$u_B$	16.58	m/s
	$c_B$	52.70	m/s
	$Ma_B$	0.315	–

The possibility of using different siloxane fluids in the facility, as well as a study of the sensitivity of the design parameters as the result of the uncertainty in the thermodynamic EoS of the fluid, is discussed in Ref. [225]. The design of the critical subsystems of the FAST experiment is detailed in the following subsections.

### 6.2.1 Fast-opening valve and charge-tube length

Due to the finite opening time of the valve, the RSW is not formed instantaneously. Instead, a finite time or, equivalently, space is required for all disturbances to coalesce into a single shock front. An estimate of the maximum allowed opening time can be obtained by imposing that the RSW is completely formed at point I located at  $x_I$ . The domain of dependence of point I is given by the region in the  $x-t$  plane bounded by the curves  $\sigma_A^-$  and  $\sigma_B^-$ . If i) dissipative effects and the influence of body forces are neglected up to the moment of shock formation, ii) if the flow-area is constant ( therefore it is assumed that the noz-

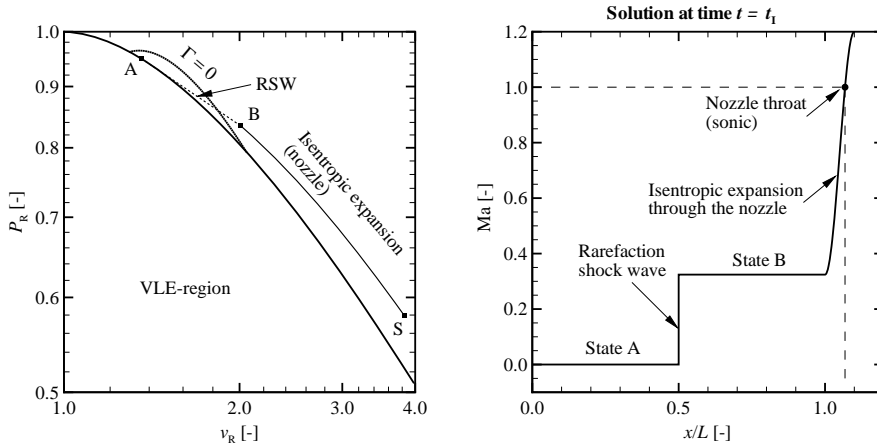


Figure 6.3: Left: Expansion in the charge tube up to the nozzle throat in the  $v_R - P_R$  plane of  $D_6$ . Data are reported in Tables 6.1 and 6.2 and were determined using the EoS in the Span-Wagner functional form for  $D_6$  as documented in Sec. 3.3. Right: Snapshot of the Mach profile at time  $t = t_I$  for a fully formed RSW.

zle length is small with respect to the shock formation distance, as is indeed the case) and iii) no additional shock waves are formed during the opening process, then the opening time  $\Delta t_{\text{open}}$  can be obtained by computing the intersections of the characteristic curves with the  $x = x_I$ -line as follows (also refer to Sec. 2.1)

$$\Delta t_{\text{open}} = (x_I - x_i) \left( \frac{1}{\sigma_A^-} - \frac{1}{\sigma_B^-} \right). \quad (6.1)$$

Here,  $\sigma_A^- = -c_A$  and  $\sigma_B^- = u_B - c_B$  are the characteristic velocities (or wave speeds).

In the FAST facility, the intersection point  $x_I$  has been chosen to be located at 5 m from the FoV, which yields  $\Delta t_{\text{open}} \approx 3.6$  ms if computations are done with the EoS documented in Sec. 3.3. Remark that if all computations are done with the Peng-Robinson [161], Stryjek-Vera modified [190], cubic EoS, then substitution of the accordingly updated pre- and post-shock states in Eq. (6.1) yields  $\Delta t_{\text{open}} \approx 3.3$  ms. Such a low value of the opening time is deemed technically feasible, even at the very high temperature of operation of the experiment (which is about 360–400 °C). A FoV satisfying the present requirements has been designed and is currently under construction (see Figs. 7.3 and 7.4 in Chap. 7). The RSW is to be completely formed as it passes the two measurement stations (these are the dynamic-pressure instruments) which are positioned close to the left end-wall of the 9-meter-long charge tube (see Fig. 6.1). From the arrival time of the wave at the dynamic-pressure instruments, the wave speed can be

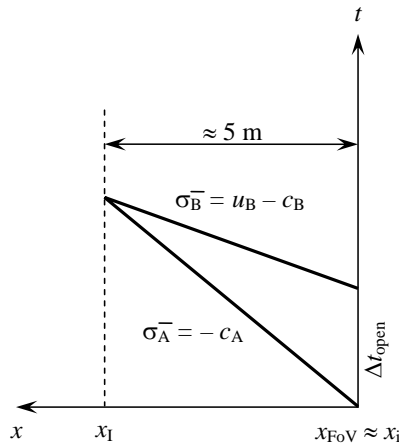


Figure 6.4: *Two left-moving waves which allow for estimating the opening time of the valve if the RSW is to be formed 5 m to the left of the inlet of the nozzle. Here it is assumed (as is also the situation in the facility as built) that i) the distance between the location of the fast-opening valve and  $x_1$  (i.e., the nozzle inlet coordinate) is very small with respect to 5 m, ii) the influence of the nozzle is small, iii) there are no additional shock waves formed, iv) dissipative effects and body forces are negligible, and v) a constant flow area.*

determined. Nonetheless, two additional measurement stations are located approximately midway the charge tube because dispersion and attenuation of the RSW can complicate the interpretation of the results. Furthermore, the charge tube is composed of 1.5-m-segments (see Chap. 7) and therefore, the location of the dynamic pressure instruments can always be changed if needed.

### 6.2.2 Charge-tube diameter

The choice of the charge-tube diameter is influenced by different requirements. On the one hand, since the working fluid is expensive and the purification process is time consuming, the diameter should be chosen as small as possible to reduce the amount of fluid to be used. On the other hand, the tube diameter should be large enough to allow for cleaning and to reduce the effects of viscous dissipation past the RSW, which leads to the weakening the RSW itself. As a compromise, a charge-tube diameter of 40 mm has been chosen. The total volume inside the charge tube is therefore about 11.3 liters, which from the initial density  $\rho_A \approx 186 \text{ kg/m}^3$  from Table 6.1, results in a total amount of 2.13 kg of working fluid contained in the charge tube.

To assess the influence of viscosity on the experiment, a one-dimensional

approximation has been adopted. In the post-shock state, the dense-gas viscosity model of Chung et. al. [25], which has an expected uncertainty of 10 % in the dense-gas region [164], gives  $\eta_B = 17.3 \cdot 10^{-6}$  Pa·s at  $P_B = 8.017$  bar and  $T_B = 364.05$  °C (note that the dynamic viscosity  $\eta$  is comparable to that of air at standard conditions). Hence, substituting  $u_B = 16.58$  m/s from Table 6.1, yields for the local Reynolds number  $Re(x) = (\rho_B u_B x) / \eta_B \approx 1.2 \cdot 10^8 \times x$ , where  $x$  is the axial distance from the shock front. It should be noted that the Reynolds number based on the tube diameter equals  $Re_D = 4.8 \cdot 10^6$  (so of the order of  $10^6$  even if uncertainties are accounted for). The Reynolds number is very high also at locations very close to the RSW. Since the transition from a laminar to a turbulent boundary layer occurs at lower shock-tube (or local) Reynolds numbers, it can be argued that if the charge-tube wall is smooth, the flow is fully turbulent past the leading shock wave.<sup>2</sup> For turbulent flows the friction factor  $\xi$  depends only on the relative surface roughness. In the present computations,  $\xi = 0.008-0.010$  because the charge-tube inner surface is electrolytically polished to a mirror finish (the value of  $\xi$  is taken from the well-known Moody diagram and is to be used in the D’Arcy-Weisbach equation). Under these conditions, and if the attenuation and dispersion of the shock wave is neglected, the flow between the RSW and the nozzle inlet can be modeled as a steady one-dimensional flow with friction, namely as a Fanno flow [198, 42].

At the tube end-wall ( $x = L = 9$  m), the pressure drop  $\Delta P_\xi$  between point B immediately after the RSW and the inlet of the nozzle is therefore computed from the D’Arcy-Weisbach equation as  $\Delta P_\xi = \frac{1}{2} \xi \frac{x}{D} \langle \rho \rangle \langle u \rangle^2 \approx 0.34$  bar, where  $\langle \rho \rangle$  and  $\langle u \rangle$  are the average fluid density and velocity, respectively. Note that for a larger friction factor of say 0.010,  $\Delta P_\xi \approx 0.42$  bar. The pressure drop due to viscous dissipation is therefore quite relevant, namely about 30-38 % of the pressure difference across the RSW. However, the pressure difference between state A and the nozzle throat is controlled by the nozzle cross-sectional area, see the next section, which can be changed to compensate for the viscous losses. Computations predict that an increase of the diameter at the nozzle throat section is sufficient to counterbalance viscous losses (details are to be presented in Ssec. 6.2.3). Figure 6.5 presents in both an  $h$ - $v$ - and  $P$ - $v$ -diagram the expansion process taking place in the charge tube.

It is remarkable that the Reynolds number past the shock-wave is very high, namely about  $\sim 10^8$ /m, whereas the wave Mach number is as low as 1.026. On the one hand, this is due to the very low value of the kinematic viscosity  $\nu = \eta/\rho$ , which in turn is related to the very high density of the states characterizing the experiment. On the other hand, the flow velocity past the shock wave is very high. This is due to the high compressibility of the fluid, which results in a density jump of about  $59$  kg/m<sup>3</sup>, or 32 % of  $\rho_A$ , even though the shock wave is weak. For mass conservation, this leads to high values of the post-shock velocity.

---

<sup>2</sup>Note that the following is only intended to give an idea of the magnitude of the pressure drop past the RSW as it moves into the charge tube towards the end-wall; it is therefore not accurate.

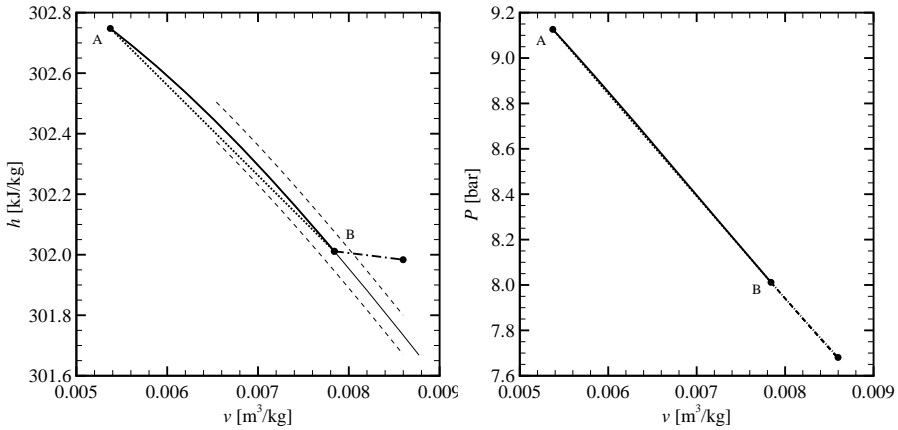


Figure 6.5: Expansion in the charge tube up to the nozzle inlet  $x_i$  in the  $h$ - $v$ -plane (left) and the  $P$ - $v$ -plane (right). A-B denotes a pressure jump due to the presence of an RSW. Past the shock wave, due to turbulence, the flow is modeled as a Fanno process. Legend: the solid line represents the Hugoniot-Rankine shock adiabat of state A, the dotted line is the Rayleigh line connecting A-B, the dashed lines indicate isentropes, and the dash-dotted line represents the Fanno curve.

### 6.2.3 Nozzle design

The nozzle between the the charge tube and the reservoir is intended to be choked during stationary operation. To compute the ratio of the area of the nozzle-throat section with respect to the charge-tube cross sectional area, the flow behind the RSW is described by assuming firstly that the total enthalpy,  $h^t$ , is conserved and that the entropy remains constant from the inlet  $x_i$  up to the throat. The entropy of state B is computed via the shock conditions treated in Sec. 2.1. Critical (sonic) conditions (S) are then computed by solving for  $v_S$  the equation  $h_S(s_B, v_S) + \frac{1}{2}c_S^2(s_B, v_S) = h_B^t$ , where  $h_B^t$  is the total specific enthalpy per unit mass of state B. Then, from the mass conservation law, one obtains

$$\frac{A_S}{A_{\text{tube}}} = \frac{\rho_B u_B}{\rho_S c_S}.$$

Substituting the values listed in Table 6.1 for the chosen initial states A and B yields  $A_S/A_{\text{tube}} \approx 0.416$ . For a 40-mm diameter tube,  $A_S \approx 522.8 \text{ mm}^2$ , which corresponds to a throat diameter of  $D_S \approx 26 \text{ mm}$ . The fluid state at the sonic throat is summarized in Table 6.2.

As was shown in the previous subsection, the Reynolds number behind the RSW based on the charge-tube diameter, is however of the order of  $Re_D =$

Table 6.2: Sonic state S computed using the EoS of  $D_6$  in the Span-Wagner functional form [33] and the values listed in Table 6.1 for the pre- and post-shock states, assuming an isentropic flow past the discontinuity and through the nozzle up to the throat.

		Value	Units
State S	$P_S$	5.57	bar
	$\rho_S$	67.82	kg/m <sup>3</sup>
	$T_S$	357.35	°C
	$\Gamma_S$	0.6337	–
	$u_S$	74.96	m/s
	$c_S$	74.96	m/s
	$Ma_S$	1.0	–

$4.8 \cdot 10^6$  implying that the flow behind the RSW is possibly fully turbulent. Consequently, although the total enthalpy is conserved (this follows from the law of conservation of energy), the total entropy does not remain constant, as was assumed in the previous paragraph) but increases due to viscous dissipation. Moreover, as the RSW, once it is formed, moves further towards the end-wall of the charge tube, the pressure at the inlet and the throat of the nozzle decreases with time. If the flow is modeled as a Fanno process, it is found that for an electrolytically polished inner surface of the charge tube,  $A_S/A_{tube} \approx 0.434 - 0.439$  (these values are valid for  $\xi = 0.008 - 0.010$ ) if the RSW is at the end-wall of the tube. The new value for  $A_S/A_{tube}$  is 3.6 – 5.5 % greater than the previously determined area ratio of 0.416 assuming isentropic flow past the RSW, and this means that as the RSW moves towards the end-wall, the area ratio has to be adapted. This is of course not possible and in this respect it is important to take the following into account:

1. For a Fanno flow behind the moving RSW whereby the area ratio of the nozzle is chosen to be  $A_S/A_{tube} \approx 0.416$ , the Mach number in the nozzle's throat can be less than unity if also the reservoir pressure is not low enough. Consequently, disturbances which can be initiated in the reservoir can potentially complicate the measurement of the RSW in the charge tube. This problem can be accounted for by using a reservoir pressure which is low enough such that the nozzle is choked;
2. For an area ratio of  $A_S/A_{tube} \approx 0.434$ , the nozzle is choked during operation, however, the RSW can possibly not be a pure down-stream sonic RSW but may feature shock-wave splitting whereby the RSW has an expansion fan as a tail. The tail is possibly obscured by the turbulent Fanno flow past the wave. Also weakening of the RSW can potentially be noticed.

Table 6.3: Sonic state S computed using the EoS of  $D_6$  in the Span-Wagner functional form [33], the values listed in Table 6.1 for the pre- and post-shock states and assuming a Fanno flow past the RSW.

		Value	Units
State S	$P_S$	5.33	bar
	$\rho_S$	63.46	kg/m <sup>3</sup>
	$T_S$	356.87	°C
	$\Gamma_S$	0.6598	–
	$u_S$	76.77	m/s
	$c_S$	76.77	m/s
	$Ma_S$	1.0	–

The above-mentioned procedure is just indicative of what can possibly occur. In practice, a trial-and-error procedure is to be followed for setting correct initial states and setting the correct  $A_S/A_{\text{tube}}$ -ratio. These preliminary calculations show that the pressure in the throat of the nozzle is about 5.33 bar and the density is approximately 63.5 kg/m<sup>3</sup>. The thermodynamic states in the throat of the nozzle when the RSW is near the end-wall and the flow past the shock wave is turbulent, are listed in Table 6.3. A detailed study taking thermoviscous effects into account for an experiment with fluid  $D_6$  is required and CFD simulations can provide some insight.

### 6.2.4 Reservoir design

The reservoir size and the initial conditions must be chosen in such a way that during the discharge process the pressure at the nozzle outlet, namely the discharge pressure, is always lower than the pressure at the nozzle throat. In this way, the nozzle remains choked during the experiment. For simplicity and to avoid disturbances due to temperature gradients along the charge tube, the initial temperature of the fluid in the reservoir is chosen to be equal to the charge tube temperature  $T_A$ , i.e., the entire facility is thermostated. Moreover, to limit the overall size of the experimental apparatus, the total volume of the reservoir is limited to 0.1 m<sup>3</sup>. The mass flowing from the charge tube into the reservoir is obtained as the product of the mass flow,  $\rho_B u_B A_{\text{tube}} = \rho_S c_S A_S$ , times the duration of the experiment. The latter is slightly longer than the time required for the RSW to reach the last measurement station or, for simplicity, the charge tube end-wall, or  $x_L - x_I = b(t_{\text{end}} - t_I)$ , where  $x_I = 5$  m and  $t_I = x_I/\sigma_A^-$ , so that  $t_{\text{end}} = 0.253$  s and therefore,  $\Delta m = \dot{m}t_{\text{end}} = [\rho_S c_S A_S] \times t_{\text{end}} = 0.672$  kg. Neglecting pressure losses due to viscosity, the internal energy in the reservoir is then increased by the quantity  $V_R \Delta(\rho_R e_R) = h_S^t \Delta m$ , with  $h_S^t$  the total specific enthalpy

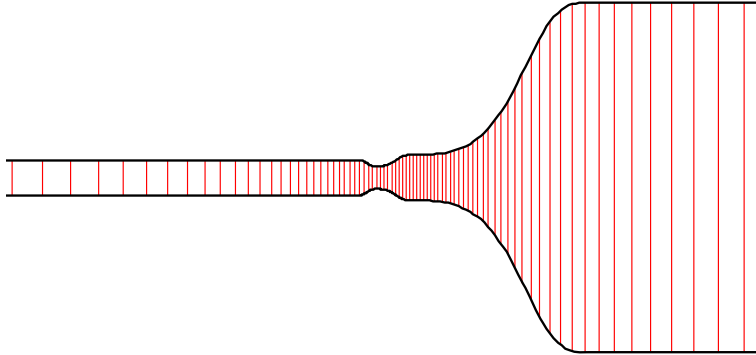


Figure 6.6: *Medium mesh of the FAST for the one-dimensional unsteady simulations performed with zFlow [35].*

per unit mass at the nozzle throat and  $V_R$  the volume of the reservoir. The reservoir pressure at the end of the experiment is then computed from the final value of the specific internal energy  $e_{R,end}$  and the specific volume  $v_{R,end}$  as  $P_{R,end} = P(e_{R,end}, v_{R,end}) = 1.08$  bar, where  $e_{R,end} = (V_R \rho_{R,0} e_{R,0} + h_S^t \Delta m) / m_{R,end}$  and  $v_{R,end} = V_R / m_{R,end}$ , with  $m_R$  total mass of the fluid in the reservoir,  $m_{R,end} = m_{R,0} + \Delta m$ , and with the subscript “0” indicating initial conditions. The maximum discharge pressure  $P_{R,end}$  is thus always lower than the sonic pressure  $P_S = 5.33$  bar.

## 6.3 Verification of the preliminary design

### 6.3.1 Numerical simulation of the FAST experiment

Numerical Eulerian simulations were performed to verify the preliminary design of the FAST setup. All simulations are performed with the CFD solver zFlow [35] using in addition to the multiparameter EoS in the Span-Wagner functional form, the Peng-Robinson Stryjek-Vera modified (PRSV) EoS and under the assumption that i) thermoviscous effects are of no importance, and ii) that the flow is quasi one-dimensional, namely the FAST setup is modeled as a variable-cross-sectional-area tube in which the local multidimensional effects are negligible with respect to the main axial flow.

A grid sensitivity study was also performed to investigate the dependence of the numerical results on the computational grid. Three different grids with increasing number of nodes, namely 835 (coarse), 1669 (medium) and 3336 (fine) nodes, respectively, were considered. The grid spacing is not uniform,

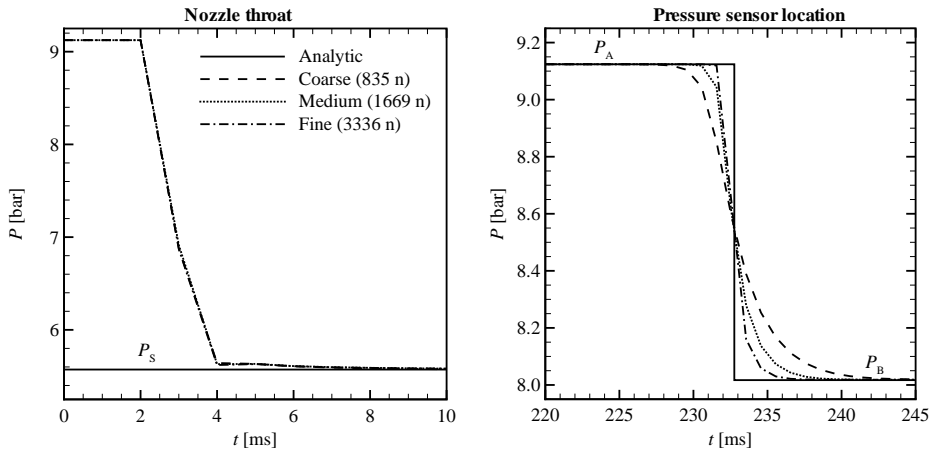


Figure 6.7: Pressure signals at the nozzle throat (left chart) and at a measurement station located 8.4 m to the left on the nozzle exit  $x_e$  (or 0.6 m to the right of the charge-tube end-wall) (right chart) as computed using three different grid resolutions. Numerical results are compared to the analytical solution, in which the flow inside the nozzle is assumed to be steady.

with nodes clustered in the regions where the cross-sectional area varies the most, e.g., inside the nozzle and at the nozzle discharge section; in the charge tube, the grid spacing is uniform. To avoid numerical spurious oscillation due to the abrupt change in the cross-sectional area at the nozzle discharge section, a smooth area variation is artificially introduced to connect the nozzle outlet to the reservoir: the cross-sectional area is assumed to vary smoothly from the nozzle throat value of  $522.8 \text{ mm}^2$  to a value of  $0.196 \text{ m}^2$  over a distance of 0.5 m. Figure 6.6 displays the medium grid used in the simulations.

The numerical results are reported in Fig. 6.7, where the pressure signal at the location of the throat and at a measurement station are shown as a function of the elapsed time for the three considered grids. The numerical results, i.e., the post-shock pressure and shock-wave speed, are found to be almost independent from the grid resolution and to converge to the analytical solution. The analytical solution is computed by assuming that the flow in the nozzle connecting the charge tube to the reservoir is stationary and choked for the entire duration of the experiment. Moreover, the RSW is assumed to be completely formed at the inlet of the nozzle, with no perturbations resulting from the interaction with the nozzle itself. The above-mentioned assumptions are relaxed in the simulation to investigate their correctness. In fact, the pressure at the nozzle throat reaches its steady-state choked value almost immediately, that is about 4 ms after the opening of the valve – which for the numerical simulation is as-

sumed to open instantaneously – and the influence of the interaction with the nozzle on the propagation time of the RSW is found to be negligible, cf. Fig. 6.7 (right).

The preliminary design is therefore confirmed by the present numerical simulations, in terms of both initial conditions leading to the occurrence of an RSW propagating in the charge tube, and to the characteristic dimensions and times of the experiment. The intermediate grid consisting of 1669 nodes is therefore used in the following subsection to assess the uncertainties due to the thermodynamic EoS of the fluid.

### 6.3.2 Uncertainties due to the thermodynamic model

The preliminary design obtained using the multiparameter EoS in the Span-Wagner form (SW) (see Sec. 3.3) is validated against the cubic Peng-Robinson, Stryjek Vera modified (PRSV), EoS of  $D_6$ . For the sake of the present discussion, the SW EoS is assumed to provide the exact thermodynamic properties of  $D_6$ , of which the PRSV EoS provides an approximation. It should be recalled that none of the EoS's are validated as far as the determination of the value of the fundamental derivative of gas dynamics,  $\Gamma$ , is concerned and therefore, the present analysis is intended only as an initial evaluation of the critical issues due to the uncertainties in the thermodynamic EoS's, similar to the study presented in Ref. [84].

According to the experimental procedure [225], the initial state A is chosen along the dew-line at the initial pressure  $P_A$ . As shown in Fig. 6.8, an RSW fulfilling the Hugoniot-Rankine jump conditions is predicted to be admissible also if the PRSV EoS of  $D_6$  is employed, whereby in this case, the RSW propagates at a slightly lower velocity. The post-shock pressure level is 8.02 bar according to the PRSV EoS; a value which is negligibly greater than the value predicted by the SW EoS reported in Table 6.1. Also the pressure jump across the RSW computed using the PRSV EoS is slightly less, namely 0.2 kPa, than that predicted with the multiparameter SW EoS. Analytical results, verified with one-dimensional CFD simulations (assuming that the valve opens instantaneously) for the flow in the charge tube and through the nozzle are reported in Tables 6.4 and 6.5, respectively, where computations are done with the PRSV cubic EoS.

### 6.3.3 Wave-speed measurement

The wave speed  $b$  of the propagating RSW is to be measured by comparing the time-of-arrival ( $\tilde{t}$ ) of the RSW at two different measurement stations, namely station 1 and 2, as displayed in Fig. 6.1. Mathematically formulated,  $b = \Delta L / \tilde{t}$ , where  $\Delta L$  is the mutual distance between the dynamic-pressure instruments. Many technical problems affect the measurement of the speed of a shock wave and these are addressed in Ref. [66]. Here, the focus is mainly on two issues that

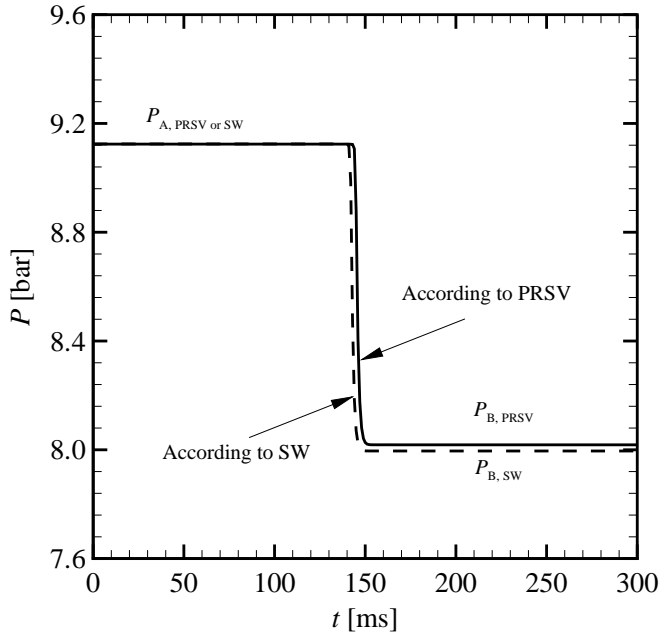


Figure 6.8:  $P$ - $t$ -plot of the FAST experiment according to the PRSV and SW EoS's. For these simulations  $A_S/A_{\text{tube}} \approx 0.416$ . The opening-time of the valve is zero.

are peculiar to nonclassical shock waves, namely the possibly non-negligible shock wave thickness, which can be of the order of 1–10  $\mu\text{m}$ , and the correct estimation of the wave Mach number, being very close to unity.

A relevant source of uncertainty is associated with sound speed measurements. To provide a conclusive proof that the measured rarefaction wave is indeed an RSW, the wave speed  $b$  should be higher than the sound speed  $c_A$  in the unperturbed state A. Since the highest expected wave Mach number is about 1.026, the relative difference between  $b$  and  $c_A$  is very low, namely  $(b - c_A)/c_A = 0.026$ . For the comparison to be possible, the uncertainties in the measurement of both  $b$  and  $c_A$  should be lower than about 0.5 %. In Fig. 6.9 the speed of the RSW and the sound speed for different saturated states is plotted. For unperturbed states in the vicinity of or inside the negative nonlinearity region, an RSW is formed and the wave speed exceeds the speed of sound, as shown in Fig. 6.9. Error bars associated with a 0.5 % uncertainty in both  $b$  and  $c_A$  are also displayed.

Figure 6.9 also suggests an alternative experimental procedure in which the speed of sound and the wave speed are both measured in the FAST facility.

Table 6.4: Pre- and post-shock states A and B computed analytically and verified by numerical simulations using the PRSV cubic EoS for  $D_6$ .

		Value	Units
RSW	$b$	35.00	m/s
	$Ma_b$	1.023	–
State A	$P_A$	9.124	bar
	$\rho_A$	188.34	kg/m <sup>3</sup>
	$T_A$	368.97	°C
	$\Gamma_A$	-0.1218	–
	$u_A$	0.0	m/s
	$c_A$	34.21	m/s
	$Ma_A$	0.0	–
State B	$P_B$	8.017	bar
	$\rho_B$	127.28	kg/m <sup>3</sup>
	$T_B$	363.71	°C
	$\Gamma_B$	0.1386	–
	$u_B$	16.79	m/s
	$c_B$	51.79	m/s
	$Ma_B$	0.324	–

Table 6.5: Sonic state S computed analytically and verified by numerical simulations using the PRSV cubic EoS of  $D_6$  and the values listed in Table 6.4 for the pre- and post-shock states, assuming an isentropic flow past the discontinuity and through the nozzle up to the throat.

		Value	Units
State S	$P_S$	5.57	bar
	$\rho_S$	66.87	kg/m <sup>3</sup>
	$T_S$	356.70	°C
	$\Gamma_S$	0.6176	–
	$u_S$	75.50	m/s
	$c_S$	75.50	m/s
	$Ma_S$	1.0	–

Sound speed measurements can be performed by firstly setting the throat area of the nozzle embedded in the FoV to almost zero, i.e.,  $A_S/A_{\text{tube}} \approx 0$ . Therefore, once the initial states for an RSW-experiment are set, namely  $P_{\text{charge tube}} = 9.13$

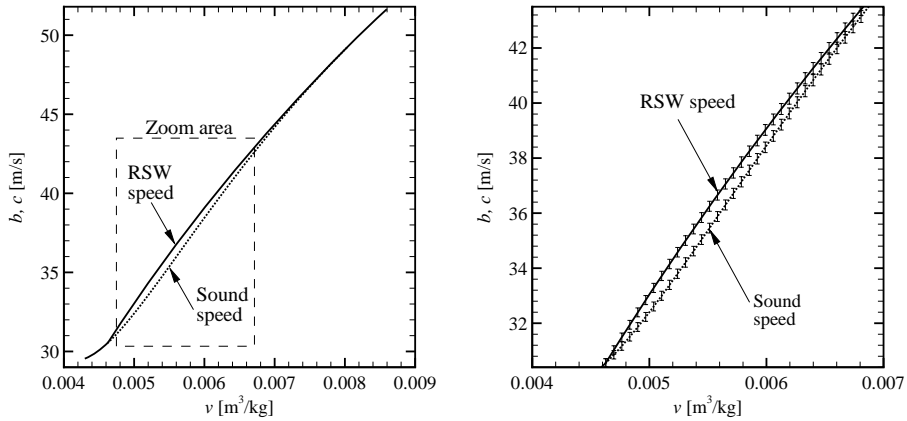


Figure 6.9: Dimensional wave speed  $b$  and thermodynamic sound speed  $c$  as a function of the reduced volume along the vapor side of the saturation curve. Error bars represent an error of 0.5 % in the evaluation of both  $b$  and  $c$ .

bar,  $P_{\text{reservoir}} \approx 1.0$  bar and  $T = 369.2$  °C, the FoV can be opened and a weak acoustic expansive disturbance (which may or may not coalesce into a shock wave) propagates into the charge tube. Using a time-of-flight technique the wave speed can be measured which ideally corresponds to the thermodynamic sound speed. Next, the initial states are set again to those theoretically giving rise to the formation of an RSW with the “correct”  $A_S/A_{\text{tube}}$ -ratio, and it is to be demonstrated that the speed of this wave is greater than that of the acoustic wave. As was anticipated, this requires a trial-and-error procedure and accurate and precise measurement instruments because of the importance of repeatability and reproducibility of the tests.

## 6.4 Experimental procedures

The assessment whether or not a rarefaction shock wave has formed, requires, among other things, the knowledge of the thermodynamic speed of sound at the fluid thermodynamic conditions set in the charge tube. If the fluid is well-measured, as is for example methane, then the reference EoS can be employed to compute the thermodynamic speed of sound with very high accuracy. That is, the predicted value of the speed of sound from the reference EoS is within the experimental uncertainty with which the property can be measured. In the case of siloxanes however, speed-of-sound data in the dense-gas region are unavailable and the EoS documented in Chap. 3 classifies as a technical type and thus

cannot predict speed-of-sound data with the level of accuracy which is needed. This can also be said for the PRSV cubic EoS. For this purpose, speed-of-sound measurements must be conducted on the spot. The way to do this has been discussed already in the previous subsection.

After the initial conditions are set and are maintained at stable values over a sufficiently long period, e.g., at least 10 minutes, the test run can be started. At first, a few seconds prior to the opening of the FoV, the static pressures and temperatures of the fluid in the charge tube and the reservoir are measured and recorded. Next, exactly 1 second prior to the opening of the FoV, a trigger is given to initiate simultaneous measurement and recording of data from the dynamic-pressure transducers positioned on the charge tube. The actuation system for the FoV is done pneumatically and the valve opens at the prescribed time. The measurement chain is in real time because accurate knowledge of the time difference is needed for computation of the speed of propagation of the wave. Note that the exact moment that the FoV opens is not known, although it can be computed based on wave measurements in the charge-tube; this however, is not a problem for synchronized pressure transducers because the time difference between two (correlated) signals is important. The pressure data which are sampled at a high (predetermined) rate are post-processed with a correlating algorithm that helps calculating the speed of the wave in an unbiased manner.

Note that the measurement system is to be subdivided into two subsystems, because setting and controlling the fluid thermodynamic conditions to the prescribed values requires some hours ( $1 - 1\frac{1}{2}$  day), e.g., the fluid pressure and especially the temperature, whereas the measurement of the time-of-flight in the charge tube is of the order of milliseconds, e.g., synchronous recording of the dynamic-pressure signals. It is therefore recommendable to separate the data-acquisition and control system for slow processes from the data-acquisition system for the synchronous recording of the dynamic-pressure data, because this allows one to use dedicated instruments.

## Nomenclature

Symbol	Description
$A$	Flow area
$b$	Shock wave velocity
$c$	Speed of sound
$D$	Diameter
$e$	Specific internal energy
$h$	Specific enthalpy
$L$	Charge-tube length
Ma	Mach number

Continued on the next page...

Continued

Symbol	Description
$m$	Mass
$\dot{m}$	Mass flow
$P$	Pressure
Re	Reynolds number
$s$	Specific entropy
$T$	Temperature
$t$	Time
$\tilde{t}$	Time of flight
$u$	Fluid velocity with respect to a laboratory reference frame
$V$	Volume
$v$	Specific volume
$x$	Axial spatial coordinate
$\Gamma$	Fundamental derivative of gas dynamics
$\Delta L$	Mutual distance between dynamic pressure instruments
$\eta$	Dynamic viscosity
$\nu$	Kinematic viscosity
$\xi$	Friction factor
$\rho$	Density
$\sigma$	Wave speed



*“I heard somebody say, “Where’s (Nelson) Mandela?” Well, Mandela’s dead. Because Saddam killed all the Mandelas.”*

President George W. Bush, Washington, D.C., September 20, 2007

# 7

## Commissioning of the FAST

### **Abstract**

*The working principle and the preliminary design of the FAST have been discussed in Chap. 6. Moreover, the justification of employing a Ludwig-tube-type facility to provide experimental evidence of the existence of rarefaction shock waves is given in Chap. 5 and Ref. [224]. The goal of the present chapter is to give a short description of the setup, as built. The focal points are the primary components of the balance of plant of the shock tube, the instrumentation, and the data acquisition and control systems (a more detailed description can be found elsewhere [155]). Also the commissioning phase is treated. The commissioning phase consists of various tests to ensure the structural integrity of the FAST facility and to check whether all specifications are met. For this purpose, two sets of tests are conducted: firstly, the temperature control of the facility is tested and the second set of tests regards measuring the time-of-flight of a normal compression shock wave in air propagating into the charge-tube. These preliminary tests are also useful as training and, from the insight which is gained during these tests, modifications to the facility or the experimental strategy can be made if necessary.*

## 7.1 The FAST, as built

### 7.1.1 Main components and assemblies of the FAST

A sketch of the process-flow diagram of the FAST is illustrated in Fig. 7.1 and pictures of the setup are presented in Figs. 7.14 and 7.15. The facility is a Ludwieg-

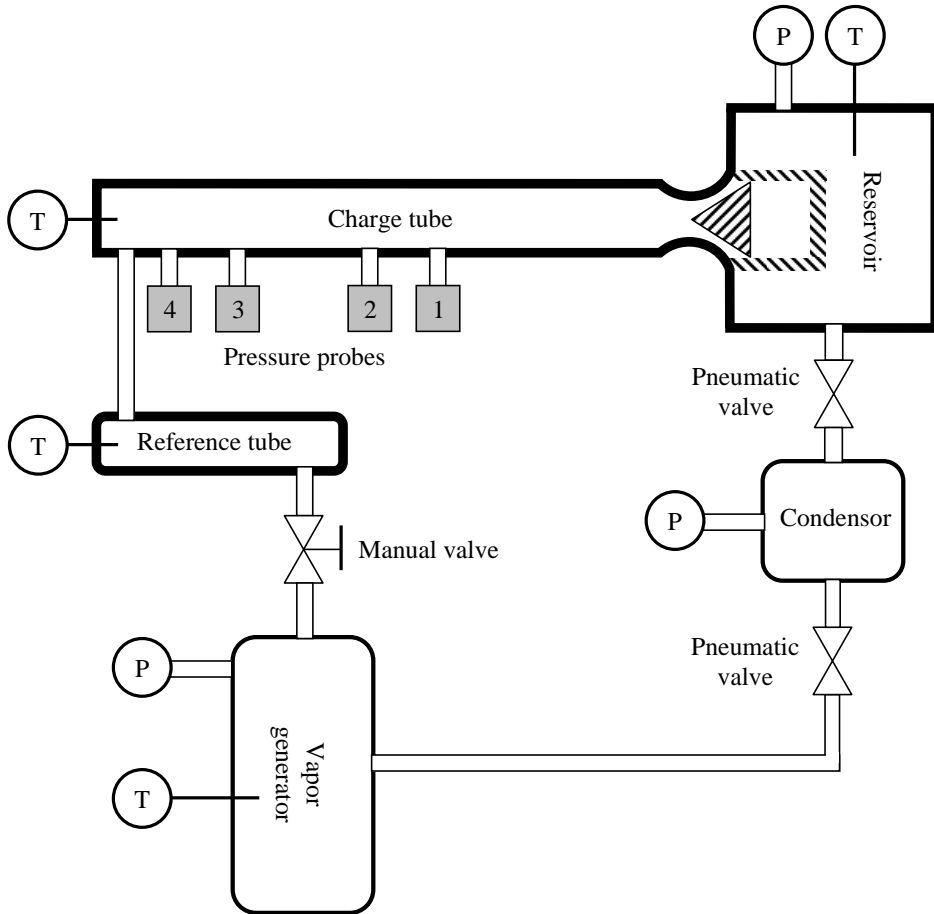


Figure 7.1: Sketch of the process flow diagram of the FAST. A detailed process-and-instrumentation diagram is available in Ref. [155]. The distances of the pressure instruments 1–4 as measured from the nozzle inlet are 3.9 m, 4.2 m, 8.4 m and 8.7 m.

tube setup; however, contrary to a typical Ludwig-tube experiment, in this study, the flow field under scrutiny is in the charge tube. The FAST can be subdivided in the following main mechanical components and assemblies, some of which are discussed in the following:

- The pipe assembly,
- The low-pressure reservoir,
- The fast-opening valve and actuation system,
- The so-called balance of plant containing the condenser, the vapor generator, the reference tube, and auxiliaries, e.g., manual and pneumatic valves, pressure-safety valves, and measurement instruments.

★ **The pipe assembly:**

The charge tube is assembled out of six pipe segments of exactly 1520 mm in length. Two of these segments, see Fig. 7.2, contain openings for placing a pair of dynamic pressure instruments. By splitting the charge tube into segments, flexibility is created because the measurement stations can be moved to other positions further from or closer to the low-pressure reservoir. Each segment has an outside diameter of 70 mm, an inside diameter of 40 mm, and is custom-made of stainless steel 316L. To get a straight pipe segment, each part is machined from a solid block. A hole with the specified diameter is drilled into the material and afterwards the outside is machined to the required specifications. It was not preferred to use cheaper standard welded pipes because they do not comply with the required straightness and because the standard thickness would not allow for the special manufacturing of the grooves for the couplings. Additionally, due to the sheer thickness and the associated large heat capacity of each segment, temperature fluctuations on the outside, depending on their frequency, are attenuated on the inside and temperature non-uniformity is reduced. Each segment contains a narrow slit which is machined on the outer surface to accommodate a k-type thermocouple used by the temperature control system.

Each pipe segment has a male-to-female connection with the adjacent segment. The male side contains a groove in which an O-ring of red copper is placed. Red-copper seals are compatible with siloxanes and offer tight sealing at high temperatures both under pressure and vacuum conditions. The pipe segments are connected to each other by means of custom-made clamped couplings. Welded flanges were ruled out given the requirements on straightness and smoothness of the total inner surface. The use of couplings however, complicates the requirement of tight sealing. At the temperatures at which the experiments in the FAST are conducted, viz.  $\sim 360^\circ\text{C}$ , thermochemical decomposition of the test fluid is a

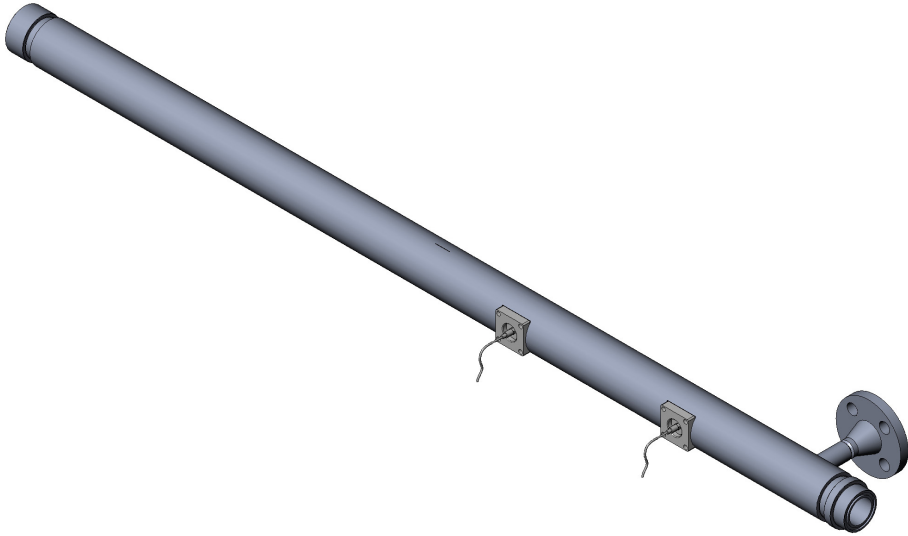


Figure 7.2: *Isometric view of the pipe segment of the charge tube which is placed the furthest from the low-pressure reservoir. Notice the two dynamic pressure transducers placed on custom-designed holders. Moreover, the right-hand side is the male part and the left-hand side is the female part. The male part of a segment is tightly connected to the female part of an adjacent segment with custom-made couplings.*

point of concern. Although the process temperature is lower than the temperature where decomposition of the fluid may occur, i.e.,  $\sim 400\text{ }^{\circ}\text{C}$ , with a safety margin, the probability that the test fluid decomposes is greater if acidic or alkaline impurities and air and water are present. This implies that, apart from degassing the test sample thoroughly, precautions must be taken in order to minimize leakage of air into the FAST.

The inner surface of the pipe segments is electrolytically polished to nearly a mirror finish (0.05 micron). This reduces the attenuation of the nonclassical wave in the pipe due to reduced friction. The charge-tube segments are the only components that are polished, while all other components are only pickled and passivated.

To minimize thermal stresses in the charge tube resulting from thermal elongation, a sliding support system was designed. The charge tube is placed on holders which can slide axially on rails.

★ **The low-pressure reservoir:**

The low-pressure reservoir is a custom-made vessel with an internal volume of about 150 liters. Part of the internal volume is occupied by the fast-opening valve (FoV), which is discussed in the subsequent item. The vessel is split into two parts, namely a main body and a cap; the cap allows for mounting or dismounting the FoV and for cleaning the vessel if for example thermochemical decomposition of the test fluid has occurred. Moreover, various openings have been created in the wall to position, among other things, optical instruments for other potential uses of the FAST in the future, e.g., visualization of the flow field through the stator of a turbine (refer to the technical report by Zamfirescu et. al. [224]).

★ **The fast-opening valve and adjustable nozzle-throat area:**

The fast-opening valve (FoV) is the most complicated component in the FAST. The FoV is custom-designed to meet the following requirements, namely i) a guaranteed opening time of at most 4 ms and ii) a seal between the high-pressure vapor in the charge tube and the low-pressure vapor in the reservoir. Moreover, the valve contains an embedded convergent-divergent nozzle with adjustable throat area. To reach the required opening time, use is made of inconel<sup>TM</sup> springs which provide pre-acceleration.

The FoV is currently under construction at HST GmbH. Figure 7.3 shows a picture of the valve and the actuation and adjustment system, and Fig. 7.4 displays a section view showing the inner parts. Notice the solid conically shaped body which can be moved axially, thereby allowing for tuning the throat area to the requirements of the experiment (refer to Sec. 6.2).

The justification for using a FoV instead of a diaphragm, which is commonly used in Ludwig tubes, is related to the fact that because of the small pressure difference between the vapor in the charge tube and that contained in the reservoir, it is expected that a diaphragm may rupture only partially and disturb the flow field which is of interest. This was also a problem experienced by Ferguson [65]. Also refer to the numerical study of Guardone [80] showing that the shock wave is weaker in terms of, for example, the pressure jump as a result of the incomplete diaphragm rupture. Furthermore, after every experimental run, the entire facility needs to be cooled down and emptied to replace the diaphragm. A diaphragm-less setup greatly increases the availability of the setup and allows for repeated and reproducible experiments.

★ **Heating elements:**

The heating elements are flexible jackets with electrical wires embedded in a silk-glass thermal insulation layer. The heating wires are spooled at the inner part of the silk-glass jacket so that they are close to the surface to be heated. The heaters are divided in segments with prescribed specifications and each is controlled separately via thyristors. The heaters can be wrapped around all the metallic parts and are tightened with velcro

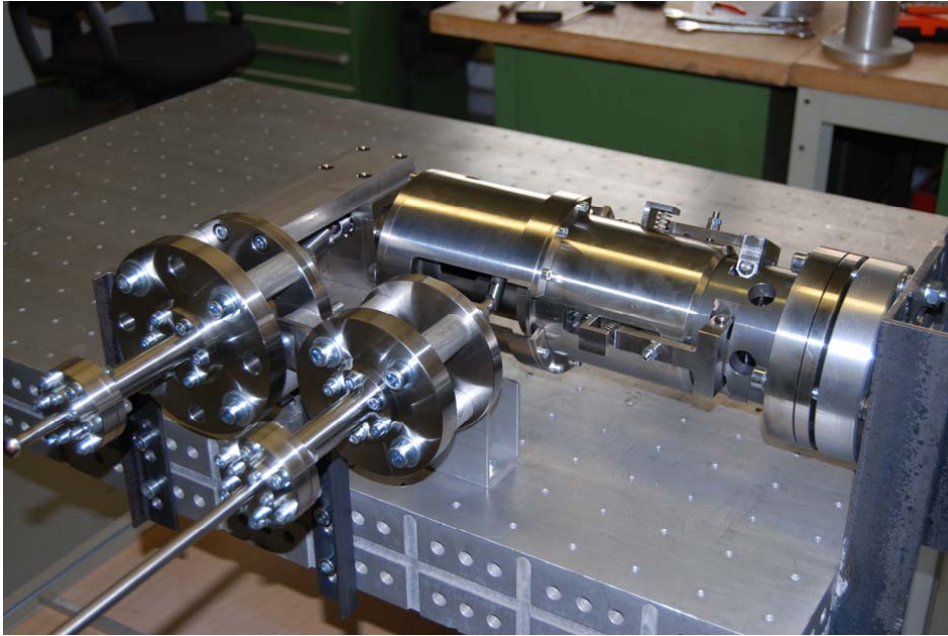


Figure 7.3: *The fast-opening valve manufactured by HST GmbH (status on 13 November 2008). Notice the actuation (outmost left) and nozzle throat adjustment system placed at 90 degrees angle with respect to the valve body.*

straps. The temperature on the outside surface of the heaters must be maintained at an acceptable value to avoid excessive heat loss to the environment and for safety reasons. Another option would have been the use of heaters where the heating wires are embedded in ceramics. Similarly to the jacket heaters, the dimensions of the heaters would be tailored to the specific needs. The use of so-named ceramic heaters allows for a fairly stable temperature of the heating element as a whole because of the large heat capacity of ceramics. Secondly, the heater is rigid; consequently there is an air-layer in between the heater and the charge tube which also buffers temperature fluctuations. The circulation of air sandwiched between the heater and the charge tube however, can promote temperature non-uniformity along the circumference. Also, the ceramic heaters cannot easily be shaped to conform with complex geometries as the low-pressure reservoir and the vapor generator. As the manufacturer of the jacket heaters guaranteed the performance, a single solution was preferred. What is more is that the jacket heaters are easy to handle.

★ **The balance of plant:**

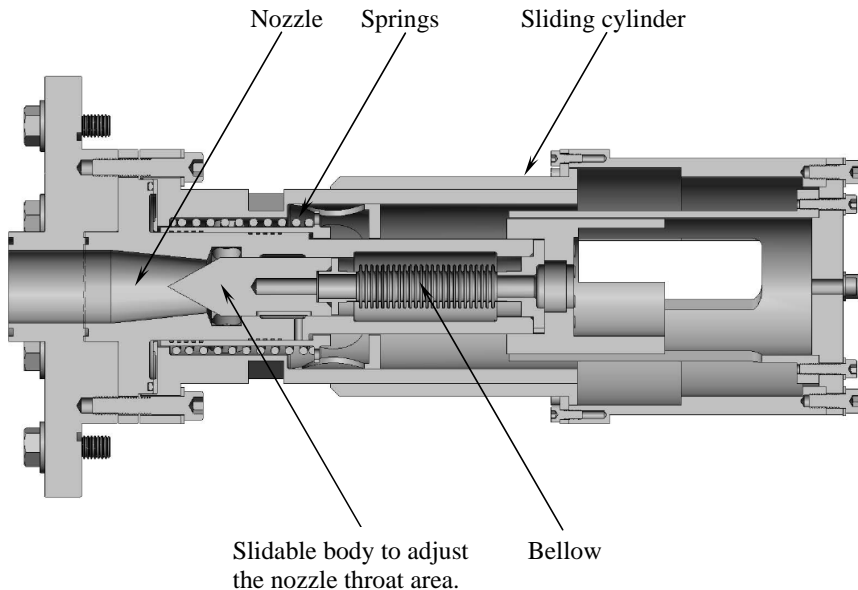


Figure 7.4: Section view showing the inner parts of the fast-opening valve (courtesy of HST GmbH). The conically shaped solid body in the center can be moved from left to right, thereby allowing for adjustment of the effective throat area of the convergent-divergent nozzle. The flow enters on the left-hand side and exits radially via large circular openings on the circumference of a sliding lightweight cylinder.

The assembly referred to as the balance of plant (BoP) consists of the following mechanical components:

- The vapor generator:

The vapor generator is a pressure vessel in which heat is added to vaporize the siloxane test fluid. It is equipped with pressure and temperature instruments which are used for reading and controlling the experimental conditions, specifically the experimental pressure. Filling as well as discharging of the test fluid is done via the vapor generator.

- The condenser:

The condenser is a small vessel placed beneath the low-pressure reservoir. To enhance the heat transfer area, 20 cooling fins are placed on the outside and air is blown over the shell with a fan. Because the cooling time is not critical, it was decided not to use a water-cooled condenser. As soon as the fluid condenses, it flows via an inclined

pipe into the vapor generator. To relieve the thermal stresses in the inclined pipe (these stresses arise as a result of the thermal elongation of the charge tube), it has a U-shaped section.

– The reference tube:

The reference tube is made of the same material as the charge-tube segments and has the same inner diameter and wall thickness. The purpose of the reference tube is for controlling the temperature of the experiment. The control system (refer to the following subsection) minimizes the difference between the temperature measured by the various k-type thermocouples on the charge-tube wall and the temperature of the reference-tube wall, which is also measured by k-type thermocouples. For this reason, the reference tube contains a small, narrow slit on the outside in which all the thermocouples are placed. The mutual distance between the thermocouples on the reference tube is kept as short as possible. Also the temperature of the wall of the reference tube is kept at a user-specified value which is greater than the temperature of the fluid in the vapor generator, i.e., the vapor in the reference tube is somewhat superheated, for example by 1 °C. Finally, it should be mentioned that the reference tube and the vapor generator are supported in such a manner that these can move axially with the charge tube.

### 7.1.2 The data-acquisition and control system

The data acquisition and control (DAQ&C) system is composed of National Instruments hardware. National Instruments software, viz. LabView, is used for monitoring and control-programming. A computer connected to the DAQ&C-system is used for the supervisory control and monitoring.

The DAQ system is dedicated to the monitoring of the data relevant for the experiment, that is, the initial thermodynamic states ( $P$  and  $T$ ) in the charge tube and the low-pressure reservoir, and the dynamic pressure signals to be correlated to obtain the wave speed. The DAQ for the short-time-scale experiment (of the order of milliseconds) is realized with two boards embedded in a dedicated chassis with a high and sustained throughput of data at a rate of 110 MB/s. One board allows for the simultaneous measurement of 8 analog channels with a maximum sampling rate of 250 kSamples/sec-channel at 16 bit resolution. This board is dedicated to the measurement of the four dynamic pressures registered during a shock-wave experiment. The second embedded board is a versatile 16-channels analog input board (250 kSamples/sec-channel, non-simultaneous measurement, 16 bit resolution) connected to register the signals from the static pressure and temperature instruments.

The control system is used to set the experimental conditions by appropriately performing a sequence of procedures. These operations are partially au-

tomated and relevant process variables can be monitored. Some of the signals from the instruments, namely those that vary on a long time scale (of the order of minutes or hours), are connected both to the DAQ- and to the control system. The control system is based on so-called compact FieldPoint (cFP) programmable automation controllers, which can work stand-alone for maximum safety and can be monitored and set from the supervisory PC connected through ethernet.

The cFP-controller is an ethernet-interfaced device for industrial applications with an embedded controller that runs LabView Real-Time. The controller offers reliability since a LabView virtual instrument can run deterministically on the hardware, and a modular I/O architecture with built-in signal conditioning. Moreover, the cFP-controller offers direct connectivity with industrial sensors and actuators by adding additional input and output modules.

The control system has been conceived with cascaded control loops and are implemented in LabView virtual instruments. In the following, a description of the implemented control loops is presented.

★ **The vapor generator pressure-control loop**

The first control loop regulates the pressure in the vapor generator and the charge tube. Because the thermodynamic state in the vapor generator is in the vapor-liquid equilibrium region, vapor-pressure control of a single component fluid indirectly implies temperature control. The pressure is set by boiling the liquid present. Since there should always be a minimum liquid level (this is to avoid local hot spots), the maximum achievable pressure is slightly lower than the critical pressure. This does not pose a limitation for the envisaged experiments because the investigated negative nonlinearity region is located at subcritical pressures. PID-controllers are employed for regulating the process variable, i.e., the vapor pressure. The PID-parameters, namely the proportionality, integral and differential time constant, have been determined using open-loop experiments using air in the entire facility. The PID-controllers issue a 0–10 V output signal which is used to steer the thyristor which modulates the power to the heater.

★ **The reference-tube & vapor-generator control loop**

This second control loop establishes and maintains the temperature in the reference tube. This temperature is regulated to a predetermined value which is greater than the saturation temperature of the fluid in the vapor generator, thus causing the vapor in the charge tube to be slightly superheated. To achieve its purpose, this control loop first compares the saturation temperature, as measured with a Pt100 in the vapor generator, to the temperature as measured with a Pt100 in the reference tube. The temperature difference is determined in a LabView virtual instrument and the temperature difference, i.e., the process variable, is regulated using PID-controllers. The PID-controller output modulates the power to the reference-tube heater via a thyristor.

★ **The charge-tube & reference-tube control loop**

The third control loop is cascaded with the previously mentioned loop, viz. the reference-tube & vapor-generator control loop. The charge-tube & reference-tube control loop consists of 13 loops that work in parallel using the same reference temperature. Thirteen differential thermocouples are used for this purpose. One end of the differential thermocouple is placed on the reference tube and the other end of the thermocouple is placed on the charge tube underneath a heater segment. Note that the reason for performing a differential temperature measurement is because of the fact that the uncertainty of k-type thermocouples is relatively high if absolute temperatures are measured; a differential temperature measurement is more accurate, especially if the temperature difference itself is very close to zero because of less intermediate signal processing. The temperature controllers compare the measured temperature differences with the reference value and act on the thyristors. The thyristors regulate the power to the heaters of the charge tube in order to minimize the temperature difference between the reference-tube wall and the charge-tube wall.

★ **The reservoir control loop**

The fourth control loop regulates the temperature of the vapor contained in the low-pressure reservoir. In this respect the vapor temperature measured with an immersed Pt100 sensor is controlled to the desired value using PID-controllers.

### 7.1.3 Procedures to conduct RSW-experiments

Details of the sequence of operations that have to be performed in order to run an experiment, but also details regarding fluid charging and discharging, startup if the facility is hot or at room temperature, can be found in the design report [155].

Before shock-wave experiments with BZT fluids can be conducted, the facility needs to be charged with the test fluid, which must be thoroughly degassed. For this purpose, the siloxane fluid is filled into a vacuumized Swagelok cylinder. This cylinder is then submerged into a flask containing liquid nitrogen, thereby freezing the siloxane. The cylinder is then pumped on to very low vacuum pressure to remove volatile components. This freezing and thawing sequence is done as many times as required to reduce the pressure of the volatilities to an acceptable value. To remove traces of water, the unfrozen sample of siloxane is pumped on for some minutes. After this degassing treatment, the siloxane fluid is filled into the vapor generator. The vapor generator as well as the entire facility is vacuumized. Assisted by gravity, the siloxane flows from the cylinder into the vapor generator. Once all the fluid is contained in the facility, the Swagelok bottle is disconnected and the system can next be heated to the

desired value.

Firstly, the vapor generator is isolated from the rest of the facility by closing off all manual and pneumatic valves. Note that also the condenser, which is at vacuum, is isolated from the rest of the system by closing off the connecting valves. The heaters are turned on (via the program implemented in LabView) and the pressure-control system regulates the vapor pressure to the desired value. Simultaneously, the other three control loops are also started in LabView and gradually, the facility under vacuum is heated to the desired temperature. The initial pressure and temperature increase is rather slow because of the high liquid heat capacity and molecular complexity. Moreover, the rate of temperature increase should not be higher than 2 K/min, especially as the critical temperature is approached. This is important because a higher heating rate may promote thermochemical decomposition of the test fluid. Consequently, heating up the complete facility from room temperature up to the experimental temperature for the RSW-experiment with siloxanes would require 1–1½ day, also because of the significant heat capacity of the metallic parts. During the heating process the FoV is kept open. If the pressure in the vapor generator is sufficiently high, the vapor generator is connected to the rest of the facility, thereby charging the system. Once the pressure in the reservoir is at its desired value (this corresponds to an absolute pressure of 1.2–1.5 bar), the FoV is closed, thereby isolating the reservoir from the charge tube. Gradually, the pressure in the charge tube (and reference tube and vapor generator) is built up. The control system regulates the thermodynamic state to the initial values for an RSW-experiment.

After the thermodynamic states are stable for at least half an hour, the RSW-experiment can start. This requires the following sequence of events, which is partly automated (a set of procedures is implemented in LabView and prompt the user to specify, for example, the throat area of the nozzle embedded in the FoV): i) the speed of sound must be measured on site and the procedure to do this was explained in Sec. 6.4), ii) the experimenter sets the predetermined throat area ratio, iii) the static pressures and temperatures of the fluid contained in the charge tube and the reservoir are recorded, iv) a digital signal is passed to the FoV which causes it to open; simultaneously, the data from the four dynamic pressure transducers are recorded at a high sampling rate (50 kSamples/sec-channels is enough in the case of RSW-experiments with siloxanes), v) the recording lasts for a second, even though the duration of the experiment is less than a second (see Ssec. 6.2.4). After the data have been recorded, post-processing can be done, whilst the facility is set to the desired thermodynamic state for another experimental run.

## 7.2 Temperature control of the charge tube

The thermodynamic state of the working fluid in the charge tube, prior to an experimental run, is only slightly superheated with respect to the saturated fluid which exits the vapor generator. This is necessary because the admissibility region for nonclassical rarefaction shock waves is rather small in terms of pressures and temperatures and is located close to the critical point and adjacent to the dew-line. Therefore, there are two reasons that the temperature control should be tight, namely condensation of the working fluid in the charge tube should be avoided, especially around the dynamic pressure instruments because condensation would only complicate the interpretation of the recorded data, and secondly because a few degrees temperature difference can imply either the admissibility or inadmissibility of rarefaction shock waves.

The goal of the temperature control test described in the following is to firstly determine PID-control parameters. This is achieved by doing open-loop heating tests. Secondly, once the PID-control parameters are determined, the performance of the control system regarding a tight temperature control must be evaluated.

Using the temperature-response recording first in open-loop configuration using air in the facility, the control parameters have been determined. Open-loop response implies that a step signal is imposed on the power to the heater and starting from that moment, the process variable, e.g., the wall temperature as measured by a k-type thermocouple, is measured and recorded. With these PID-control parameters, a heating test was performed using the reference-tube & vapor-generator control loop and the charge-tube & reference-tube control loop. The vapor-generator pressure control loop was not included in this test, because the PID-control parameters were determined for air and were not well-optimized. However in the case that siloxanes are used, the PID-control parameters can be quite different particularly because in the case of siloxanes, phase change is involved and the liquid heat capacity of siloxanes is quite high. It must also be mentioned that for the PID-control parameters which were determined for air, the temperature response of the Pt100 of the vapor generator was not satisfactory. Therefore, since the temperature of the air in the reference tube and the charge tube are controlled using the air temperature in the vapor generator, the second and third control loop would also display unsatisfactory behavior.

For the test described in the following, the set-point for the temperature difference between the temperature of the air contained in the reference tube with respect to that contained in the vapor generator is set to a value of 50 °C. Figure 7.5 shows the history over a period of 12 hours of the actual temperature difference. It can be seen that the air-temperature difference can be regulated to within 0.06 °C of the set-point value.

For the charge-tube & reference-tube cascaded control loop the temperature difference between the charge-tube wall temperature with respect to the reference-tube wall temperature is set to -1 °C, i.e., the charge-tube wall tem-

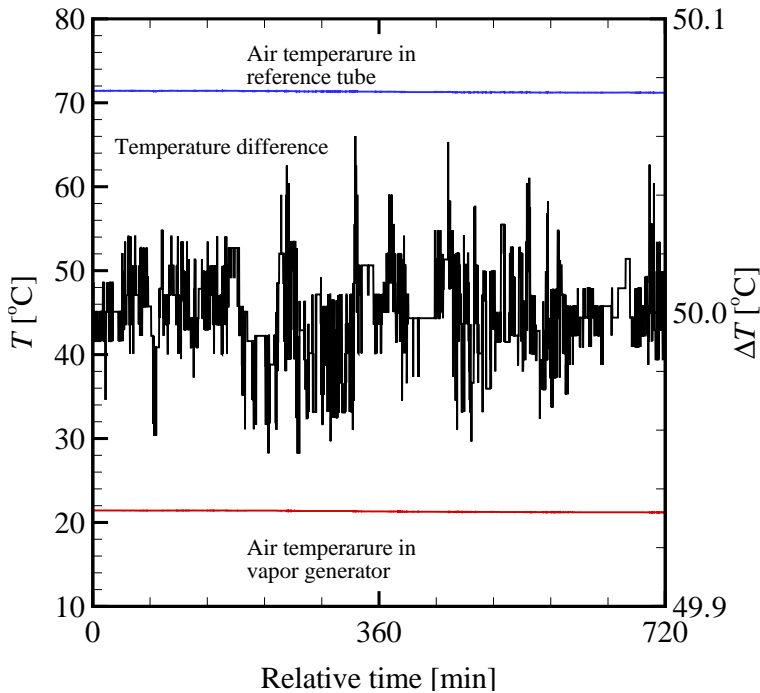


Figure 7.5: *The absolute air temperature in the vapor generator and the reference tube, and the temperature difference in time for a period of 12 hours. Although not clearly visible due to the choice of the scale, the temperature of the air in the vapor generator decreased in the same period from 21.4 to 21.2 °C*

perature is less than the reference-tube wall temperature. It is observed that in the case of the charge tube, the temperature difference can be regulated within 0.01 °C.

However, if the absolute temperature of air contained in the reference tube is plotted over the same 12-hour period, it is observed that actually the air temperature in the reference tube decreased over the same period in time. The reason for this is that during the 12 hours of the heating experiment, the temperature of the surroundings decreased, causing the vapor generator air temperature also to decrease. These results demonstrate the need for accurate temperature control of the medium contained in the vapor generator.

Finally, it should be noted that the heat flux at the outer wall of the pipe segments is not constant, therefore, the resulting periodic fluctuations of the outer wall temperature penetrate into the material. Applying a fast-Fourier-transform

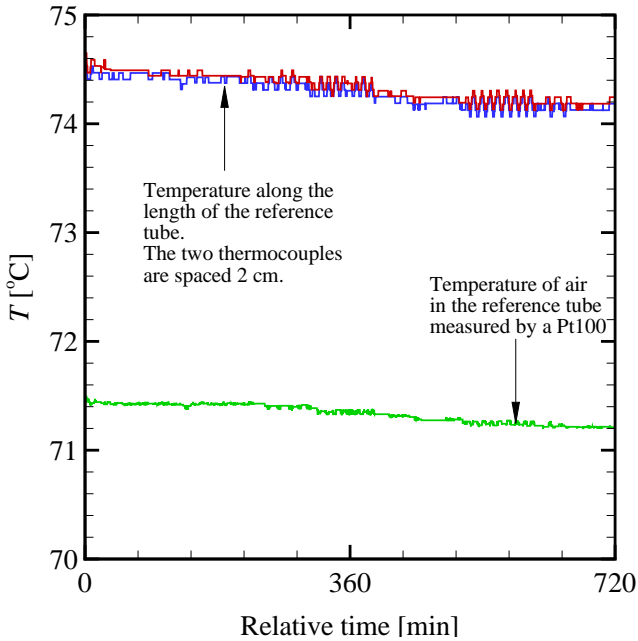


Figure 7.6: *The reference-tube wall temperature at two different axial positions (indicated by the red and blue lines) and the air temperature inside the reference tube (green line) over a 12-hour period. The fact that there is a slight gradient visible along the reference-tube wall may or may not necessarily imply that there is indeed a temperature gradient present, because the associated temperature difference is within the uncertainty of the k-type thermocouples.*

to the data output of the PID-controllers (see Fig. 7.7), it is found that the lowest frequency is between 2 and 3 Hz. In the case of a semi-infinite flat plate which is subjected to periodic heat flux changes at one end, it is found that the amplitude of the temperature fluctuation attenuates by a factor of 1000 over a penetration distance of 5 mm. Although this figure is not expected to be the same for a cylinder, the attenuation value determined for the flat plate does indicate that the inner wall temperature fluctuation of the charge-tube wall is negligibly small.

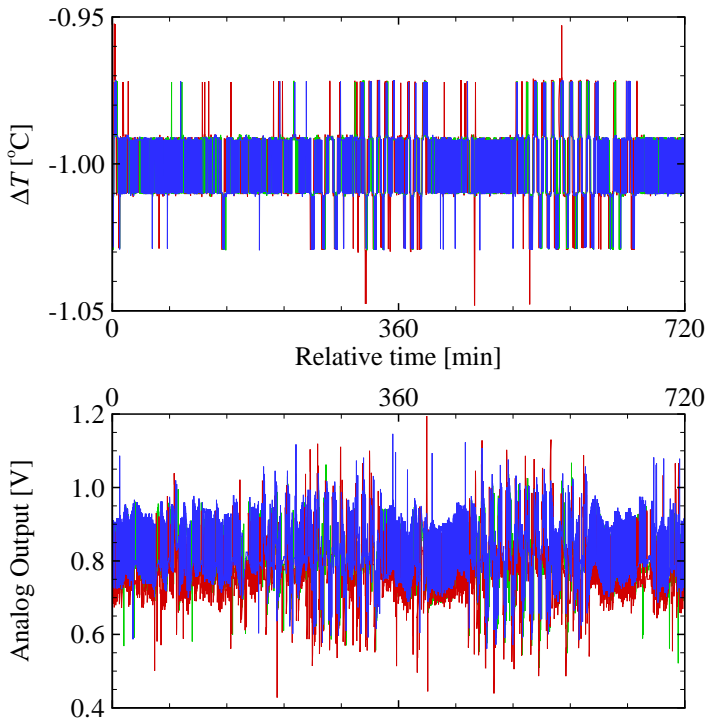


Figure 7.7: Above: The local pipe-segment wall temperature minus that of the local reference-tube wall temperature of three adjacent pipe-segments as a function of the relative time over a period of 12 hours. The set-point value for the temperature difference is  $-1\text{ }^{\circ}\text{C}$ . Below: the output of the PID-controllers to the thyristors.

### 7.3 Compression-shock-wave experiment using air

The subsequent paragraphs within this section treat one experiment of many conducted using the FAST whereby a compression shock wave was created in air and relevant quantities were measured, recorded and correlated. The compression shock wave was created using a diaphragm made of synthetic material; the diaphragm was ruptured by employing a hot-wire. The flanges used to clamp the diaphragm and the hot-wire are shown in Fig. 7.8. The goals of the experiment were:

- To determine the time-of-flight (ToF) of the incident wave and its speed of propagation with assigned uncertainties.
- To use this opportunity for training and software development.

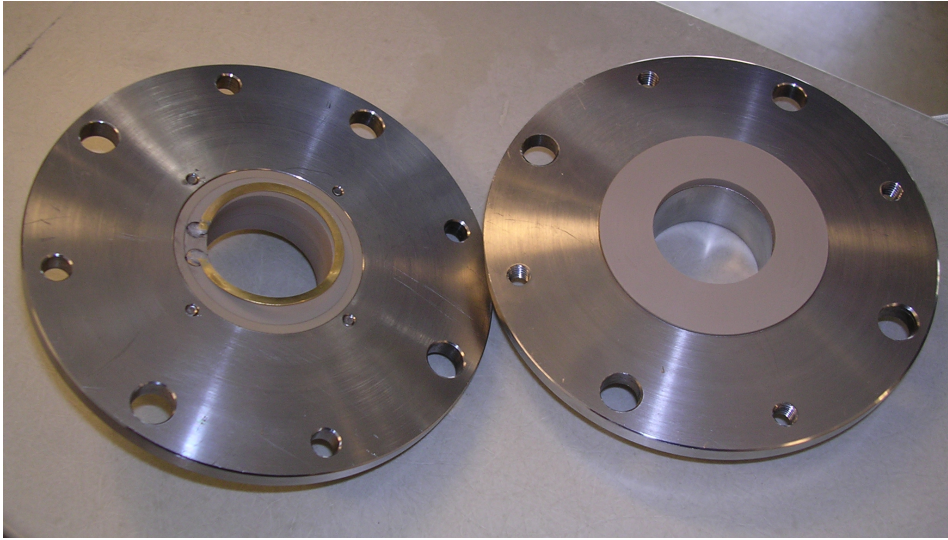


Figure 7.8: Two flanges which are employed to fix the diaphragm used for generating a compression shock wave in air. The flange on the left contains a copper hot-wire with a thickness of 0.1 mm and a width of about 2 mm. By passing a suitably chosen amount of power through the hot-wire, the diaphragm is locally melted, thereby opening as a flap due to the pressure difference across it.

In this particular experiment which is documented in the following, the experimental temperature of the air contained in the charge tube was  $27.0 \pm 0.400$  °C, as determined with a Pt100 device. Furthermore, the charge tube, the reference tube and the vapor generator were pumped on using a vacuum pump connected to the drain of the vapor generator, until the pressure was equal to 0.020 bar. The reason for choosing such a low pressure was related to the fact that the aim was to create a shock wave with a Mach number in between 1.5–2. It should be noted that the static pressure instrument has been calibrated by the supplier at 400 °C as per requirements of the foreseen experiment with BZT fluids. At the foreseen temperatures therefore, the uncertainty in pressure data is 0.1 % of the full-scale, i.e., 20 mbar. At temperatures different from 400 °C, the uncertainty increases by  $|T - 400| \times 0.015$  %. This implies that at the low experimental temperature, the uncertainty in the pressure is of the same order as the pressure value itself. Note that the “Nederlands Meetinstituut (NMI)” has been contracted to calibrate all instruments and to determine the uncertainty of the entire measurement chain. The reservoir was kept open to the atmosphere and remained so during the run, and thus the high-pressure state remained constant. That is, the atmospheric pressure was  $1.0 \pm 0.058$  bar. The surrounding air temperature was  $26.3 \pm 0.400$  °C.

Notice that in this respect, the operation of the FAST is different than in a conventional shock tube or as is intended for the RSW-experiments with BZT fluids, namely siloxanes. In the case of a shock tube for example, once the high-pressure compartment is connected to the low-pressure compartment, a rarefaction fan stabilizes the pressure behind the contact surface and thus the compression shock wave. In the experiment documented herein however, it is expected that as soon as the low-pressure charge tube is connected to the atmospheric pressure, there is flow of air into the pipe to  $Ma = 1$ -conditions (sonic conditions) at a location in the charge tube very close to its inlet (the pressure at this sonic state is about 0.52 bar, assuming an ideal gas (in)flow without friction). From this sonic state, an unsteady expansive fan decreases the pressure even further. There is also a contact surface ahead of the expansion fan and ahead of the contact surface there is a weak compression shock wave which propagates at supersonic velocity. A sketch of the expected  $x-t$ -diagram is shown in Fig. 7.11. The ToF can be determined for the incident wave, which is one of the aims of this experiment.

Before the experiment can start, it is first of all necessary to establish the time and the power which is required to melt the diaphragm. The melting should be kept as short as possible and a trial-and-error procedure yielded that under the imposed pressure difference, 160 W of power was enough to rupture the diaphragm which had a thickness of 0.1 mm, in 1–2 seconds (note that this is not the diaphragm rupture time). Once the ruptured diaphragm was replaced, the compression-shock-wave experiment started by sending a signal to the power supply of the hot-wire to turn on. At almost the same time, the data-acquisition system was started which sampled data from all four dynamic-pressure instruments simultaneously at 250 kSamples/sec for each channel.

Results of the experiment conducted in the manner as just described, are shown in Figs. 7.9 and 7.10. As has already been mentioned, the data-acquisition started as soon as the power supply to the hot wire was triggered. It can be seen in Fig. 7.9 that the diaphragm ruptured under the imposed pressure difference and the thermal power in about 1.6 sec from the moment the trigger was given. Zooming into the area where the initial rise in pressure is recorded, it is seen that firstly, the pressure increases rather sharply by  $\Delta P \approx 0.03$  bar, followed by a somewhat gradual pressure increase. The gradual pressure increase immediately past the frontrunner wave is due to the filling of the charge tube. This is not what was expected, since a time interval was expected past the incident shock wave where the pressure is stable (refer to Fig. 7.11). One may also question the suitability of the digital noise filtering, since determination of the capacitors for filtering out noise in the dynamic pressure signals, was based on experiments with siloxanes, where lower wave speeds can be expected. The filtering causes step functions to be recorded as asymptotically stable exponential responses; consequently, the stable pressure state is obscured. What is more is that after the initial sharp pressure rise, the subsequent gradual pressure increase measured by  $PI_1$  has a steeper slope than the signal measured by  $PI_2$ . A possible

explanation for this observation is that due to the filling behind the frontrunner wave (which, anticipating the results listed in Table 7.1 is a classical compression shock wave propagating at supersonic speed with respect to the quiescent medium upstream of the wave), it and the entire wave-train behind it, accelerate in time. Note that also if friction is considered past the shock wave, the pressure should increase somewhat. Therefore, the resulting  $x-t$ -diagram is not as simple as depicted in Fig. 7.11. That is, the wave lines are probably not straight. However, it must be mentioned that if the  $x-t$ -diagram does contain straight lines, a change of slope between the reading of the two adjacent pressure instruments, is also observed. Nevertheless, the influence of the filling, that of the inflow, as well as planarity of the waves, must be considered.

At  $t \approx 1.6675$  ms when the pressure change is about 0.10 bar, it is observed in Fig. 7.10 that for the signal from  $PI_1$  there is a 2<sup>nd</sup> clearly perceivable change in slope in the recording. The 2<sup>nd</sup> slope-change in the recording is also visible in the data of  $PI_2$ , although not as clear as for  $PI_1$ . This is most probably the result of secondary waves which arise due to the fact that it was found that actually the pipe segments were not aligned well, therefore bumps were encountered by the flow.

Finally, what should also be noted in Fig. 7.10 is that the pressure behind the reflected wave is not constant, but increases in time. This is because in between the last dynamic pressure instrument,  $PI_4$ , and the end-wall of the charge tube, refer to Fig. 7.1, there is the connection with the reference tube and the vapor generator. Consequently, as soon as the first incident wave passes this connection, there is a flow of air to the reference tube (and also the vapor generator if the manual valve between the vapor generator and the reference tube is open). This complicates the situation significantly, since behind the reflected wave, the flow velocity is non-zero. It should also be mentioned that although the hot-wire was designed such that the diaphragm opened as a flap, it was difficult to control this and frequently, the diaphragm detached and was carried by the flow into the charge tube.

Using the visual information displayed in Fig. 7.10, it is found that for the two dynamic pressure instruments, namely  $PI_1$  and  $PI_2$  with  $\Delta_{12} = 30$  cm, i.e., the mutual distance between the two instruments, the time-of-arrival of the compression wave is 0.470 ms, whereas for the two instruments which are placed the furthest apart, namely  $PI_1$  and  $PI_4$  with  $\Delta_{14} = 480$  cm, the time-of-arrival equals 7.03 ms. The values just determined are affected by a certain level of arbitrariness, because the judgement whether the wave has arrived at a transducer is based on when it is perceived by the operator that the recorded signal exceeds a certain threshold, e.g., as indicated by the upper dashed line in Fig. 7.10. So when the signal is outside the noise band. The uncertainty in the time-of-flight determined in this manner is equal to  $5.65 \mu\text{s}$ . This value of the uncertainty is based on a 250 kHz sampling rate of each channel, assuming a high signal to noise ratio, and assuming that all sensors have the same response time (the bandwidth of the sensors is 150 kHz). It should be mentioned that choosing the

correct sampling rate and having sensors with a high, but more importantly, the same response time is crucial, as can be explained using Fig. 7.12. The qualitative  $P$ - $t$ -chart depicted in Fig. 7.12 shows for example the fact that if the sensors do not have the same response time, there can be a significant fractional error in the ToF-measurement, especially if the ToF itself is a small numerical value. Results of the wave speed determined in this manner (which basically involves the manual alignment of two signals), are listed in Table 7.1.

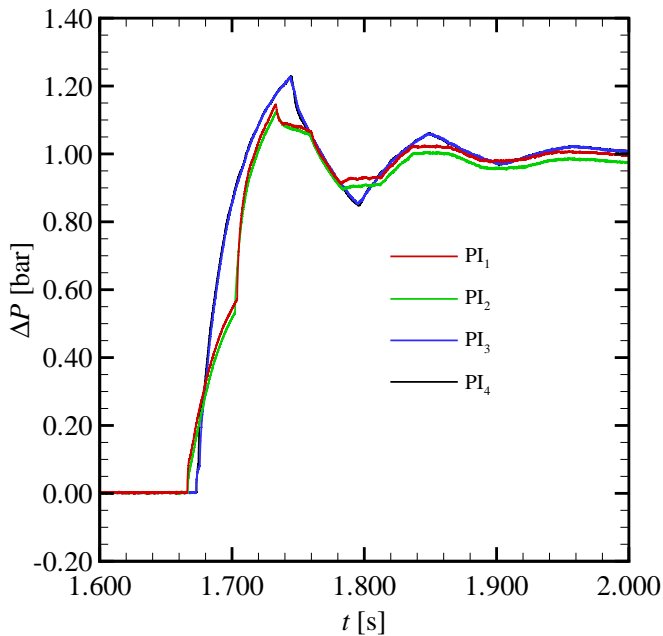


Figure 7.9: The measured pressure-difference as a function of the relative time (note that the data shown does not involve the total pressure). The uncertainty in the pressure measurement is at least 3 %.

In order to remove the influence of the above-mentioned arbitrariness associated with the signal-alignment method to determine the ToF, use can be made of the cross-correlation method. Cross correlation is a mathematical tool which is frequently used in signal processing. The cross-correlation function essentially quantifies the similarity of two wave forms as a function of a time-shift which is applied to one of the signals. Consider for example two real-valued continuous functions of time, e.g.,  $p_1(t)$  and  $p_2(t)$ , where the only difference between these two functions is that  $p_2(t)$  is shifted in time by an amount  $\tilde{t}$  with respect to  $p_1(t)$ . The cross-correlation function of these two signals then im-

Table 7.1: The time-of-flight (ToF) determined in three different ways, the distance between the dynamic pressure instruments ( $\Delta$ ) and the wave speed ( $b$ ) for a CSW-test performed in the FAST with air. Pressure instrument 1 is located the nearest to the nozzle throat whereas pressure instrument 4 is located the furthest. Note that average wave speeds are employed because the frontrunner wave accelerates.

	Tag	PI <sub>1</sub>	PI <sub>2</sub>	PI <sub>3</sub>	PI <sub>4</sub>
From signal alignment:	PI <sub>1</sub>	–	0.470	6.58	7.03
ToF [ms]	PI <sub>2</sub>	0.470	–	6.11	6.56
uncertainty = 5.65 $\mu$ s	PI <sub>3</sub>	6.58	6.11	–	0.450
From cross-correlation:	PI <sub>1</sub>	–	0.484	6.59	7.04
ToF [ms]	PI <sub>2</sub>	0.484	–	6.11	6.56
	PI <sub>3</sub>	6.59	6.11	–	0.448
From squared-difference method:	PI <sub>1</sub>	–	0.492	6.58	7.04
ToF [ms]	PI <sub>2</sub>	0.492	–	6.11	6.56
	PI <sub>3</sub>	6.58	6.11	–	0.452
$\Delta$ [cm]	PI <sub>1</sub>	–	30.0	450	480
	PI <sub>2</sub>	30.0	–	420	450
	PI <sub>3</sub>	450	420	–	30.0
From signal alignment:	PI <sub>1</sub>	–	638	684	683
$\langle b \rangle$ [m/s]	PI <sub>2</sub>	638	–	687	686
	PI <sub>3</sub>	684	687	–	667
From cross-correlation:	PI <sub>1</sub>	–	620	683	682
$\langle b \rangle$ [m/s]	PI <sub>2</sub>	620	–	687	686
	PI <sub>3</sub>	683	687	–	670
From squared-difference method :	PI <sub>1</sub>	–	610	684	682
$\langle b \rangle$ [m/s]	PI <sub>2</sub>	610	–	687	686
	PI <sub>3</sub>	684	687	–	664

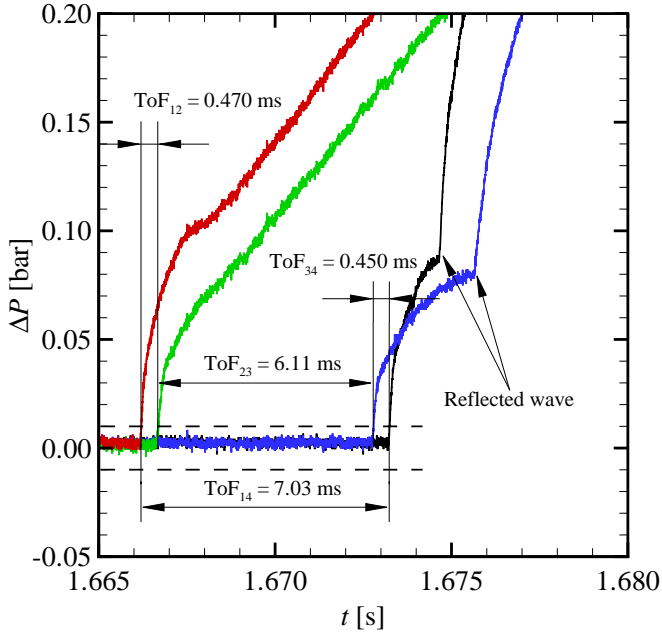


Figure 7.10: Zoomed: The measured pressure-difference as a function of the relative time. Also included are values of the time-of-flight (ToF) between the various dynamic-pressure instruments. The charge-tube pressure is equal to 0.020 bar  $\pm 5.8\%$  (probably an even higher uncertainty), the atmospheric pressure is equal to 1.0 bar  $\pm 5.8\%$  and the temperature of the experiment is  $27 \pm 0.40^\circ\text{C}$ . The data sampling rate is 250 kHz and the sensor bandwidth is 150 kHz. The line-legend is indicated in Fig. 7.9.

plies shifting  $p_2(t)$  with respect to  $p_1(t)$  by a predetermined value and calculating the integral of the product of the two signals. By continuing the shift, if the two functions match, the integral of the product exhibits a maximum; the maximum occurs at a time-shift of  $\tilde{t}$ . In the case of discrete signals however, as are the dynamic pressure data recorded by instruments  $PI_1$  and  $PI_2$ , i.e.,  $P_{1,i}$  and  $P_{2,i}$ , the cross correlation  $r$  between these sets is defined as

$$r(\tilde{t}_j) = \frac{\sum_i (P_{1,i} - \langle P_1 \rangle) \times (P_{2,i-\tilde{t}_j} - \langle P_2 \rangle)}{N}, \quad (7.1)$$

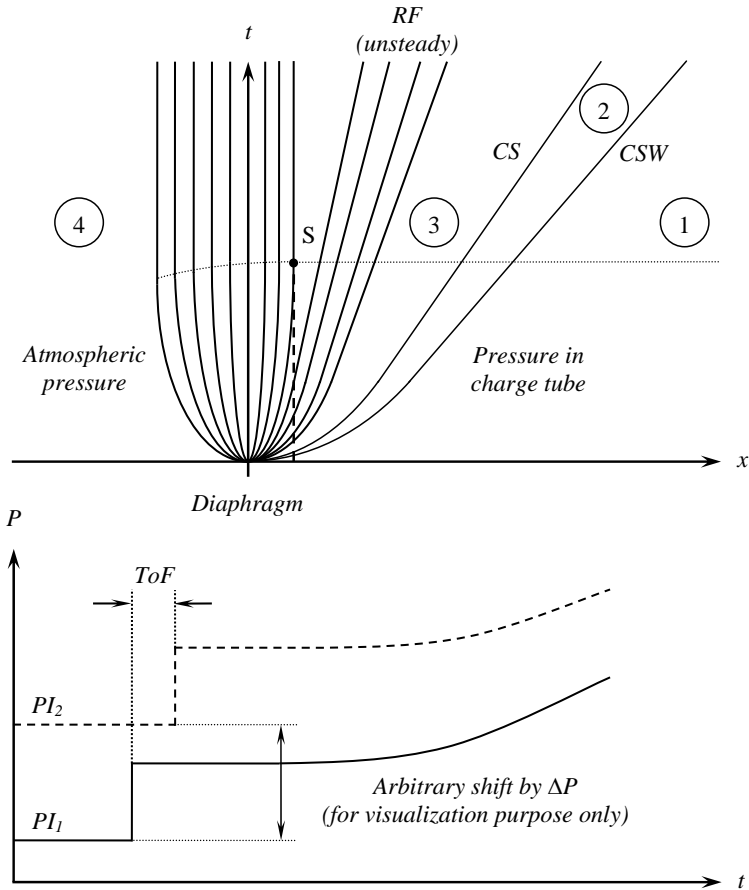


Figure 7.11: Sketch of the  $x-t$ -diagram for the compression shock experiment with air. Also shown are expected recordings from the dynamic pressure instruments  $PI_1$  and  $PI_2$ . Note that the air, once the diaphragm ruptures, flushes into the pipe, where it reaches sonic conditions,  $S$ , at a location slightly to the right of the inlet. From the sonic point onward, the flow expands further by means of unsteady rarefaction waves. Ahead of these rarefaction waves is the CS and the CSW.

where the  $\langle \rangle$ -symbol indicates the mean value of the corresponding series and

$$N = \sqrt{\sum_i (P_{1,i} - \langle P_1 \rangle)^2} \sqrt{\sum_i (P_{2,i-\bar{t}_j} - \langle P_2 \rangle)^2} \quad (7.2)$$

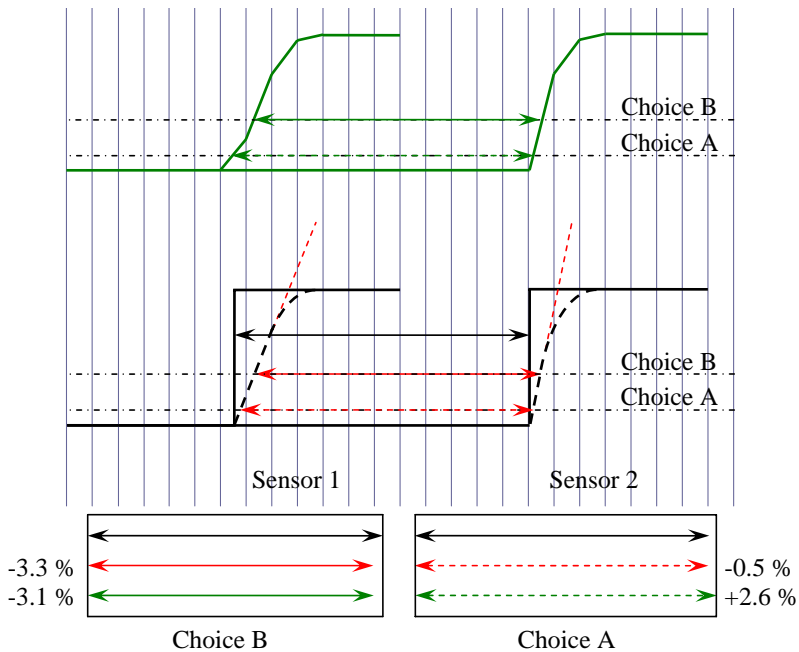


Figure 7.12: Qualitative chart illustrating the influence of the sensor response time-constant and the influence of the data sampling rate. The black lines represent the ideal signal, whereas the green lines represent the sampled signals. If the signal-alignment method is used, then, depending on choice A or B, the uncertainty in the ToF-measurement is indicated.

The value of  $\tilde{t}_j$  for which  $r(\tilde{t}_j)$  is maximal, indicates maximal correlation between the two signals  $P_1$  and  $P_2$ , therefore, the thus obtained value of  $\tilde{t}_j$  corresponds to the ToF between, in this case,  $P_{1,i}$  and  $P_{2,i}$ . For discrete data the procedure to determine the cross correlation  $r(\tilde{t}_j)$  requires the identification of a time window because only data in this window are used to maximize  $r$ . However, cross correlation yields a series which has twice the length of the original series. Therefore, it must be decided what to do with data to the left and right of the window. Here, as is the common approach, data points outside the selected window are set to zero. Results of ToF-data determined using signal cross correlation are also listed in Table 7.1. An uncertainty is not assigned to the ToF-value determined using the cross-correlation method, because here specifically, the time window also influences the uncertainty because of the fact that the signals depicted in Fig. 7.10 do not exhibit stable pre- and post shock pressures but rather the post-shock pressure increases with time. Moreover, the post-shock pressure-increase of  $PI_1$  has a different slope than that of  $PI_2$ . Consequently, the cross-correlation functions which should be a triangle that exhibits a max-

imum at the ToF, has a distorted triangular shape, making an estimate of the ToF-uncertainty in this case difficult.

Alternatively, a technique which is similar to least-square fitting can be used. The procedure is analogous to the cross-correlation method with the only difference that the objective function, namely

$$F = \int_{\mathcal{T}} (f(t) - g(t - \tilde{t}))^2 dt, \tag{7.3}$$

is minimized. The interval  $\mathcal{T}$  represents an appropriately selected time window which encloses the shock wave. Since discrete signals are involved, the  $\tilde{t}_j$  for which the series,

$$F(\tilde{t}_j) = \sum_{k=1}^M (f(t_k) - g(t_k - \tilde{t}_j))^2, \tag{7.4}$$

albeit in its normalized form, displays a minimum, corresponds to the ToF. Using this procedure, ToF's for all the pressure signals displayed in Fig. 7.10 are computed and are indicated in Table 7.1.

So in summary,

$T_{\text{reservoir}}$	26.3	±	0.400	°C
$T_{\text{charge-tube}}$	27.0	±	0.400	°C
$P_{\text{reservoir}}$	1.0	±	0.058	bar
$P_{\text{charge-tube}}$	0.020	±	0.0012–0.020	bar
$c$	349	±	~5	m/s
ToF <sub>1,2</sub>	0.470	±	5.65	μs
ToF <sub>1,4</sub>	7.03	±	5.65	μs
$\langle b \rangle_{1,2}$	638	±	~8	m/s
$\langle b \rangle_{1,4}$	683	±	~0.5	m/s
Ma <sub>1,2</sub>	1.828	±	0.035 (1.9 %)	–
Ma <sub>1,4</sub>	1.957	±	0.028 (1.4 %)	–

Finally, it is to be noted that the average wave speed determined using instruments PI<sub>1</sub> and PI<sub>2</sub> between the three methods do not agree well, if the uncertainty of 8 m/s is considered for  $\langle b \rangle_{1,2}$  determined using the alignment method. This can also be stated for  $\langle b \rangle_{1,4}$  considering the uncertainty of 0.5 m/s. However, a 1 m/s difference is acceptable.

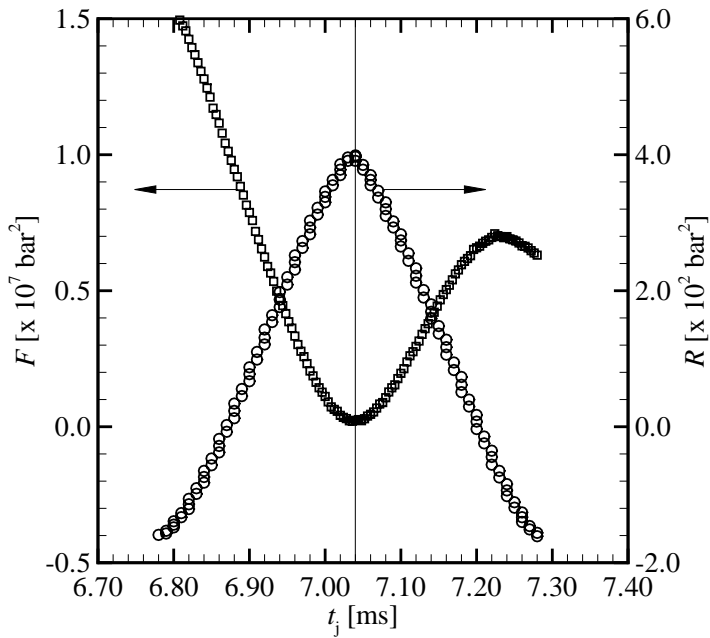


Figure 7.13: Results of the squared-difference method  $F$  (indicated by squares) and the cross-correlation technique  $R = r \times N$  (indicated by circles) applied to  $PI_1$  and  $PI_4$ . The minimum, respectively maximum, is located at  $\tilde{t}_j = 7.04$  ms which corresponds to the ToF

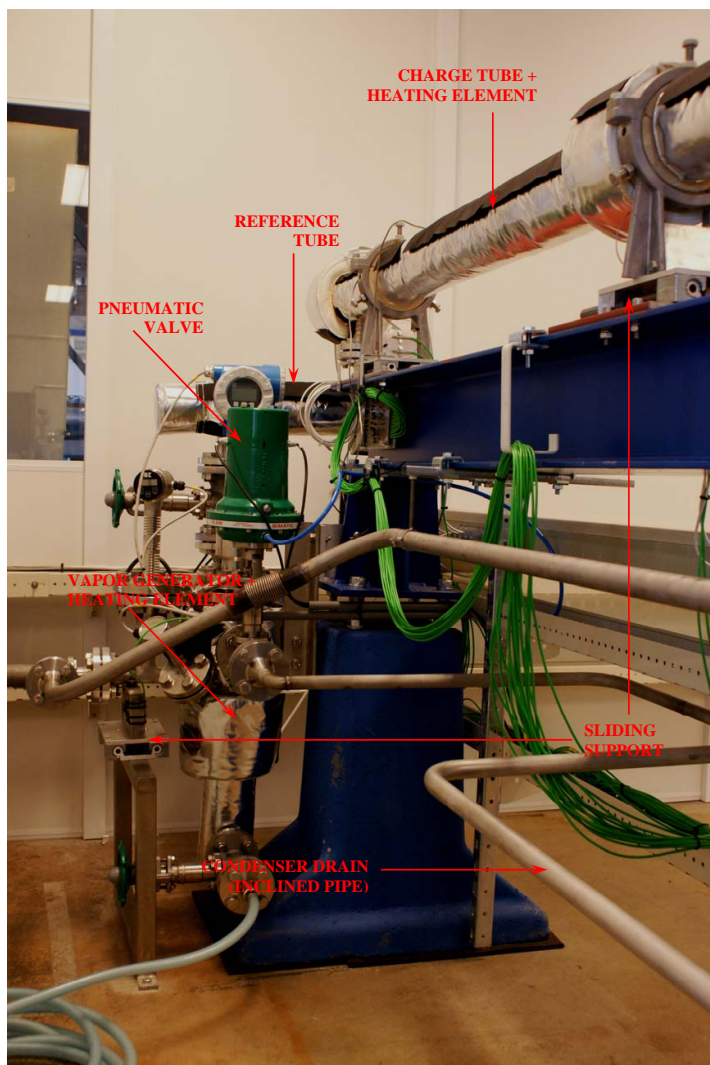


Figure 7.14: Picture of the tank in which the test fluid is charged and vaporized. Behind it, the horizontally positioned RT can be seen. Also notice the sliding supports of the charge tube and the vapor generator.

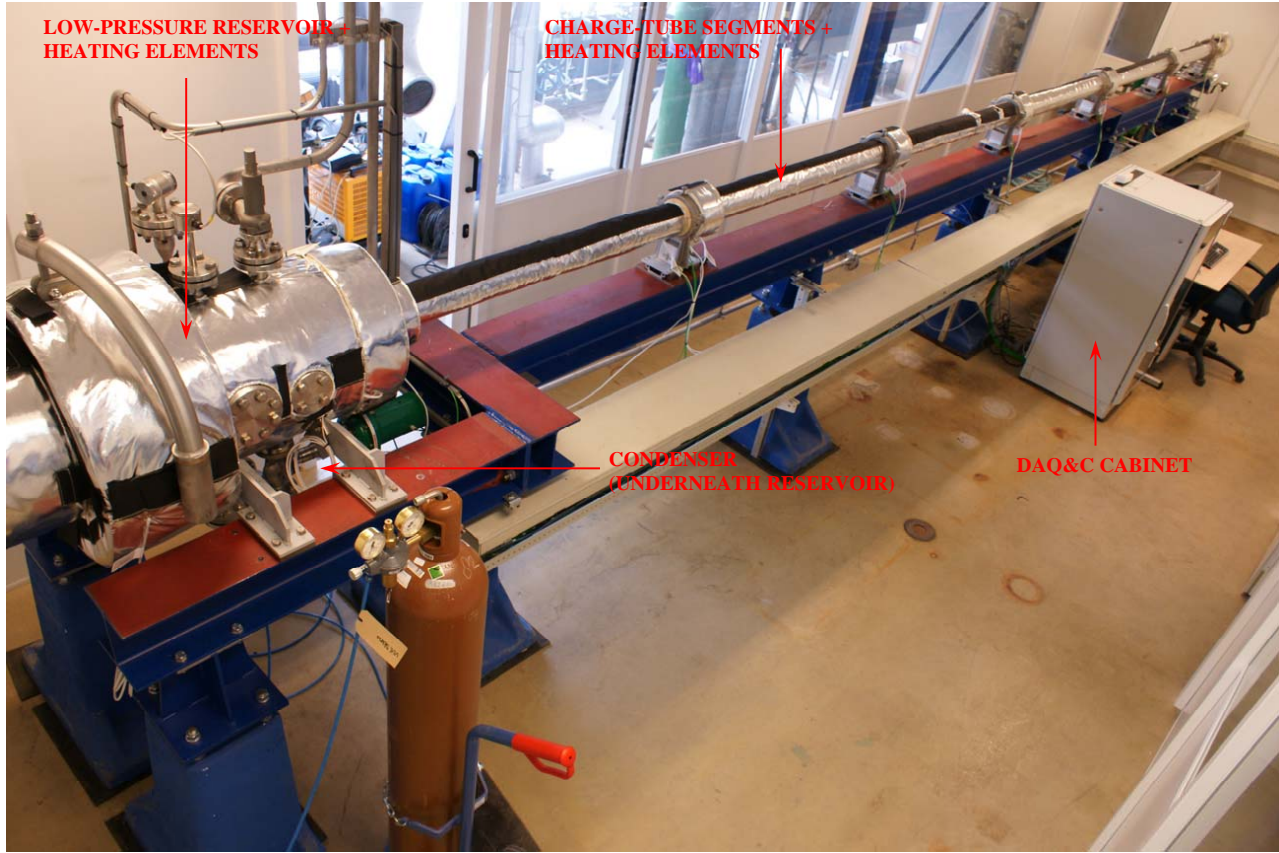


Figure 7.15: *The Flexible Asymmetric Shock Tube (FAST), as built. Main assemblies are labeled. Ryan is not shown.*

**Nomenclature**

Symbol	Description
$b$	Wave velocity
$c$	Speed of sound
$F$	Function to be minimized in the squared-difference method
Ma	Mach number
$P$	Pressure
$r$	Cross-correlation function or series
$T$	Temperature
$\mathcal{T}$	Time-window of sampled data
$t$	Time
$\tilde{t}$	Time of flight (ToF)
$x$	Axial spatial coordinate
$\Delta_{ij}$	Mutual distance between dynamic pressure instruments $i$ and $j$

*“There is no doubt in my mind when history was written, the final page will say: Victory was achieved by the United States of America for the good of the world.”*

President George W. Bush, Camp Arifjan, Kuwait, January 12, 2008

# 8

## Conclusions and recommendations for future research

### 8.1 Conclusions

The study documented herein has shown that it is both theoretically and technically possible to create an unsteady nonclassical expansion shock wave in a polyatomic substance classifying as a Bethe-Zel'dovich-Thompson (BZT) fluid. This has resulted in the design and building of the Flexible Asymmetric Shock Tube (FAST) – a unique facility for high-temperature gas-dynamic experiments in organic fluids – equipped with a novel fast-opening valve. To this purpose, it was first of all necessary to identify potential BZT candidate fluids featuring several thermophysical and technological characteristics which make them suitable for an experiment aiming at the demonstration of nonclassical gas-dynamic phenomena. This requires sophisticated thermodynamic modeling of the fluid, taking into account other aspects, like fluid flammability and toxicity, costs and thermochemical stability of the substance. Based on a previous study documented by Colonna and Silva [37], the use of model equations of state (EoS's) showed that selected fluids within the dimethylsiloxanes family exhibit an embedded region of negative nonlinearity. However, as indicated in Ref. [37], the predictions of  $\Gamma$  were significantly affected by the large uncertainty in the ideal-gas isobaric heat capacity correlation, viz. 25 %. Therefore, as reported in this thesis, firstly, acoustic resonance frequency measurements were conducted yielding accurate speed-of-sound data. Using these measurements and results

obtained from ab initio calculations, accurate ideal-gas isobaric heat capacities were predicted which have an estimated uncertainty of no more than 5–6 %. With these data and thermal and caloric property data documented elsewhere, modern EoS's formulated in terms of the Helmholtz free energy have been developed. Using these new multiparameter EoS's, but also model EoS's, e.g., the Peng-Robinson, Stryjek-Vera modified cubic EoS, it has been found that MD<sub>3</sub>M and linear dimethylsiloxanes of greater molecular complexity and D<sub>6</sub> and cyclic dimethylsiloxanes of greater molecular complexity qualify as BZT fluids, even if the uncertainty in the heat capacity correlation is taken into consideration (see Ref. [30]).

The fundamental derivative of gas dynamics  $\Gamma$ , i.e., the thermodynamic property that governs the qualitative and quantitative behavior of compressible flows, cannot be obtained easily by direct measurements in the dense-gas region which is of interest, since  $\Gamma$  is a higher-order derivative of primary thermodynamic properties. Consequently,  $\Gamma$  must be determined from thermodynamic models (also refer to the discussion in Chap. 4). Previous studies however, have shown a high degree of uncertainty in computations of  $\Gamma$ , if relatively simple thermodynamic models are employed. It was therefore necessary to assess if  $\Gamma$  could indeed be calculated with the accuracy which is required for the design of a facility to demonstrate BZT effects, such as the FAST. This required a study whereby the reference equations of state (EoS's) developed for molecularly complex fluids were used as a benchmark. The performance of simple EoS's, like cubic EoS's which currently have to be employed out of necessity due to the unavailability of experimental thermal and caloric property data for the thermodynamic modeling of potential BZT candidates, was then assessed against the reference EoS's. Additionally, this study allowed for estimating an uncertainty with which simple EoS's can predict  $\Gamma$ . The main findings of this study documented in Chap. 4 were that:

1. If highly accurate thermodynamic models are employed,  $\Gamma$  can be calculated with a degree of uncertainty that is suitable for dense-gas applications.
2. For fluids made of complex molecules, it is possible to achieve a comparatively higher level of accuracy in the estimation of  $\Gamma$  with respect to molecularly simpler fluids, if experimental data are available. If a sufficient number of accurate experimental data are available, technical multiparameter EoS can be developed and result in an appreciable improvement with respect to the uncertainty of the estimation of  $\Gamma$ .

In addition, using scaled fundamental equations it is found that the region of negative nonlinearity is located partly in the critical region and is therefore under the influence of critical phenomena (critical anomalies). Application of the scaled fundamental equation of methane, water and carbon dioxide has yielded that in the single-phase critical region of these pure fluids,  $\Gamma$  diverges weakly to

$+\infty$ , which confirms Emanuel's result documented in Ref. [61]. However, using thermodynamic relations developed for the two-phase region of a single component fluid, use of the scaled fundamental equation of methane displays a weak divergence of  $\Gamma$  to  $-\infty$ , which to the knowledge of the author is new result. Since the physical behavior of pure fluids near the vapor-liquid critical point is universal, it is believed that all fluids display a  $\Gamma < 0$ -region in the two-phase near-critical region. Therefore, in principle expansion shock waves, including expansion-condensation shock waves are possible if thermodynamic equilibrium between two homogeneously dispersed phases is assumed.

An investigation on possible options to demonstrate phenomena which ensue from negative values of  $\Gamma$ , namely BZT effects, has been conducted and has yielded various theoretically feasible options. Based on a comparative analysis whereby arguments for and against each experimental option/strategy have been assessed (the assessment was based on aspects like, accuracy requirements, repeatability and reproducibility of the experiments, availability of the facility, costs, etc.), a setup has been chosen, designed and built that aims at the production of an unsteady rarefaction shock wave with maximal supersonic-to-sonic speed change. The experimental facility, namely the previously mentioned Flexible Asymmetric Shock Tube, incorporates both the operational aspects of a simple shock tube and a Ludwieg tube.

The facility as built has been tested; during the commissioning phase various tests have been done to ensure the structural integrity of the facility and to check whether all specifications are met. To this purpose, a temperature control test has been performed aimed at firstly, the determination of optimal PID-control parameters and secondly, if using these parameters, tight temperature control of the shock tube and the balance of plant can be achieved. The second set of tests that was done was related to the measurement of the time-of-flight of a created unsteady classical compression shock wave in air. Both these sets of tests were successful, since it was possible to regulate the temperature of the charge tube to within 0.01 °C and the wave Mach number, which in turn depends also on the time-of-flight, could be computed with an uncertainty of less than 2 %. It is expected that in the case of rarefaction-shock-wave experiments in siloxanes, the Mach number can be computed with a lower uncertainty, because, due to the lower wave speeds, the relative uncertainty in the time-of-flight measurement is less than that in air for the given instrumentation and facility.

There are however some open questions which can only be answered once the experiment is conducted in the FAST. For example, the flow Reynolds number past the generated wave train, which develops as the fast-opening valve is opened, may cause the rarefaction wave never to coalesce into a shock wave. This conclusion can only be drawn after many repeated runs of experiments. Furthermore, many polyatomic gases exhibit a single vibrational relaxation process. If this is also assumed for BZT fluids, then relaxation was found to occur completely inside the shock wave and not downstream of it. However, vibra-

tional relaxation can also be nonlinear and currently, nothing is known about vibrational relaxation in dimethylsiloxanes classifying as BZT fluids, like  $D_6$ , therefore relaxation can potentially complicate the flow field.

## 8.2 Recommendations

Soon,<sup>1</sup> experiments aimed at generating nonclassical unsteady rarefaction shock waves will be performed using the FAST. This will require a trial and error procedure because, due to the presence of a transitional or turbulent boundary layer quite close to the wave and due to the uncertainty of the thermodynamic EoS of the fluid, the opening of the nozzle's throat (which is built into the fast-opening valve) is to be tuned. Also the setting of the correct initial states prior to the opening of the valve, viz. the pressures and temperatures in the charge tube and the low-pressure reservoir, is crucial. There are still some open questions, e.g., it is not known if the initially formed rarefaction wave even coalesces into a shock wave due to the potentially strong boundary layer immediately behind the frontrunner wave, or, if a shock wave is indeed formed, whether or not it attenuates and disperses into a sonic wave before it reaches the dynamic pressure instruments. Furthermore, nonlinear vibrational relaxation may pose additional complications and, in the worst case, thermochemical decomposition of the working fluid can occur. All these aspects can only be discussed in more detail once tests are performed under the exact experimental conditions.

Aside from the envisaged rarefaction-shock-wave tests, research in the near-future should be aimed at the theoretical, numerical and experimental study of:

1. The application of BZT fluids and the exploitation of nonclassical gas dynamic phenomena in organic Rankine cycle engines (ORCE's)

ORCE's are small energy conversion systems of the order of a few kilowatts (30 kW) to a few Megawatts (1–3 MW), for decentralized terrestrial and space applications (see Angelino and Invernizzi [7] and references therein). The working principle of ORCE's is the same as that of conventional steam Rankine power cycles, with the main difference that the working fluid is an organic compound instead of water. Currently, non-BZT fluids such as the dimethylsiloxanes MM and MDM, are employed as working fluids in ORCE's and it is in principle possible to develop and design power units which employ more molecularly complex substances of the same fluid family, e.g.,  $D_6$  which classifies as a BZT fluid. Due to the high molecular weight of a fluid such as  $D_6$  however, the optimal power output for which the ORCE can be designed, is low, e.g., of the order of 2–3 kW<sub>e</sub> (with co-generation, the total power output is up to 12 kW). Nevertheless, the nonclassical gas dynamic phenomena which ensue from the

---

<sup>1</sup>Update: 26 March 2009

fact that  $D_6$  has an embedded region of negative- $\Gamma$ , can be exploited in order to improve the cycle efficiency. The concept of exploiting BZT effects in ORC-turbines is based on earlier, more fundamental, studies conducted by Cramer and Park [49] and Kluwick [113]. By solving the compressible Navier-Stokes equations coupled to a real-gas thermodynamic model, Cramer and Park [49] demonstrated, using a benchmark problem of the reflection of an oblique shock wave from a laminar boundary layer on a flat adiabatic plate, that, if a BZT fluid was expanded under similar pressure and temperature conditions as what is encountered in ORC-turbines, boundary layer separation did not occur. The suppression of boundary layer detachment was the result of the fact that compression shock waves were inadmissible and, in fact, they disintegrated instead into smooth compression fans. Additionally, it was found that the pressure-gradient is more important regarding boundary layer detachment than the overall compressive pressure change and thus detachment of the boundary layer does not occur if the fan is smooth enough. If an expansion shock wave was admitted, there was no adverse pressure gradient and therefore the boundary layer remained attached. Thus the study of Cramer and Park shows that it is possible to eliminate the loss mechanisms in ORC-turbines if the turbine inlet and outlet conditions are well-chosen. Brown and Argrow [19] extended this work further and conducted a proof-of-concept study of the exploitation of BZT effects in ORCE's. The potential turbine-efficiency improvement was assessed in a two-dimensional cascade analysis using a real cascade geometry of a symmetric impulse turbine and both a supersonic inlet and outlet. The outcome of Brown and Argrow's [19] investigation was that if only the irreversible effects due to the presence of shock waves was accounted for, the efficiency improvement of the ORC-turbine could be as high as 3 %, notwithstanding the fact that greater improvements are possible if also losses due to boundary layer detachment are considered.

The limitation of these studies is that only the turbine is considered and not the thermodynamic performance of the cycle as a whole. The computations of the efficiency improvements for example should be done taking the entire cycle into account and not only improving the efficiency of one component and deteriorating the overall cycle performance. Also the off-design behavior must be included in the assessment of the proof-of-concept especially because of the fact that ORCE's often operate in part-load conditions. It is in part-load conditions that BZT effects may be most suitable.

## 2. Nonclassical gas dynamics in mixtures classifying as BZT fluids

In the study conducted by Colonna and Silva [37] it was demonstrated using the Peng-Robinson, Stryjek-Vera modified, cubic EoS combined with

the Wong-Sandler mixing rules, that mixtures of siloxanes can exhibit a region of  $\Gamma < 0$  in the single-phase dense-gas regime. This work should be extended to other mixtures, e.g., perfluorocarbon-siloxane mixtures. It is expected that due to the additional degree of freedom, namely the composition, the interval of thermodynamic states that exhibit  $\Gamma < 0$ -values can be tuned. Initially, the investigation of BZT effects in mixtures should be mostly theoretical.

### 3. Nonclassical gas dynamics in the near-critical single- and two-phase region of pure fluids

It was demonstrated in Sec. 4.5 that the fundamental derivative of gas dynamics exhibits anomalous behavior as the vapor-liquid critical point of a single-component fluid is approached. Since in the vapor-liquid equilibrium (VLE) region,  $\Gamma$  diverges to  $-\infty$ , rarefaction shock waves featuring vapor-liquid phase transition are admissible, as can be demonstrated using the shock admissibility conditions. That  $\Gamma$  is negative in the two-phase region close to the critical point may also be of use in studies related to atomization (for example of fuel in internal combustion engines), and in studies on spray-drying for producing particles with supercritical  $\text{CO}_2$ . In the last-mentioned process for example, the density gradient is an important parameter which determines the particle size. Near-critical shock waves must also be investigated from a theoretical viewpoint where one must account for the validity of the assumptions of thermodynamic equilibrium between homogeneously dispersed phases. Once the theoretical aspects are well-understood, experiments should be conducted to demonstrate near-critical expansion shock waves, in particular those displaying condensation. These types of experiments can be conducted at relatively low temperature, like at room temperature, because unlike the negative nonlinearity region in the single-phase dense-gas regime, the negative value of  $\Gamma$  in the near-critical VLE-region is independent of the molecular complexity of the substance. These experiments can be done with the FAST, however, the influence of gravity must be assessed.

Remark that  $\Gamma \rightarrow \pm\infty$  from a physical viewpoint, is meaningless. In fact,  $\Gamma$  will just becomes arbitrarily large as the critical point is approached and levels off to a fixed, large value.

Finally, thermodynamic modeling of the working fluid is important, not only for the design of an experiment and determination of the thermodynamic states prior to a run, but also for the design and analysis of a technical application that can exploit BZT effects. Thermodynamic data for potential BZT fluids however are scarce, mostly because measurements have to be done at elevated temperatures and a general lack of interest of knowing the thermodynamic properties in the dense-gas region of molecularly complex fluids, such as dimethylsilox-

anes and perfluorocarbons. Future work thus has to include the measurement of thermal and caloric property data of molecularly complex fluids in the dense-gas and critical region, in particular the siloxanes considered in this study.

### Nomenclature

Symbol	Description
$\Gamma$	Fundamental derivative of gas dynamics



*“There’s an old saying in Tennessee – I know it’s in Texas, probably in Tennessee – that says, fool me once, shame on – shame on you. Fool me – you can’t get fooled again.”*

President George W. Bush, Nashville, Tennessee, September 17, 2002



## Experimental speed-of-sound data for fluids $D_4$ , $[(CH_3)_2-Si-O]_4$ , and $D_5$ , $[(CH_3)_2-Si-O]_5$

The following tables list speed-of-sound values for octamethylcyclotetrasiloxane and decamethylcyclopentasiloxane, that were measured at NIST, Gaithersburg, MD, during the period between 15 September 2005–15 November 2005. Relevant information can be found in Chap. 3, including the nomenclature.

Table A.1: Experimental speed-of-sound data for  $D_4$  at certain values for pressure and temperature. The experimental uncertainties are also listed.

$T$ [K]	$P$ [kPa]	$c$ [m/s]	$10^4 \cdot \sigma_u$ [m/s]
450	38.90	110.351	252.0
	46.70	109.656	89.8
	57.41	108.801	72.2
	62.89	108.299	17.0
	69.33	107.727	16.4
465	31.29	113.043	638.9
	40.99	112.320	123.0
	49.18	111.723	69.2
	58.99	110.976	20.2

Continued on the next page...

Table A.1 – Continued

$T$ [K]	$P$ [kPa]	$c$ [m/s]	$10^4 \cdot \sigma_u$ [m/s]
	70.69	110.062	16.5
	77.48	109.530	24.9
	92.89	108.286	9.9
	101.01	107.535	14.3
	111.40	106.695	5.3
	121.67	105.761	7.4
465	36.51	112.753	138.6
	47.85	111.913	37.2
	57.21	111.202	25.3
	68.51	110.332	14.4
	74.87	109.829	10.7
	81.72	109.278	26.5
	97.68	107.963	270.8
	106.95	107.179	89.7
	116.93	106.300	335.1
465	32.63	112.986	242.5
	46.84	111.935	53.3
	61.46	110.824	18.8
	73.59	109.872	15.3
	87.87	108.720	9.0
	105.11	107.277	15.0
	123.48	105.664	17.4
480	42.70	114.022	56.2
	54.67	113.202	18.1
	65.08	112.478	36.1
	71.30	112.038	24.6
	85.50	111.071	24.9
	92.46	110.502	12.1
	109.21	109.241	4.5
	118.88	108.493	3.1
	129.21	107.675	6.8
	140.39	106.769	11.2
	152.36	105.769	8.6
	165.42	104.642	6.3
495	27.45	117.135	200.8
	36.20	116.658	71.6
	47.54	115.985	15.6
	143.41	109.744	283.3
	159.70	108.434	20.5
	160.40	108.391	105.0

Continued on the next page...

Table A.1 – Continued

$T$ [K]	$P$ [kPa]	$c$ [m/s]	$10^4 \cdot \sigma_u$ [m/s]
	174.53	107.346	44.6
	186.64	106.439	78.7
	198.61	105.492	1287.4
	224.52	103.408	31.8

Table A.2: Experimental speed-of-sound data for D<sub>5</sub> at certain values for pressure and temperature. The experimental uncertainties are also listed.

$T$ [K]	$P$ [kPa]	$c$ [m/s]	$10^4 \cdot \sigma_u$ [m/s]
485	82.92	97.275	62.3
	64.42	99.132	101.4
	49.43	100.666	75.2
485	85.12	97.170	56.7
	74.85	98.380	97.0
	63.60	99.197	119.9
	55.24	100.360	44.5
	43.63	101.141	450.6
	35.39	101.908	238.9
500	116.60	96.555	219.5
	105.42	97.603	59.0
	95.37	98.558	54.0
	85.90	99.495	65.5
	74.95	100.631	17.9
	64.64	101.500	31.9
	55.42	102.199	161.5
	42.70	103.271	134.2
	33.93	103.964	215.7
	26.30	104.683	16.3
500	78.98	100.217	28.6
	47.88	102.870	32.7
	31.33	104.222	75.4
500	22.48	104.919	126.8
	73.64	100.810	63.4
	64.96	101.440	122.6
	51.58	102.577	0.6
	39.90	103.532	26.2
	32.27	104.140	11.9

Continued on the next page...

Table A.2 – Continued

$T$ [K]	$P$ [kPa]	$c$ [m/s]	$10^4 \cdot \sigma_u$ [m/s]
510	22.13	104.938	0.0
	110.69	99.980	120.1
	89.89	100.871	49.5
	57.10	103.487	52.7
	34.55	105.200	31.7
510	103.28	99.891	82.5
	92.75	100.754	5.9
	82.51	101.583	20.3
	72.53	102.369	5.4
	62.78	103.980	261.9
	51.27	104.860	55.7
	43.26	104.679	19.2

*“As Luce reminded me, he said, without data, without facts, without information, the discussions about public education mean that a person is just another opinion.”*

President George W. Bush, Jacksonville, Florida, September 9, 2003

# B

## Relevant expressions for computing the fundamental derivative of gas dynamics from a canonical Helmholtz function

For the computation of the fundamental derivative of gas dynamics and other thermodynamic properties, first-order, second-order, and composite derivatives of pressure with respect to specific volume and temperature are required. Expressions for the computation of thermodynamic properties from a canonical Helmholtz equation of state are presented in the following (see also Span [184] and Colonna et. al. [30]). The Helmholtz function can be formulated as (refer to Chap. 4 for the nomenclature)  $\Psi(T, \rho) / (RT) = [\psi^0(\tau, \delta) + \psi^R(\tau, \delta)]$ , where  $\delta \equiv \rho / \rho_C = v_C / v$  and  $\tau \equiv T_C / T$ . The ideal-gas part of the reduced Helmholtz function is

$$\psi^0(\tau, \delta) = \frac{h_0^0 \tau}{RT_C} - \frac{s_0^0}{R} - 1 + \ln \left( \frac{\tau_0 \delta}{\delta_0 \tau} \right) - \frac{\tau}{R} \int_{\tau_0}^{\tau} \frac{C_P^0}{\tau^2} d\tau + \frac{1}{R} \int_{\tau_0}^{\tau} \frac{C_P^0}{\tau} d\tau, \quad (\text{B.1})$$

where  $\delta_0 = \rho_0 / \rho_C$  and  $\tau_0 = T_C / T_0$  and represent the reduced density and the inverse of the reduced temperature, respectively at a pre-defined or prescribed reference state  $(T_0, \rho_0)$ . The values of  $h_0^0$  and  $s_0^0$  (at the reference temperature  $T_0$  and specific volume  $v_0$ ) are chosen based on recommendations of the Interna-

tional Union of Pure and Applied Chemistry (IUPAC) or according to conventions used in industry.

The pressure is determined from

$$\frac{Pv}{RT} = Z = 1 + \delta \left( \frac{\partial \psi^R}{\partial \delta} \right)_\tau, \quad (\text{B.2})$$

and the pressure derivatives are computed from

$$\left( \frac{\partial P}{\partial v} \right)_T = - \frac{RT}{v^2} \left[ 1 + 2\delta \left( \frac{\partial \psi^R}{\partial \delta} \right)_\tau + \delta^2 \left( \frac{\partial^2 \psi^R}{\partial \delta^2} \right)_\tau \right] \quad (\text{B.3})$$

$$\left( \frac{\partial P}{\partial T} \right)_v = \frac{R}{v} \left[ 1 + \delta \left( \frac{\partial \psi^R}{\partial \delta} \right)_\tau - \delta \tau \left( \frac{\partial^2 \psi^R}{\partial \tau \partial \delta} \right)_{\tau, \delta} \right] \quad (\text{B.4})$$

$$\left( \frac{\partial^2 P}{\partial v^2} \right)_T = \frac{RT}{v^3} \left[ 2 + 6\delta \left( \frac{\partial \psi^R}{\partial \delta} \right)_\tau + 6\delta^2 \left( \frac{\partial^2 \psi^R}{\partial \delta^2} \right)_\tau + \delta^3 \left( \frac{\partial^3 \psi^R}{\partial \delta^3} \right)_\tau \right] \quad (\text{B.5})$$

$$\begin{aligned} \left( \frac{\partial^2 P}{\partial T \partial v} \right)_{T,v} &= \frac{R}{v^2} \left[ \tau \delta \left\{ 2 \left( \frac{\partial^2 \psi^R}{\partial \tau \partial \delta} \right)_{\delta, \tau} + \delta \left( \frac{\partial^3 \psi^R}{\partial \tau \partial^2 \delta} \right)_{\delta, \tau} \right\} - \right. \\ &\quad \left. \frac{R}{v^2} \left[ \left\{ 1 + 2\delta \left( \frac{\partial \psi^R}{\partial \delta} \right)_\tau + \delta^2 \left( \frac{\partial^2 \psi^R}{\partial \delta^2} \right)_\tau \right\} \right] \right] \quad (\text{B.6}) \end{aligned}$$

$$\left( \frac{\partial^2 P}{\partial T^2} \right)_v = \frac{R}{Tv} \left[ \delta \tau^2 \left( \frac{\partial^3 \psi^R}{\partial \tau^2 \partial \delta} \right)_{\tau, \delta} \right]. \quad (\text{B.7})$$

The isochoric specific heat and its first-order derivative with respect to the temperature read

$$C_v = - R\tau^2 \left[ \left( \frac{\partial^2 \psi^0}{\partial \tau^2} \right)_\delta + \left( \frac{\partial^2 \psi^R}{\partial \tau^2} \right)_\delta \right] \quad (\text{B.8})$$

$$\begin{aligned} \left( \frac{\partial C_v}{\partial T} \right)_v &= \frac{R\tau}{T} \left[ 2\tau \left( \frac{\partial^2 \psi^0}{\partial \tau^2} \right)_\delta + 2\tau \left( \frac{\partial^2 \psi^R}{\partial \tau^2} \right)_\delta + \tau^2 \left( \frac{\partial^3 \psi^0}{\partial \tau^3} \right)_\delta \right] + \\ &\quad \frac{R\tau}{T} \left[ \tau^2 \left( \frac{\partial^3 \psi^R}{\partial \tau^3} \right)_\delta \right]. \quad (\text{B.9}) \end{aligned}$$

The fundamental derivative of gas dynamics can then be computed from

$$\begin{aligned} \Gamma &= \frac{v^3}{2c^2} \left\{ \left( \frac{\partial^2 P}{\partial v^2} \right)_T - 3 \frac{T}{C_v} \left( \frac{\partial P}{\partial T} \right)_v \left( \frac{\partial^2 P}{\partial v \partial T} \right) + \left[ \frac{T}{C_v} \left( \frac{\partial P}{\partial T} \right)_v \right]^2 \right. \\ &\quad \left. \left[ 3 \left( \frac{\partial^2 P}{\partial T^2} \right)_v + \frac{1}{T} \left( \frac{\partial P}{\partial T} \right)_v \left( 1 - \frac{T}{C_v} \left( \frac{\partial C_v}{\partial T} \right)_v \right) \right] \right\}. \quad (\text{B.10}) \end{aligned}$$

*"I can only speak to myself."*

President George W. Bush, Washington, D.C., April 28, 2005



## Equations valid in the critical region – The revised and extended linear model

According to theory, the thermodynamic behavior of fluids near the critical point can be described using a scaled fundamental equation with universal critical exponents (refer to Table C.1) and system-dependent constants [180]. The scaled fundamental equation adopted herein uses the functional form proposed by Balfour et al. [10] (refer to Chap. 4 for the nomenclature). The functional form is expressed in terms of the intensive (field) variables pressure  $P$ , temperature  $T$  and chemical potential  $\mu$  and reads:

$$\tilde{P} = 1 + \sum_{i=1}^3 \tilde{P}_i (\Delta\tilde{T})^i + \Delta\tilde{\mu} (1 + \tilde{P}_{11}\Delta\tilde{T}) + \Delta\tilde{P}, \quad (\text{C.1})$$

with

$$\Delta\tilde{T} = \tilde{T} + 1 \quad (\text{C.2})$$

and

$$\Delta\tilde{\mu} = \tilde{\mu} - \tilde{\mu}_C - \sum_{i=1}^4 \tilde{\mu}_i (\Delta\tilde{T})^i, \quad (\text{C.3})$$

Table C.1: Values of universal constants in the revised and extended linear model (see also Ref [125]).

$\bar{\beta}$	=	0.325	$\bar{\delta}$	=	4.82
$\bar{b}^2$	=	1.3757	$\bar{\Delta}_1$	=	0.50
$p_{00}$	=	0.586535	$p_{20}$	=	-1.026243
$p_{40}$	=	0.612903	$p_{01}$	=	0.10325
$p_{21}$	=	0.16032	$p_{41}$	=	-0.16986
$s_{00}$	=	1.109430	$s_{20}$	=	-1.981395
$s_{01}$	=	0.24692	$s_{21}$	=	-0.84341

whereby

$$\tilde{T} \equiv -\frac{T_C}{T}, \quad \tilde{\mu} \equiv \frac{\mu}{T} \frac{\rho_C T_C}{P_C}, \quad \tilde{P} \equiv \frac{P}{T} \frac{T_C}{P_C}. \quad (\text{C.4})$$

In Eqns. (C.1)-(C.4),  $\tilde{P}_i$  and  $\tilde{P}_{11}$  are the pressure background constants and these are specific to a fluid,  $\tilde{\mu}_i$  are referred to as the thermal background constants and are also substance specific,  $\rho$  denotes the density, and subscript “C” represents the critical-point value of a property. The critical-point singularities are accounted for by the  $\Delta\tilde{P}$ -term in Eq. (C.1). This singular part of the scaled fundamental equation is expressed as a function of so-called parametric variables  $r$  and  $\theta$ ; the variable denoted by  $r$  gives the distance of a thermodynamic state with respect to the critical point and the variable denoted by  $\theta$  gives the location of the thermodynamic state on a line of constant- $r$ , such that  $\theta = -1$  is the dew-line and  $\theta = +1$  is the bubble-line ( $-1 \leq \theta \leq +1$ ). From the fundamental equation, i.e., Eq. (C.1), all other thermodynamic properties can be determined using the relationships (C.5)–(C.12).

$$\frac{\rho}{\rho_C} = \left[ 1 + \tilde{P}_{11} \Delta \tilde{T} + \Delta \tilde{P}_{\Delta \tilde{\mu}} \right] \quad (\text{C.5})$$

$$\frac{\rho_C}{P_C} \left( \frac{\partial P}{\partial \rho} \right)_T = - \left[ \frac{\tilde{\rho}}{\tilde{T} \Delta \tilde{P}_{\Delta \tilde{\mu}, \Delta \tilde{\mu}}} \right] \quad (\text{C.6})$$

$$\frac{T_C}{P_C} \left( \frac{\partial P}{\partial T} \right)_\rho = - \tilde{T} \left[ \sum_{i=1}^3 i \tilde{P}_i (\Delta \tilde{T})^{i-1} + \tilde{P}_{11} \Delta \tilde{\mu} + \Delta \tilde{P}_{\Delta \tilde{T}} - \tilde{\rho} \frac{(\tilde{P}_{11} + \Delta \tilde{P}_{\Delta \tilde{\mu}, \Delta \tilde{T}})}{\Delta \tilde{P}_{\Delta \tilde{\mu}, \Delta \tilde{\mu}}} - \frac{\tilde{P}}{\tilde{T}} \right] \quad (\text{C.7})$$

$$\frac{\rho_C^2}{P_C} \left( \frac{\partial^2 P}{\partial \rho^2} \right)_T = - \left[ \frac{\Delta \tilde{P}_{\Delta \tilde{\mu}, \Delta \tilde{\mu}}^2 - \tilde{\rho} \Delta \tilde{P}_{\Delta \tilde{\mu}, \Delta \tilde{\mu}, \Delta \tilde{\mu}}}{\tilde{T} \Delta \tilde{P}_{\Delta \tilde{\mu}, \Delta \tilde{\mu}}^3} \right] \quad (\text{C.8})$$

$$\begin{aligned} \frac{T_C^2}{P_C} \left( \frac{\partial^2 P}{\partial T^2} \right)_\rho &= - \tilde{T}^3 \left[ \sum_{i=2}^3 i(i-1) \tilde{P}_i (\Delta \tilde{T})^{i-2} - \frac{(\tilde{P}_{11} + \Delta \tilde{P}_{\Delta \tilde{\mu}, \Delta \tilde{T}})^2}{\Delta \tilde{P}_{\Delta \tilde{\mu}, \Delta \tilde{\mu}}} - \frac{\tilde{\rho} \Delta \tilde{P}_{\Delta \tilde{\mu}, \Delta \tilde{T}, \Delta \tilde{T}}}{\Delta \tilde{P}_{\Delta \tilde{\mu}, \Delta \tilde{\mu}}} \right] \\ &\quad - \tilde{T}^3 \Delta \tilde{P}_{\Delta \tilde{T}, \Delta \tilde{T}} - \frac{\tilde{T}^3 \tilde{\rho} (\tilde{P}_{11} + \Delta \tilde{P}_{\Delta \tilde{\mu}, \Delta \tilde{T}})}{\Delta \tilde{P}_{\Delta \tilde{\mu}, \Delta \tilde{\mu}}^2} \times \\ &\quad \left\{ \Delta \tilde{P}_{\Delta \tilde{\mu}, \Delta \tilde{\mu}, \Delta \tilde{T}} + \Delta \tilde{P}_{\Delta \tilde{\mu}, \Delta \tilde{T}, \Delta \tilde{\mu}} - \Delta \tilde{P}_{\Delta \tilde{\mu}, \Delta \tilde{\mu}, \Delta \tilde{\mu}} \frac{(\tilde{P}_{11} + \Delta \tilde{P}_{\Delta \tilde{\mu}, \Delta \tilde{T}})}{\Delta \tilde{P}_{\Delta \tilde{\mu}, \Delta \tilde{\mu}}} \right\} \quad (\text{C.9}) \end{aligned}$$

$$\frac{\rho_C T_C}{P_C} \left( \frac{\partial^2 P}{\partial \rho \partial T} \right)_{\rho, T} = \frac{\tilde{\rho}}{\Delta \tilde{P}_{\Delta \tilde{\mu}, \Delta \tilde{\mu}}} \left[ 1 + \frac{\tilde{T}}{\Delta \tilde{P}_{\Delta \tilde{\mu}, \Delta \tilde{\mu}}} \left( \Delta \tilde{P}_{\Delta \tilde{\mu}, \Delta \tilde{T}, \Delta \tilde{\mu}} - \Delta \tilde{P}_{\Delta \tilde{\mu}, \Delta \tilde{\mu}, \Delta \tilde{\mu}} \frac{(\tilde{P}_{11} + \Delta \tilde{P}_{\Delta \tilde{\mu}, \Delta \tilde{T}})}{\Delta \tilde{P}_{\Delta \tilde{\mu}, \Delta \tilde{\mu}}} \right) \right] \quad (\text{C.10})$$

$$\begin{aligned} \frac{\rho_C T_C}{P_C} C_v &= \frac{\tilde{T}^2}{\tilde{\rho}} \left[ \sum_{i=2}^3 i(i-1) \tilde{P}_i (\Delta \tilde{T})^{i-2} + \Delta \tilde{P}_{\Delta \tilde{T} \Delta \tilde{T}} - \frac{(\tilde{P}_{11} + \Delta \tilde{P}_{\Delta \tilde{\mu}, \Delta \tilde{T}})^2}{\Delta \tilde{P}_{\Delta \tilde{\mu}, \Delta \tilde{\mu}}} \right] \\ &\quad - \tilde{T}^2 \sum_{i=2}^4 i(i-1) \tilde{\mu}_i (\Delta \tilde{T})^{i-2} \end{aligned} \quad (\text{C.11})$$

$$\begin{aligned} \frac{\rho_C T_C^2}{P_C} \left( \frac{\partial C_v}{\partial T} \right)_{\rho} &= \frac{\tilde{T}^4}{\tilde{\rho}} \left[ \sum_{i=3}^3 i(i-1)(i-2) \tilde{P}_i (\Delta \tilde{T})^{i-3} + \Delta \tilde{P}_{\Delta \tilde{T}, \Delta \tilde{T}, \Delta \tilde{T}} - \frac{(\tilde{P}_{11} + \Delta \tilde{P}_{\Delta \tilde{\mu}, \Delta \tilde{T}})}{\Delta \tilde{P}_{\Delta \tilde{\mu}, \Delta \tilde{\mu}}} \times \right. \\ &\quad \left. \left\{ 2\Delta \tilde{P}_{\Delta \tilde{\mu}, \Delta \tilde{T}, \Delta \tilde{T}} - \Delta \tilde{P}_{\Delta \tilde{\mu}, \Delta \tilde{\mu}, \Delta \tilde{T}} \frac{(\tilde{P}_{11} + \Delta \tilde{P}_{\Delta \tilde{\mu}, \Delta \tilde{T}})}{\Delta \tilde{P}_{\Delta \tilde{\mu}, \Delta \tilde{\mu}}} \right\} \right. \\ &\quad \left. + \frac{(\tilde{P}_{11} + \Delta \tilde{P}_{\Delta \tilde{\mu}, \Delta \tilde{T}})^2}{\Delta \tilde{P}_{\Delta \tilde{\mu}, \Delta \tilde{\mu}}^2} \times \left\{ 2\Delta \tilde{P}_{\Delta \tilde{\mu}, \Delta \tilde{T}, \Delta \tilde{\mu}} - \Delta \tilde{P}_{\Delta \tilde{\mu}, \Delta \tilde{\mu}, \Delta \tilde{\mu}} \frac{(\tilde{P}_{11} + \Delta \tilde{P}_{\Delta \tilde{\mu}, \Delta \tilde{T}})}{\Delta \tilde{P}_{\Delta \tilde{\mu}, \Delta \tilde{\mu}}} \right\} \right. \\ &\quad \left. - \tilde{\rho} \sum_{i=3}^4 i(i-1)(i-2) \tilde{\mu}_i (\Delta \tilde{T})^{i-3} - \Delta \tilde{P}_{\Delta \tilde{T} \Delta \tilde{T}, \Delta \tilde{\mu}} \frac{(\tilde{P}_{11} + \Delta \tilde{P}_{\Delta \tilde{\mu}, \Delta \tilde{T}})}{\Delta \tilde{P}_{\Delta \tilde{\mu}, \Delta \tilde{\mu}}} \right] + \frac{2\tilde{C}_v \tilde{T}}{\tilde{\rho}}. \end{aligned} \quad (\text{C.12})$$

In Eq. (C.5),  $\tilde{\rho} \equiv \rho/\rho_C$ , and in Eq. (C.12),  $\tilde{C}_v/\tilde{\rho} = C_v(\rho_C T_C)/P_C$ .

The parametric equations for the singular terms (these are  $\Delta\tilde{P}$ ,  $\Delta\tilde{T}$ ,  $\Delta\tilde{\mu}$ , and the derivatives of  $\Delta\tilde{P}$  with respect to  $\Delta\tilde{T}$  and  $\Delta\tilde{\mu}$ ) are presented in Table C.2 and the auxiliary functions for the parametric equations are given in Table C.3.

The equations listed in Tables C.1–C.3 together with Eqns. (C.1)–(C.12) can be used to determine the fundamental derivative of gas dynamics, appropriately transformed as:

$$\Gamma = 1 + \frac{\rho}{c} \left( \frac{\partial c}{\partial \rho} \right)_s \Leftrightarrow \Gamma = \frac{1}{2c^2 \rho^3} (\bar{\Gamma}_1 + \bar{\Gamma}_2 + \bar{\Gamma}_3), \quad (\text{C.13})$$

where

$$\bar{\Gamma}_1 = \rho^4 \left( \frac{\partial^2 P}{\partial \rho^2} \right)_T + 2\rho^3 \left( \frac{\partial P}{\partial \rho} \right)_T, \quad (\text{C.14a})$$

$$\bar{\Gamma}_2 = 3 \frac{T\rho^2}{C_v} \left( \frac{\partial P}{\partial T} \right)_\rho \left( \frac{\partial^2 P}{\partial \rho \partial T} \right)_{T,\rho}, \quad (\text{C.14b})$$

$$\bar{\Gamma}_3 = \left[ \frac{T}{C_v} \left( \frac{\partial P}{\partial T} \right)_\rho \right]^2 \times \left[ 3 \left( \frac{\partial^2 P}{\partial T^2} \right)_\rho + \frac{1}{T} \left( \frac{\partial P}{\partial T} \right)_\rho \left( 1 - \frac{T}{C_v} \left( \frac{\partial C_v}{\partial T} \right)_\rho \right) \right], \quad (\text{C.14c})$$

and the thermodynamic speed of sound,  $c$ , is computed from

$$c^2 = \left( \frac{\partial P}{\partial \rho} \right)_T + \frac{T}{\rho^2 C_v} \left( \frac{\partial P}{\partial T} \right)_\rho^2. \quad (\text{C.14d})$$

Other relevant caloric properties are the specific internal energy ( $e$ ), the specific enthalpy ( $h$ ) and the specific entropy ( $s$ ):

$$\frac{\rho_C}{P_C} e = \frac{\tilde{e}}{\tilde{\rho}} = \frac{1}{\tilde{\rho}} \left[ \sum_{i=1}^3 i \tilde{P}_i \Delta \tilde{T}^{i-1} - \tilde{\rho} \sum_{i=1}^4 i \tilde{\mu}_i \Delta \tilde{T}^{i-1} + \tilde{P}_{11} \Delta \tilde{\mu} + \Delta \tilde{P}_{\Delta \tilde{T}} \right], \quad (\text{C.15})$$

$$\frac{\rho_C}{P_C} h = \left[ \frac{\tilde{e}}{\tilde{\rho}} - \frac{\tilde{P}}{\tilde{T} \tilde{\rho}} \right], \quad (\text{C.16})$$

$$\frac{\rho_C T_C}{P_C} s = \left[ \frac{\tilde{P}}{\tilde{\rho}} - \tilde{\mu} - \tilde{T} \frac{\tilde{e}}{\tilde{\rho}} \right]. \quad (\text{C.17})$$

Table C.2: Parametric equations for the singular terms. The scaling-field parameters  $\alpha$ ,  $k_0$ ,  $k_1$ , and  $c$  are specific to a substance.

$$\begin{aligned}
 \Delta \tilde{\mu} &= \alpha r^{\bar{\beta}\bar{\delta}} (1 - \theta^2) \\
 \Delta \tilde{T} &= r (1 - \bar{b}^2 \theta^2) - c \Delta \tilde{\mu} \\
 \Delta \tilde{P} &= \alpha r^{\bar{\beta}(\bar{\delta}+1)} \left[ k_0 \hat{p}_0(\theta) + r^{\bar{\Delta}_1} k_1 \hat{p}_1(\theta) \right] \\
 \Delta \tilde{P}_{\Delta \tilde{T}} &= \left( \frac{\partial \Delta \tilde{P}}{\partial \Delta \tilde{T}} \right)_{\Delta \tilde{\mu}} = \alpha r^{\bar{\beta}(\bar{\delta}+1)-1} \left[ k_0 \hat{s}_0(\theta) + r^{\bar{\Delta}_1} k_1 \hat{s}_1(\theta) \right] \\
 \Delta \tilde{P}_{\Delta \tilde{\mu}} &= \left( \frac{\partial \Delta \tilde{P}}{\partial \Delta \tilde{\mu}} \right)_{\Delta \tilde{T}} = r^{\bar{\beta}} \left[ k_0 + r^{\bar{\Delta}_1} k_1 \right] \theta + c \left( \frac{\partial \Delta \tilde{P}}{\partial \Delta \tilde{T}} \right)_{\Delta \tilde{\mu}} \\
 \Delta \tilde{P}_{\Delta \tilde{T}, \Delta \tilde{T}} &= \left( \frac{\partial^2 \Delta \tilde{P}}{\partial \Delta \tilde{T}^2} \right)_{\Delta \tilde{\mu}} = \alpha r^{\bar{\beta}(\bar{\delta}+1)-2} \left[ k_0 \hat{w}_0(\theta) + r^{\bar{\Delta}_1} k_1 \hat{w}_1(\theta) \right] \\
 \Delta \tilde{P}_{\Delta \tilde{\mu}, \Delta \tilde{\mu}} &= \left( \frac{\partial^2 \Delta \tilde{P}}{\partial \Delta \tilde{\mu}^2} \right)_{\Delta \tilde{T}} = \alpha^{-1} r^{\bar{\beta}(1-\bar{\delta})} \left[ k_0 \hat{u}_0(\theta) + r^{\bar{\Delta}_1} k_1 \hat{u}_1(\theta) \right] + \\
 &\quad 2c r^{\bar{\beta}-1} \left[ k_0 \hat{v}_0(\theta) + r^{\bar{\Delta}_1} k_1 \hat{v}_1(\theta) \right] + c^2 \left( \frac{\partial^2 \Delta \tilde{P}}{\partial \Delta \tilde{T}^2} \right)_{\Delta \tilde{\mu}} \\
 \Delta \tilde{P}_{\Delta \tilde{\mu}, \Delta \tilde{T}^\dagger} &= \left( \frac{\partial^2 \Delta \tilde{P}}{\partial \Delta \tilde{T} \partial \Delta \tilde{\mu}} \right)_{\Delta \tilde{T}, \Delta \tilde{\mu}} = r^{\bar{\beta}-1} \left[ k_0 \hat{v}_0(\theta) + r^{\bar{\Delta}_1} k_1 \hat{v}_1(\theta) \right] + c \left( \frac{\partial^2 \Delta \tilde{P}}{\partial \Delta \tilde{T}^2} \right)_{\Delta \tilde{\mu}}
 \end{aligned}$$

Continued on the next page...

Table C.2 – Continued

$\Delta\tilde{P}_{\Delta\tilde{T},\Delta\tilde{T},\Delta\tilde{T}}$	$= \left( \frac{\partial^3 \Delta\tilde{P}}{\partial \Delta\tilde{T}^3} \right)_{\Delta\tilde{\mu}}$	$= \alpha r^{\bar{\beta}(\bar{\delta}+1)-3} \left[ k_0 \hat{x}_0(\theta) + r^{\bar{\Delta}_1} k_1 \hat{x}_1(\theta) \right]$
$\Delta\tilde{P}_{\Delta\tilde{\mu},\Delta\tilde{T},\Delta\tilde{T}^*}$	$= \left( \frac{\partial^3 \Delta\tilde{P}}{\partial \Delta\tilde{T}^2 \partial \Delta\tilde{\mu}} \right)_{\Delta\tilde{T},\Delta\tilde{\mu},\Delta\tilde{\mu}}$	$= r^{\bar{\beta}-2} \left[ k_0 \hat{y}_0(\theta) + r^{\bar{\Delta}_1} k_1 \hat{y}_1(\theta) \right] + \mathbf{c} \left( \frac{\partial^3 \Delta\tilde{P}}{\partial \Delta\tilde{T}^3} \right)_{\Delta\tilde{\mu}}$
$\Delta\tilde{P}_{\Delta\tilde{\mu},\Delta\tilde{T},\Delta\tilde{\mu}^\ddagger}$	$= \left( \frac{\partial^3 \Delta\tilde{P}}{\partial \Delta\tilde{\mu} \partial \Delta\tilde{T} \partial \Delta\tilde{\mu}} \right)_{\Delta\tilde{T},\Delta\tilde{\mu},\Delta\tilde{T}}$	$= \alpha^{-1} r^{\bar{\beta}(1-\bar{\delta})-1} \left[ k_0 \hat{z}_0(\theta) + r^{\bar{\Delta}_1} k_1 \hat{z}_1(\theta) \right] +$ $2\mathbf{c} \left( \frac{\partial^3 \Delta\tilde{P}}{\partial \Delta\tilde{T}^2 \partial \Delta\tilde{\mu}} \right)_{\Delta\tilde{T},\Delta\tilde{\mu},\Delta\tilde{\mu}} - \mathbf{c}^2 \left( \frac{\partial^3 \Delta\tilde{P}}{\partial \Delta\tilde{T}^3} \right)_{\Delta\tilde{\mu}}$
$\Delta\tilde{P}_{\Delta\tilde{\mu},\Delta\tilde{\mu},\Delta\tilde{\mu}}$	$= \left( \frac{\partial^3 \Delta\tilde{P}}{\partial \Delta\tilde{\mu}^3} \right)_{\Delta\tilde{T}}$	$= \alpha^{-2} r^{\bar{\beta}(1-2\bar{\delta})} \left[ k_0 \hat{m}_0(\theta) + r^{\bar{\Delta}_1} k_1 \hat{m}_1(\theta) \right] + \mathbf{c}^3 \left( \frac{\partial^3 \Delta\tilde{P}}{\partial \Delta\tilde{T}^3} \right)_{\Delta\tilde{\mu}} -$ $3\mathbf{c}^2 \left( \frac{\partial^3 \Delta\tilde{P}}{\partial \Delta\tilde{T}^2 \partial \Delta\tilde{\mu}} \right)_{\Delta\tilde{T},\Delta\tilde{\mu},\Delta\tilde{\mu}} + 3\mathbf{c} \left( \frac{\partial^3 \Delta\tilde{P}}{\partial \Delta\tilde{\mu} \partial \Delta\tilde{T} \partial \Delta\tilde{\mu}} \right)_{\Delta\tilde{T},\Delta\tilde{\mu},\Delta\tilde{T}}$
†	$\Delta\tilde{P}_{\Delta\tilde{\mu},\Delta\tilde{T}}$	$= \Delta\tilde{P}_{\Delta\tilde{T},\Delta\tilde{\mu}}$
*	$\Delta\tilde{P}_{\Delta\tilde{T},\Delta\tilde{\mu},\Delta\tilde{T}}$	$= \Delta\tilde{P}_{\Delta\tilde{\mu},\Delta\tilde{T},\Delta\tilde{T}} = \Delta\tilde{P}_{\Delta\tilde{T},\Delta\tilde{T},\Delta\tilde{\mu}}$
‡	$\Delta\tilde{P}_{\Delta\tilde{T},\Delta\tilde{\mu},\Delta\tilde{\mu}}$	$= \Delta\tilde{P}_{\Delta\tilde{\mu},\Delta\tilde{T},\Delta\tilde{\mu}} = \Delta\tilde{P}_{\Delta\tilde{\mu},\Delta\tilde{\mu},\Delta\tilde{T}}$

Table C.3: Auxiliary functions used in the parametric equations listed in Table C.2. Also refer to Table C.1 listing the required universal constants.

---


$$\begin{aligned} \hat{p}_i(\theta) &= p_{0i} + p_{2i}\theta^2 + p_{4i}\theta^4 \quad (i = 0, 1) \\ \hat{s}_i(\theta) &= s_{0i} + s_{2i}\theta^2 \quad (i = 0, 1) \\ \hat{s}'_i(\theta) &= 2s_{2i}\theta \quad (i = 0, 1) \\ \hat{s}''_i(\theta) &= 2s_{2i} \quad (i = 0, 1) \\ \hat{q}(\theta) &= 1 + [\bar{b}^2(2\bar{\beta}\bar{\delta} - 1) - 3]\theta^2 - \bar{b}^2(2\bar{\beta}\bar{\delta} - 3)\theta^4 \\ \hat{q}'(\theta) &= 2[\bar{b}^2(2\bar{\beta}\bar{\delta} - 1) - 3]\theta - 4\bar{b}^2(2\bar{\beta}\bar{\delta} - 3)\theta^3 \\ \hat{u}_0(\theta) &= [1 - \bar{b}^2(1 - 2\bar{\beta})\theta^2] / \hat{q}(\theta) \\ \hat{u}'_0(\theta) &= [-2\bar{b}^2(1 - 2\bar{\beta})\theta - \hat{u}_0(\theta)\hat{q}'(\theta)] / \hat{q}(\theta) \\ \hat{u}_1(\theta) &= [1 - \bar{b}^2(1 - 2\bar{\beta} - 2\bar{\Delta}_1)\theta^2] / \hat{q}(\theta) \\ \hat{u}'_1(\theta) &= [-2\bar{b}^2(1 - 2\bar{\beta} - 2\bar{\Delta}_1)\theta - \hat{u}_1(\theta)\hat{q}'(\theta)] / \hat{q}(\theta) \\ \hat{v}_0(\theta) &= [\bar{\beta}(1 - 3\theta^2)\theta - \bar{\beta}\bar{\delta}(1 - \theta^2)\theta] / \hat{q}(\theta) \end{aligned}$$

Continued on the next page...

Table C.3 – Continued

$$\begin{aligned}
 \hat{v}'_0(\theta) &= [\bar{\beta}(1-9\theta^2) - \bar{\beta}\bar{\delta}(1-3\theta^2) - \hat{v}_0(\theta)\hat{q}'(\theta)]/\hat{q}(\theta) \\
 \hat{v}_1(\theta) &= [(\bar{\beta} + \bar{\Delta}_1)(1-3\theta^2)\theta - \bar{\beta}\bar{\delta}(1-\theta^2)\theta]/\hat{q}(\theta) \\
 \hat{v}'_1(\theta) &= [(\bar{\beta} + \bar{\Delta}_1)(1-9\theta^2) - \bar{\beta}\bar{\delta}(1-3\theta^2) - \hat{v}_1(\theta)\hat{q}'(\theta)]/\hat{q}(\theta) \\
 \hat{w}_0(\theta) &= [(\bar{\beta}\bar{\delta} + \bar{\beta} - 1)(1-3\theta^2)\hat{s}_0(\theta) - \bar{\beta}\bar{\delta}(1-\theta^2)\theta\hat{s}'_0(\theta)]/\hat{q}(\theta) \\
 \hat{w}'_0(\theta) &= [-6(\bar{\beta}\bar{\delta} + \bar{\beta} - 1)\theta\hat{s}_0(\theta) + (\bar{\beta} - 1)(1-3\theta^2)s'_0(\theta) - \bar{\beta}\bar{\delta}(1-\theta^2)\theta\hat{s}''_0(\theta) \\
 &\quad - \hat{w}_0(\theta)\hat{q}'(\theta)]/\hat{q}(\theta) \\
 \hat{w}_1(\theta) &= [(\bar{\beta}\bar{\delta} + \bar{\beta} - 1 + \bar{\Delta}_1)(1-3\theta^2)\hat{s}_1(\theta) - \bar{\beta}\bar{\delta}(1-\theta^2)\theta\hat{s}'_1(\theta)]/\hat{q}(\theta) \\
 \hat{w}'_1(\theta) &= [-6(\bar{\beta}\bar{\delta} + \bar{\beta} - 1 + \bar{\Delta}_1)\theta\hat{s}_1(\theta) + (\bar{\beta} - 1 + \bar{\Delta}_1)(1-3\theta^2)\hat{s}'_1(\theta) \\
 &\quad - \bar{\beta}\bar{\delta}(1-\theta^2)\theta\hat{s}''_1(\theta) - \hat{w}_1(\theta)\hat{q}'(\theta)]/\hat{q}(\theta) \\
 \hat{x}_0(\theta) &= [(\bar{\beta}\bar{\delta} + \bar{\beta} - 2)(1-3\theta^2)\hat{w}_0(\theta) - \bar{\beta}\bar{\delta}(1-\theta^2)\theta\hat{w}'_0(\theta)]/\hat{q}(\theta) \\
 \hat{x}_1(\theta) &= [(\bar{\beta}\bar{\delta} + \bar{\beta} - 2 + \bar{\Delta}_1)(1-3\theta^2)\hat{w}_1(\theta) - \bar{\beta}\bar{\delta}(1-\theta^2)\theta\hat{w}'_1(\theta)]/\hat{q}(\theta) \\
 \hat{y}_0(\theta) &= [(\bar{\beta} - 1)(1-3\theta^2)\hat{v}_0(\theta) - \bar{\beta}\bar{\delta}(1-\theta^2)\theta\hat{v}'_0(\theta)]/\hat{q}(\theta)
 \end{aligned}$$

Continued on the next page...

Table C.3 – Continued

$$\hat{y}_1(\theta) = [(\bar{\beta} - 1 + \bar{\Delta}_1)(1 - 3\theta^2)\hat{v}_1(\theta) - \bar{\beta}\bar{\delta}(1 - \theta^2)\theta\hat{v}'_1(\theta)] / \hat{q}(\theta)$$

$$\hat{z}_0(\theta) = [(\bar{\beta} - 1)2\bar{b}^2\theta\hat{v}_0(\theta) + (1 - \bar{b}^2\theta^2)\hat{v}'_0(\theta)] / \hat{q}(\theta)$$

$$\hat{z}_1(\theta) = [(\bar{\beta} - 1 + \bar{\Delta}_1)2\bar{b}^2\theta\hat{v}_1(\theta) + (1 - \bar{b}^2\theta^2)\hat{v}'_1(\theta)] / \hat{q}(\theta)$$

$$\hat{m}_0(\theta) = [(\bar{\beta} - \bar{\beta}\bar{\delta})2\bar{b}^2\theta\hat{u}_0(\theta) + (1 - \bar{b}^2\theta^2)\hat{u}'_0(\theta)] / \hat{q}(\theta)$$

$$\hat{m}_1(\theta) = [(\bar{\beta} - \bar{\beta}\bar{\delta} + \bar{\Delta}_1)2\bar{b}^2\theta\hat{u}_1(\theta) + (1 - \bar{b}^2\theta^2)\hat{u}'_1(\theta)] / \hat{q}(\theta)$$


---

*“I’m the decider, and I decide what is best. And what’s best is for Don Rumsfeld to remain as the Secretary of Defense”*

President George W. Bush, Washington, D.C., April 18, 2006

# D

## Thermodynamic properties in the VLE-region of a single-component fluid

The following equations are derived under the assumption that the vapor- and the liquid phase of the single-component fluid form a homogeneous mixture and that the two phases are always in thermodynamic equilibrium. This implies that there is mass and heat transfer between the phases and that the timescale of an arbitrary process is slower than that of evaporation or condensation. Conversely, if the timescale of an arbitrary process is faster than that of evaporation or condensation, then there is insufficient time for thermodynamic equilibrium to establish and as a result, the vapor quality cannot change (fast enough). The speed of sound in the vapor-liquid equilibrium (VLE) region of a single component fluid can be calculated from (refer to Chap. 4 for the nomenclature)

$$c^{\varpi, T^{\text{sat}}} = \sqrt{\frac{-\left(v^{\varpi, T^{\text{sat}}}\right)^2}{\varpi \left[ \left(\frac{dv^{\text{V}}}{dP}\right) - \left(\frac{dv^{\text{L}}}{dP}\right) \right] + (v^{\text{V}} - v^{\text{L}}) \left(\frac{\partial \varpi}{\partial P}\right)_s^{\varpi, T^{\text{sat}}} + \left(\frac{dv^{\text{L}}}{dP}\right)}, \quad (\text{D.1})$$

where  $\varpi$  is the vapor quality defined as the ratio of the vapor mass with respect to the total mass of vapor and liquid (here and for all the following equations which contain the variable  $\varpi$ ,  $0 < \varpi < 1$ ; the saturated state, i.e., where  $\varpi$  is either 0 or 1, is the limiting situation of a thermodynamic state in the *single-phase*

region<sup>1</sup>),  $T^{\text{sat}}$  denotes the saturation temperature,  $P$  represents the pressure,  $v$  is the specific volume in the VLE-region (it is thus a function of both  $\varpi$  and  $T^{\text{sat}}$ ), and

$$\left(\frac{\partial \varpi}{\partial P}\right)_s^{\varpi, T^{\text{sat}}} = \left(\frac{\varpi - 1}{s^{\text{V}} - s^{\text{L}}}\right) \left(\frac{ds^{\text{L}}}{dP}\right) - \left(\frac{\varpi}{s^{\text{V}} - s^{\text{L}}}\right) \left(\frac{ds^{\text{V}}}{dP}\right), \quad (\text{D.2})$$

$$\left(\frac{dv^{\text{V,L}}}{dP}\right) = -\frac{\left(\frac{\partial P}{\partial T}\right)_{v=v^{\text{V,L}}, T^{\text{sat}}}}{\left(\frac{\partial P}{\partial v}\right)_T^{v=v^{\text{V,L}}, T^{\text{sat}}}} \frac{1}{\left(\frac{dP}{dT}\right)^{\text{sat}}} + \frac{1}{\left(\frac{\partial P}{\partial v}\right)_T^{v=v^{\text{V,L}}, T^{\text{sat}}}}, \quad (\text{D.3})$$

and

$$\left(\frac{ds^{\text{V,L}}}{dP}\right) = \frac{C_P^{v=v^{\text{V,L}}}}{T^{\text{sat}}} \frac{1}{\left(\frac{dP}{dT}\right)^{\text{sat}}} + \frac{\left(\frac{\partial P}{\partial T}\right)_{v=v^{\text{V,L}}, T^{\text{sat}}}}{\left(\frac{\partial P}{\partial v}\right)_T^{v=v^{\text{V,L}}, T^{\text{sat}}}}. \quad (\text{D.4})$$

In Eqns. (D.2)–(D.4),  $s$  represents the entropy. Furthermore, superscripts “V” and “L” denote the vapor and liquid phase, respectively. Note that thermodynamic functions with a  $\partial$ -symbol, like  $(\partial P/\partial T)_{v=v^{\text{V,L}}, T^{\text{sat}}}$ , represent functions that depend on two independent variables, e.g., either  $(v = v^{\text{V}}, T^{\text{sat}})$  or  $(v = v^{\text{L}}, T^{\text{sat}})$ , in the limit that the saturated state is approached from the single-phase region. Similarly,  $C_P^{v=v^{\text{V,L}}}$  is the isobaric heat capacity of either the vapor or the liquid phase in the limit that the saturated state is approached from the single-phase region and consequently  $C_P^{v=v^{\text{V,L}}}$  is a function of two independent thermodynamic properties.<sup>2</sup> However, thermodynamic functions with a  $d$ -symbol, e.g.,  $(dv^{\text{V,L}}/dP)$ , represent functions that are dependent on only one thermodynamic property, i.e., either the saturated pressure or temperature, and they are evaluated along a line representing saturation, for example  $(dv^{\text{V}}/dP)$  is computed along the dew-line in a  $P$ - $v$ -diagram and  $(ds^{\text{L}}/dP)$  is calculated along the bubble-line in a  $P$ - $s$ -diagram. The function  $(dP/dT)^{\text{sat}}$  is the slope of the saturation line in the  $P$ - $T$ -plane and it is calculated with the Clapeyron equation

$$\left(\frac{dP}{dT}\right)^{\text{sat}} = \frac{s^{\text{V}} - s^{\text{L}}}{v^{\text{V}} - v^{\text{L}}}. \quad (\text{D.5})$$

In the VLE-region the fundamental derivative of gas dynamics is computed from (see next page)

<sup>1</sup>Remark that certain thermodynamic properties like the speed of sound and the isochoric heat capacity display discontinuities at phase boundaries, see for example Refs. [110, 163].

<sup>2</sup>The isobaric heat capacity in the VLE-region is meaningless.

$$\Gamma^{\varpi, T^{\text{sat}}} = \frac{(c^{\varpi, T^{\text{sat}}})^4}{(v^{\varpi, T^{\text{sat}}})^3} \left[ \left( \frac{dv^{\text{V}}}{dP} \right) - \left( \frac{dv^{\text{L}}}{dP} \right) \right] \left( \frac{\partial \varpi}{\partial P} \right)_s^{\varpi, T^{\text{sat}}} + \frac{(c^{\varpi, T^{\text{sat}}})^4}{2(v^{\varpi, T^{\text{sat}}})^3} \times \left\{ \varpi \left[ \left( \frac{d^2 v^{\text{V}}}{dP^2} \right) - \left( \frac{d^2 v^{\text{L}}}{dP^2} \right) \right] + (v^{\text{V}} - v^{\text{L}}) \left( \frac{\partial^2 \varpi}{\partial P^2} \right)_s^{\varpi, T^{\text{sat}}} + \left( \frac{d^2 v^{\text{L}}}{dP^2} \right) \right\}, \quad (\text{D.6})$$

with

$$\left( \frac{\partial^2 \varpi}{\partial P^2} \right)_s^{\varpi, T^{\text{sat}}} = \frac{2 \left( \frac{\partial \varpi}{\partial P} \right)_s^{\varpi, T^{\text{sat}}} \left[ \left( \frac{ds^{\text{L}}}{dP} \right) - \left( \frac{ds^{\text{V}}}{dP} \right) \right] + (\varpi - 1) \left( \frac{d^2 s^{\text{L}}}{dP^2} \right) - \varpi \left( \frac{d^2 s^{\text{V}}}{dP^2} \right)}{s^{\text{V}} - s^{\text{L}}}, \quad (\text{D.7})$$

$$\left( \frac{d^2 v^{\text{V,L}}}{dP^2} \right) = \left( \frac{\partial \left( \frac{dv^{\text{V,L}}}{dP} \right)}{\partial v} \right)_T^{v=v^{\text{V,L}}, T^{\text{sat}}} \left( \frac{dv^{\text{V,L}}}{dP} \right) + \left( \frac{\partial \left( \frac{dv^{\text{V,L}}}{dP} \right)}{\partial T} \right)_v^{v=v^{\text{V,L}}, T^{\text{sat}}} \frac{1}{\left( \frac{dP}{dT} \right)^{\text{sat}}}, \quad (\text{D.8})$$

$$\left( \frac{d^2 s^{\text{V,L}}}{dP^2} \right) = \left( \frac{\partial \left( \frac{ds^{\text{V,L}}}{dP} \right)}{\partial v} \right)_T^{v=v^{\text{V,L}}, T^{\text{sat}}} \left( \frac{ds^{\text{V,L}}}{dP} \right) + \left( \frac{\partial \left( \frac{ds^{\text{V,L}}}{dP} \right)}{\partial T} \right)_v^{v=v^{\text{V,L}}, T^{\text{sat}}} \frac{1}{\left( \frac{dP}{dT} \right)^{\text{sat}}}, \quad (\text{D.9})$$

$$\begin{aligned}
 \left( \frac{\partial \left( \frac{dv^{V,L}}{dP} \right)}{\partial v} \right)_T^{v=v^{V,L}, T^{\text{sat}}} &= - \frac{\left( \frac{\partial^2 P}{\partial v \partial T} \right)_{v,T}^{v=v^{V,L}, T^{\text{sat}}}}{\left( \frac{\partial P}{\partial v} \right)_T^{v=v^{V,L}, T^{\text{sat}}} \left( \frac{dP}{dT} \right)^{\text{sat}}} \\
 &- \frac{\left[ \left( \frac{dP}{dT} \right)^{\text{sat}} - \left( \frac{\partial P}{\partial T} \right)_v^{v=v^{V,L}, T^{\text{sat}}} \right] \left( \frac{dP}{dT} \right)^{\text{sat}} \left( \frac{\partial^2 P}{\partial v^2} \right)_T^{v=v^{V,L}, T^{\text{sat}}}}{\left[ \left( \frac{\partial P}{\partial v} \right)_T^{v=v^{V,L}, T^{\text{sat}}} \left( \frac{dP}{dT} \right)^{\text{sat}} \right]^2}, \tag{D.10}
 \end{aligned}$$

$$\begin{aligned}
 \left( \frac{\partial \left( \frac{ds^{V,L}}{dP} \right)}{\partial v} \right)_T^{v=v^{V,L}, T^{\text{sat}}} &= \frac{\left( \frac{\partial C_P}{\partial v} \right)_T^{v=v^{V,L}, T^{\text{sat}}}}{T^{\text{sat}} \left( \frac{dP}{dT} \right)^{\text{sat}}} + \frac{\left( \frac{\partial^2 P}{\partial v \partial T} \right)_{v,T}^{v=v^{V,L}, T^{\text{sat}}}}{\left( \frac{\partial P}{\partial v} \right)_T^{v=v^{V,L}, T^{\text{sat}}}} \\
 &- \frac{\left( \frac{\partial P}{\partial T} \right)_v^{v=v^{V,L}, T^{\text{sat}}} \left( \frac{\partial^2 P}{\partial v^2} \right)_T^{v=v^{V,L}, T^{\text{sat}}}}{\left[ \left( \frac{\partial P}{\partial v} \right)_T^{v=v^{V,L}, T^{\text{sat}}} \right]^2}, \tag{D.11}
 \end{aligned}$$

$$\begin{aligned}
\left( \frac{\partial \left( \frac{dv^{\text{V,L}}}{dT} \right)}{\partial T} \right)_v^{v=v^{\text{V,L}}, T^{\text{sat}}} &= \frac{\left( \frac{d^2P}{dT^2} \right)^{\text{sat}} - \left( \frac{\partial^2 P}{\partial T^2} \right)_v^{v=v^{\text{V,L}}, T^{\text{sat}}}}{\left( \frac{\partial P}{\partial v} \right)_T^{v=v^{\text{V,L}}, T^{\text{sat}}} \left( \frac{dP}{dT} \right)^{\text{sat}}} - \left[ \left( \frac{dP}{dT} \right)^{\text{sat}} - \left( \frac{\partial P}{\partial T} \right)_v^{v=v^{\text{V,L}}, T^{\text{sat}}} \right] \times \\
&\frac{\left[ \left( \frac{dP}{dT} \right)^{\text{sat}} \left( \frac{\partial^2 P}{\partial T \partial v^2} \right)_{T, T, v}^{v=v^{\text{V,L}}, T^{\text{sat}}} + \left( \frac{\partial P}{\partial v} \right)_T^{v=v^{\text{V,L}}, T^{\text{sat}}} \left( \frac{d^2P}{dT^2} \right)^{\text{sat}} \right]}{\left[ \left( \frac{\partial P}{\partial v} \right)_T^{v=v^{\text{V,L}}, T^{\text{sat}}} \left( \frac{dP}{dT} \right)^{\text{sat}} \right]^2}, \tag{D.12}
\end{aligned}$$

$$\begin{aligned}
\left( \frac{\partial \left( \frac{ds^{\text{V,L}}}{dT} \right)}{\partial T} \right)_v^{v=v^{\text{V,L}}, T^{\text{sat}}} &= \frac{\left( \frac{\partial C_P}{\partial T} \right)_v^{v=v^{\text{V,L}}, T^{\text{sat}}}}{T^{\text{sat}} \left( \frac{dP}{dT} \right)^{\text{sat}}} - \frac{C_P^{v=v^{\text{V,L}}} \left[ \left( \frac{dP}{dT} \right)^{\text{sat}} + T^{\text{sat}} \left( \frac{d^2P}{dT^2} \right)^{\text{sat}} \right]}{\left[ T^{\text{sat}} \left( \frac{dP}{dT} \right)^{\text{sat}} \right]^2} \\
&+ \frac{\left( \frac{\partial^2 P}{\partial T^2} \right)_v^{v=v^{\text{V,L}}, T^{\text{sat}}}}{\left( \frac{\partial P}{\partial v} \right)_T^{v=v^{\text{V,L}}, T^{\text{sat}}}} - \frac{\left( \frac{\partial P}{\partial T} \right)_v^{v=v^{\text{V,L}}, T^{\text{sat}}} \left( \frac{\partial^2 P}{\partial v \partial T} \right)_{v, T}^{v=v^{\text{V,L}}, T^{\text{sat}}}}{\left[ \left( \frac{\partial P}{\partial v} \right)_T^{v=v^{\text{V,L}}, T^{\text{sat}}} \right]^2}, \tag{D.13}
\end{aligned}$$

$$\left(\frac{d^2P}{dT^2}\right)^{\text{sat}} = \frac{\left(\frac{dP}{dT}\right)^{\text{sat}}}{v^{\text{V}} - v^{\text{L}}} \left[ \left(\frac{ds^{\text{V}}}{dP}\right) - \left(\frac{ds^{\text{L}}}{dP}\right) - \left[ \left(\frac{dv^{\text{V}}}{dP}\right) - \left(\frac{dv^{\text{L}}}{dP}\right) \right] \left(\frac{dP}{dT}\right)^{\text{sat}} \right], \quad (\text{D.14})$$

$$C_P^{v=v^{\text{V,L}}} = C_v^{v=v^{\text{V,L}}} - T^{\text{sat}} \frac{\left[ \left(\frac{\partial P}{\partial T}\right)_{v=v^{\text{V,L}}, T^{\text{sat}}} \right]^2}{\left(\frac{\partial P}{\partial v}\right)_T}, \quad (\text{D.15})$$

where  $C_v^{v=v^{\text{V,L}}}$  is the isochoric heat capacity of either the vapor or the liquid phase in the limit that the saturated state is approached from the single-phase region. The isochoric heat capacity in the VLE-region is determined from [220] ( $\mu$  is the chemical potential):

$$C_v^{\varpi, T^{\text{sat}}} = -T \left(\frac{d^2\mu}{dT^2}\right)^{\text{sat}} + T v_{\varpi, T^{\text{sat}}} \left(\frac{d^2P}{dT^2}\right)^{\text{sat}} \Leftrightarrow$$

$$C_v^{\varpi, T^{\text{sat}}} = \left( P - T \left(\frac{dP}{dT}\right)^{\text{sat}} \right) \left[ (v^{\text{V}} - v^{\text{L}}) \left(\frac{\partial \varpi}{\partial P}\right)_u + \varpi \left[ \left(\frac{dv^{\text{V}}}{dP}\right) - \left(\frac{dv^{\text{L}}}{dP}\right) \right] + \left(\frac{dv^{\text{L}}}{dP}\right) \right].$$

$$\begin{aligned}
\left(\frac{\partial C_P}{\partial v}\right)_T^{v=v^{V,L},T^{\text{sat}}} &= T \left(\frac{\partial^2 P}{\partial T^2}\right)_v^{v=v^{V,L},T^{\text{sat}}} - \frac{2T^{\text{sat}} \left(\frac{\partial P}{\partial T}\right)_v^{v=v^{V,L},T^{\text{sat}}} \left(\frac{\partial^2 P}{\partial v \partial T}\right)_{v,T}^{v=v^{V,L},T^{\text{sat}}}}{\left(\frac{\partial P}{\partial v}\right)_T^{v=v^{V,L},T^{\text{sat}}}} \\
&+ \frac{T^{\text{sat}} \left[\left(\frac{\partial P}{\partial T}\right)_v^{v=v^{V,L},T^{\text{sat}}}\right]^2 \left(\frac{\partial^2 P}{\partial v^2}\right)_T^{v=v^{V,L},T^{\text{sat}}}}{\left[\left(\frac{\partial P}{\partial v}\right)_T^{v=v^{V,L},T^{\text{sat}}}\right]^2}, \tag{D.16}
\end{aligned}$$

and

$$\begin{aligned}
\left(\frac{\partial C_P}{\partial T}\right)_v^{v=v^{V,L},T^{\text{sat}}} &= \left(\frac{\partial C_v}{\partial T}\right)_v^{v=v^{V,L},T^{\text{sat}}} + \frac{T^{\text{sat}} \left[\left(\frac{\partial P}{\partial T}\right)_v^{v=v^{V,L},T^{\text{sat}}}\right]^2 \left(\frac{\partial^2 P}{\partial v \partial T}\right)_{v,T}^{v=v^{V,L},T^{\text{sat}}}}{\left[\left(\frac{\partial P}{\partial v}\right)_T^{v=v^{V,L},T^{\text{sat}}}\right]^2} \\
&- \frac{\left[\left(\frac{\partial P}{\partial T}\right)_v^{v=v^{V,L},T^{\text{sat}}}\right]^2 + 2T^{\text{sat}} \left(\frac{\partial P}{\partial T}\right)_v^{v=v^{V,L},T^{\text{sat}}} \left(\frac{\partial^2 P}{\partial T^2}\right)_v^{v=v^{V,L},T^{\text{sat}}}}{\left(\frac{\partial P}{\partial v}\right)_T^{v=v^{V,L},T^{\text{sat}}}}. \tag{D.17}
\end{aligned}$$



# Bibliography

- [1] ABBOTT, M. M. Cubic equations of state. *AIChEJ.* 19 (1973), 596–601.
- [2] ALBRIGHT, P. C., EDWARDS, T. J., CHEN, Z. Y., AND SENGERS, J. V. A scaled fundamental equation for the thermodynamic properties of carbon dioxide in the critical region. *J. Chem. Phys.* 87, 3 (1987), 1717–1725.
- [3] ALY, F. A., AND LEE, L. L. Self-consistent equations for calculating the ideal gas heat capacity, enthalpy, and entropy. *Fluid Phase Equilib.* 6 (1981), 169–179.
- [4] ANGELINO, G., AND COLONNA, P. Multicomponent working fluids for organic Rankine cycles (ORCs). *Energy* 23, 6 (1998), 449–463.
- [5] ANGELINO, G., AND COLONNA, P. Air cooled siloxane bottoming cycle for molten carbonate fuel cells. In *2000 Fuel Cell Seminar* (Portland, Oregon, October - November 2000), no. 114, pp. 667–670.
- [6] ANGELINO, G., AND COLONNA, P. Organic Rankine cycles for energy recovery from molten carbonate fuel cells. In *35<sup>th</sup> Intersociety Energy Conversion Engineering (IECEC) Conference and Exhibit* (Reston, VA, July 2000), no. AIAA 2000-3052, AIAA.
- [7] ANGELINO, G., AND INVERNIZZI, C. Cyclic methylsiloxanes as working fluids for space power cycles. *J. Sol. Energ. - Trans. ASME* 115, 3 (1993), 130–137.
- [8] ANGELINO, G., AND INVERNIZZI, C. Supercritical heat pump cycles. *Int. J. Refrig.* 17, 8 (1994), 543–554.
- [9] ANISIMOV, M. A., KISELEV, S. B., SENGERS, J. V., AND TANG, S. Crossover approach to global critical phenomena in fluids. *Physica A* 188 (1992), 487–525.
- [10] BALFOUR, F. W., SENGERS, J. V., MOLDOVER, M. R., AND LEVELT-SENGERS, J. M. H. Universality, revisions and corrections to scaling in fluids. *Phys. Lett. A* 65 (1978), 223–225.
- [11] BARKER, L. M., AND HOLLENBACH, R. E. Shock-wave studies of PMMA, fused silica, and sapphire. *J. Appl. Phys.* 41 (1970), 4208–4226.

- 
- [12] BECKER, R. Stoßwelle und Detonation. *Z. Phys.* 8 (1922), 321–362.
- [13] BENEDICT, M., WEBB, G. B., AND RUBIN, L. C. An empirical equation for thermodynamic properties of light hydrocarbons and their mixtures I. Methane, ethane, propane and n-butane. *J. Chem. Phys.* 8 (1940), 334–345.
- [14] BETHE, H. A. The theory of shock waves for an arbitrary equation of state. Technical paper 545, Office Sci. Res. & Dev., 1942.
- [15] BLOCH, H., AND SOARES, C. *Turboexpanders and process applications*. Gulf Professional Publishing, 2001.
- [16] BÖHMA, H., AND BRAUN-UNKHOFF, M. Numerical study of the effect of oxygenated blending compounds on soot formation in shock tubes. *Combust. Flame* 153, 1-2 (2008), 84–96.
- [17] BORISOV, A. A., BORISOV, AL. A., KUTATELADZE, S. S., AND NAKORYAKOV, V. E. Rarefaction shock wave near the critical liquid-vapor point. *J. Fluid Mech.* 126 (1983), 59–73.
- [18] BOUKARI, H., SHAUMEYER, J. N., BRIGGS, M. E., AND GAMMON, R. W. Critical speeding up in pure fluids. *Phys. Rev. A* 41, 4 (1990), 2260–2263.
- [19] BROWN, B. P., AND ARGROW, B. M. Application of Bethe-Zel'dovich-Thompson fluids in organic Rankine cycle engines. *J. Propul. Power* 16, 6 (November-December 2000), 1118–1123.
- [20] BROWN, M. A., AND CHURCHILL, S. W. Finite-difference computation of the wave motion generated in a gas by a rapid increase in the bounding temperature. *Comput. Chem. Eng.* 23, 3 (1999), 357–376.
- [21] BUECKER, D., AND WAGNER, W. A reference equation of state for the thermodynamic properties of ethane for temperatures from the melting line to 675 K and pressures up to 900 MPa. *J. Phys. Chem. Ref. Data* 35, 1 (2006), 205–266.
- [22] BUECKER, D., AND WAGNER, W. Reference equations of state for the thermodynamic properties of fluid phase n-butane and isobutane. *J. Phys. Chem. Ref. Data* 35, 2 (2006), 929–1019.
- [23] CARLÈS, P. Thermoacoustic waves near the liquid-vapor critical point. *Phys. Fluids* 18, 126102 (2006), 7 pages.
- [24] CHANDRASEKAR, D., AND PRASAD, P. Transonic flow of a fluid with positive and negative nonlinearity through a nozzle. *Phys. Fluids A* 3, 3 (1991), 427–438.

- 
- [25] CHUNG, T. H., AJLAN, M., LEE, L. L., AND STARLING, K. E. Generalized multiparameter correlation for non-polar and polar fluid transport properties. *Ind. Eng. Chem. Res.* 27 (1988), 671–679.
- [26] COLGATE, S. O., SONA, C. F., REED, K. R., AND SIVARAMAN, A. Experimental ideal gas reference state heat capacities of gases and vapors. *J. Chem. Eng. Data* 35 (1990), 1–5.
- [27] COLONNA, P. *Fluidi di lavoro multi componenti per cicli termodinamici di potenza (Multicomponent working fluids for power cycles)*. PhD thesis, Politecnico di Milano, October 1996.
- [28] COLONNA, P., AND CALDERAZZI, L. Thermal stability of R-134a, R-141b, R-131I, R-7146, R-125 associated with stainless steel as a containing material. *Int. J. Refrig.* 20, 6 (1997), 381–389.
- [29] COLONNA, P., AND GUARDONE, A. Molecular interpretation of nonclassical gas dynamics of dense vapors under the Van der Waals model. *Phys. Fluids* 18 (2006), 056101–1–14.
- [30] COLONNA, P., GUARDONE, A., AND NANNAN, N. R. Siloxanes: a new class of candidate Bethe-Zel'dovich-Thompson fluids. *Phys. Fluids* 19, 086102 (2007), 12 pages.
- [31] COLONNA, P., GUARDONE, A., NANNAN, N. R., AND ZAMFIRESCU, C. Design of the dense gas Flexible Asymmetric Shock Tube. *J. Fluid Eng.-T. ASME* 130, 034501 (2008), 6 pages.
- [32] COLONNA, P., HARINCK, J., REBAY, S., AND GUARDONE, A. Real-gas effects in organic Rankine cycle turbine nozzles. *J. Propul. Power* 24, 2 (March–April 2008), 282–294.
- [33] COLONNA, P., NANNAN, N. R., AND GUARDONE, A. Multiparameter equations of state for siloxanes:  $[(\text{CH}_3)_3\text{-Si-O}_{1/2}]_2\text{-[O-Si-(CH}_3)_2]_{i=1\dots 3}$ , and  $[\text{O-Si-(CH}_3)_2]_6$ . *Fluid Phase Equilib.* 263, 2 (2008), 115–130.
- [34] COLONNA, P., NANNAN, N. R., GUARDONE, A., AND LEMMON, E. W. Multiparameter equations of state for selected siloxanes. *Fluid Phase Equilib.* 244, 2 (2006), 193–211.
- [35] COLONNA, P., AND REBAY, S. Numerical simulation of dense gas flows on unstructured grids with an implicit high-resolution upwind Euler solver. *Int. J. Numer. Methods Fluids* 46, 7 (2004), 735–765.
- [36] COLONNA, P., REBAY, S., AND VAN DER STELT, T. P. zFlow: A CFD program using accurate thermodynamic properties of fluids. software, ©2001-2005.

- 
- [37] COLONNA, P., AND SILVA, P. Dense gas thermodynamic properties of single and multi-component fluids for fluid dynamics simulations. *J. Fluid Eng.-T. ASME* 125, 3 (2003), 414–427.
- [38] COLONNA, P., AND VAN DER STELT, T. P. FluidProp: A program for the estimation of thermophysical properties of fluids. Energy Technology Section, Delft University of Technology, The Netherlands ([www.fluidprop.com](http://www.fluidprop.com)), 2005.
- [39] COURANT, R., AND FRIEDRICHS, K. O. *Supersonic flows and shock waves*. Interscience Publishers, Inc., 1948.
- [40] CRAMER, M. Oblique shock waves in steady transonic flow of pressurized gases. In *35<sup>th</sup> AIAA Thermophysics Conference* (Anahaim, CA, 11-14 June 2001), no. AIAA 2001 - 2751, AIAA, pp. 1–10.
- [41] CRAMER, M., AND FRY, N. Nozzle flows of dense gases. *Phys. Fluids A* 5, 5 (1993), 1246–1259.
- [42] CRAMER, M., MONACO, J., AND FABENY, B. Fanno processes in dense gases. *Phys. Fluids* 6 (1994), 674–683.
- [43] CRAMER, M., AND SEN, R. Exact solutions for sonic shocks in Van der Waals gases. *Phys. Fluids* 30, 2 (1987), 377–385.
- [44] CRAMER, M. S. Negative nonlinearity in selected fluorocarbons. *Phys. Fluids A* 11, 1 (1989), 1894–1897.
- [45] CRAMER, M. S. *Nonclassical dynamics of classical gases*, vol. Nonlinear Waves in Real Fluids of *International Center for Mechanical Sciences, Courses and Lectures*. Springer-Verlag, Berlin, October 1991.
- [46] CRAMER, M. S. On the Mach number variation in steady flows of dense hydrocarbons. *J. Fluids Eng.* 113 (1991).
- [47] CRAMER, M. S., AND BEST, L. M. Steady, isentropic flows of dense gases. *Phys. Fluids A* 3, 1 (1991), 219–226.
- [48] CRAMER, M. S., AND KLUWICK, A. On the propagation of waves exhibiting both positive and negative nonlinearity. *J. Fluid Mech.* 142 (1984), 9–37.
- [49] CRAMER, M. S., AND PARK, S. On the suppression of shock-induced separation in Bethe-Zel'dovich-Thompson fluids. *J. Fluid Mech.* 393 (1999), 1–21.
- [50] DA REGO, I., SATO, K., KUGIMIYA, S., AOKI, T., MIYOSHI, Y., ANDO, T., GOTO, K., AND SAKAMOTO, M. Development of a large diameter diaphragmless shock tube for gas-dynamic laser studies. *Mater. Sci. Forum* 566 (2008), 9–14.

- 
- [51] DAUBERT, T. E., DANNER, R. P., SIBEL, H. M., AND STEBBINS, C. C. *Physical and thermodynamic properties of pure chemicals: Data compilation*. Taylor & Francis, Washington, D. C., 1997.
- [52] DEFREES, D. J., AND MCLEAN, A. D. Molecular orbital predictions of the vibrational frequencies of some molecular ions. *J. Chem. Phys.* 82 (1985), 333–341.
- [53] DELALE, C. F., AND SCHNERR, G. H. Transient effects of nucleation in steady and unsteady condensing flows. *Int. J. Multiphase Flow* 22, 4 (1996), 767–781.
- [54] DICKINSON, E., AND MCLURE, I. A. Thermodynamics of *n*-alkane + dimethylsiloxane mixtures. Part 1.– Gas-liquid critical temperatures and pressures. *J. Chem. Soc. Faraday Trans.* 70 (1974), 2313 – 2320.
- [55] DONALDSON, C. P., AND SULLIVAN, R. D. The effect of wall friction on the strength of shock waves in tubes and hydraulic jumps in channels. Technical Note TN 1942, National Advisory Committee for Aeronautics NACA, 1949.
- [56] DRAKON, A. V., EMELIANOV, A. V., AND EREMIN, A. V. Nonequilibrium processes at the shock wave front in inert gases with a small amount of (FeCO)<sub>5</sub> impurity. *Tech. Phys.* 53, 8 (2008), 1022–1028.
- [57] DUHEM, P. On the propagation of shock waves in fluids. *Z. Phys. Chem* 69 (1909), 169–186.
- [58] EDWARDS, T. J. *Specific heat measurements near the critical point of carbon dioxide*. PhD thesis, University of Western Australia, 1984.
- [59] EMANUEL, G. *Advanced classical thermodynamics*. AIAA Education Series. AIAA, New York, 1987.
- [60] EMANUEL, G. Assessment of the Martin-Hou equation for modeling a nonclassical fluid. *J. Fluids Eng.* 116 (December 1994), 883–884.
- [61] EMANUEL, G. Analysis of a critical point with application to fluid mechanics. AME Report 96-1, University of Oklahoma, Norman, Oklahoma, USA, 1996.
- [62] EMANUEL, G., AND ARGROW, B. M. Linear dependence of the bulk viscosity on shock wave thickness. *Phys. Fluids* 6, 9 (1994), 3203–3205.
- [63] FERGASON, B., AND ARGROW, B. Construction and operation of a dense gas shock tube. In 35<sup>th</sup> AIAA Thermophysics Conference, Anaheim, CA (Reston, VA, June 2001), AIAA, pp. 1–10.

- 
- [64] FERGASON, B., HO, T., ARGROW, B., AND EMANUEL, G. Theory for producing a single-phase rarefaction shock wave in a shock tube. *J. Fluid Mech.* 445 (2001), 37–54.
- [65] FERGASON, S. *Dense Gas Shock Tube*. PhD thesis, University of Colorado, Boulder, Aerospace Engrg. Sciences Dept., University of Colorado, Boulder, 2001.
- [66] FERGASON, S., GUARDONE, A., AND ARGROW, B. Construction and validation of a dense gas shock tube. *J. Thermophys. Heat Transfer* 17, 3 (2003), 326–333.
- [67] FERIOLO, F. *Experimental characterization of laser-induced plasmas and application to gas composition measurements*. PhD thesis, University of Maryland, MD, USA, 2005.
- [68] FINK, M. J., HALLER, K. J., WEST, R., AND MICHL, J. Tetramesitylcyclo-disiloxane: A cyclic siloxane with an unusual structure. *J. Am. Chem. Soc.* 106 (1984), 822–823.
- [69] FLANINGAM, O. L. Vapor pressures of poly(dimethylsiloxane) oligomers. *J. Chem. Eng. Data* 31, 3 (1986), 266–272.
- [70] FREIRE, J. J., PIEROLA, I. F., AND HORTA, A. Conformational analysis of methyl-phenyl-siloxane chains. *Macromolecules* 29 (1996), 5143–5148.
- [71] FRIEND, D. G., ELY, J. F., AND INGHAM, H. Thermophysical properties of methane. *J. Phys. Chem. Ref. Data* 18, 2 (1989), 583–638.
- [72] FRIEND, D. G., INGHAM, H., AND ELY, J. F. Thermophysical properties of ethane. *J. Phys. Chem. Ref. Data* 20, 2 (1991), 275–347.
- [73] FRISCH, M. J., TRUCKS, G. W., SCHLEGEL, H. B., AND *et. al.* GAUSSIAN 98 Revise A.6, 1998. Pittsburg, PA.
- [74] FULLE, D., DIB, A., KIEFER, J. H., ZHANG, Q., YAO, J., AND KERN, R. D. Pyrolysis of furan at low pressures: Vibrational relaxation, unimolecular dissociation, and incubation times. *J. Phys. Chem. A* 102, 38 (1998), 7480–7486.
- [75] GAETANI, P., GUARDONE, A., AND PERSICO, G. Shock tube flows past partially opened diaphragms. *J. Fluid Mech.* 602 (2008), 267–286.
- [76] GILLIS, K. A. Thermodynamic properties of seven gaseous halogenated hydrocarbons from acoustic measurements:  $\text{CHClFCF}_3$ ,  $\text{CHF}_2\text{CF}_3$ ,  $\text{CF}_3\text{CH}_3$ ,  $\text{CHF}_2\text{CH}_3$ ,  $\text{CF}_3\text{CHFCHF}_2$ ,  $\text{CF}_3\text{CH}_2\text{CF}_3$ , and  $\text{CHF}_2\text{CF}_2\text{CH}_2\text{F}$ . *Int. J. Thermophys.* 18, 1 (1997), 73–135.

- 
- [77] GILLIS, K. A., AND MOLDOVER, M. R. Practical determination of gas densities from the speed of sound using square-well potentials. *Int. J. Thermophys.* 17, 6 (1996), 1305–1324.
- [78] GNUTEK, R., AND COLONNA, P. Modular lumped-parameters dynamic model for gas turbines: validation and application to a small scale externally fired gas turbine. In *2005 ASME International Mechanical Engineering Congress and Exposition (IMECE)*, (2005), no. 2005-80720, ASME.
- [79] GUARDONE, A. *Nonclassical gasdynamics: thermodynamic modeling and numerical simulation of multidimensional flows of BZT fluids*. PhD thesis, Politecnico di Milano, Italy, 2001.
- [80] GUARDONE, A. Three-dimensional shock tube flows for dense gases. *J. Fluid Mech.* 583 (2007), 423–442.
- [81] GUARDONE, A., AND ARGROW, B. M. Nonclassical gasdynamic region of selected fluorocarbons. *Physics of Fluids* 17, 11 (2005), 116102.
- [82] GUARDONE, A., AND COLONNA, P. Point explosions in dense gases. In *9<sup>th</sup> AIAA/ASME Joint Thermophysics and Heat Transfer Conference* (San Francisco, CA, USA, 5-8 June 2006), no. AIAA 2006-3391, AIAA/ASME, pp. 1–10.
- [83] GUARDONE, A., AND VIGEVANO, L. Finite element/volume solution to axisymmetric conservation laws. *J. Comput. Phys.* 224 (2007), 489518.
- [84] GUARDONE, A., VIGEVANO, L., AND ARGROW, B. M. Assessment of thermodynamic models for dense gas dynamics. *Phys. Fluids* 16, 11 (November 2004), 3878–3887.
- [85] GULEN, S. C., THOMPSON, P. A., AND CHO, H. J. Rarefaction and liquefaction shock waves in regular and retrograde fluids with near-critical end states. In *IUTAM Symposium: Adiabatic Waves in Liquid-Vapor Systems* (Berlin Heidelberg, Germany, 1989), G. E. A. Meier and P. A. Thompson, Eds., Springer-Verlag, pp. 281–290.
- [86] HARRISON, B. K., AND SEATON, W. H. Solution to missing group problem for estimation of ideal gas heat capacities. *Ind. Eng. Chem. Res.* 27 (1988), 1536–1540.
- [87] HARTUNIAN, R. A. Shock curvature due to boundary-layer effects in a shock tube. *Phys. Fluids* 4, 9 (1961), 1059–1063.
- [88] HARTUNIAN, R. A., AND MARRONE, P. V. Viscosity of dissociated gases from shock-tube heat-transfer measurements. *Phys. Fluids* 4, 5 (1961), 535–543.

- 
- [89] HAYES, W. D. *Fundamentals of gasdynamics*, vol. 3. Princeton University Press, 1958, ch. The basic theory of gas dynamic discontinuities, p. 426.
- [90] HERTEL, T., JAKOB, J., MINKWITZ, R., AND OBERHAMMER, H. Bonding properties of siloxanes: Gas phase structures of N,N-Bis(trifluoromethyl)-O-(trimethylsilyl)hydroxylamine,  $\text{Me}_3\text{SiON}(\text{CF}_3)_2$ , and Trimethylsilyl Nitrate,  $\text{Me}_3\text{SiONO}_2$ . *Inorg. Chem.* 37 (1998), 5092–5096.
- [91] HILL, J. R., AND SAUER, J. Molecular mechanics potential for silica and zeolite catalysts based on ab initio calculations. 1. Dense and microporous silica. *J. Phys. Chem.* 98 (1994), 1238–1244.
- [92] HIRSCHFELDER, J. O., BUEHLER, R. J., H. A. MCGEE, J., AND SUTTON, J. R. Generalized equation of state for gases and liquids. *Ind. Eng. Chem.* 50, 3 (1958), 375–385.
- [93] HOFFREN, J., TALONPOIKA, T., LARJOLA, J., AND SIIKONEN, T. Numerical simulation of real-gas flow in a supersonic turbine nozzle ring. *J. Eng. Gas Turb. Power* 124, 2 (April 2002), 395–403.
- [94] HOLLYER JR., R. N. Attenuation in the shock tube: I. Laminar flow. *J. Appl. Phys.* 27, 3 (1956), 254–261.
- [95] HONMA, H., AND GLASS, I. I. Weak spherical shock-wave transitions of N-waves in air with vibrational excitation. *Proc. R. Soc. Lond. A* 391, 1800 (1984), 55–83.
- [96] HOUT, R. F., LEVI, B. A., AND HEHRE, W. J. Effect of electron correlation on theoretical vibrational frequencies. *J. Comput. Chem.* 3 (1982), 234–250.
- [97] HUGONIOT, P.-H. Sur la propagation du mouvement dans les corps et spécialement dans les gaz parfaits. *J. Ecole Polytechnique* 57 (1887), 3–98.
- [98] HUNTER, M. J., WARRICK, E. L., HYDE, J. F., AND CURRIE, C. C. Organosilicon polymers. II. The open chain dimethylsiloxanes with trimethylsiloxy end-groups. *J. Amer. Chem. Soc.* 68 (1946), 2284–2290.
- [99] HURD, C. B. Studies of siloxanes. I. The specific volume and viscosity in relation to temperature and constitution. *J. Am. Chem. Soc.* 68 (1946), 364–370.
- [100] IHMELS, E. C. Helmholtz type fundamental equations of state - some practice applications. In *Thermo International 2006: Sixteenth Symposium on Thermophysical Properties* (July-August 2006), National Institute of Standards and Technology, pp. 1–11.

- 
- [101] IRIKURA, K. K., III, R. D. J., , AND KACKER, R. N. Uncertainties in scaling factors for ab initio vibrational frequencies. *J. Phys. Chem. A* 109 (2005), 8430–8437.
- [102] IUPAC. Atomic weights of the elements 1999. *J. Phys. Chem. Ref. Data* 30, 3 (2001), 701–712.
- [103] IVANOV, A. G., AND NOVIKOV, S. A. Rarefaction shock waves in iron and steel. *Zh. Eksp. Teor. Fiz.* 40, 4 (1961), 1880–1882.
- [104] J. M. H. LEVELT-SENGERS, GREER, W. L., AND SENEGERS, J. V. Scaled equation of state parameters for gases in the critical region. *J. Phys. Chem. Ref. Data* 5, 1 (1976), 1–51.
- [105] JAGADEESH, G. Industrial applications of shock waves. *P. I. Mech. Eng. G.-J. Aer* 222, 5 (2008), 575–583.
- [106] JOUGUET, E. On the propagation of the discontinuities in fluids. *Comptes Rendues de l'Academie des Sciences* 132 (1901), 673–676.
- [107] KAHL, G. D., AND MYLIN, D. C. Rarefaction shock possibility in a Van der Waals-Maxwell fluid. *Phys. Fluids* 12 (1969), 2283–2291.
- [108] KIEFER, J. H., BUZYNA, L. L., DIB, A., AND SUNDARAM, S. Observation and analysis of nonlinear vibrational relaxation of large molecules in shock waves. *J. Chem. Phys.* 113, 1 (2000), 48–58.
- [109] KIEFER, J. H., SAHUKAR, G. C., SANTHANAM, S., SRINIVASAN, N. K., AND TRANTER, R. S. Vibrational relaxation in methyl hydrocarbons at high temperatures: Propane, isobutene, isobutane, neopentane, and toluene. *J. Chem. Phys.* 120, 2 (2004), 918925.
- [110] KIEFFER, S. W. Sound speed in liquid-gas mixtures: Water-air and water-steam. *J. Geophys. Res.* 82, 20 (1977), 2895–2904.
- [111] KIRILLOV, N. Analysis of modern natural gas liquefaction technologies. *Chem. Petrol. Eng.* 40, 7-8 (2004), 401–406.
- [112] KLUWICK, A. Transonic nozzle flows of dense gases. *J. Fluid Mech.* 247 (1993), 661–688.
- [113] KLUWICK, A. Interacting laminar boundary layers of dense gases. *Acta Mech.* 4 (1994), 335–349.
- [114] KLUWICK, A. *Handbook of shock waves*. Academic Press, 2001, ch. 3.4. Rarefaction shocks, pp. 339–411.

- 
- [115] KRASILNIKOV, A., MAKAREVICH, G., AND MICHAÏLOV, A. Experimental researches of supersonic hydrocarbon fuels combustion. In *13<sup>th</sup> AIAA/CIRA International Space Planes and Hypersonic Systems and Technologies Conference* (2005), vol. 2, pp. 1132–1137.
- [116] KUDO, T., HASHIMOTO, F., AND GORDON, M. S. Ab initio study of cyclic siloxanes (H<sub>2</sub>SiO)<sub>n</sub>: n = 3,4, 5. *J. Comp. Chem.* 17 (1996), 1163–1170.
- [117] KUNZ, O., KLIMECK, B., WAGNER, W., AND JAESCHKE, M. The GERG-2004 wide-range reference equation of state for natural gases and other mixtures GERG TM 15 2007. *Fortschr.-Ber. VDI, VDI-Verlag* 557 (2007).
- [118] KURUMOV, D. S., OLCHOWY, G. A., AND SENEGERS, J. V. Thermodynamic properties of methane in the critical region. *Int. J. Thermophys.* 9, 1 (1988), 73–84.
- [119] KUTATELADZE, S. S., NAKORYAKOV, V. E., AND BORISOV, A. A. Rarefaction waves in liquid and gas-liquid media. *Ann. Rev. Fluid Mech.* 19 (1987), 577–600.
- [120] LAMBERT, J. D. Vibration-translation and vibration-rotation energy transfer in polyatomic molecules. *J. Chem. Soc., Faraday Trans. 2* 68 (1972), 364–373.
- [121] LAMBERT, J. D. *Vibrational and rotational relaxation in gases*. The International Series of Monographs on Chemistry. Clarendon Press, Oxford, 1977.
- [122] LAMBRAKIS, K. C., AND THOMPSON, P. A. Existence of real fluids with negative fundamental derivative. *Phys. Fluids* 15, 5 (1972), 933–935.
- [123] LANDAU, L. D., AND LIFSHITZ, E. M. *Fluid mechanics*. Addison-Wesley, Reading, Mass., 1959, p. 373.
- [124] LAX, P. D. Hyperbolic systems of conservation laws II. *Comm. Pure Appl. Math.* 10 (1957), 537–566.
- [125] LE GUILLOU, J. C., AND ZINN-JUSTIN, J. Critical exponents from field theory. *Phys. Rev. B* 21, 9 (1980), 3976–3998.
- [126] LEI, Z., FAROUK, B., AND ORAN, E. Numerical simulation of ‘piston effect’ in supercritical carbon dioxide. No. HT2005-72401, ASME, pp. 1–6.
- [127] LEMMON, E., AND SPAN, R. Short fundamental equations of state for 20 industrial fluids. *J. Chem. Eng. Data* 51, 3 (2006), 785–850.
- [128] LEMMON, E. W., AND HUBER, M. L. Thermodynamic properties of n-dodecane. *Energ. Fuel.* 18 (2004), 960–967.

- 
- [129] LEMMON, E. W., MCLINDEN, M. O., AND HUBER, M. L. REFPROP - REFERENCE fluid PROPERTIES. software, ©NIST 2002.
- [130] LEVELT-SENGERS, J. From Van der Waals' equation to scaling laws. *Physica* 73, 1 (1973), 73–106.
- [131] LEVELT-SENGERS, J. M. H. Scaling predictions for thermodynamic anomalies near the gas-liquid critical point. *Ind. Eng. Chem. Fundam.* 9, 3 (1970), 470–480.
- [132] LEVELT-SENGERS, J. M. H., MORRISON, G., AND CHANG, R. F. Critical behavior in fluids and fluid mixtures. *Fluid Phase Equilib.* 14 (1983), 19–44.
- [133] LINDLEY, D. D., AND HERSHEY, H. C. The orthobaric region of octamethyltrisiloxane. *Fluid Phase Equilib.* 55 (1990), 109–124.
- [134] LUO, X., PRAST, B., VAN DONGEN, M. E. H., HOEIJMAKERS, H. W. M., AND YANG, J. On phase transition in compressible flows: Modelling and validation. *J. Fluid Mech.* 548 (2006), 403–430.
- [135] MARCOS, D., LINDLEY, D., WILSON, K., KAY, W., AND HERSHEY, H. A  $(P, v, T)$  study of tetramethylsilane, hexamethyldisiloxane, octamethyltrisiloxane, and toluene from 423 K to 573 K in the vapor phase. *J. Chem. Thermodyn.* 15 (1983), 1003–1014.
- [136] MARTIN, J. J., AND HOU, Y. C. Development of an equation of state for gases. *AIChEJ.* 1, 2 (June 1955), 142–151.
- [137] MARTIN, J. J., KAPOOR, R. M., AND NEVERS, N. D. An improved equation of state for gases. *AIChEJ.* 5, 2 (1959), 159–160.
- [138] MARTIN, W. A. An experimental study of the boundary layer behind a moving plane shock wave. Technical report 47, UTIA, 1957.
- [139] MCLURE, I. A. Isobaric heat capacities of five dimethylsiloxane oligomers at 303.15 and 323.85 K from sound velocity and  $PvT$  data. *Thermochim. Acta.* 21 (1977), 153–156.
- [140] MCLURE, I. A., AND NEVILLE, J. F. An analysis of the gas-liquid critical properties of the dimethylsiloxanes establishing tetramethylsilane as the forerunner of the series. *J. Chem. Thermodyn.* 9 (1977), 957–961.
- [141] MCLURE, I. A., PRETTY, A. J., AND SADLER, P. A. Specific volumes, thermal pressure coefficients, and derived quantities of five dimethylsiloxane oligomers from 25 to 140 ° C. *J. Chem. Eng. Data* 22, 4 (1977), 372–376.
- [142] MEHL, J. B., AND MOLDOVER, M. R. Precondensation phenomena in acoustic measurements. *J. Chem. Phys.* 77 (1982), 455–465.

- 
- [143] MICHELS, A., SENGER, J. V., AND VAN DER GULIK, P. S. The thermal conductivity of carbon dioxide in the critical region II. Measurements and conclusions. *Physica* 28, 12 (1962), 1216–1237.
- [144] MIRELS, H. Laminar boundary layer behind shock advancing into stationary fluid. Technical Note TN 3401, National Advisory Committee for Aeronautics, March 1955.
- [145] MIRELS, H., AND BRAUN, W. H. Nonuniformities in shock-tube flow due to unsteady-boundary-layer action. Tech. Rep. NACA TN 4021, National Advisory Committee for Aeronautics NACA, 1957.
- [146] MIYAMOTO, H., AND WATANABE, K. A thermodynamic property model for fluid-phase propane. *Int. J. Thermophys.* 21, 5 (2000), 1045–1072.
- [147] MIYAMOTO, H., AND WATANABE, K. A thermodynamic property model for fluid-phase n-butane. *Int. J. Thermophys.* 22, 2 (2001), 459–475.
- [148] MIYAMOTO, H., AND WATANABE, K. A thermodynamic property model for fluid-phase isobutane. *Int. J. Thermophys.* 23, 2 (2002), 477–499.
- [149] MOLDOVER, M. R., TRUSLER, J. P. M., EDWARDS, T. J., MEHL, J. B., AND DAVIS, R. S. Measurement of the universal gas constant  $R$  using a spherical acoustic resonator. *J. Res. NBS.* 93, 2 (1988), 85–144.
- [150] MONACO, J. F., CRAMER, M. S., AND WATSON, L. T. Supersonic flows of dense gases in cascade configurations. *J. Fluid Mech.* 330 (1997), 31–59.
- [151] MORAN, M. J., AND SHAPIRO, H. N. *Fundamentals of engineering thermodynamics*, 3<sup>rd</sup> ed. John Wiley & Sons Ltd., Baffins Lane, Chichester, West Sussex PO19 1UD, England, 1998.
- [152] NANNAN, N., COLONNA, P., AND VAN DER STELT, T. P. Thermodynamic properties of single component fluids in the vapour-liquid-equilibrium region (version 1). Tech. Rep. ET-2333, Delft University of Technology, Leeghwaterstraat 44, 2628 CA Delft, November 2008.
- [153] NANNAN, N. R., COLONNA, P., TRACY, C. M., ROWLEY, R. L., AND HURLY, J. J. Ideal-gas heat capacities of dimethylsiloxanes from speed-of-sound measurements and ab initio calculations. *Fluid Phase Equilibria* 257, 1 (2007), 102–113.
- [154] NANNAN, N. R., HURLY, J. J., AND COLONNA, P. Speed of sound and ideal-gas heat capacity data for selected siloxanes from acoustic measurements:  $[(\text{CH}_3)_2\text{-Si-O}]_4$  and  $[(\text{CH}_3)_2\text{-Si-O}]_5$ . In *Thermo International 2006: Sixteenth Symposium on Thermophysical Properties* (July-August 2006), G. Hardin, C. Muzny, and D. Friend, Eds., National Institute of Standards and Technology, pp. 1–19.

- 
- [155] NANNAN, N. R., ZAMFIRESCU, C., AND COLONNA, P. Detailed design of the flexible asymmetric shock tube (FAST) facility at the P&E department of the Delft University of Technology. Tech. Rep. ET-2263, Delft University of Technology, Leeghwaterstraat 44, 2628 CA Delft, October 2007.
- [156] NOVIKOV, I. I. Existence of shock wave rarefaction. *Dokl. Acad. Nauk SSSR* 59 (1948), 1545–1546.
- [157] OEHLSCHLAEGER, M. A., DAVIDSON, D. F., JEFFRIES, J. B., AND HANSON, R. K. Carbon dioxide thermal decomposition: Observation of incubation. *Z. Phys. Chem.* 219, 5 (2005), 555–567.
- [158] OLEINIK, O. Uniqueness and stability of the generalized solution of the Cauchy problem for a quasi-linear problem. *Usp. Math. Nauk.* 14 (1959), 165–170.
- [159] PATNODE, W., AND WILCOCK, D. F. Methylpolysiloxanes. *J. Amer. Chem. Soc.* 68 (1946), 359–363.
- [160] PEETERS, P., PIETERSE, G., HRUBÝ, J., AND VAN DONGEN, M. E. H. Multi-component droplet growth. I. Experiments with supersaturated n-nonane vapor and water vapor in methane. *Phys. Fluids* 16, 7 (2004), 2567–2574.
- [161] PENG, D. Y., AND ROBINSON, D. B. A new two-constant equation of state. *Ind. Eng. Chem. Fundam.* 15 (1976), 59–64.
- [162] PIECHÓR, K. The shock structure by model equations of capillarity. *Arch. Mech.* 49 (1997), 767–790.
- [163] POLIKHRONIDI, N. G., ABDULAGATOV, I. M., MAGEE, J. W., AND BATYROVA, R. G. Isochoric heat capacity of toluene near phase transitions and the critical point. *J. Chem. Eng. Data* 46 (2001), 1064–1071.
- [164] POLING, B. E., PRAUSNITZ, J. M., AND O'CONNELL, J. P. *The properties of gases and liquids*, 5<sup>th</sup> ed. Chemical Engineering Series. McGraw-Hill, New York, 2001.
- [165] POPLE, J. A., SCHLEGEL, H. B., KRISHNAN, R., DEFREES, D. J., BINKLEY, J., FRISCH, M. J., WHITESIDE, R. A., HOUT, R. F., AND J. HEHRE, W. Molecular orbital studies of vibrational frequencies. *Int. J. Quantum Chem., Quantum Chem. Symp.* 15 (1981), 269–278.
- [166] R., M., AND J., P. B. The Riemann problem for fluid flow of real material. *Rev. Mod. Phys.* 61(1) (1989), 75–130.
- [167] RANKINE, W. J. M. On the thermodynamic theory of waves of finite longitudinal disturbance. *Phyl. Trans.* 160 (1870), 277–288.

- 
- [168] RAYLEIGH, L. Aerial plane waves of finite amplitude. *Proc. Roy. Soc. A* 84 (1910), 247–284.
- [169] REDLICH, O., AND KWONG, J. N. S. On the thermodynamics of solutions. V. An equation of state. fugacities of gaseous solutions. *Chem. Rev* 44 (1949), 233–244.
- [170] RIEMANN, G. Über die Fortpflanzung ebener Luftwellen von endlicher Schwingungsweite. In *Gesammelte Werke* (Leipzig, 1876). reprinted by Dover New York, 1953.
- [171] ROWLEY, R. L. *Statistical mechanics for thermophysical property calculations*. Prentice-Hall, New Jersey, 1994.
- [172] ROWLEY, R. L., WILDING, W. V., OSCARSON, J. L., YANG, Y., ZUNDEL, N. A., DAUBERT, T. P., AND DANNER, R. P. *DIPPR data compilation of pure chemical properties*. Taylor & Francis Publishing Company, New York, NY, 2004.
- [173] SANTHANAM, S., KIEFER, J. H., TRANTER, R. S., AND SRINIVASAN, N. K. A shock tube, laser-schlieren study of the pyrolysis of isobutene: Relaxation, incubation, and dissociation rates. *Int. J. Chem. Kinet.* 35, 8 (2003), 381–390.
- [174] SCHLAMP, S., AND RÖSGEN, T. Flow in near-critical fluids induced by shock and expansion waves. *Shock Waves* 14, 1-2 (2005), 93–101.
- [175] SCHNERR, G., AND LEIDNER, P. Two-dimensional nozzle flows of dense gases. In *Fluids Engineering Conference* (1993), no. ASME Paper No. 93–FE–8.
- [176] SCOTT, A. P., AND RADOM, L. Harmonic vibrational frequencies: An evaluation of Hartree-Fock, Møller-Plesset, Quadratic Configuration Interaction, Density Functional Theory, and semi empirical scale factors. *J. Phys. Chem.* 100 (1996), 16502–16513.
- [177] SCOTT, D. W., MESSERLY, J. F., TODD, S. S., GUTHRIE, G. B., MOORE, I. A. R. T., OSBORN, A., BERG, W. T., AND MCCULLOUGH, J. P. Hexamethyldisiloxane: chemical thermodynamic properties and internal rotation about the siloxane linkage. *J. Phys. Chem.* 65 (1961), 1320–1326.
- [178] SEDOV, L. I. *Similarity and dimensional methods in mechanics*. Academic Press, 1959.
- [179] SENGENS, J. V., AND LEVELT-SENGENS, J. M. H. A universal representation of the thermodynamic properties of fluids in the critical region. *Int. J. Thermophys.* 5, 2 (1984), 195–208.

- 
- [180] SENGERS, J. V., AND LEVELT-SENGERS, J. M. H. Thermodynamic behavior of fluids near the critical-point. *Annu. Rev. Phys. Chem.* 37 (1986), 189–222.
- [181] SETZMANN, U., AND WAGNER, W. A new equation of state and tables of thermodynamic properties for methane covering the range from the melting line to 625 K at pressures up to 1000 MPa. *J. Phys. Chem. Ref. Data* 20, 6 (1991), 1061–1151.
- [182] SKOROKHODOV, I. I., DITSENT, V. E., THERENTÉVA, N. A., AND ZOLOTAREVA, M. N. Pressure of the saturated vapor of polydiorganosiloxane. 1. Polydimethylsiloxane. *Deposited Doc. VINITI N2725-71 dep.* (1971), 11.
- [183] SOAVE, G. Equilibrium constants from a modified Redlich-Kwong equation of state. *Chem. Eng. Sci.* 27, 6 (June 1972), 1197–1203.
- [184] SPAN, R. *Multiparameter equations of state - An accurate source of thermodynamic property data.* Springer-Verlag, Berlin, 2000.
- [185] SPAN, R., AND WAGNER, W. A new equation of state for carbon dioxide covering the fluid region from the triple-point temperature to 1100 K at pressures up to 800 MPa. *J. Phys. Chem. Ref. Data* 25, 6 (1996), 1509–1596.
- [186] SPAN, R., AND WAGNER, W. Equations of state for technical applications. I. Simultaneously optimized functional forms for nonpolar and polar fluids. *Int. J. Thermophys.* 24, 1 (January 2003), 1–39.
- [187] SPAN, R., AND WAGNER, W. Equations of state for technical applications. II. Results for nonpolar fluids. *Int. J. Thermophys.* 24, 1 (January 2003), 41–109.
- [188] SPAN, R., WAGNER, W., LEMMON, E. W., AND JACBOSEN, R. T. Multiparameter equations of state - recent trends and future challenges. *Fluid Phase Equilib.* 183-184 (2001), 1–20.
- [189] STARLING, K. E. *Equation of state and computer prediction - Fluid thermodynamic properties for light petroleum substances.* Gulf Publishing Co., Huston, TX, 1973.
- [190] STRYJEK, R., AND VERA, J. H. PRSV: An improved Peng-Robinson equation of state for pure compounds and mixtures. *Can. J. Chem. Eng.* 64 (1986), 323–333.
- [191] STULL, D. R. Vapor pressure of pure substances. *Ind. Eng. Chem.* 39, 4 (1947), 517–540.
- [192] STUPOCHENKO, Y. V., LOSEV, S. A., AND OSIPOV, A. I. *Experimental study of shock-wave structure*, vol. 1 of *Applied physics and engineering.* Springer-Verlag, 1967, ch. 1, pp. 43–45.

- 
- [193] STUPOCHENKO, Y. V., LOSEV, S. A., AND OSIPOV, A. I. *Relaxation in shock waves*, vol. 1 of *Applied physics and engineering*. Springer-Verlag, 1967.
- [194] TANNO, H., KOMURO, T., TAKAHASHI, M., TAKAYAMA, K., OJIMA, H., AND ONAYA, S. Unsteady force measurement technique in shock tubes. *Rev. Sci. Instrum.* 75, 2 (2004), 532–536.
- [195] TAYLOR, J. R. *An introduction to error analysis : the study of uncertainties in physical measurements*. Sausalito : University Science Books, 1997.
- [196] THOMPSON, P. A fundamental derivative in gasdynamics. *Phys. Fluids* 14, 9 (16-19 August 1971), 1843–1849.
- [197] THOMPSON, P. A. *Compressible fluid dynamics*. McGraw-Hill, New York, NY, 1988, ch. 8.5, pp. 390–391.
- [198] THOMPSON, P. A. *Compressible fluid dynamics*. McGraw-Hill, New York, NY, 1988.
- [199] THOMPSON, P. A., CAROFANO, G. C., AND KIM, Y. Shock waves and phase changes in a large-heat-capacity fluid emerging from a tube. *J. Fluid Mech.* 166 (1986), 57–92.
- [200] THOMPSON, P. A., CHAVES, H., MEIER, G. E. A., KIM, Y., AND SPECKMANN, H.-D. Wave splitting in a fluid of large heat capacity. *J. Fluid Mech.* 185 (1987), 385–414.
- [201] THOMPSON, P. A., AND LAMBRAKIS, K. C. Negative shock waves. *J. Fluid Mech.* 60 (1973), 187–208.
- [202] THOMPSON, P. A., AND SULLIVAN, D. A. On the possibility of complete condensation shocks in retrograde fluids. *J. Fluid. Mech.* 70 (1975), 639–649.
- [203] THOMPSON, R. Heats of combustion and formation of some linear polydimethylsiloxanes; the Si-C and Si-O bond-energy terms. *J. Chem. Soc.* (1953), 1908 – 1914.
- [204] TRIMPI, R. L., AND COHEN, N. B. A nonlinear theory for predicting the effects of unsteady laminar, turbulent, or transitional boundary layers on the attenuation of shock waves in shock tubes. Technical Note TN 4347, National Advisory Committee for Aeronautics NACA, 1958.
- [205] TRUSLER, J. P. M. *Physical acoustics and metrology of fluids*. The Adam Hilger series on measurement science and technology. Adam Hilger (IOP Publishing Ltd.), Bristol, England, 1991.

- 
- [206] UDAGAWA, S., GAREN, W., MEYERER, B., AND MAENO, K. Motion analysis of a diaphragmless driver section for a narrow channel shock tube. *Shock Waves* 18, 5 (2008), 345–351.
- [207] VAN PUTTEN, H., AND COLONNA, P. Dynamic model of a small biomass fired steam power plant. In 3<sup>rd</sup> *International Energy Conversion Engineering Conference (IECEC)* (2008), no. 2005-5638, AIAA.
- [208] VAN DYKE, M. *An album of fluid motion*. The parabolic press, Stanford, CA., USA, 1982.
- [209] VASU, S. S., DAVIDSON, D. F., AND HANSON, R. K. Jet fuel ignition delay times: Shock tube experiments over wide conditions and surrogate model predictions. *Combust. Flame* 152, 1-2 (2008), 125–143.
- [210] VORONKOV, M. G., PAVLOV, S. F., AND DUBINSKAYA, E. I. Cleavage of the Si-O-Si grouping by tetrachlorosilane and organylchlorosilanes. *Dokl. Chem.* 227 (1976), 198–201.
- [211] VORONKOV, M. G., PAVLOV, S. F., AND DUBINSKAYA, E. I. Reaction of organylalkoxysilanes with iodotrimethylsilane. *Dokl. Chem.* 227 (1976), 218.
- [212] WAGNER, W., AND PRUSS, A. The IAPWS formulation 1995 for the thermodynamic properties of ordinary water substance for general and scientific use. *J. Phys. Chem. Ref. Data* 31, 2 (2002), 387–535.
- [213] WATERMAN, H. I., VAN HERWIJEN, W., AND DENHARTOG, H. W. Statistical-graphical survey of series of linear and cyclic dimethylsiloxanes. *J. Appl. Chem.* 8 (1958), 625.
- [214] WEISSLER, A. Ultrasonic investigation of molecular properties of liquids III. Linear polymethylsiloxanes. *J. Am. Chem. Soc.* 71 (1949), 93–95.
- [215] WEN, J., THOMPSON, M., AND LIGHTSTONE, M. Numerical study of carbonaceous nanoparticle formation behind shock waves. *Combust. Theor. Model.* 10, 2 (2006), 257–272.
- [216] WILCOCK, D. F. Vapor pressure-viscosity relations in methylpolysiloxanes. *J. Am. Chem. Soc.* 68 (1946), 691–696.
- [217] WILCOCK, D. F. Vapor pressure-viscosity relations in methylpolysiloxanes. *J. Chem. Am. Soc.* 68 (April 1946), 691–696.
- [218] WONG, D. S. H., AND SANDLER, S. I. A theoretically correct mixing rule for cubic equations of state. *AIChEJ.* 38 (1992), 671–680.
- [219] WYCZALKOWSKA, A. K., AND SENEGERS, J. V. Thermodynamic properties of sulfurhexafluoride in the critical region. *J. Chem. Phys.* 111, 4 (1999), 1551–1560.

- 
- [220] YANG, C. N., AND YANG, C. P. Critical point in liquid-gas transitions. *Phys. Rev. Lett.* 13, 9 (1964), 303–305.
- [221] YOUNG, C. Gas-liquid critical temperatures of polydimethylsiloxanes mixtures. *J. Chem. Soc., Faraday Trans., II* 68 (1972), 580–585.
- [222] ZABELINSKII, I., NABOKO, I., TARASENKO, M., AND SHATALOV, O. Distortion of the shock front in a shock tube with a divergent conical transition section. *Fluid Dyn.* 26, 4 (1991), 593–598.
- [223] ZAMFIRESCU, C., COLONNA, P., AND GUARDONE, A. Maximum wave Mach number of rarefaction shocks in selected BZT fluids. In *5<sup>th</sup> International Conference on Heat Transfer, Fluid Mechanics and Thermodynamics (HEFAT2007)* (Sun City, South Africa, 1-4 July 2007), no. ZC1, pp. 1–6.
- [224] ZAMFIRESCU, C., COLONNA, P., GUARDONE, A., AND NANNAN, R. Experimental options to investigate BZT effects in dense gases. Tech. Rep. ET-2188, Delft University of Technology, 3mE Faculty, Mekelweg 2, 2628 CD Delft, January 2005.
- [225] ZAMFIRESCU, C., GUARDONE, A., AND COLONNA, P. Preliminary design of the FAST dense gas Ludwieg tube. In *9<sup>th</sup> AIAA/ASME Joint Thermophysics and Heat Transfer Conference* (San Francisco, CA, June 2006), no. AIAA 2006-3249, American Institute of Aeronautics and Astronautics, pp. 1–14.
- [226] ZAMFIRESCU, C., GUARDONE, A., AND COLONNA, P. Admissibility region for rarefaction shock waves in dense gases. *J. Fluid Mech.* 599 (2008), 363–381.
- [227] ZAPPOLI, B. The response of a nearly supercritical pure fluid to a thermal disturbance. *Phys. Fluids A* 4, 5 (1992), 1040–1048.
- [228] ZAPPOLI, B., BAILLY, D., GARRABOS, Y., LE NEINDRE, B., GUENOUN, P., AND BEYSENS, D. Anomalous heat transport by the piston effect in supercritical fluids under zero gravity. *Phys. Rev. A* 85 (1990), 2264–2267.
- [229] ZAPPOLI, B., AND CARLÈS, P. Acoustic saturation of the critical speeding up. *Physica D* 89, 3-4 (1996), 381–394.
- [230] ZAPPOLI, B., CARLÈS, P., AMIROUDINE, S., AND OUAZZANI, J. Inversion of acoustic waves reflection rules in near critical pure fluids. *Phys. Fluids* 7, 9 (1995), 2283–2287.
- [231] ZEL'DOVICH, Y. B. On the possibility of rarefaction shock waves. *Zh. Eksp. Teor. Fiz.* 4 (1946), 363–364.
- [232] ZEL'DOVICH, Y. B., AND RAIZER, Y. P. *Physics of shock waves and high-temperature hydrodynamic phenomena*, vol. 1-2. Academic Press, New York, 1966-1967.

- 
- [233] ZÉMPLEN, G. On the possibility of negative shock waves in gas. *Comptes rendues de l'Académie des Sciences 141* (1905), 710–713.
- [234] ZHUKOV, V. P., SECHENOVA, V. A., AND STARIKOVSKIIA, A. YU. Autoignition of n-decane at high pressure. *Combust. Flame 153*, 1-2 (2008), 130–136.



# Acknowledgements - short version

During these 4+ years I have learned much and have come to know many people, many of which I consider good friends. This work is also the result of their valuable support during this research period and therefore, I dedicate this work to them.

First of all, I would like to thank with much sincerity, my supervisor, Piero Colonna. From the start in 2004 you have taught me much. Though it has been a bit difficult from time to time, we were almost always successful in our efforts. This work is also to a great extent due of your skills in guiding research and your preparatory work in the past.

Secondly, I would like to thank my other collaborators, whom I also consider my supervisors, Calin Zamfirescu and Alberto Guardone. They were pillars during my work. People with whom I could talk about scientific work and also with whom I could have a good time. I have benefited from their experience and input. I am also indebted to Prof. Rini van Dongen for critically reviewing this work and dedicating time to it. Thank you for the feedback. I would also like to thank Ruud van den Boom for assisting in the preliminary design phase of the facility and Andre Buurman and DEMO staff members for helping with the programming of the DAQ&C-system.

I greatly appreciate the support I got from my parents and my family here in the Netherlands. I can boast that I have finished this work because of you. In this respect I am indebted to my aunt Seetha who was the person to motivate me in taking on this job and being there if I needed someone to talk to or needed help. Many thanks for this.

I would like to express my gratitude to the people I met in the US during the period I spent at NIST. I express my thankfulness to Mike Moldover, John Hurly and Roberto Gavioso. My words of gratitude go also to Laurell and Carol. Finally, I would like to thank my peers, especially my office mates. Thanks Marcin, Eleonora, Jacopo for listening to my frequent (probably too frequent) complaints about almost everything. Thank you Frits and Bert for your support in the laboratory. Thanks, Gianluca, Mattia, Teus and Monica for the company. A special word of gratitude goes to Hans and John, with whom I have worked a lot in these years and from whom I have learned much about modeling. Finally, I would like to thank my very good friends Andrea, Miguel, Sergio, Alberto and Martina, and the guys in Suriname, Danny and Amrish, for all their help and for

---

making this work more than just mental masturbation.

Although I filled this work with a lot of Bushisms, I do have to place the following quote from Watchmen (it says something about who and the type of person I am): Rorschach: "None of you understand. I'm not locked up in here with you. You're locked up in here with me."

# Curriculum Vitae

Ryan Nannan was born on November 7, 1980 in Paramaribo, Suriname. In Suriname, after graduating from the Algemene Middelbare School (AMS) in 1998, he started his studies in mechanical engineering at the University of Suriname, AdeKUS. There, he obtained his BSc degree in December 2002 with honors and pursued a Masters degree in the field of Process and Energy Technology in the Netherlands at the Delft University of Technology. In 2004, he obtained his MSc degree with honors and soon after, he started his doctoral research in the field of advanced energy systems. During this period, he has worked as a guest researcher at the National Institute of Standards and Technology (NIST) in the U.S. for two months and has extensively collaborated with researchers from the U.S. and Italy. Since 2007 he is also a part-time lecturer at the AdeKUS.

## Publications

### Peer-reviewed journals:

Colonna, P., Nannan, N.R., Guardone, A., Stelt van der, T.P., "On the computation of the fundamental derivative of gas dynamics  $\Gamma$ , using equations of state", *Fluid Phase Equilibria* (2009) (accepted for publication).

Nannan, N.R., Colonna, P., "Improvement on multiparameter equations of state for dimethylsiloxanes by adopting more accurate ideal-gas isobaric heat capacities: supplementary to P. Colonna, N.R. Nannan, A. Guardone, E.W. Lemmon, *Fluid Phase Equilib.* 244, 193 (2006)", *Fluid Phase Equilibria* (2009) (in press).

Nannan, N.R., Lucchini, A., Colonna, P., "Admissibility of nonclassical shock waves in near-critical single-component fluids – new findings", *Annual Report & Research Programme 2007-2008* (2009) (JMBC Highlight).

Colonna, P., Guardone, A., Nannan, N.R., Zamfirescu, C., "Design of the dense gas flexible asymmetric shock tube", *Journal of Fluids Engineering, Transactions of the ASME* (2008) 130 (3), pp. 0345011-0345016.

Colonna, P., Nannan, N.R., Guardone, A., "Multiparameter equations of state for siloxanes:  $[(\text{CH}_3)_3\text{-Si-O}_{1/2}]_2\text{-[O-Si-(CH}_3)_2]_{i=1,\dots,3}$  and  $[\text{O-Si-(CH}_3)_2]_6$ ", *Fluid Phase Equilibria* (2008) 263 (2), pp. 115-130.

---

Nannan, N.R., Colonna, P., Tracy, C.M., Rowley, R.L., Hurly, J.J., “Ideal-gas heat capacities of dimethylsiloxanes from speed-of-sound measurements and ab initio calculations”, *Fluid Phase Equilibria* (2007) 257 (1), pp. 102-113.

Colonna, P., Guardone, A., Nannan, N.R., “Siloxanes: A new class of candidate Bethe-Zel’dovich-Thompson fluids”, *Physics of Fluids* (2007) 19, art. no. 086102 (12 pages).

Colonna, P., Nannan, N.R., Guardone, A., Lemmon, E.W., “Multiparameter equations of state for selected siloxanes”, *Fluid Phase Equilibria* (2006) 244 (2), pp. 193-211.

### **Conference publications:**

Colonna, P., Guardone, A., Nannan, N.R., “The thermodynamic region of negative nonlinearity in selected siloxanes predicted by modern thermodynamic models”, in 15<sup>th</sup> U. S. National Congress on Theoretical and Applied Mechanics, (Boulder, CO), June 25-29, 2006.

Nannan, N.R., Hurly, J.J., Colonna, P., “Speed of sound and ideal-gas heat capacity data of selected siloxanes from acoustic measurements:  $[(\text{CH}_3)_2\text{SiO}]_4$  and  $[(\text{CH}_3)_2\text{SiO}]_5$ ”, in Thermo International 2006/Sixteenth Symposium on Thermophysical Properties (G. Hardin, C. Muzny, and D. Friend, eds.), pp. 1-19, NIST, ASME, AIChE, IACT, and IUPAC, July-August 2006.

### **(Selected) Internal reports:**

Zamfirescu, C., Nannan, N.R., Marin, M., Infante-Ferreira, C.A., “Oil-free two-phase ammonia(water) compressor”, Final Report K-336, Delft University of Technology, P&E department, January 2004 (BSE-NEO 0268.02.03.03.0002).

Zamfirescu, C., Colonna, P., Nannan, N.R., Guardone, A., “Experimental options to investigate BZT effects in dense gases”, Technical Report ET-2188, Delft University of Technology, P&E department, January 2005.

Nannan, N.R., Zamfirescu, C., Colonna, P., “Detailed design of the Flexible Asymmetric Shock Tube (FAST) at the P&E department of the Delft University of Technology”, Technical Report ET-2263, Delft University of Technology, P&E department, October 2007.

Colonna, P., Albrigo, D.M., Nannan, N.R., “Binary organic Rankine turbogenerator: a viable option for record high efficiency”, Technical Report ET-2270, Delft

---

University of Technology, P&E department, December 2007 (CONFIDENTIAL).

Nannan, N.R., Stelt van der, T.P., Colonna, P., "Thermodynamic properties of single-component fluids in the vapor-liquid equilibrium region", Technical Report ET-2333, Delft University of Technology, P&E department, November 2008.